PINCER COMPLEXES OF PRECIOUS METALS

Javier Grajeda

A dissertation submitted to the faculty at the University of North Carolina at Chapel Hill in partial fulfillment of the requirements for the degree of Doctor of Philosophy in the Department of Chemistry.

Chapel Hill
2018

Approved by:

Alexander J. M. Miller

Thomas J. Meyer

Gerald J. Meyer

Frank A. Leibfarth

Jeffrey S. Johnson

ABSTRACT

Javier Grajeda: Pincer Complexes of Precious Metals
(Under the direction of Alexander J. M. Miller)

The synthesis and characterization of several new iridium(I) and iridium(III) carbonyl complexes supported by aminophosphinite pincer ligands is reported. A surprising diversity of reaction pathways were accessible upon treatment of Ir carbonyl complexes with salts of redox-inactive alkali, alkaline earth, and lanthanide metal cations. Iridium(III) hydridocarbonyl chloride complexes underwent either halide abstraction or halide substitution reactions, whereas iridium(I) carbonyl complexes underwent protonative oxidative addition reactions. When the nitrogen donor of the pincer ligand is an aza-crown ether macrocycle, cation–macrocycle interactions can be supported, leading to divergent reactivity in some cases.

New iridium and rhodium complexes supported by aminophosphinite pincer-crown ether ligands were synthesized. Iridium-catalyzed hydroformylation of allylbenzene was explored. Catalytic amounts of LiOTf (OTf = trifluoromethanesulfonate) doubled the rate of hydrofunctionalization. The iridium pincer complexes were found to undergo remetallation pathways under the conditions of catalysis. This guided the design of a new, more active iridium catalyst supported by a pincer ligand with a methoxy substituent incorporated to prevent remetallation. Rhodium-catalyzed hydroformylation of 1-octene was explored as well. A systematic decrease in the n (linear) to iso (branched) aldehyde ratio was observed in

the presence of increasingly bulky ammonium additives. However, catalyst stability studies showed that rhodium pincer complexes undergo decomposition under hydroformylation conditions and presumably simply act as pre-catalysts.

The first mononuclear gold(III) PNP pincer complexes (PNP = bis(2-diisopropylphosphinophenyl)amide) are reported. The chloro complex [(PNP)Au(Cl)][OAc^F] (OAc^F = OCOCF$_3$) was synthesized by microwave irradiation of a tetrachloroaurate salt and the neutral PNHP ligand. Dehalogenation with AgOAc^F afforded the trifluoroacetate-bound complex [(PNP)Au(OAc^F)][OAc^F]. Electronic absorption spectroscopy and time-dependent density functional theory studies assigned the electronic transition that imbues the complexes with a deep royal blue color. The Au(III) trifluoroacetate complex is surprisingly stable, and no reactivity towards ethylene was observed, even under high pressures and at high temperatures. Density functional theory calculations suggest that the lack of reactivity is due to the high energy of the putative dicationic ethylene-bound intermediate invoked in a formal insertion reaction.

ACKNOWLEDGEMENTS

TABLE OF CONTENTS

LIST OF FIGURES

xii

xvi

LIST OF SCHEMES

LIST OF TABLES

LIST OF ABBREVIATIONS AND SYMBOLS

°	degree(s)
α	Greek alpha: crystallographic angle
β	Greek beta: crystallographic angle
γ	Greek gamma: crystallographic angle
δ	Greek delta: denotes chemical shift reference scale
η	Greek eta: ligand hapticity
κ	Greek kappa: denotes coordination to metal by x atoms
ν	Greek mu: IR absorption band frequency
π	Greek pi: denotes bond
θ	Greek theta: general angle
σ	Greek sigma: denotes coordination to a metal via a single atom
Δ	Greek capital delta: denotes separation between values or applied heat
a,b,c	crystallographic unit cell parameters
Å	angstrom(s)
atm	Atmosphere
Ar	general aromatic
BAr^F_4	tetrakis(3,5-trifluoromethylphenyl)borate
^{13}C	Carbon NMR
C	Celsius
cm^{-1}	wavenumber
°	Degree
D	Deuterium

d	doublet
DFT	Density Functional Theory
DBU	1,8-diazabicyclo[5.4.0]undec-7-ene
e^-	Electron
$\Delta G°$	standard Gibbs energy
eq	equation
equiv	equivalents
Et	ethyl, $-CH_2CH_3$
^{19}F	Fluorine NMR
g	Gram
h	hour(s)
Hz	Hertz
PF_6^-	Hexafluorophosphate
IR	infrared
Ir-H	Iridium-hydrogen bond
Ir-O	Iridium-oxygen bond
$^xJ_{YZ}$	magnetic coupling between atoms X and Y through a distance of x bonds
K	Kelvin
kcal	kilocalorie
L	general ligand, usually 2 e^- donor
M	Molar
M	general metal atom
μL	Microliter

mg	Milligram
mL	Milliliter
mM	Millimolar
mmol	Millimole
min	Minute
m	multiplet
m	meta
Me	methyl, $-CH_3$
min	minute(s)
mol	mole
*n*Bu	*n*-butyl, $-C_4H_9$
NMR	nuclear magnetic resonance
o	ortho
OAc^F	trifluoroacetate: $OCOCF_3$
OTf	triflate, trifluoromethane sulfonate: $CF_3SO_3^-$
^{31}P	Phosphorous NMR
p	para
Ph	phenyl, $-C_6H_5$
ppm	parts per million
^1H	Proton NMR
q	quartet
R	general alkyl group
R, R_W	crystallographic refinement quality indicators

s	singlet (NMR data)
s	second
*s*Bu	*s*-butyl, $CH(CH_3)CH_2CH_3$
t	triplet
*t*Bu	tertiary butyl, $-C(CH_3)_3$
TD-DFT	Time-Dependent Density Functional Theory
THF	tetrahydrofuran
TOF	Turnover frequency
TON	Turnover number
X	general halogen atom

Chapter 1   PINCER COMPLEXES AND THEIR APPLICATIONS IN ALKENE FUNCTIONALIZATION

Section 1.1   Pincer Ligands: Tunable Ligand Platforms

Since the first reports of pincer ligands in the 1970s, this class of ligands has proven to be a highly versatile platform in the field of coordination chemistry.[1] The term "pincer", first coined by van Koten in 1989, originally referred to a tridentate ligand framework composed of a central, monoanionic aryl group, flanked by two donors (PR_2, NR_2, SR) further capable of binding the metal center to enforce a meridional coordination environment.[2] With the advent of new ligand designs, the term has evolved to encompass a far wider range of ligands. Herein, the term is used to refer to ligands that adopt a tridentate, meridional coordination mode (Figure 1.1).
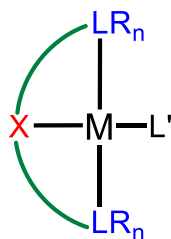
LR_n *steric control by variations in R*
electronic control by variations in L and R

X *electronic control (trans influence)*

linker effects via ring size and bite angle effects

Figure 1.1 Design factors of pincer ligands.

In 1974, Shaw and Uttley reported that bulky tertiary phosphine ligands yielded PC-cyclometallated species of platinum (Figure 1.2).[3] Recognizing the potential of this type of ligand backbone, Shaw and Moulton hypothesized that installing a second bulky phopshine *ortho* to the metallated carbon site would yield a tridentate-bound metal complex.[4] In this seminal work, the reported PCP ligand was metallated with group 9 and 10 metals to afford the first examples of transition metal pincer complexes (Figure 1.3).
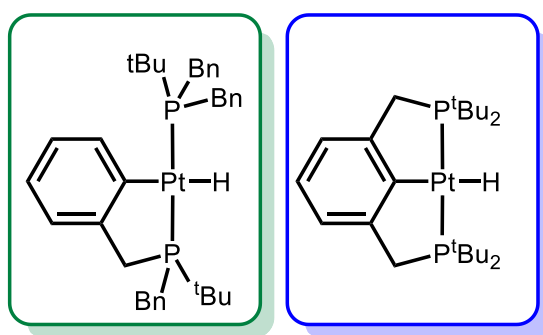
Figure 1.2 Bidentate and tridentate cyclometalated complexes of platinum.

P^{t}Bu$_2$ P^{t}Bu$_2$

M—X   M—Cl

P^{t}Bu$_2$ H

     P^{t}Bu$_2$

M = Ni, Pd, Pt   M = Rh, Ir
X = Cl, H
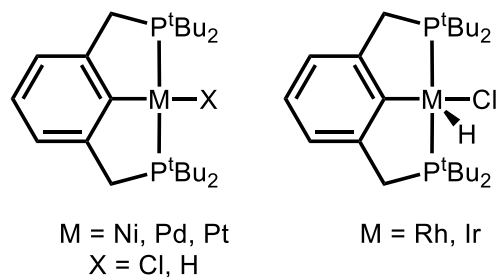
Figure 1.3 Selected examples of group 9 and 10 pincer complexes reported by Shaw and co-workers.

Since this early report, many classes of pincer ligands have been developed, which can span from neutral to mono-, di-, and trianionic.[5] The anionic (X) donors can be located across different sites of the pincer. The position and nature of different donor groups, X or neutral (L) donors, can be rationally designed to promote specific reactivity of the resulting metal complexes. The modular nature of these ligand scaffolds allows for incorporation of different steric and electronic profiles to influence the reactivity at the metal center. The ligand backbone can also be modified to control the electronic properties at the metal center.

Pincer complexes have been widely used to catalyze various organic transformations.[6–8] The tridentate binding mode imparts stability to the resulting metal complexes, enabling them to successfully withstand a variety of reaction conditions. Pincer complexes of iridium have been successfully used as catalysts for alkane dehydrogenation (Scheme 1.1). The thermal stability conferred by these pincer ligand frameworks allows these catalysts to operate at very high temperatures (200-250 °C). However, under certain reaction conditions, decomposition of pincer complexes to afford M(0) species is possible, processes often triggered by dissociation of one of the chelating arms.[9,10] This is an important consideration when invoking mechanisms for organic transformations catalyzed by pincer complexes.
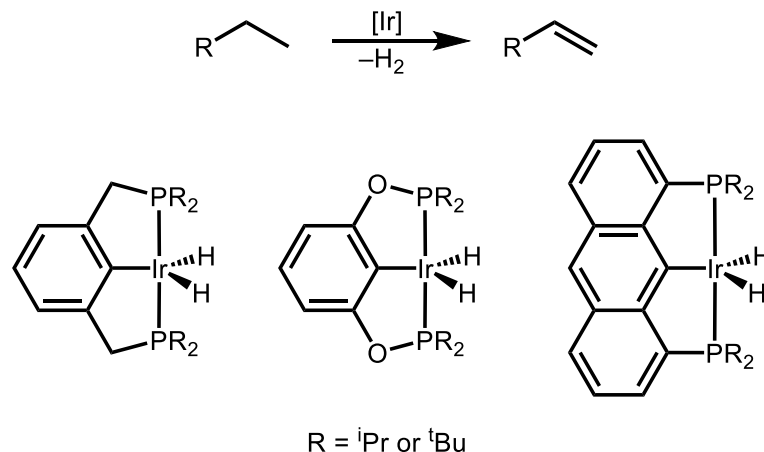
Scheme 1.1 Alkane dehydrogenation and selected examples of iridium pincer complexes used in this transformation.

Section 1.2   Pincer Ligands with New Functionalities

Since the early work by Shaw, the field has rapidly progressed to include many new capabilities by variation of central anchors, linker sizes, and flanking donors. For example, new pincer ligand designs allow for the isomerization between meridional and facial tridentate coordination modes.[5,11,12] A typical example comes from PSiP ligands, where the sp^3 hybridization at the Si central donor allows for meridional/facial ligand rearrangement (Scheme 1.2).[13] For the PSiP complex of iridium shown, the traditional meridional pincer coordination mode was found to be favored at lower temperatures.
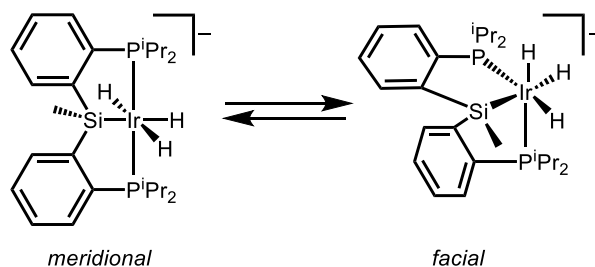
Scheme 1.2 Interconversion between meridional and facial coordination modes with an iridium PSiP system.

One of the most exciting developments in the field has been the incorporation of hemilability, defined as the property of hybrid polydentate ligands where a weak donor in the framework can dissociate from the metal to provide a site for a substrate to bind, while other strong donors remain coordinated.[14] By extending the arm length of PCN pincer ligands, Milstein and co-workers discovered new reactivity pathways promoted by amine dissociation from a platinum metal center (Scheme 1.3).[15] Upon binding of H_2 to the metal center, the amine donor acts as an internal base to generate a Pt–H species and dissociates as a cationic $[RNHMe_2]^+$ group. Amine dissociation triggers reductive elimination of the hydride onto the aryl backbone. The resulting Pt(0) species eventually funnels into the platinum cluster depicted in Scheme 1.3. Conversely, the analogue with a shorter methylene linker did not react with H_2.
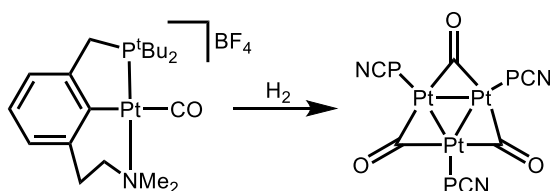
Scheme 1.3 Formation a platinum cluster, promoted by amine arm hemilability.

The Milstein group also reported the synthesis of a ruthenium complex supported by a neutral PNN, which in the presence of KO^tBu undergoes deprotonation at the benzylic phopshine arm, rather than at the metal hydride (Scheme 1.4).[16] This complex has been used in numerous catalytic applications, including dehydrogenative alcohol esterification,[16] dehydrogenative coupling of alcohols and amines to yield amides,[17] and alkene isomerization.[18] The aromatization/dearomatization of the ligand backbone, as well as dissociation of the hemilabile amine donor from the metal center, have been invoked as likely steps in catalytic cycles with this complex.[19]

5
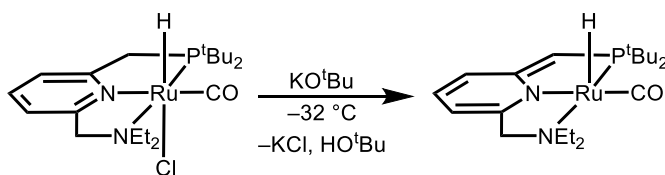
Scheme 1.4 Dearomatization of a Ru PNN pincer complex.

More recently, new approaches have emerged to further control and enhance reactivity with pincer complexes.[20] A promising approach involves the incorporation of Lewis acidic/basic groups on the secondary coordination sphere of the pincer framework. Szymczak and co-workers have studied this approach using terpyridine-based pincer ligands bearing Lewis acidic and/or basic sites. They reported a vanadium complex with a morpholino and borane substituents, capable of stabilizing the first example of an η^2-[N$_2$H$_3$]$^-$ ligand on vanadium obtained upon reaction with N$_2$H$_4$ and NEt$_3$ (Scheme 1.5).[21] The [N$_2$H$_3$]$^-$ ligand interacts with both the Lewis acidic and basic appended functional groups. An iron complex supported by a similar system, but bearing two Lewis acidic substituents, afforded cleavage of the N–N bond of N$_2$H$_4$, with the resulting amido fragments stabilized by the Lewis acidic borane groups (Scheme 1.6).[22] The amido ligands could be protonated to generate NH$_3$ ligands that still interacted with the boranes. These NH$_3$ ligands could then be released upon further addition of N$_2$H$_4$.
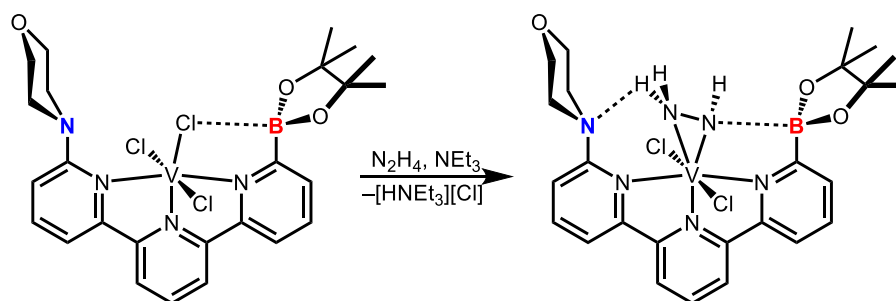
Scheme 1.5 Terpyridine-based complex bearing Lewis acidic/basic appended groups and its reactivity towards N$_2$H$_4$.
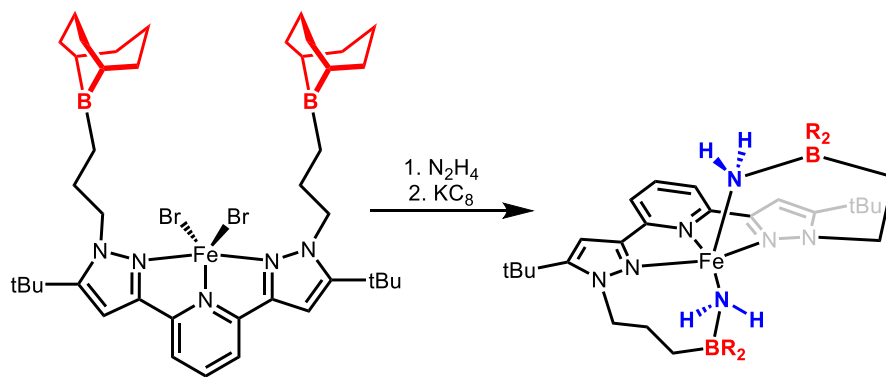
Scheme 1.6 N–N bond cleavage by an iron NNN pincer complex bearing Lewis acidic boranes.

Pincer-crown ether ligands with an appended macrocycle capable of binding Lewis acids represent a new avenue to control reactivity at metal pincer complexes.[23] Kita and Miller reported the synthesis of an NCOP iridium hydridochloride pincer complex (Scheme 1.7). [24] In weakly coordinating solvents like methylene chloride, the oxygen donors of the macrocycle complete the coordination sphere at iridium. Abstracting the halide *cis* to the hydride afforded a pentadentate, cationic complex capable of catalyzing allylbenzene isomerization to β-methylstyrene.[25] Catalysis could be turned off by addition of chloride to reform the hydridochloride complex. In the presence of Na$^+$ and Li$^+$ additives, impressive rate enhancements were observed for the isomerization reaction, increasing the turnover frequency from ~2 h^{-1} to 2000 h^{-1} in the presence of catalytic amounts of Li$^+$ additive. Understanding the effects of cationic additives on the reactivity of pincer-crown ether complexes will enable better control over their use in a variety organic transformations. To this end, the reactivity of pincer-crown ether complexes of iridium with a variety of Lewis acidic additives is discussed in Chapter 2.
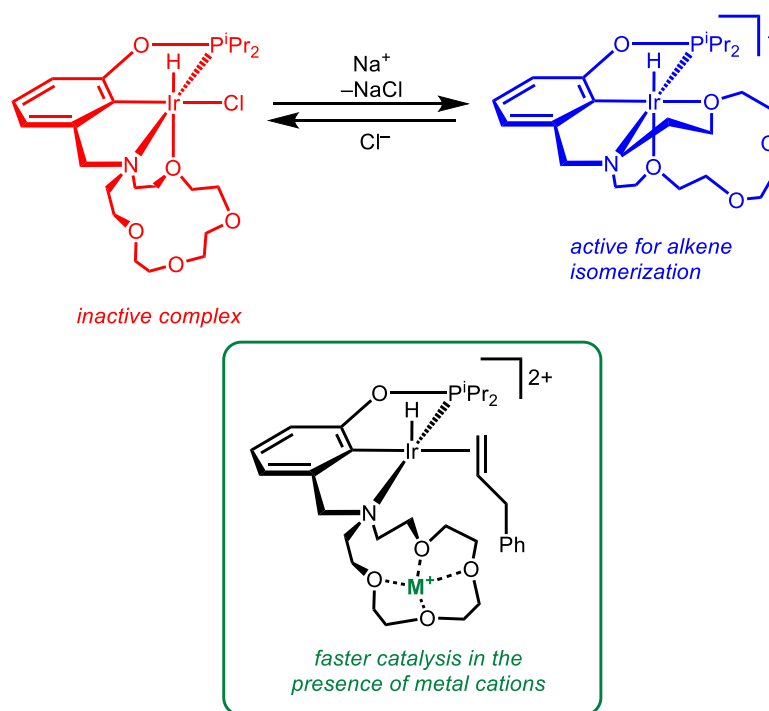
Scheme 1.7 Pincer-crown ether complexes of iridium and different available binding modes and catalytic states.

Section 1.3   Pincer Complexes in Alkene Functionalization

Homogeneous Alkene Functionalization in the Chemical Industry

In the mid-20th century, the discovery and development of catalytic reactions of alkenes had a major impact in the chemical industry.[26] One of the most notable examples is the Wacker process, in which ethylene is oxidized to acetaldehyde, catalyzed by aqueous solutions of $PdCl_2$ with $CuCl_2$ as a co-catalyst (Scheme 1.8).[27,28] The catalytic cycle involves the formation of Pd(0), with $CuCl_2$ acting as an oxidant to regenerate a Pd(II) species. First reported in the 1950s, this homogeneously-catalyzed process remains the primary means of production of acetaldehyde, an important intermediate in the production of butanol, 2-ethylhexanol, chlorinated acetaldehydes, alkyl amines, and other chemicals.[29] More than a half century later the mechanism of this reaction remains the subject of intense study.[30]

$$\text{---} \quad + \quad ^1/_2\ O_2 \quad \xrightarrow[\text{H}_2\text{O}]{\text{PdCl}_2/\text{CuCl}_2} \quad \diagdown\!\!\diagup\!\!\diagdown_\text{O}$$
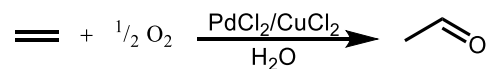
Scheme 1.8 Pd/Cu-catalyzed oxidation of ethylene to acetaldehyde (Wacker process).

Alkene hydrocyanation is another highly relevant example of industrial-scale alkene functionalization.[31] The reaction involves the addition of HCN across a C=C bond to yield nitriles. Researchers at DuPont reported the use of nickel phosphite catalysts for the double hydrocyanation of 1,3-butadiene to adiponitrile (Scheme 1.9).[32,33] This process generates about one million tons of adiponitrile annually, which is further funneled into the production of nylon-6,6.[34]

$$\diagup\!\!\diagdown\!\!\diagup \quad \xrightarrow[\text{HCN}]{\text{Ni/L}} \quad \diagup\!\!\diagdown\!\!\diagup_\text{CN} \quad \xrightarrow[\text{HCN}]{\text{Ni/L, Lewis acid}} \quad \text{NC}\diagdown\!\!\diagup\!\!\diagdown\!\!\diagup_\text{CN}$$

adiponitrile
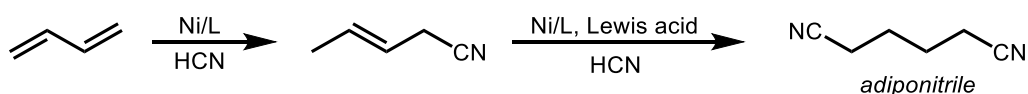
Scheme 1.9 Double hydrocyanation of 1,3-butadiene (DuPont process).

Hydroformylation refers to the addition of a formyl (CHO) group and a hydrogen atom to an alkene, generating either linear (normal, *n*) or branched (*iso*) aldehydes. This process represents one of the most successful and highly studied examples of homogeneous catalysis applied on an industrial scale.[35] During 2008, almost 10.4 million metric tons of aldehydes were produced for further use in the synthesis of alcohols, esters, and amines. The hydroformylation of propylene, typically catalyzed by rhodium complexes (Scheme 1.10), is the most important example of this functionalization carried out on an industrial scale.[36] A number of chemicals, including butanol, butylamine, and 2-ethylhexanol, are derived from butyraldehyde. Hydroformylation is the subject of Chapter 3 of this dissertation.
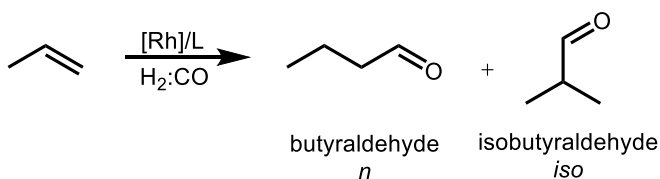
Scheme 1.10 Hydroformylation of propylene to afford *n* and *iso* aldehydes.

Alkene functionalization has been used successfully in the pharmaceutical industry as well.[37] In the synthesis of anti-inflammatory drug Naproxen, a Heck coupling of 2-bromo-6-methoxynaphthalene and ethylene yields 2-methoxy-6-vinylnaphthalene (Scheme 1.11).[38] Hydroxycarbonylation of this terminal alkene yields Naproxen. In the context of alkene hydroxy- and alkoxycarbonylation, direct esterification of alkenes with organic acids has long been recognized as a valuable and more direct route to a variety of esters.[39] In Chapter 4 we discuss our efforts towards achieving this goal using pincer complexes.
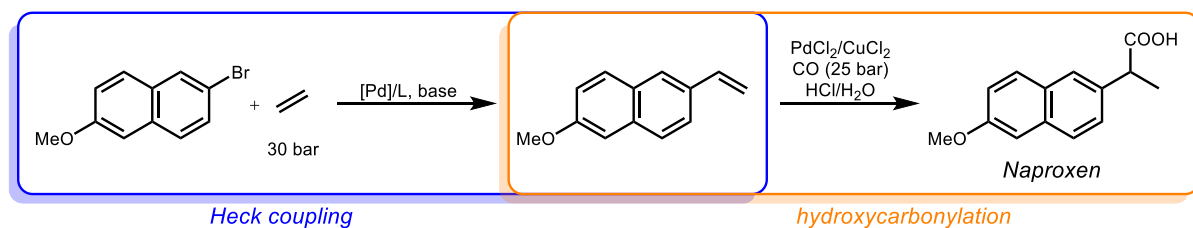
Scheme 1.11 Synthesis of Naproxen via Heck coupling and alkene hydroxycarbonylation.

Pincer Chemistry of Industrially Relevant Alkene Reactions

In the realm of pincer-catalyzed alkene functionalization, a vast amount of work has been done with palladium complexes.[6,7] Milstein and co-workers first reported the use of PCP pincer complexes for Heck coupling of olefins with aryl iodides and bromides (Scheme 1.12).[40] They stated that the pincer complexes were so thermally stable that they did not undergo decomposition even at 180 °C. Typical Heck reaction mechanisms involve a Pd(0)/Pd(II) cycle. Given that monoanionic pincer complexes of palladium decompose upon

10

reduction to Pd(0), a mechanism involving a Pd(II)/Pd(IV) catalytic cycle was proposed. A

similar mechanism was proposed by the Jensen group for the Heck coupling of alkenes and

aryl chlorides, involving the oxidative addition of styrene to a Pd(II) center (Scheme 1.13).[41]

X = Br, I
R = COOMe

[Pd]=

R' = ^{i}Pr, ^{t}Bu
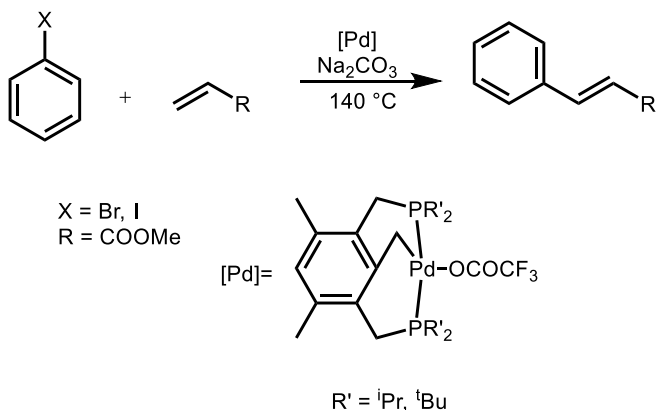
Scheme 1.12 Heck coupling catalyzed by Pd-pincer complexes.
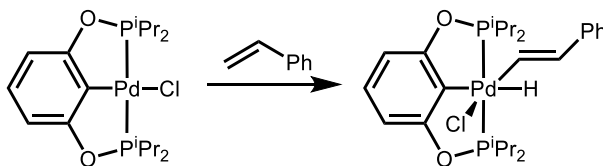
Scheme 1.13 Proposed oxidative addition of styrene to a Pd(II) POCOP complex.

These assertions were made on the basis that the pincer complexes were recovered

seemingly intact after the reaction. This Pd(II)/Pd(IV) cycle remains controversial, however.

It is now widely accepted that under the high temperatures required for these reactions, the

palladium pincers undergo degradation to afford catalytically active Pd(0).[9,10,42–44] In some

instances, the pincer complexes can be regenerated, but Pd(0) even in trace amounts of has

been shown to be very active in this type of coupling reaction.[45]

Using hypervalent iodonium salts as aryl sources, Szabó and co-workers have shown

that pincer complexes of palladium can plausibly catalyze the arylation of alkenes *via* a

Pd(II)/Pd(IV) cycle (Scheme 1.14).[46] These reactions could be carried out using milder

temperatures (50-65 °C). To confirm that Pd(0) was not the active species in these reactions they performed the mercury-drop test, carrying out the reactions in the presence of 150 equiv of mercury relative to palladium, obtaining essentially the same yields (>90%). Hypervalent iodonium salts have also been used in C–H borylation of alkenes catalyzed by palladium PNP pincer complexes.[47]
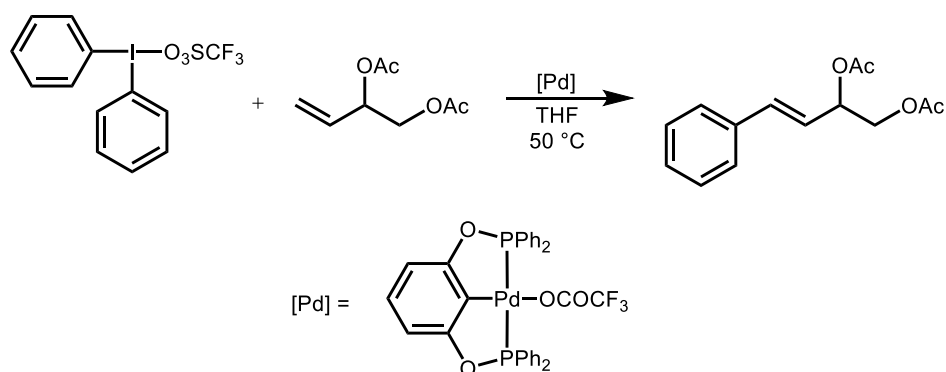
Scheme 1.14 Arylation of alkenes with a palladium pincer complex, using an iodonium salt as aryl source.

Pincer complexes with metals other than palladium have also been reported in catalytic alkene functionalization. Hydrosilylation of alkenes has been carried out with pincer complexes of iron.[48] Peng et al. utilized phosphinite-iminopyridine (PONN) complexes of iron to hydrosilylate various alkenes with high chemoselectivity (Scheme 1.15).[49] These complexes showed high selectivity for reactivity with alkenes in the presence of various functional group such as amides, esters, and ketones. NNN pincer complexes of nickel catalyze the tandem isomerization/hydrosilylation of internal alkenes (Scheme 1.16).[50] This remarkable tandem cycle was found to be tolerant of various functionalities as well, including esters, ethers, and amides.
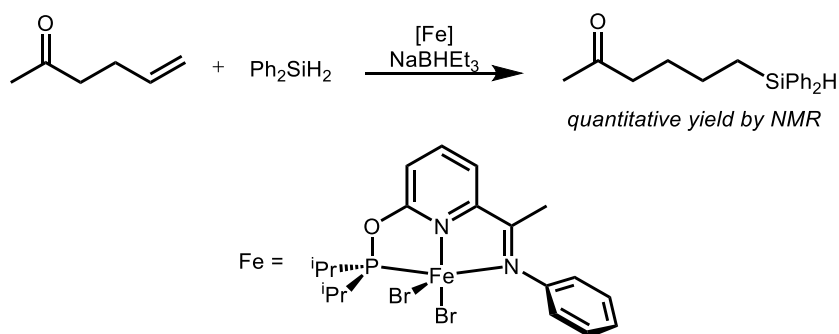
Scheme 1.15 Hydrosilylation of alkenes bearing carbonyl groups, catalyzed by an iron PONN pincer complex.
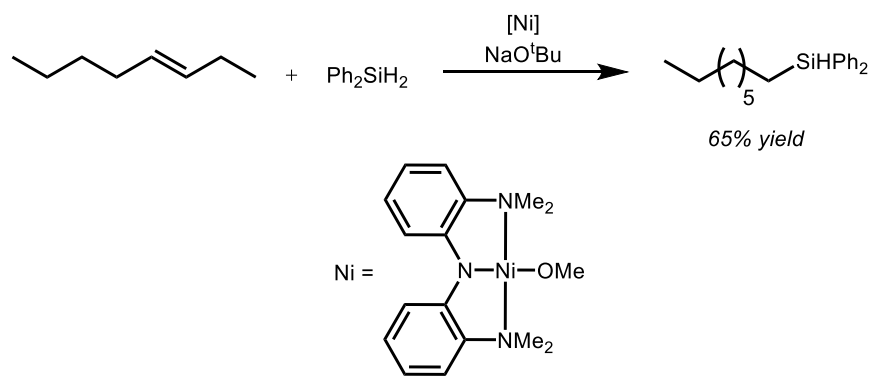
Scheme 1.16 Tandem isomerization/hydrosilylation of internal alkenes, catalyzed by a NNN Ni pincer complex.

Meek and co-workers have developed new rhodium bis(phopshine)carbodicarbene pincer complexes for diene hydroarylation (Scheme 1.17).[51] They found that catalytic activity is triggered by addition of Lewis acids like Li^+, Au^+, or Ag^+. They hypothesized that upon binding of a metal salt to the CDC backbone, electron density at rhodium and π-backbonding ability decrease, facilitating ligand substitution of styrene by the diene substrate. This type of pincer complexes has been further used for the hydroamination and hydroalkylation of dienes.[52–54]
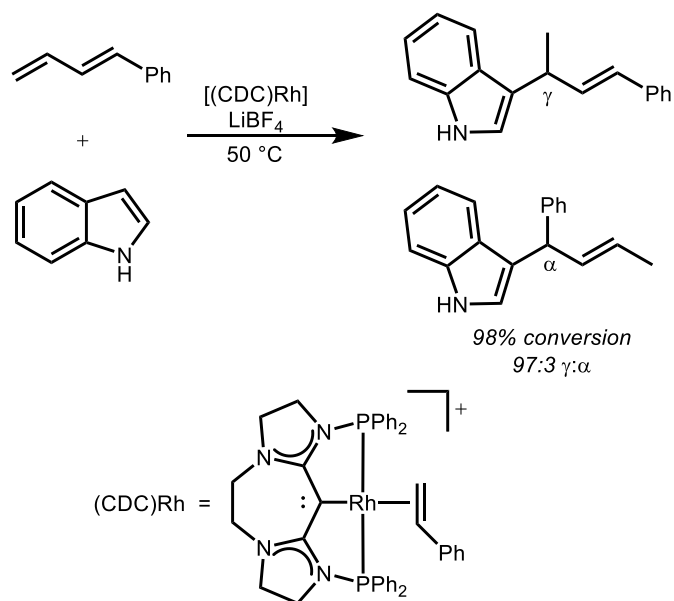
Scheme 1.17 Hydroarylation of alkenes with CDC pincer complexes of rhodium in the presence of Lewis acidic Li^+.

Pincer complexes have also been used in alkene hydroformylation. The groups of Mathey and Chen developed different PNP pincer ligands (Figure 1.4) that can be used in the rhodium-catalyzed hydroformylation of cyclic alkenes.[55,56] These ligands were added *in situ* in catalytic runs, with a $Rh(acac)(CO)_2$ metal precursor.
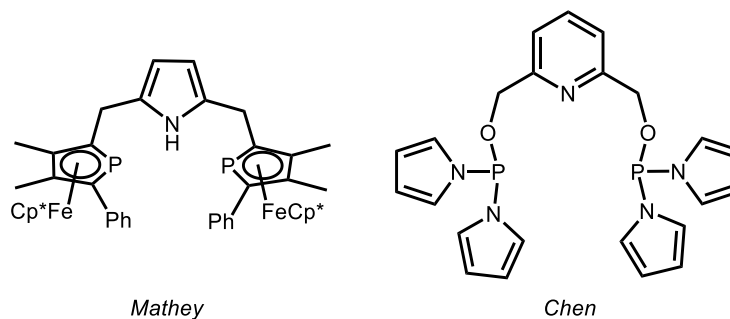
Figure 1.4 Selected examples of PNP ligands used for rhodium-catalyzed hydroformylation of cyclic alkenes.

Gelman and co-workers reported the use of $PC(sp^3)P$ pincer complexes of iridium and rhodium in alkene hydroformylation (Scheme 1.18).[57] The pincer ligand design incorporates a dangling hydroxyl group. They proposed a metal-ligand cooperative mechanism in which

14

the OH group assists in catalysis by releasing a proton to liberate the aldehyde product,

generating an iridium-alkoxide in the process (Scheme 1.19). Subsequent incorporation of H_2

regenerates an iridium hydride species with a dangling hydroxide group. In the case of

iridium, typical *n* (linear) to *iso* (branched) ratios of aldehydes were ~0.1:1. Hydrogenation

pathways were suppressed by performing the reactions in 1:24 mixtures of H_2:CO. The

rhodium complex displayed *n:iso* selectivity ranging from 0.5:1 to ~1:1, without any

hydrogenation detected.
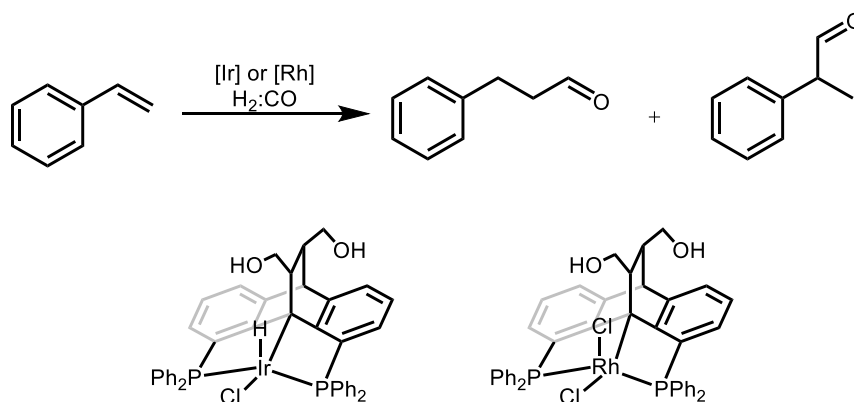
Scheme 1.18 Hydroformylation of styrene with iridium or rhodium PC(sp^3)P pincer complexes.
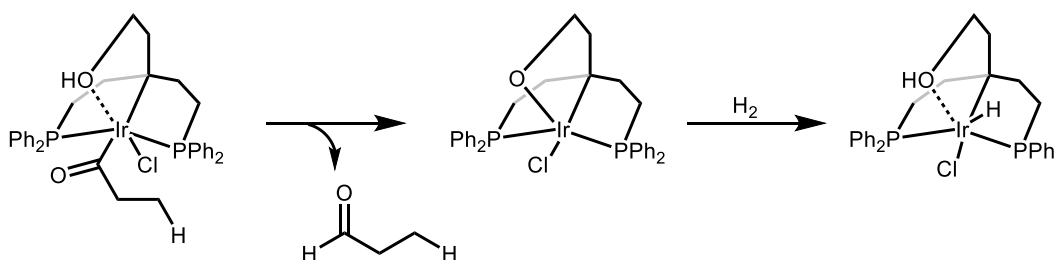
Scheme 1.19 Proposed metal-ligand cooperative mechanism for aldehyde release with an iridium PC(sp^3)P pincer complex.

Since the first report of pincer complexes, many breakthroughs have been reported on

new ways to promote reactivity with these versatile ligands. In catalytic alkene

functionalization, a significant amount of the work has been reported using pincer complexes

of palladium. With the advent of new ligand designs, pincer complexes with various metals have started to attract more attention. Understanding the effects of appended functionalities on pincer ligands will enable their efficient use in the field of alkene functionalization. Studies on deactivation pathways will serve as guidelines to design more thermally robust pincer complexes capable of withstanding the often harsh conditions required for catalysis. A mechanistic understanding of how pincer complexes react with alkenes will further allow for improvements in ligand design, such that these versatile ligand frameworks could be utilized in industrially relevant processes.

REFERENCES

(1)   Chase, P. A.; Gossage, R. A.; van Koten, G. Modern Organometallic Multidentate Ligand Design Strategies: The Birth of the Privileged "Pincer" Ligand Platform. *Top. Organomet. Chem.* **2016**, *54*, 1–16.

(2)   van Koten, G. Tuning the Reactivity of Metals Held in a Rigid Ligand Environment. *Pure Appl. Chem.* **1989**, *61* (10), 1681–1694.

(3)   Shaw, B. L.; Uttley, M. F. Dihydro-platinum(II) and Related Complexes. *J. Chem. Soc. Chem. Commun.* **1974**, No. 22, 918.

(4)   Moulton, C. J.; Shaw, B. L. Transition Metal–carbon Bonds. Part XLII. Complexes of Nickel, Palladium, Platinum, Rhodium and Iridium with the Tridentate Ligand 2,6-Bis[(di-t-Butylphosphino)methyl]phenyl. *J. Chem. Soc., Dalton Trans.* **1976**, No. 11, 1020–1024.

(5)   Peris, E.; Crabtree, R. H. Key Factors in Pincer Ligand Design. *Chem. Soc. Rev.* **2018**, *47* (6), 1959–1968.

(6)   Szabó, K. J. Pincer Complexes as Catalysts in Organic Chemistry. *Top. Organomet. Chem.* **2013**, *40*, 203–242.

(7)   Selander, N.; Szabó, K. J. Catalysis by Palladium Pincer Complexes. *Chem. Rev.* **2011**, *111* (3), 2048–2076.

(8)   Choi, J.; MacArthur, A. H. R.; Brookhart, M.; Goldman, A. S. Dehydrogenation and Related Reactions Catalyzed by Iridium Pincer Complexes. *Chem. Rev.* **2011**, *111* (3), 1761–1779.

(9)   Eberhard, M. R. Insights into the Heck Reaction with PCP Pincer Palladium(II) Complexes. *Org. Lett.* **2004**, *6* (13), 2125–2128.

(10)   Sommer, W. J.; Yu, K.; Sears, J. S.; Ji, Y.; Zheng, X.; Davis, R. J.; Sherrill, C. D.; Jones, C. W.; Weck, M. Investigations into the Stability of Tethered Palladium(II) Pincer Complexes during Heck Catalysis. *Organometallics* **2005**, *24* (18), 4351–4361.

(11)   Wingard, L. A.; White, P. S.; Templeton, J. L. Synthesis and Oxidation of d[6] Tungsten Pincer Complexes: A Complete Series of Tungsten(ii) Hydridocarbonyl and Halocarbonyl Pincer Complexes. *Dalton Trans.* **2012**, *41* (37), 11438.

(12)   Bernal, M. J.; Martín, M.; Sola, E. Arene and Hydride Complexes of Ruthenium with Fac PSiP Pincer Ligands. *Z. Anorg. Allg. Chem.* **2015**, *641* (12–13), 2122–2128.

(13)   Suárez, E.; Plou, P.; Gusev, D. G.; Martín, M.; Sola, E. Cationic, Neutral, and Anionic Hydrides of Iridium with PSiP Pincers. *Inorg. Chem.* **2017**, *56* (12), 7190–7199.

(14)   Jeffrey, J. C.; Rauchfuss, T. B. Metal Complexes of Hemilabile Ligands. Reactivity and Structure of Dichlorobis(o-(diphenylphosphino)anisole)ruthenium(II). *Inorg. Chem.* **1979**, *18* (10), 2658–2666.

(15)   Poverenov, E.; Gandelman, M.; Shimon, L. J. W.; Rozenberg, H.; Ben-David, Y.;

Milstein, D. Pincer "Hemilabile" Effect. PCN Platinum(II) Complexes with Different Amine "Arm Length." *Organometallics* **2005**, *24* (6), 1082–1090.

(16) Zhang, J.; Leitus, G.; Ben-David, Y.; Milstein, D. Facile Conversion of Alcohols into Esters and Dihydrogen Catalyzed by New Ruthenium Complexes. *J. Am. Chem. Soc.* **2005**, *127*, 10840–10841.

(17) Gunanathan, C.; Ben-David, Y.; Milstein, D. Direct Synthesis of Amides from Alcohols and Amines with Liberation of H_2. *Science* **2007**, *317* (5839), 790–792.

(18) Perdriau, S.; Chang, M.-C.; Otten, E.; Heeres, H. J.; de Vries, J. G. Alkene Isomerisation Catalysed by a Ruthenium PNN Pincer Complex. *Chem. Eur. J.* **2014**, *20* (47), 15434–15442.

(19) Gunanathan, C.; Milstein, D. Metal–Ligand Cooperation by Aromatization–Dearomatization: A New Paradigm in Bond Activation and "Green" Catalysis. *Acc. Chem. Res.* **2011**, *44* (8), 588–602.

(20) *Pincer and Pincer-Type Complexes*; Szabó, K. J., Wendt, O. F., Eds.; Wiley-VCH Verlag GmbH & Co. KGaA: Weinheim, Germany, 2014.

(21) Tutusaus, O.; Ni, C.; Szymczak, N. K. A Transition Metal Lewis Acid/Base Triad System for Cooperative Substrate Binding. *J. Am. Chem. Soc.* **2013**, *135* (9), 3403–3406.

(22) Kiernicki, J. J.; Zeller, M.; Szymczak, N. K. Hydrazine Capture and N–N Bond Cleavage at Iron Enabled by Flexible Appended Lewis Acids. *J. Am. Chem. Soc.* **2017**, *139* (50), 18194–18197.

(23) Miller, A. J. M. Controlling Ligand Binding for Tunable and Switchable Catalysis: Cation-Modulated Hemilability in Pincer-Crown Ether Ligands. *Dalton Trans.* **2017**, *46* (36), 11987–12000.

(24) Kita, M. R.; Miller, A. J. M. Cation-Modulated Reactivity of Iridium Hydride Pincer-Crown Ether Complexes. *J. Am. Chem. Soc.* **2014**, *136* (41), 14519–14529.

(25) Kita, M. R.; Miller, A. J. M. An Ion-Responsive Pincer-Crown Ether Catalyst System for Rapid and Switchable Olefin Isomerization. *Angew. Chem. Int. Ed.* **2017**, *56* (20), 5498–5502.

(26) McDonald, R. I.; Liu, G.; Stahl, S. S. Palladium(II)-Catalyzed Alkene Functionalization via Nucleopalladation: Stereochemical Pathways and Enantioselective Catalytic Applications. *Chem. Rev.* **2011**, *111* (4), 2981–3019.

(27) Smidt, J.; Hafner, W.; Jira, R.; Sedlmeier, J.; Sieber, R.; Rüttinger, R.; Kojer, H. Katalytische Umsetzungen von Olefinen an Platinmetall-Verbindungen Das Consortium-Verfahren Zur Herstellung von Acetaldehyd. *Angew. Chemie* **1959**, *71* (5), 176–182.

(28) Smidt, J.; Hafner, W.; Jira, R.; Sieber, R.; Sedlmeier, J.; Sabel, A. The Oxidation of Olefins with Palladium Chloride Catalysts. *Angew. Chemie Int. Ed. English* **1962**, *1* (2), 80–88.

(29)   Eckert, M.; Fleischmann, G.; Jira, R.; Bolt, H. M.; Golka, K. Acetaldehyde. In *Ullmann's Encyclopedia of Industrial Chemistry*; Wiley-VCH Verlag GmbH & Co. KGaA: Weinheim, Germany, 2006; Vol. 1, pp 191–207.

(30)   Keith, J. A.; Henry, P. M. The Mechanism of the Wacker Reaction: A Tale of Two Hydroxypalladations. *Angew. Chem. Int. Ed.* **2009**, *48* (48), 9038–9049.

(31)   Royer, M. E. Hydrocyanation of Alkenes. In *C-1 Building Blocks in Organic Synthesis 1*; van Leeuwen, Ed.; Georg Thieme Verlag: Stuttgart, 2014; pp 309–339.

(32)   Tolman, C. A. Steric and Electronic Effects in Olefin Hydrocyanation at Du Pont: A Scientific and Industrial Success Story. *J. Chem. Educ.* **1986**, *63* (3), 199–201.

(33)   Tolman, C. A.; Seidel, W. C.; Druliner, J. D.; Domaille, P. J. Catalytic Hydrocyanation of Olefins by nickel(0) Phosphite Complexes - Effects of Lewis Acids. *Organometallics* **1984**, *3* (1), 33–38.

(34)   Bini, L.; Müller, C.; Vogt, D. Mechanistic Studies on Hydrocyanation Reactions. *ChemCatChem* **2010**, *2* (6), 590–608.

(35)   Franke, R.; Selent, D.; Börner, A. Applied Hydroformylation. *Chem. Rev.* **2012**, *112* (11), 5675–5732.

(36)   de Vries, J. G. Hydroformylation of Alkenes: Industrial Applications. In *Science of Synthesis: C-1 Building Blocks in Organic Synthesis 1*; 2014; pp 193–227.

(37)   Torborg, C.; Beller, M. Recent Applications of Palladium-Catalyzed Coupling Reactions in the Pharmaceutical, Agrochemical, and Fine Chemical Industries. *Adv. Synth. Catal.* **2009**, *351* (18), 3027–3043.

(38)   de Vries, J. G. The Heck Reaction in the Production of Fine Chemicals. *Can. J. Chem.* **2001**, *79* (5–6), 1086–1092.

(39)   Morin, R. D.; Bearse, A. E. Catalytic Esterification of Olefins with Organic Acids. *Ind. Eng. Chem.* **1951**, *43* (7), 1596–1600.

(40)   Ohff, M.; Ohff, A.; van der Boom, M. E.; Milstein, D. Highly Active Pd(II) PCP-Type Catalysts for the Heck Reaction. *J. Am. Chem. Soc.* **1997**, *119* (48), 11687–11688.

(41)   Morales-Morales, D.; Redón, R.; Yung, C.; Jensen, C. M. High Yield Olefination of a Wide Scope of Aryl Chlorides Catalyzed by the Phosphinito Palladium PCP Pincer Complex: [PdCl{$C_6H_3(OPPr^i_2)_2$-2,6}]. *Chem. Commun.* **2000**, *3* (17), 1619–1620.

(42)   Phan, N. T. S.; Van Der Sluys, M.; Jones, C. W. On the Nature of the Active Species in Palladium Catalyzed Mizoroki–Heck and Suzuki–Miyaura Couplings – Homogeneous or Heterogeneous Catalysis, A Critical Review. *Adv. Synth. Catal.* **2006**, *348* (6), 609–679.

(43)   Beletskaya, I. P.; Cheprakov, A. V. Palladacycles in Catalysis – a Critical Survey. *J. Organomet. Chem.* **2004**, *689* (24), 4055–4082.

(44)   Bergbreiter, D. E.; Osburn, P. L.; Frels, J. D. Mechanistic Studies of SCS-Pd Complexes Used in Heck Catalysis. *Adv. Synth. Catal.* **2005**, *347*, 172–184.

(45) Dupont, J.; Consorti, C. S.; Spencer, J. The Potential of Palladacycles: More Than Just Precatalysts. *Chem. Rev.* **2005**, *105* (6), 2527–2572.

(46) Aydin, J.; Larsson, J. M.; Selander, N.; Szabó, K. J. Pincer Complex-Catalyzed Redox Coupling of Alkenes with Iodonium Salts via Presumed Palladium(IV) Intermediates. *Org. Lett.* **2009**, *11* (13), 2852–2854.

(47) Selander, N.; Willy, B.; Szabó, K. J. Selective C-H Borylation of Alkenes by Palladium Pincer Complex Catalyzed Oxidative Functionalization. *Angew. Chem. Int. Ed.* **2010**, *49* (24), 4051–4053.

(48) Tondreau, A. M.; Atienza, C. C. H.; Weller, K. J.; Nye, S. A.; Lewis, K. M.; Delis, J. G. P.; Chirik, P. J. Iron Catalysts for Selective Anti-Markovnikov Alkene Hydrosilylation Using Tertiary Silanes. *Science* **2012**, *335* (6068), 567–570.

(49) Peng, D.; Zhang, Y.; Du, X.; Zhang, L.; Leng, X.; Walter, M. D.; Huang, Z. Phosphinite-Iminopyridine Iron Catalysts for Chemoselective Alkene Hydrosilylation. *J. Am. Chem. Soc.* **2013**, *135* (51), 19154–19166.

(50) Buslov, I.; Becouse, J.; Mazza, S.; Montandon-Clerc, M.; Hu, X. Chemoselective Alkene Hydrosilylation Catalyzed by Nickel Pincer Complexes. *Angew. Chem. Int. Ed.* **2015**, *54* (48), 14523–14526.

(51) Roberts, C. C.; Matías, D. M.; Goldfogel, M. J.; Meek, S. J. Lewis Acid Activation of Carbodicarbene Catalysts for Rh-Catalyzed Hydroarylation of Dienes. *J. Am. Chem. Soc.* **2015**, *137* (20), 6488–6491.

(52) Goldfogel, M. J.; Roberts, C. C.; Meek, S. J. Intermolecular Hydroamination of 1,3-Dienes Catalyzed by Bis(phosphine)carbodicarbene–Rhodium Complexes. *J. Am. Chem. Soc.* **2014**, *136* (17), 6227–6230.

(53) Goldfogel, M. J.; Meek, S. J. Diastereoselective Synthesis of Vicinal Tertiary and N-Substituted Quaternary Stereogenic Centers by Catalytic Hydroalkylation of Dienes. *Chem. Sci.* **2016**, *7* (7), 4079–4084.

(54) Goldfogel, M. J.; Roberts, C. C.; Manan, R. S.; Meek, S. J. Diastereoselective Synthesis of γ-Substituted 2-Butenolides via (CDC)-Rh-Catalyzed Intermolecular Hydroalkylation of Dienes with Silyloxyfurans. *Org. Lett.* **2017**, *19* (1), 90–93.

(55) Tian, R.; Ng, Y.; Ganguly, R.; Mathey, F. A New Type of Phosphaferrocene–Pyrrole–Phosphaferrocene P-N-P Pincer Ligand. *Organometallics* **2012**, *31* (6), 2486–2488.

(56) Wu, Q.; Zhou, F.; Shu, X.; Jian, L.; Xu, B.; Zheng, X.; Yuan, M.; Fu, H.; Li, R.; Chen, H. Synthesis and Application of PNP Pincer Ligands in Rhodium-Catalyzed Hydroformylation of Cycloolefins. *RSC Adv.* **2016**, *6* (109), 107305–107309.

(57) Musa, S.; Filippov, O. A.; Belkova, N. V.; Shubina, E. S.; Silantyev, G. a.; Ackermann, L.; Gelman, D. Ligand-Metal Cooperating PC(sp^3)P Pincer Complexes as Catalysts in Olefin Hydroformylation. *Chem. Eur. J.* **2013**, *19* (50), 16906–16909.

Chapter 2   DIVERSE CATION-PROMOTED REACTIVITY OF IRIDIUM CARBONYL PINCER-CROWN ETHER COMPLEXES

Section 2.1   Introduction

Transition metal complexes and Lewis acidic metal cations have a rich history of cooperative reactivity.[1–3] In catalysis, Lewis acid activation of substrates or intermediates can lower kinetic barriers or alter reaction outcomes.[2,4–7] In sensing applications, Lewis acids and transition metals can work synergistically to improve sensitivity or selectivity.[8,9] In oxidation-reduction reactions, Lewis acids can modulate electron transfer rates by tuning reduction potentials.[10–15] Understanding fundamental reactivity trends of transition metals with Lewis acids might spark progress in these and other areas.[3,16–18]

Pincer-crown ether ligands, featuring a macrocyclic amine donor as part of an aminophosphinite (NCOP) pincer framework, provide an opportunity to study the reactivity of transition metals with cationic Lewis acids with the aid of cation–macrocycle binding.[19,20] In this Chapter, we discuss how new iridium carbonyl complexes supported by NCOP pincer ligands exhibit a diverse range of reactivity in addition to the expected cation–macrocycle interactions. Halide abstraction, halide exchange, metal protonation, and cation-macrocycle binding are all independently observed. The reaction pathway depends on the Lewis acidity of the cation as well as the nature of its counter anion. The role of the macrocycle was probed

by comparing the reactivity with control complexes supported by non-macrocyclic NCOP ligands. Some of the cation-promoted reactions require a macrocyclic ligand, while others proceed readily with either complex. These findings highlight the diverse reactivity that is possible on a single platform in the presence of various salts, and may guide the development of cation-assisted catalytic reactions. Specifically, the use of water as a proton source for transition metal complexes is unusual and interesting in relation to recent studies of water oxidative addition at transition metal centers.[21]

Section 2.2   Synthesis of Ir(III) and Ir(I) Carbonyl Complexes

Iridium(III) hydridocarbonylchloride complexes were accessed using Ir(*p*-toluidine)(CO)$_2$(Cl),[22] which afforded (^{15c5}NCOP^{iPr})Ir(H)(CO)(Cl) (**1^{15c5}**) as a brownish-yellow solid in 95% yield after refluxing in toluene with the aminophosphinite ligand (^{15c5}NCOP^{iPr})H (Scheme 2.1). The ^{1}H NMR spectrum of **1^{15c5}** features two sets of *iso*-propyl methine resonances and diastereotopic resonances for the benzylic linker, consistent with the presence of inequivalent positions perpendicular to the pincer ligand. The hydride resonated as a doublet (δ −18.3, $^2J_{PH} = 20.6$ Hz) in a region typical of a six-coordinate Ir(III) hydride *trans* to a chloride ligand.[23–25] A singlet was observed by ^{31}P{^{1}H} NMR spectroscopy (δ 154), 6 ppm downfield of the free (^{15c5}NCOP^{iPr})H ligand. The presence of the CO ligand was confirmed by IR spectroscopy ($\nu_{CO} = 2010$ cm^{-1}), as well as by ^{13}C{^{1}H} NMR spectroscopy (δ 182, $^2J_{PC} = 2.9$ Hz).
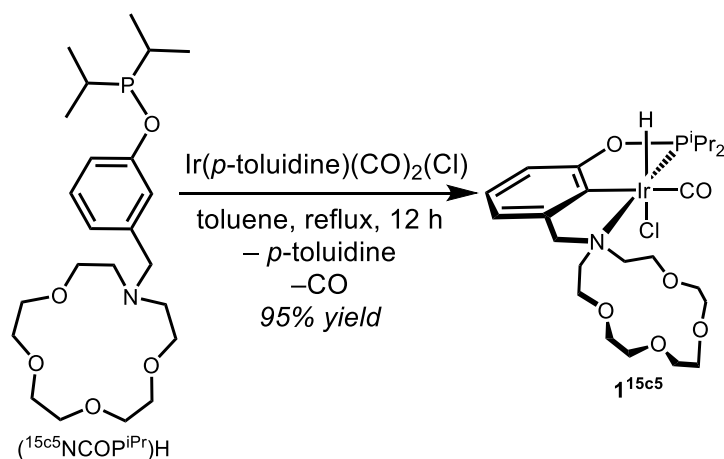
Scheme 2.1 Synthesis of 1^{15c5}.

Pale yellow single crystals of 1^{15c5} suitable for X-ray diffraction were grown from a concentrated solution in benzene layered with pentane. A *trans*-hydridochloride geometry, with bond distances typical of (pincer)Ir(H)(CO)(Cl) complexes,[23,24] is apparent in the molecular structure rendering (Figure 2.1). The Ir–C$_{ipso}$ distance (2.036(5) vs. 1.979(5) Å) and the Ir–P distance (2.236(1) vs. 2.1825(14) Å) are longer than previously observed in a tetradentate *cis* hydridochloride pincer-crown ether complex, where an oxygen from the crown-ether binds *trans* to the hydride.[19]
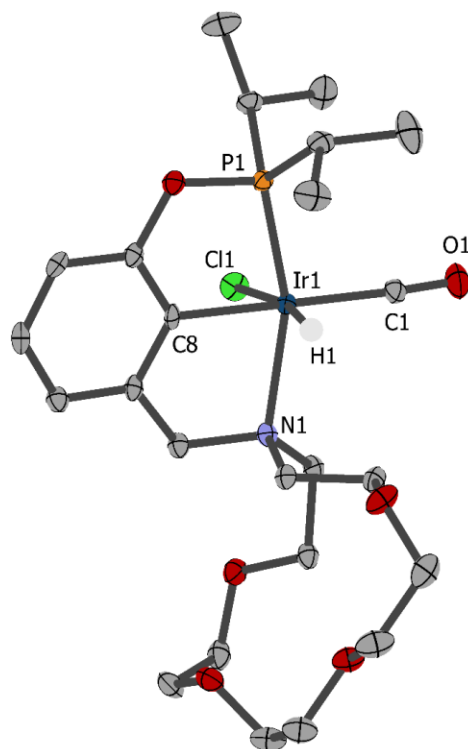
Figure 2.1 Structural representation of **1^{15c5}** with ellipsoids drawn at the 50% probability level. Hydrogen atoms of the ^{15c5}NCOP^{iPr} ligand are omitted for clarity. The hydride was found in the electron density difference map and the Ir−H bond distance was restrained to 1.9 Å. Selected distances (Å) and angles (deg): Ir1−P1 2.236(1), Ir1−C8 2.036(5), Ir1−N1 2.237(4), Ir1−Cl1 2.475(1), Ir1−C1 1.935(5), C1−O1 1.119(6); N1−Ir1− Cl1 88.1(1), O1−C1−Ir1 177.3(5).

Formation of a *trans* hydridochloride product is noteworthy in light of a recent study

of Ir pincer complexes that investigated the impact of phosphine substituents on the product

of metallation with Ir(*p*-toluidine)(CO)$_2$(Cl).[23] In that study, bulkier *tert*-butyl groups

produced Ir(I) pincer carbonyl complexes, while less sterically demanding *iso*-propyl groups

led to Ir(III) hydridocarbonylchloride complexes. The origin of the ligand-specific

metallation products is not fully clear, but steric crowding from the *tert*-butyl groups might

promote chloride dissociation, leaving a cationic hydride that is sufficiently acidic to be

deprotonated by *p*-toluidine *in situ*. Attempts at spectrophotometric titration of Ir(III)

hydridochloride 1^{15c5} using DBU (conjugate acid pK_a 24.3;[26] DBU is 1,8-diazabicyclo[5.4.0]undec-7-ene) led to stoichiometric deprotonation to form (^{15c5}NCOP^{iPr})Ir(CO) (2^{15c5}) in acetonitrile (Figure 2.2). On the other hand, addition of up to 100 equiv NEt$_3$ (conjugate acid pK_a 18.8)[26] resulted in no observable deprotonation, bracketing the acidity of 1^{15c5} in acetonitrile: $19 < pK_a(1^{15c5}) < 24$. The estimated acidity of 1^{15c5} is consistent with the experimental observation that p-toluidine (pK_a ~ 11)[26] does not effect hydrodehalogenation (instead acting as an easily displaced ligand during metallation).
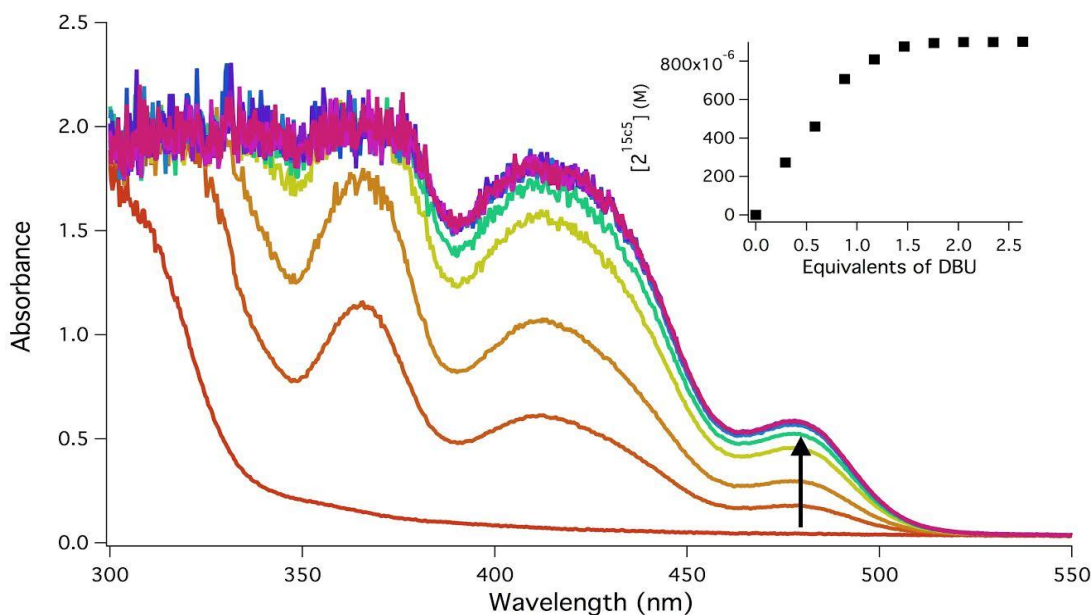
Figure 2.2 UV-vis spectra obtained during titration of 1^{15c5} with DBU. The inset shows that the Ir(I) species 2^{15c5} was formed after addition of only ~1 equiv DBU, indicating essentially irreversible deprotonation with this base.

A non-macrocyclic analogue, (^{Et}NCOP^{iPr})Ir(H)(CO)(Cl) (1^{Et}), was synthesized in a similar fashion by refluxing Ir(p-toluidine)(CO)$_2$(Cl) and the diethylamine-containing ligand, (^{Et}NCOP^{iPr})H,[27] in toluene (Scheme 2.2). The spectroscopic features of complex 1^{Et} are quite similar to those of 1^{15c5}, starting with the ^{31}P{^{1}H} NMR spectrum (δ 154, s). The doublet corresponding to the hydride ligand (δ –18.5, $^2J_{PH}$ = 20.7 Hz) is almost identical to the hydride signal in 1^{15c5}. The ethyl groups of the amine appeared as four diastereotopic

25

methylene protons between δ 2.5 and 4.2 and two CH_3 triplets that overlap with the CH_3 resonances of the *iso*-propylphosphine.
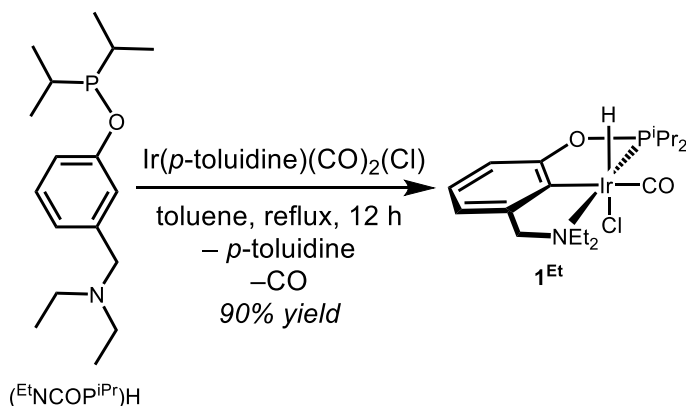
Scheme 2.2 Synthesis of **1^{Et}**.

Iridium(I) species were obtained by dehydrohalogenation of the Ir(III) hydridochloride complexes. Addition of 1.5 equivalents of potassium *tert*-butoxide (KO^{t}Bu) to **1^{15c5}** in benzene generated (^{15c5}NCOP^{iPr})Ir(CO) (**2^{15c5}**; Scheme 2.3) as a bright yellow solid in 78% yield. In benzene solvent, precipitation of KCl precludes any cation-crown interactions.
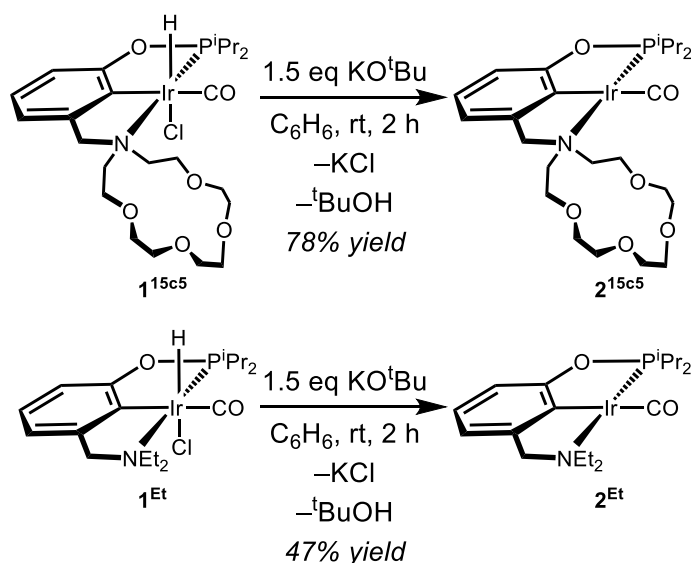
Scheme 2.3 Synthesis of **2^{15c5}** and **2^{Et}**.

The increased symmetry afforded by the square planar geometry is evident in the ^{1}H NMR spectrum of **2^{15c5}**. For example, a single *iso*-propyl methine resonance is observed, and the benzylic linker appears as a singlet (δ 4.1). The ^{31}P{^{1}H} NMR spectrum of **2^{15c5}** features a singlet shifted 17 ppm downfield relative to **1^{15c5}** (δ 171 for **2^{15c5}**; δ 154 for **1^{15c5}**). The infrared spectrum of **2^{15c5}** exhibits a strong CO stretch (ν_{CO} = 1921 cm^{-1}) that is consistent with formal reduction to an Ir(I) center capable of increased π-back-donation (ν_{CO} is reduced by 89 cm^{-1} relative to **1^{15c5}**).

Slow evaporation of a pentane solution of **2^{15c5}** yielded bright yellow crystals suitable for single crystal X-ray diffraction, which confirmed the expected square planar geometry around Ir (Figure 2.3). The two independent molecules of **2^{15c5}** present in the asymmetric unit possessed essentially identical bond distances. Metal–ligand distances shortened in the Ir(I) complex **2^{15c5}** compared to those in the Ir(III) complex **1^{15c5}**. Notably, the Ir–P distance shortened to 2.187(2) Å in **2^{15c5}** from 2.236(1) Å in **1^{15c5}** and the Ir–CO bond shortened to 1.898(8) Å in **2^{15c5}** from 1.935(5) Å in **1^{15c5}**, consistent with increased back-donation from a

27

more electron-rich metal center. The Ir–C–O bond angle (174.7(8)°) is slightly more acute

than the value typically observed in Ir(I) pincer carbonyl complexes (~180°).[23,28,29]
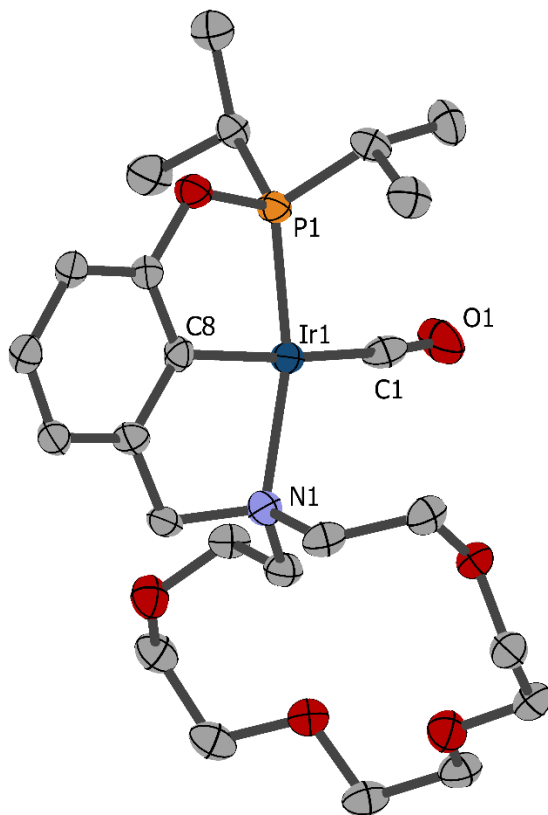
Figure 2.3 Structural representation of one of the two independent molecules of 2^{15c5} in the asymmetric unit, with ellipsoids drawn at the 50% probability level. Hydrogen atoms are omitted for clarity. Selected distances (Å) and angles (deg): Ir1−P1 2.187(2), Ir1−C8 2.017(7), Ir1−N1 2.206(7), Ir1−C1 1.898(9), C1−O1 1.14(1); Ir1−C1− O1 174.8(8).

The diethylamine-containing complex 2^{Et} was accessed in the same manner via

dehydrohalogenation with KO^{t}Bu (Scheme 2.3). Extraction with pentane afforded the

complex as a yellow solid in 47% yield. Complex 2^{Et} exhibits a CO stretch (v_{CO} = 1922 cm^{-1})

and a ^{31}P{^{1}H} NMR signal (δ 172, s) that are very similar to the macrocyclic analogue 2^{15c5},

suggesting similar electronic environments. With pairs of Ir(III) and Ir(I) complexes in hand,

we set out to explore the reactivity of these species with several salts of redox-inactive alkali, alkaline earth, and lanthanide metal cations.

Section 2.3   Reactivity of (^{15c5}NCOP^{iPr})Ir(H)(CO)(Cl) with Metal Cations

The reactivity of octahedral Ir(III) pincer-crown ether complexes was assessed with Na$^+$, Ca^{2+}, and La^{3+} salts. Typical experiments were conducted in NMR tubes with equimolar Ir/salt mixtures in CD$_3$CN solvent. Mixing one equivalent of NaBAr$^F_4$ (Ar^F is 3,5-bis(trifluoromethyl)phenyl) with **1**^{15c5} in CD$_3$CN results in partial conversion to a new species. Addition of up to 3 equivalents of NaBAr$^F_4$ shifted the mixture further towards the new species (Figure 2.4). The presence of a doublet (δ −19.6, $^2J_{PH}$ = 21.9 Hz) in the hydride region of the ^{1}H NMR spectrum nearby the starting material, and a ^{31}P{^{1}H} NMR singlet (δ 154) near that of **1**^{15c5} (δ 155), suggested an Ir(III) product. Compared to **1**^{15c5} (ν_{CO} = 2024 cm^{-1} in acetonitrile), the product CO stretch shifted slightly to higher energy (ν_{CO} = 2031 cm^{-1}).
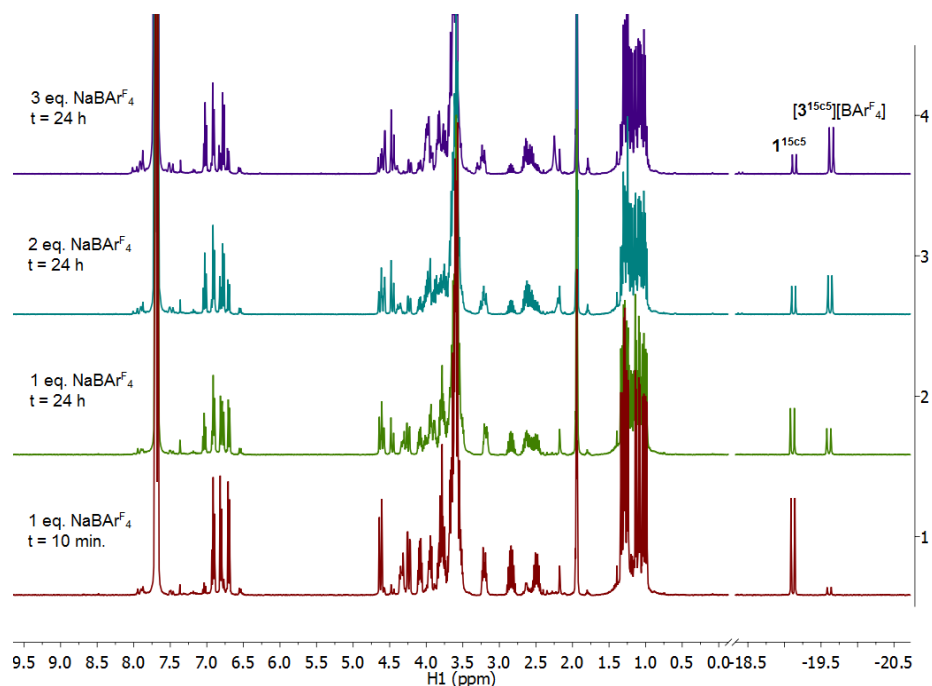
Figure 2.4 ^{1}H NMR spectra of conversion of $\mathbf{1^{15c5}}$ to $[\mathbf{3^{15c5}}][BAr^F_4]$ in CD_3CN.

An ^{1}H–^{13}C HMBC NMR experiment revealed a correlation between the hydride and a carbon resonance at δ 124 that is assigned to the quaternary carbon atom of an Ir-bound acetonitrile molecule (Figure 2.5).[30] When NaBAr$^F_4$ was added to $\mathbf{1^{15c5}}$ in a 1:1 CD_3CN:CH_3CN mixture, a sharp singlet at δ 2.32 protruded from the broad singlet of free acetonitrile in the ^{1}H NMR spectrum (Figure 2.6). This was assigned to the methyl protons of the Ir-bound acetonitrile ligand. The spectroscopic evidence indicates that sodium is performing a halide abstraction, followed by coordination of CD_3CN, generating the cationic complex $[(^{15c5}NCOP^{iPr})Ir(H)(CO)(NCCD_3)][BAr^F_4]$ ($[\mathbf{3^{15c5}}][BAr^F_4]$; Scheme 2.4). In a prior study, we observed that halide and nitrile ligands *trans* to the hydride influenced the chemical shift similarly.[19] Formation of $[\mathbf{3^{15c5}}][BAr^F_4]$ was also observed in the presence of one equivalent of H_2O, ruling out competitive binding between H_2O and acetonitrile under these conditions. The acetonitrile ligand is apparently quite weakly bound, hampering complete characterization. Subjecting $[\mathbf{3^{15c5}}]^+$ to vacuum and dissolving in CD_2Cl_2 revealed

30

loss of the acetonitrile ligand and formation of a new species formulated as the tetradentate complex $[\kappa^4-(^{15c5}NCOP^{iPr})Ir(H)(CO)]^{+}$,[31] featuring an upfield hydride resonance (δ –25.7, $^2J_{PH}$ = 21.4 Hz) consistent with a weak ether donor *trans* to the hydride.[19] Addition of ~8 equiv CH_3CN resulted in partial conversion to acetonitrile complex $[\mathbf{3^{15c5}}]^+$ (Ir–H δ –19.8, $^2J_{PH}$ = 21.8 Hz; Ir–NCCH_3 δ 2.37). The nitrile ligand was also lost in mass spectrometry experiments. Analogous macrocycle hemilability has been observed in other Ir and Ni pincer-crown ether complexes.[19,20]
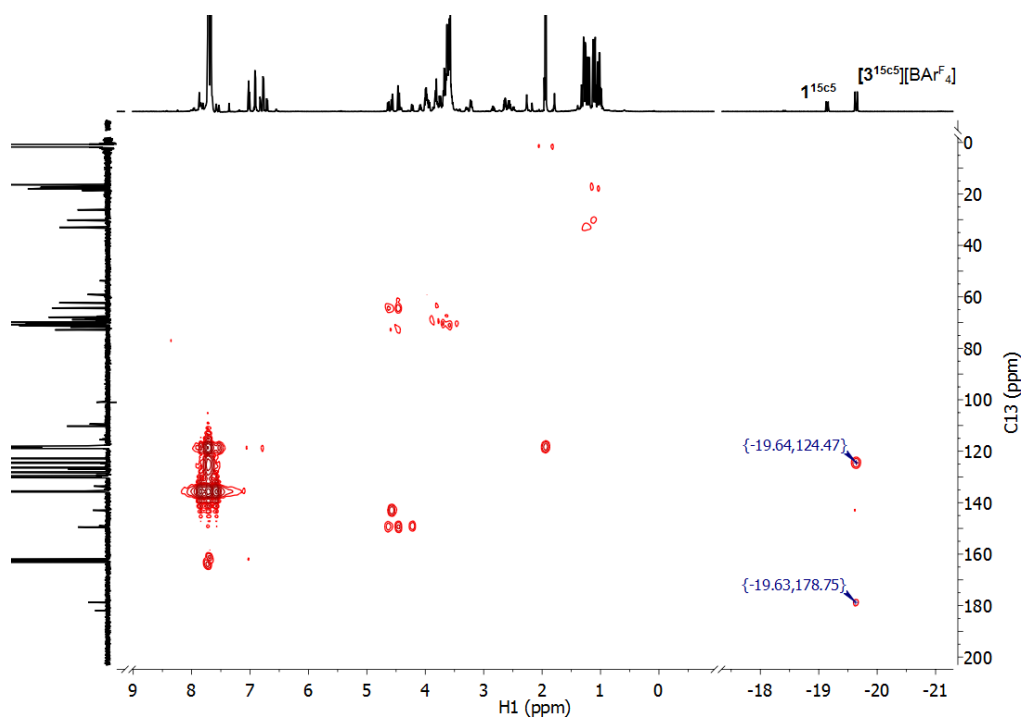
Figure 2.5 ^1H–^{13}C HMBC NMR spectrum of $[\mathbf{3^{15c5}}][BAr^F_4]$ in CD_3CN.
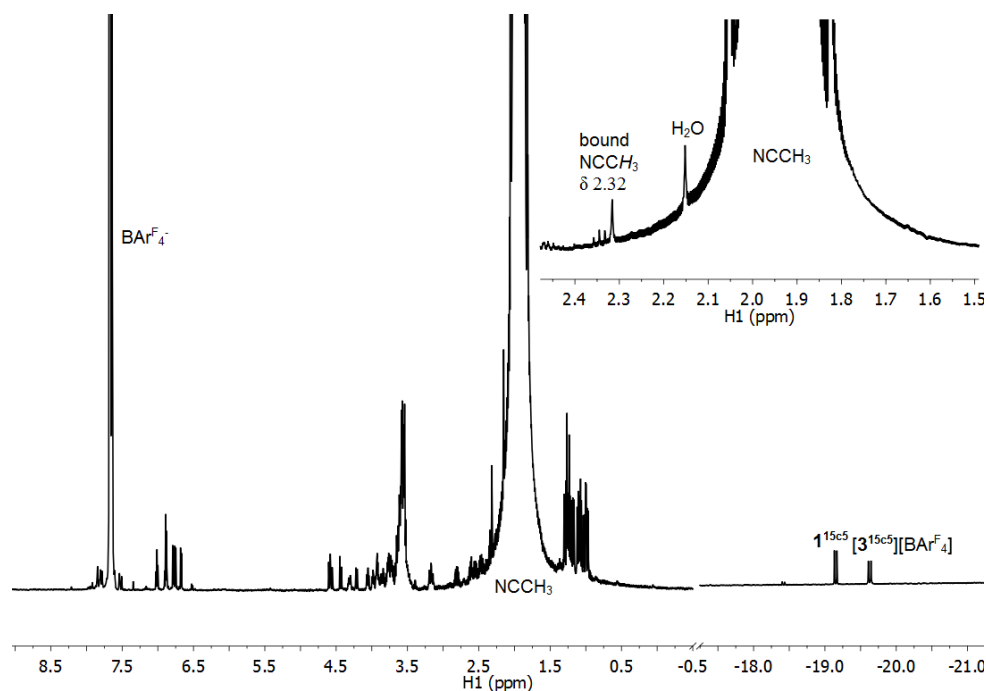
Figure 2.6 ^{1}H NMR spectrum of [3^{15c5}][BAr$^F_4$] formed upon addition of NaBAr$^F_4$ to 1^{15c5} in a 1:1 mixture of CD$_3$CN and CH$_3$CN.
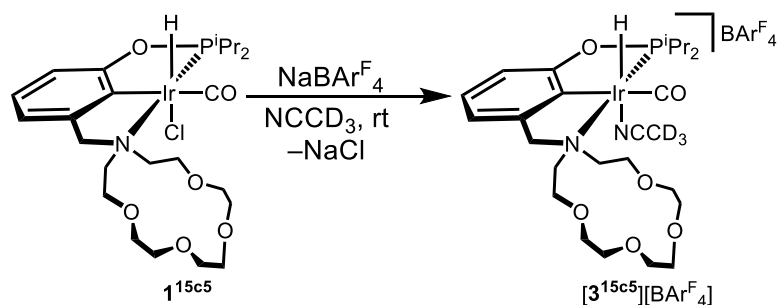
Scheme 2.4 Syntheis of [3^{15c5}][BAr$^F_4$].

Because excess NaBAr$^F_4$ was required to effect complete halide abstraction, some of

the remaining Na$^+$ would be capable of interacting with the macrocyclic ligand. Rapid,

reversible cation−crown binding involving Na$^+$ and unreacted 1^{15c5} is indeed evident from

systematic shifting of selected resonances in ^{1}H NMR spectra. The hydride resonance of 1^{15c5}

shifted 0.01 ppm upfield with each equivalent of NaBAr$^F_4$ added, while the crown multiplet

shifted similarly downfield. The resonances for the diastereotopic benzylic protons also

32

exhibited shifts of 0.01 ppm away from each other upon addition of increasing equivalents of

NaBAr$^F_4$ (Figure 2.7). Smaller shifts are apparent in the resonances of [3^{15c5}]$^+$.
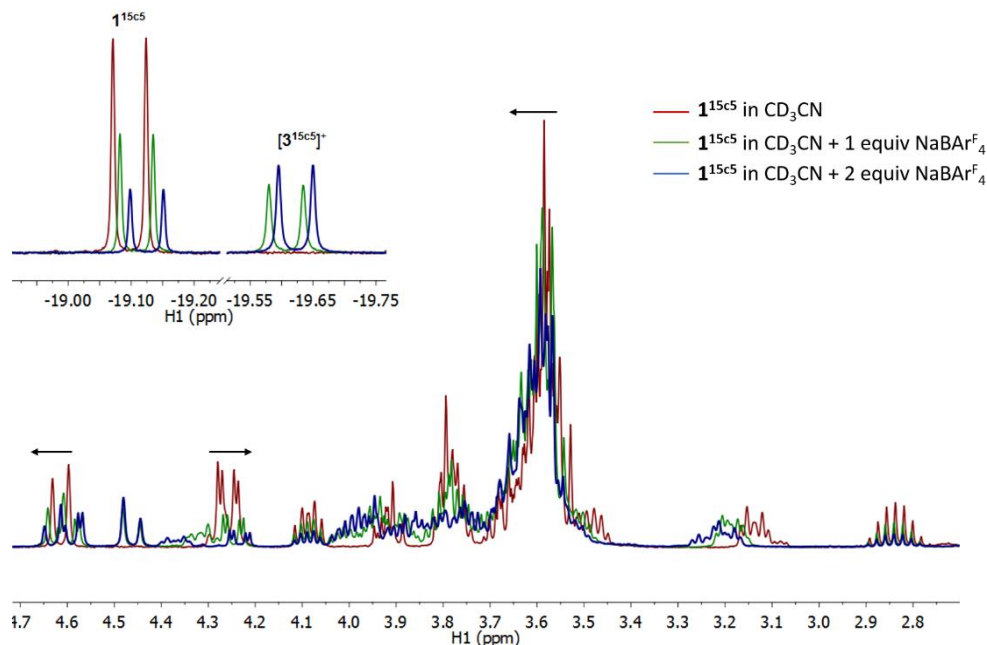
Figure 2.7 Superimposed ^{1}H NMR spectra showing cation-crown interactions between unreacted NaBAr$^F_4$ and 1^{15c5} in CD$_3$CN. The crown multiplet shifted downfield upon addition of NaBAr$^F_4$. The resonances for the diastereotopic benzylic protons (δ ~4.25 and δ ~4.65) exhibited shifts of 0.01 ppm away from each other upon addition of increasing equivalents of NaBAr$^F_4$. The inset shows the shifts in the hydride region.

Addition of either Ca(OTf)$_2$ or La(OTf)$_3$ to CH$_3$CN solutions of 1^{15c5} in the presence

of one equivalent of water similarly leads to formation of [3^{15c5}][OTf]. The La^{3+} salt was

more effective, reaching 70% conversion with one equiv added, versus ~30% conversion

with one equiv NaBAr$^F_4$ or Ca(OTf)$_2$. This could be due to relative Lewis acidity, or relative

solubility of the resulting salts. In synthetic practice, halide abstractions using Na$^+$ are

usually driven by precipitation events from less polar solvents such as CH$_2$Cl$_2$.[32,33]

When sodium is paired with an iodide anion, halide exchange and iodide coordination

is observed. The reaction between 1^{15c5} and NaI in CH$_3$CN does not go to completion. Taking

inspiration from the Finkelstein reaction,[34] we next tried acetone as the solvent. Addition of

NaI to 1^{15c5} in acetone-d_6 led to precipitation of NaCl and formation of the corresponding

hydridoiodide complex (^{15c5}NCOP^{iPr})Ir(H)(CO)(I) (4^{15c5}; Scheme 2.5), identified by NMR

spectroscopy and high-resolution mass spectrometry. The hydride resonance of 4^{15c5} (δ

−16.5, $^2J_{PH}$ = 19.4 Hz) is consistent with an iodide *trans* to the hydride ligand.[35] Similar

halide exchange was observed upon mixing LaI$_3$ with hydridochloride complex 1^{15c5} in

CD$_3$CN; the hydridoiodide complex 4^{15c5} was formed quantitatively (Scheme 2.5). The

driving force for halide exchange is likely the formation of products that match hard acids

and hard bases (e.g. NaCl) and match soft acids and soft bases (i.e. the Ir–I bond in 4^{15c5}).[36,37]
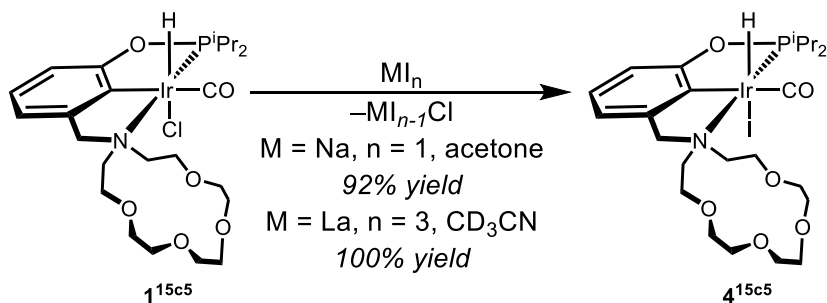
Scheme 2.5 Synthesis of 4^{15c5}.

Following initial halide exchange, addition of excess LaI$_3$ to 4^{15c5} led to systematic

shifts in the ^{1}H NMR spectrum that are indicative of a weak cation-macrocycle interaction

(Scheme 2.6). Addition of aliquots of LaI$_3$ to the hydridoiodide complex 4^{15c5} in acetone-d_6

led to a steady upfield shift in the iridium hydride ^{1}H NMR resonance (Figure 2.8). Similar

shifts were observed in the diastereotopic benzylic protons of the linker and in protons

attributed to the ethylene units of the macrocycle. In contrast, the phenyl backbone and *iso*-

propyl protons did not shift to any appreciable extent, suggesting that the interaction is

localized in the macrocycle (and perhaps involving the axial iodide ligand, which would

affect the hydride chemical shift) as shown in Scheme 2.6.
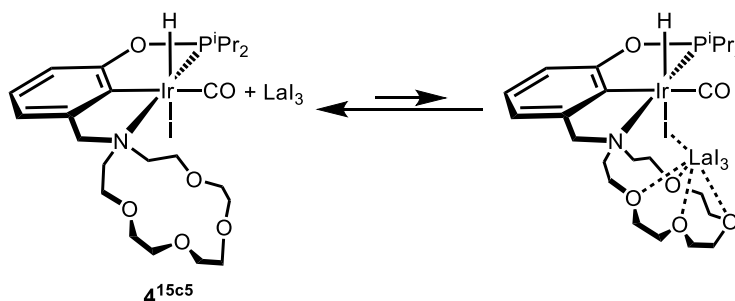
Scheme 2.6 Cation-crown interactions between **4**[15c5] and LaI₃.
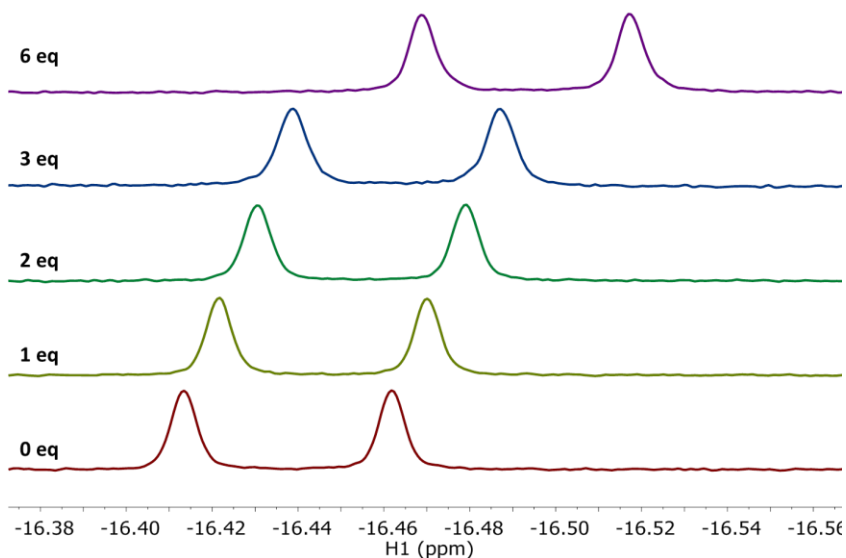
Figure 2.8 ¹H NMR spectra (hydride region) showing the effects of addition of increasing amounts of LaI₃ to **4**[15c5] in acetone-d_6.

The ¹H NMR data suggest that any cation−macrocycle interaction between **4**[15c5] and LaI₃ occurs with relatively low binding affinity. The hydride resonance shifts upfield by roughly 0.01 ppm per equivalent of LaI₃, and the magnitude of the shift is roughly constant within the limits of LaI₃ solubility. Strong cation−macrocycle interactions reach a limiting chemical shift with increasing cation concentration, so the linear trend suggests weak binding, with only partial incorporation of La into the macrocycle.[38] A weak interaction is consistent with the pincer-crown ether macrocycle acting as a tetradentate donor to La, with the Ir–N bond intact. Studies on lanthanide(III) complexation have shown that hexadentate

18-crown-6 and pentadentate 15-crown-5 macrocycles bind lanthanides more strongly than tetradentate 12-crown-4.[39]

The foregoing data suggest that addition of LaI$_3$ to $\mathbf{1^{15c5}}$ involves three separate interactions: initial chloride abstraction from the primary coordination sphere of Ir by La^{3+}, halide exchange with iodide, and cation-macrocycle interactions in the secondary coordination sphere of the Ir center.

Section 2.4   Reactivity of (^{Et}NCOP^{iPr})Ir(H)(CO)(Cl) with Metal Cations

To assess the role of the macrocycle in halide exchange and halide abstraction reactivity, the non-macrocyclic diethylamino complex $\mathbf{1^{Et}}$ was treated with LaI$_3$ and NaBAr$^F_4$. Within minutes of mixing $\mathbf{1^{Et}}$ with 1 equiv LaI$_3$ in CD$_3$CN, complete conversion to hydridoiodide complex $\mathbf{4^{Et}}$ was observed by ^{1}H NMR spectroscopy. The reaction of $\mathbf{1^{Et}}$ with LaI$_3$ therefore proceeds similarly to the analogous reaction of $\mathbf{1^{15c5}}$ with LaI$_3$.
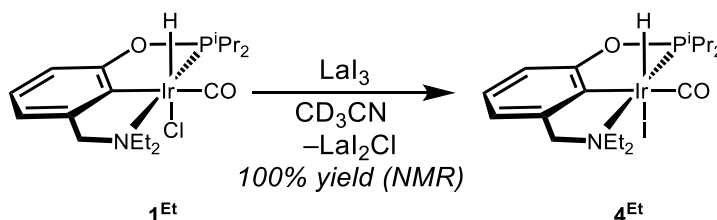
Scheme 2.7 Synthesis of $\mathbf{4^{Et}}$.

Addition of 1 equiv NaBAr$^F_4$ to $\mathbf{1^{Et}}$ in CD$_3$CN led to ~15% acetonitrile cation $\mathbf{3^{Et}}$ within minutes. After ~24 h, a roughly 1:1 ratio of $\mathbf{1^{Et}}$:$\mathbf{3^{Et}}$ was observed. As with halide exchange, the halide abstraction reaction rate and product ratios closely mimic the behavior of the macrocycle-containing complex $\mathbf{1^{15c5}}$. These experiments suggest that the macrocycle does not facilitate (or hinder) the reaction, at least in the case of the halide exchange and

halide abstraction. The lack of inhibition is noteworthy, since macrocycle binding can render the cationic guest less Lewis acidic.[40]

Section 2.5   Reactivity of (^{15c5}NCOP^{iPr})Ir(CO) with Metal Cations

Upon addition of one equivalent of nominally anhydrous LaI$_3$ to $\mathbf{2^{15c5}}$, the bright yellow solution rapidly decolorized and NMR spectroscopy revealed quantitative formation of the Ir(III) hydridoiodide complex $\mathbf{4^{15c5}}$. The proton source was identified as adventitious H$_2$O bound to the LaI$_3$ salt, based on the presence of a broad O−H stretch in an IR spectrum of the material. Attempts to dehydrate samples of LaI$_3$ proved unsuccessful, with the harsh conditions leading to decomposition and possible formation of LaOI and HI.[41,42]

The observed protonation was surprising because the Ir(I) complex $\mathbf{2^{15c5}}$ does not react with excess H$_2$O in CD$_3$CN in the absence of LaI$_3$, even after extended periods of time and high temperatures. Aquo ligands of metal cations have long been recognized to be considerably more acidic than water itself,[43] and we hypothesize that the water bound to the Lewis acidic cation is acting as a Brønsted acid to protonate the Ir center. This sort of cation-triggered protonation has seldom been explored in the context of proton transfers to organotransition metal complexes, so we initiated a more thorough study of the reactivity of Ir(I) complexes with water in the presence of a series of salts of varying Lewis acidity.
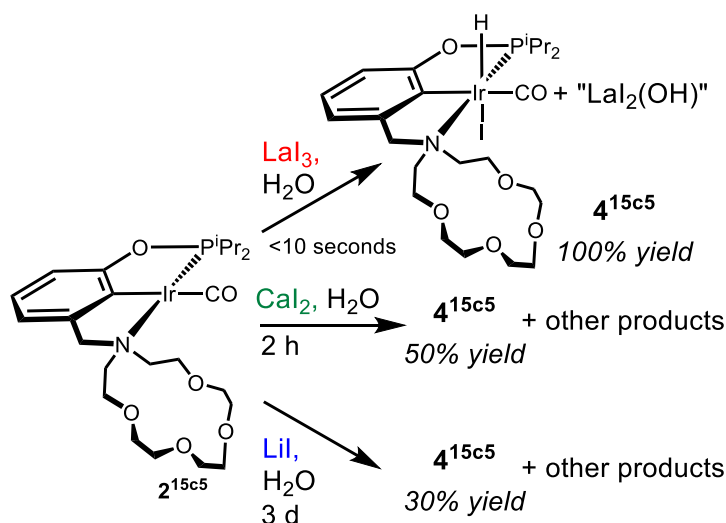
Scheme 2.8 Reactivity of 2^{15c5} with different iodide salts in the presence of water in CD$_3$CN.

The iodide salts of La^{3+}, Ca^{2+}, and Li$^+$ were explored first, as shown in Scheme 2.8. Addition of one equivalent of LaI$_3$ to 2^{15c5} in the presence of one equivalent of H$_2$O in CD$_3$CN leads to formation of Ir(III) hydridoiodide 4^{15c5} within seconds. ^{1}H NMR spectral monitoring revealed that the resonance for free H$_2$O diminished as the Ir–H resonance appeared. With protonation by water having formed an iridium iodide product, the fate of the hydroxide was examined. A downfield singlet (δ 5.4, 1H) observed by ^{1}H NMR spectroscopy is consistent with a metal aquo or hydroxide, and underwent broadening upon addition of more H$_2$O. A [139]La NMR spectrum obtained shortly after mixing LaI$_3$ and 2^{15c5} revealed a broad resonance, δ 250, roughly 100 ppm upfield of LaI$_3$ in CD$_3$CN (δ 357), consistent with a significant change in the coordination environment around La (Figure 2.9).[44] We speculate that a La–OH species is formed initially and maintained in solution through cation–macrocycle interactions (evident in ^{1}H NMR spectra showing subtle shifts in the crown-ether protons). A white precipitate was observed upon standing, suggesting that the La eventually precipitates as an insoluble mixed La$_7$(I)$_x$(OH)$_y$ species, such as La$_7$I$_3$(OH)$_{18}$.[45]
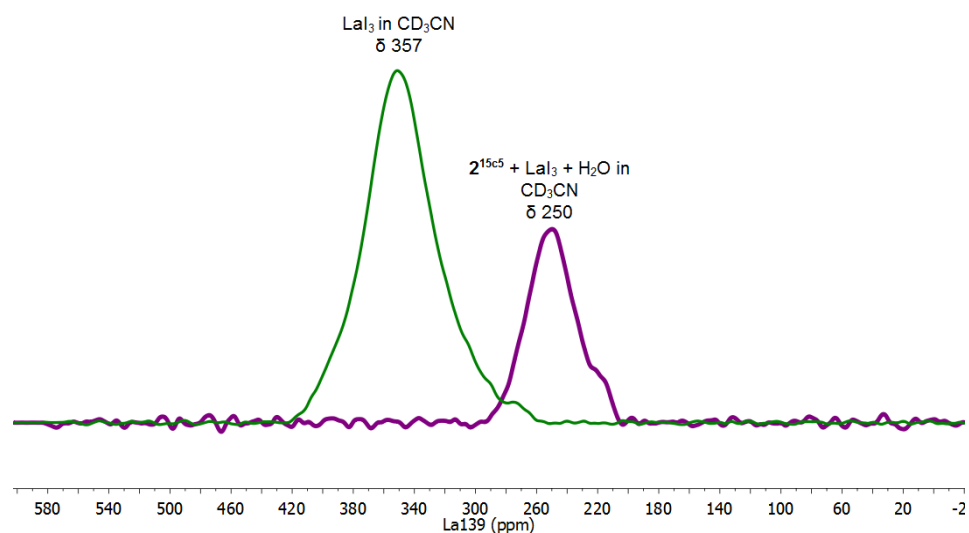
Figure 2.9 ^{139}La NMR spectrum of of LaI$_3$ in CD$_3$CN (green) and ^{139}La NMR spectrum of LaI$_3$ after reacting with Ir^{I} complex **2^{15c5}** and H$_2$O in CD$_3$CN (purple).

The reaction was monitored *in situ* by UV-vis spectroscopy. The Ir(I) complex **2^{15c5}** is bright yellow, with a series of absorption maxima at 480, 412, and 366 nm. In contrast, the resulting Ir(III) hydridoiodide **4^{15c5}** has almost no absorbance above 325 nm. A solution of **2^{15c5}** and excess H$_2$O in CH$_3$CN was injected into a cuvette charged with excess LaI$_3$ and stirred. From the time-course spectra obtained (Figure 2.10) the reaction was determined to reach completion in approximately 7 s.
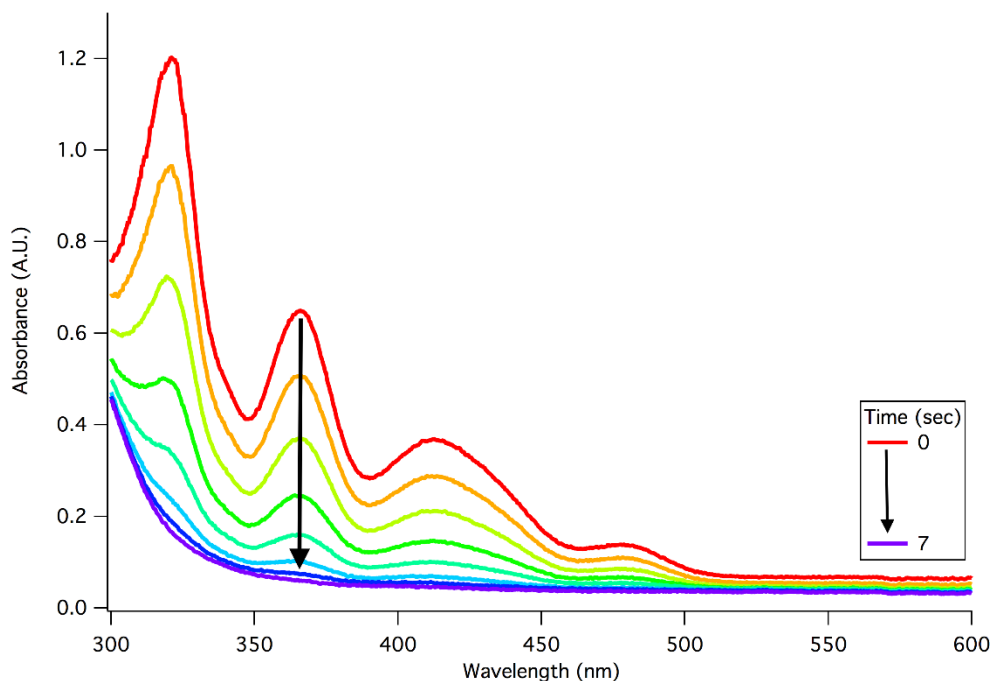
Figure 2.10 Time-course UV-vis spectra (one second intervals) following injection of a solution of 2^{15c5} and H_2O in CH_3CN to a cuvette charged with LaI_3. The loss of absorbance is attributed to protonation of 2^{15c5} to form 4^{15c5}.

The reaction of 2^{15c5} with CaI_2 in the presence of H_2O also led to rapid protonation (within 15 minutes) to form 4^{15c5} in 50% yield, along with other unidentified products. The reaction of 2^{15c5} with LiI, on the other hand, was quite sluggish: it took three days to produce only ~30% yield of hydridoiodide 4^{15c5}, in addition to another unidentified product. The ^1H NMR signals for unreacted 2^{15c5} broadened and shifted slightly after Li^+ addition, suggesting the presence of dynamic cation–crown interactions.

The reactivity of metal salts of the less strongly coordinating triflate (OTf) anion was also explored. Addition of one equivalent of $La(OTf)_3$ to 2^{15c5} in the presence of one equivalent of H_2O in CD_3CN led to rapid formation of the cationic acetonitrile complex $[3^{15c5}][OTf]$ (Scheme 2.9), presumably with concomitant formation of $La(OTf)_2OH$. As with LaI_3, protonation to form an Ir(III) complex was evidenced by discoloration of the bright

40

yellow Ir(I) solution within the time of mixing. The strong Lewis acids $Zn(OTf)_2$ and

$Sc(OTf)_3$ displayed reactivity similar to $La(OTf)_3$, with clean formation of the cationic

acetonitrile complex [3^{15c5}][OTf]. The yellow solutions became colorless within seconds of

mixing, indicating rapid cation-triggered protonation.
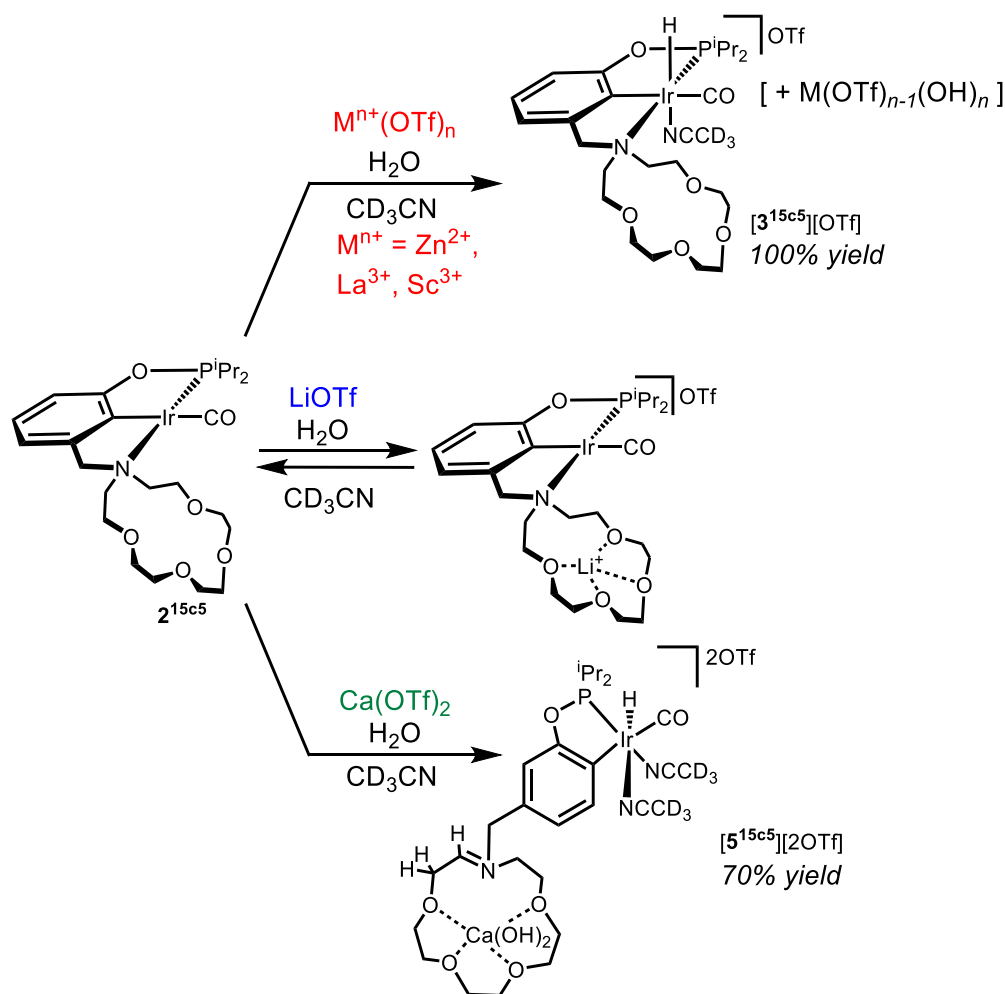
Scheme 2.9 Reactivity of 2^{15c5} with different triflate salts in the presence of water in CD_3CN.

In contrast, addition of one equivalent of $Ca(OTf)_2$ to 2^{15c5} in the presence of one

equivalent of H_2O in CD_3CN led initially to a mixture of protonation products containing the

acetonitrile complex [3^{15c5}][OTf] in just 28% yield, along with another as-yet-unidentified

hydride-containing intermediate (δ –19.13, $^2J_{PH}$ = 14.0 Hz). Over the course of 48 hours,

however, the majority of the Ir had converted to a new hydride-containing species [5^{15c5}]$^{2+}$ (δ

–19.36, $^2J_{PH}$ = 22.0 Hz) in 70% yield. Subsequent addition of a second equivalent of

Ca(OTf)$_2$ often gave even higher yields of [5^{15c5}]$^{2+}$.

The product [5^{15c5}]$^{2+}$ has several unusual spectroscopic features. The pincer backbone

features an atypical pattern of three resonances including a doublet of doublets (δ 6.97 J =

6.8, 2.3 Hz) and a weakly coupled doublet (δ 7.03 J = 1.7 Hz) overlapping with another

apparent doublet of doublets (Figure 2.11). The aromatic resonances are inconsistent with the

pincer connectivity observed in the other Ir complexes discussed here. The data suggest a

pincer backbone metallated at the other C–H bond *ortho* to the phosphinite (Scheme 2.9).
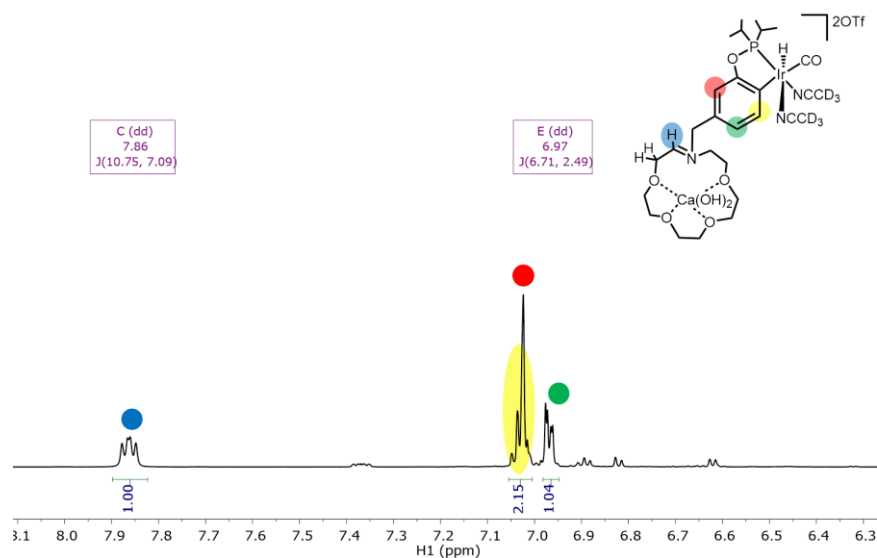
Figure 2.11 ^{1}H NMR spectrum (aromatic region) of [5^{15c5}]$^{2+}$ in CD$_3$CN.

Another striking spectroscopic feature is the downfield doublet of doublets (δ 7.87 J

= 10.9, 7.1 Hz; Figure 2.11). Multidimensional and multinuclear NMR experiments are

indicative of an iminium structure. The resonance at δ 7.87 is assigned to an iminium

R$_2$N=C$\underline{H}$R proton, derived from formal oxidation of the aza-crown ether macrocycle, coupling with the diastereotopic protons α to the iminium (by ^{1}H-^{1}H COSY). One-bond coupling between the resonance at δ 7.87 and a ^{13}C resonance at δ 170.34 (by ^{1}H-^{13}C HMQC), and two-bond coupling between the ^{13}C resonance at δ 170.34 and the diastereotopic protons α to the iminium (δ 3.29, by ^{1}H-^{13}C HMBC) further confirms the assignment. A medium intensity band at 1617 cm^{-1} in the infrared spectrum is also consistent with the presence of an iminium C=N double bond (Figure 2.12).
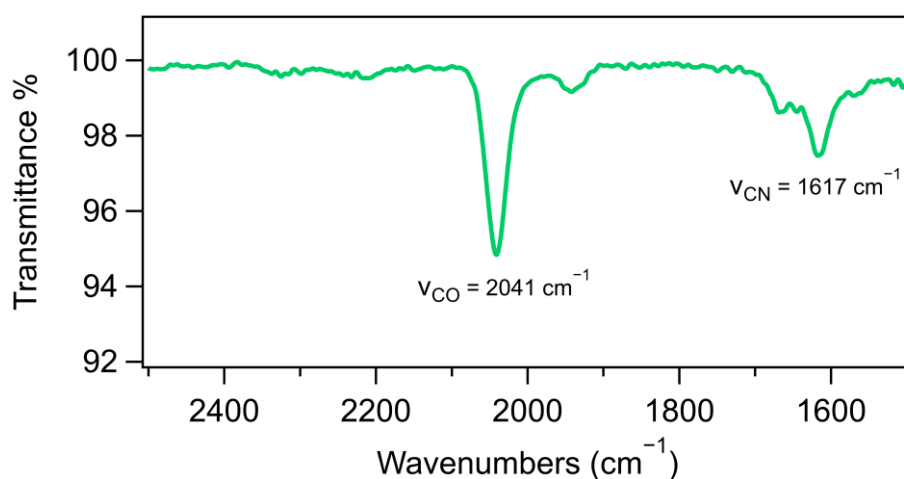
Figure 2.12 Solid-state IR spectrum of [**5^{15c5}**]$^{2+}$.

The rest of the Ir coordination environment in [**5^{15c5}**]$^{2+}$ is proposed to include a carbonyl (by IR spectroscopy, v_{CO} = 2041 cm^{-1}) and two acetonitrile ligands (by NMR studies, including a correlation between the Ir–H and the quaternary carbon of Ir–NCCH$_3$). Electrospray ionization—mass spectrometry studies suggest that the calcium ion is maintained in the macrocycle, based on the observation of ion fragments containing Ir, the pincer-crown ether ligand, and Ca. Unfortunately, extensive attempts to crystallize [**5^{15c5}**]$^{2+}$ afforded only amorphous, oily solids. Nonetheless, Ca^{2+} is unique amongst the Lewis acids examined here in promoting dissociative amine oxidation and structural rearrangements.

The reaction was performed in the presence of D_2O in an attempt to better understand the mechanism. Interestingly, substantial deuterium labeling of the hydride of the minor initial intermediate [3^{15c5}]$^+$ was observed, whereas the unidentified hydride-containing intermediate (δ −19.13) showed no apparent deuterium incorporation. The presence of an initial intermediate without deuterium incorporation suggests that C–H activation (for example, of a methylene in the macrocycle) might be involved in formation of iminium species [5^{15c5}]$^{2+}$. The product showed deuterium incorporation only in the hydride ligand (which is expected to be susceptible to H/D exchange with D_2O in solution). While exploring the potential role of bases in promoting this reaction, we discovered that addition of LaI$_3$ to 2^{15c5} in CD$_3$CN in the presence of NEt$_3$ generated a species that is spectroscopically very similar to [5^{15c5}]$^{2+}$. This finding suggests that balancing Lewis acidity and proton transfer ability may be necessary for this transformation, but the detailed mechanism is unclear at this stage.

Addition of LiOTf to Ir(I) complex 2^{15c5} in the presence of one equivalent of H_2O did not trigger protonation. Instead, the Li$^+$ cation binds the crown, as evidenced by broadening and shifting of ^{1}H NMR resonances (Figure 2.13), similar to those observed for LiI. The resonance for the methylene linker shifted upfield (δ 4.46 to 4.43) and the multiplet for the crown-ether protons shifted downfield (δ 3.61 to 3.73). The signal for H_2O was still present and shifted downfield as well (δ 2.14 to 2.54). The magnitude of these shifts suggest that Li$^+$ binds the macrocycle of 2^{15c5} more strongly than La^{3+} in 4^{15c5}.
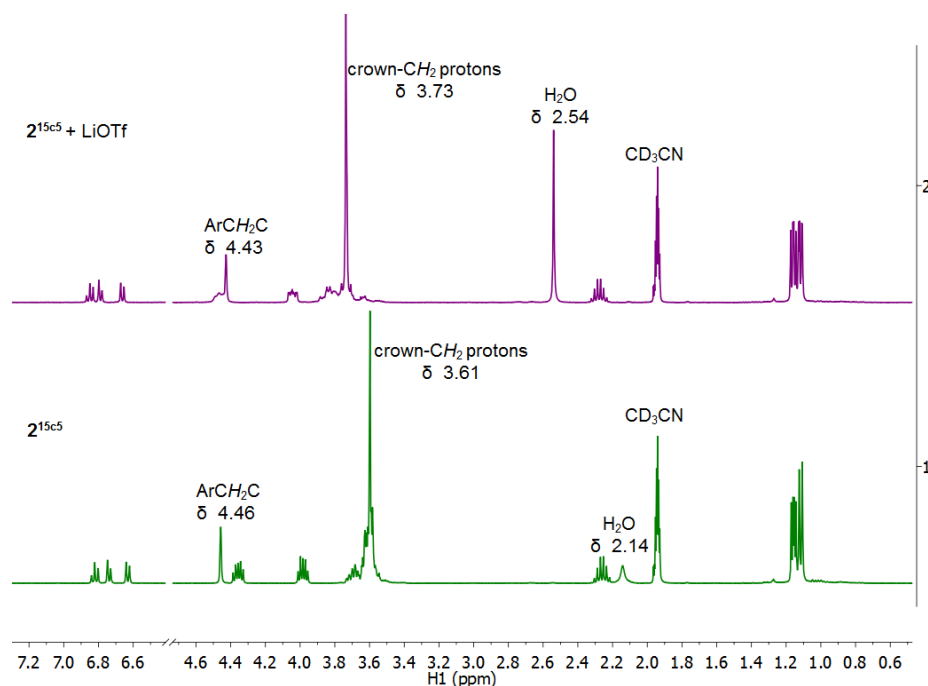
Figure 2.13 ^{1}H NMR spectra showing Li$^+$-macrocycle interactions by addition of LiOTf to 2^{15c5} in CD$_3$CN in the presence of one equivalent of H$_2$O.

Section 2.6   Reactivity of (^{Et}NCOP^{iPr})Ir(CO) with Metal Cations

In order to assess the role of the pendent macrocycle, analogous experiments were conducted with the diethylamine analogues (Scheme 2.10). One equivalent of LiOTf, Ca(OTf)$_2$, or La(OTf)$_3$ was added to solutions of 2^{Et} in CD$_3$CN containing 1 equiv of H$_2$O. In contrast to the reactivity with 2^{15c5}, Li(OTf) did not react with 2^{Et}: neither protonation nor cation interactions with the Ir center was observed (although the resonance for free water did shift downfield slightly in the ^{1}H NMR, indicating a Li$^+$–OH$_2$ interaction). As expected in the absence of a macrocycle capable of binding cations, no shifts in the ^{1}H NMR resonances of 2^{Et} were observed. Addition of La(OTf)$_3$ triggered protonation to yield [3^{Et}][OTf] (δ −19.63, $^2J_{PH} = 21.8$ Hz), a reactivity trend that closely matched that of the complex containing the macrocyclic ligand.

45
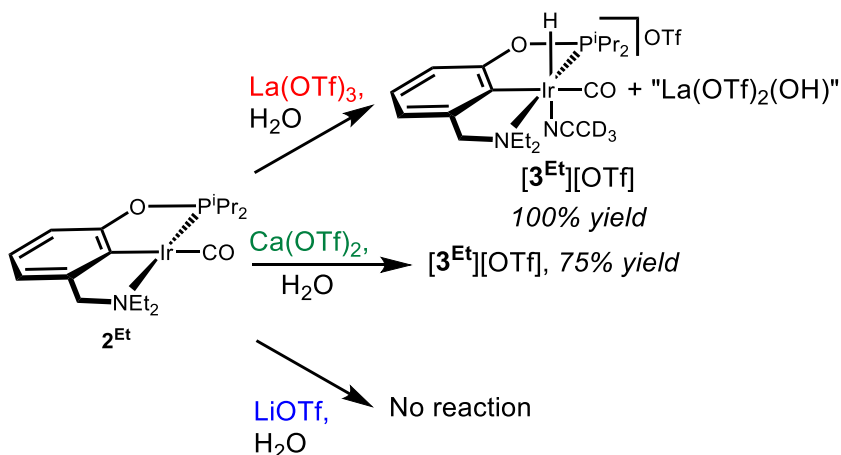
Scheme 2.10 Reactivity of 2^{Et} with different triflate salts in the presence of water in CD_3CN.

Whereas $Ca(OTf)_2$ has a unique reactivity pattern with 2^{15c5}, the reactivity of 2^{Et} with $Ca(OTf)_2$ was found to be qualitatively similar to that observed for other alkali metals. Addition of $Ca(OTf)_2$ led to 75% conversion to $[3^{Et}][OTf]$ over the course of 3 hours. No change in the site of metallation, nor iminium formation was observed, even after monitoring for extended periods. Calcium-macrocycle interactions apparently are required to trigger amine oxidation and dechelation as well as metallation at a different position along the pincer-crown ether arene backbone. Even when 2^{Et} was treated with $Ca(OTf)_2$ and H_2O in the presence of free 12-crown-4 in solution, only protonation was observed (no change in metallation or iminium formation).

As shown in Scheme 2.10, cation-triggered protonation by H_2O depends on the specific salt employed. More Lewis acidic metals would render cation-bound H_2O a stronger Brønsted acid, but the protonation reactivity is also affected by the solvent medium and hydrogen bonding. For example, when $Ca(OTf)_2$ was added to 2^{Et} as an aqueous solution (rather than a 1:1 $Ca(OTf)_2$:H_2O ratio), almost no protonation was observed over the course

of 3 h. The reduced reactivity in the presence of excess H_2O is attributed to hydrogen bonding between water molecules in the secondary coordination sphere and those in the primary coordination sphere, which would render the cation-bound H_2O less Brønsted acidic. The stronger Lewis acid LaI_3 was not inhibited by excess water, consistent with the ability of lanthanide salts to act as good Lewis acids in aqueous catalysis.[40]

Section 2.7   Conclusions

The reactivity of new Ir(I) and Ir(III) carbonyl complexes with various Lewis acidic metal cations has been characterized. In the Ir(III) state, halide abstraction, halide exchange, and cation–macrocycle interactions are all observed, depending on the choice of metal salt. The solvent also plays an important role, as precipitation can drive one reaction over another. At the Ir(I) state, protonation by water is dominant, but, again, the choice of metal salt can dictate the rate of protonation and the yield of the resulting Ir(III) hydride product. Schemes 2.9 and 2.10 highlight the distinct reaction pathways possible when the Ir(I) carbonyl complexes are treated with metal triflate salts in the presence of water. In the case of Li^+, only cation–macrocycle interactions are observed, whereas stronger Lewis acids such as $Sc(OTf)_3$ and $La(OTf)_3$ trigger protonation at the Ir center.

The observed reactivity trends appear to correlate with the average of reported pK_a values of the corresponding metal aquo complexes.[43] More Lewis acidic metal cations tend to support aquo complexes with lower pK_a values.[46] The strongest Lewis acids, Sc^{3+}, Zn^{2+}, and La^{3+} (aquo pK_a of 4.9, 8.9, and 9.5 respectively) cleanly and rapidly protonated the Ir(I) site; the weaker Lewis acid Li^+ (aquo $pK_a = 13.7$) did not protonate the Ir(I) site. Intriguingly, the cation of intermediate acidity, Ca^{2+} (aquo $pK_a = 12.7$) initially resulted in protonation to give two species, but it eventually funneled to the alternate metalation iminium product [**5^{15c5}**]$^{2+}$.

The protonation reactivity of the strong Lewis acid La^{3+} was not inhibited by the presence of large amounts of water, whereas the weaker Lewis acid Ca^{2+} showed almost complete loss of reactivity.

When combined with an early metal cation, (NCOP)Ir(CO) complexes react with water in a different fashion than other Ir(I) complexes.[47] As shown in Scheme 2.14, some Ir(I) complexes undergo O–H oxidative addition at the Ir center (path A).[48–51] Simple ligand association is another common reaction of water (path B), with formation of Ir–OH$_2$ species observed in lieu of oxidative addition reactivity.[52] (NCOP)Ir(CO) complexes react with water to form Ir–H products (path C), but we see no evidence of Ir(H)(OH) species that would be indicative of formal O–H oxidative addition of water. Instead, we hypothesize that water binds to the Lewis acidic cations, rendering the water molecule a stronger Brønsted acid capable of protonation at Ir and leaving the hydroxide ligand bound to the hard early metal cation. An analogous mechanism has been proposed for water oxidative addition to Pt centers flanked with H-bond donors or boranes in the secondary coordination sphere.[18,53] The ability of a specific salt to trigger protonation by H_2O depends on the Lewis acidity of the cation and the amount of H_2O present; more Lewis acidic cations lead to bound H_2O that is more Brønsted acidic, but this acidity can be tempered by hydrogen bonding by excess H_2O in the secondary coordination sphere of the cation.

$$L_nIr^I + H_2O \xrightarrow{\ \ \ \ } \begin{array}{c} \overset{H}{\underset{|}{L_nIr}}-OH \\ \\ L_nIr-OH_2 \\ \\ \overset{+}{L_nIr}-H \\ + \\ M-OH \end{array}$$

A

B

C

M⁺
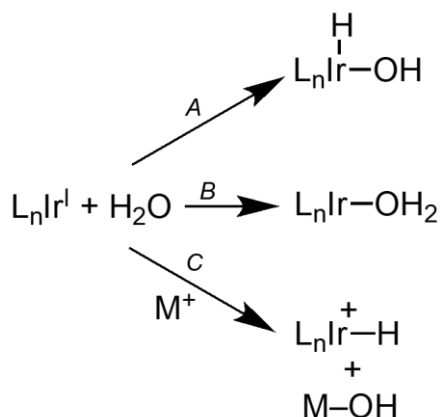
Figure 2.14 Different reactivity pathways of Ir(I) complexes with water.

One goal of this project was to examine the role of the pendent macrocycle in the pincer-crown ether ligand. The macrocycle is important in some reactions, but plays no apparent role in others. Halide abstraction and halide exchange reactions, for example, proceed similarly with or without a macrocyclic ligand. On the other hand, cation–macrocycle interactions are fostered only by complexes supported by the pincer-crown ether ligand. The host-guest complexation is weak when LaI$_3$ interacts with the Ir(III) complex **4^{15c5}**, whereas stronger interactions are indicated by the larger change in chemical shift observed in mixtures of **2^{15c5}** and LiOTf. The non-macrocyclic NCOP ligand does not interact with cations in solution, as evidenced by the lack of any changes in ^{1}H NMR resonances in the presence of various salts. The other reaction unique to the pincer-crown ether ligands is a complicated reaction that results in iminium formation and a change in the metallation site of the ligand backbone.

Section 2.8   Experimental Details

General Considerations. All manipulations were carried out using standard Schlenk or glovebox techniques under a N$_2$ atmosphere. Under standard glovebox operating conditions, pentane, diethyl ether, benzene, toluene, and tetrahydrofuran were used without purging,

such that traces of those solvents were present in the atmosphere and in the solvent bottles. ^{1}H, ^{31}P, ^{13}C, and ^{139}La NMR spectra were recorded on 400, 500 or 600 MHz spectrometers at 298 K. NMR solvents were purchased from Cambridge Isotopes Laboratories, Inc. Acetone-d_6, acetonitrile-d_3 (CD$_3$CN), and benzene-d_6 (C$_6$D$_6$) were freeze-pump-thaw degassed three times before drying by passage through a small column of activated alumina. ^{1}H and ^{13}C chemical shifts are reported in ppm relative to residual proteo solvent resonances. ^{31}P chemical shifts are reported relative to 85% H$_3$PO$_4$ external standard (δ 0). ^{139}La resonances are reported relative to a 0.1 M solution of La(ClO$_4$)$_3$·6H$_2$O in 80:20 H$_2$O:D$_2$O (δ 0). The compounds (^{15c5}NCOP^{iPr})H,[19] (^{Et}NCOP^{iPr})H,[27] and Ir(p-toluidine)(CO)$_2$(Cl)[22] were synthesized according to literature procedures. All other reagents were commercially available and used without further purification. Elemental analyses were performed by Robertson Microlit Labs (Ledgewood, NJ). UV-Vis spectra were collected with an Ocean Optics USB2000+ spectrometer with a DT-MINI-2GS deuterium/tungsten halogen light source. Infrared spectroscopy was carried out with a Bruker Alpha FT-IR equipped with an ATR module or a Thermo Scientific Nicolet iS5 FT-IR equipped with Quest Single Reflection ATR Accessory. Mass spectrometry was carried out with a LTQ FT (ICR 7T) (ThermoFisher, Bremen, Germany) mass spectrometer. Measurements were made on complexes dissolved in acetonitrile. Samples were introduced via a micro-electrospray source at a flow rate of 3 μL/min. Xcalibur (ThermoFisher, Breman, Germany) was used to analyze the data. Molecular formula assignments were determined with Molecular Formula Calculator (v 1.2.3). Low-resolution mass spectrometry (linear ion trap) provided independent verification of molecular weight distributions. All observed species were singly charged, as verified by unit *m/z* separation between mass spectral peaks corresponding to the

^{12}C and ^{13}C^{12}C$_{c-1}$ isotope for each elemental composition. Single crystal X-ray diffraction data was collected on a Bruker APEX-II CCD diffractometer at 100 K with Cu Kα radiation (λ = 1.54175 Å). Using Olex2,[54] the structures were solved with the olex2.solve[55] structure solution program using Charge Flipping and refined with the XL[56] refinement program using Least Squares minimization.

Synthesis of (^{15c5}NCOP^{iPr})Ir(H)(CO)(Cl) (1^{15c5}). A Schlenk flask was charged with 0.211 g (0.539 mmol) Ir(p-toluidine)(CO)$_2$(Cl) and suspended in 5 mL toluene. The ligand (^{15c5}NCOP^{iPr})H (0.240 g, 0.544 mmol) was dissolved in 5 mL toluene and added to the Ir precursor suspension to yield a yellow solution that was further diluted with an additional 10 mL toluene. The mixture was refluxed for 14 h, at which point the mixture was allowed to cool and the solvent removed under vacuum. The residue was washed with pentane (2 × 5 mL) and extracted with benzene (10 mL). The resulting orange benzene solution was evaporated under vacuum to yield 0.356 g of a brown-yellow solid (95% yield). ^{1}H NMR (400 MHz, C$_6$D$_6$): δ 6.96 (t, J = 7.6 Hz, 1H, ArH), 6.91 (d, J = 7.8 Hz, 1H, ArH), 6.75 (d, J = 7.1 Hz, 1H, ArH), 4.95 (d, J = 13.2 Hz, 1H, ArCHHN), 4.61 (d, J = 14.2 Hz, 1H, crown-CH), 4.13 (dt, J = 9.7, 6.5 Hz, 1H, crown-CH), 3.98 – 3.90 (m, 1H), 3.87 (dd, J = 13.4, 3.8 Hz, 1H, ArCHHN), 3.80 (ddd, J = 9.7, 6.6, 4.9 Hz, 1H, crown-CH), 3.58 (ddd, J = 11.4, 7.2, 4.4 Hz, 1H, crown-CH), 3.48 (dq, J = 12.1, 6.1 Hz, 1H, crown-CH), 3.41 – 3.12 (m, 14H, , crown-CH_2), 2.93 (dp, J = 14.7, 7.3 Hz, 1H, CH(CH$_3$)$_2$), 1.94 (dp, J = 12.2, 7.0 Hz, 1H, CH(CH$_3$)$_2$), 1.32 (dd, J = 18.5, 7.3 Hz, 3H, CH(CH_3)$_2$), 1.11 (dd, J = 16.2, 7.1 Hz, 3H, CH(CH_3)$_2$), 0.81 (overlapping dd, J = 19.0, 15.7, 7.0 Hz, 2×3H, CH(CH_3)$_2$), –18.30 (d, $^2J_{PH}$ = 20.8 Hz, 1H, Ir–H). ^{13}C{^{1}H} NMR (151 MHz, C$_6$D$_6$): δ 181.88 (d, J = 2.9 Hz, Ir–CO), 161.93 (d, J = 2.5 Hz, C_{Ar}), 149.22 (d, J = 4.9 Hz, C_{Ar}), 148.67 (d, J = 2.2 Hz, C_{Ar}), 126.17 (s, C_{Ar}), 117.63 (s, C_{Ar}),

109.05 (d, $J = 12.3$ Hz, C_{Ar}), 71.30 (s, crown-CH_2), 71.25 (d, $J = 2.5$ Hz, crown-CH_2), 71.17 (s, ArCH_2N), 70.79 (d, $J = 9.6$ Hz, crown-CH_2), 70.68 (d, $J = 4.6$ Hz, crown-CH_2), 70.50, (s, crown-CH_2), 68.13 (d, $J = 1.0$ Hz, crown-CH_2), 64.01, (s, crown-CH_2), 59.50 (d, $J = 2.5$ Hz, crown-CH_2), 32.42 (d, $J = 33.7$ Hz, $CH(CH_3)_2$), 29.46 (d, $J = 42.3$ Hz, $CH(CH_3)_2$), 18.36 (d, $J = 5.0$ Hz, CH($CH_3)_2$), 18.02, (s, CH($CH_3)_2$), 17.70 (d, $J = 2.7$ Hz, CH($CH_3)_2$), 16.02 (s, CH($CH_3)_2$). ^{31}P{^{1}H} NMR (162 MHz, C_6D_6): δ 153.73. IR (solid, cm^{-1}): ν_{CO} 2010 cm^{-1}, ν(Ir−H) 2198 cm^{-1}. IR (solution, CH_3CN, cm^{-1}): ν_{CO} 2024 cm^{-1}. Anal. Calcd for $C_{24}H_{40}ClIrNO_6P$: C, 41.34; H, 5.78; N, 2.01. Found: C, 42.15; H, 5.62; N, 1.98. HRMS (ESI$^+$) m/z [$\mathbf{1^{15c5}}$+Na]$^+$ Calcd for $C_{24}H_{40}ClIrNNaO_6P$ 720.1809; Found 720.1817.
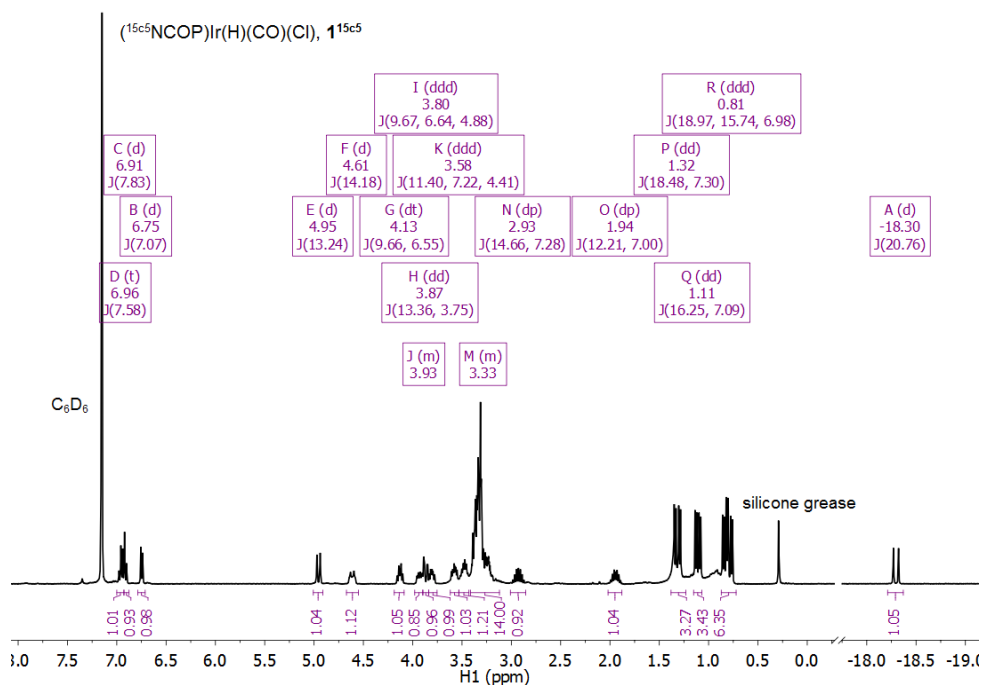
Figure 2.15 ^{1}H NMR spectrum of (^{15c5}NCOP^{iPr})Ir(H)(CO)(Cl) ($\mathbf{1^{15c5}}$) in C_6D_6.

52
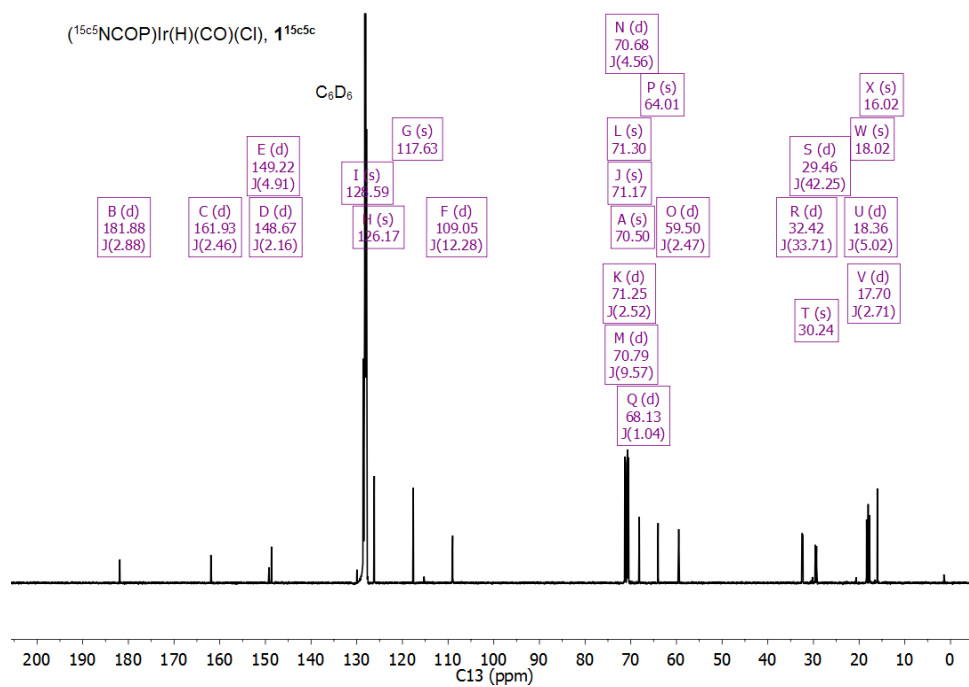
Figure 2.16 $^{13}C\{^1H\}$ NMR spectrum of $(^{15c5}NCOP^{iPr})Ir(H)(CO)(Cl)$ ($\mathbf{1^{15c5}}$) in C_6D_6.
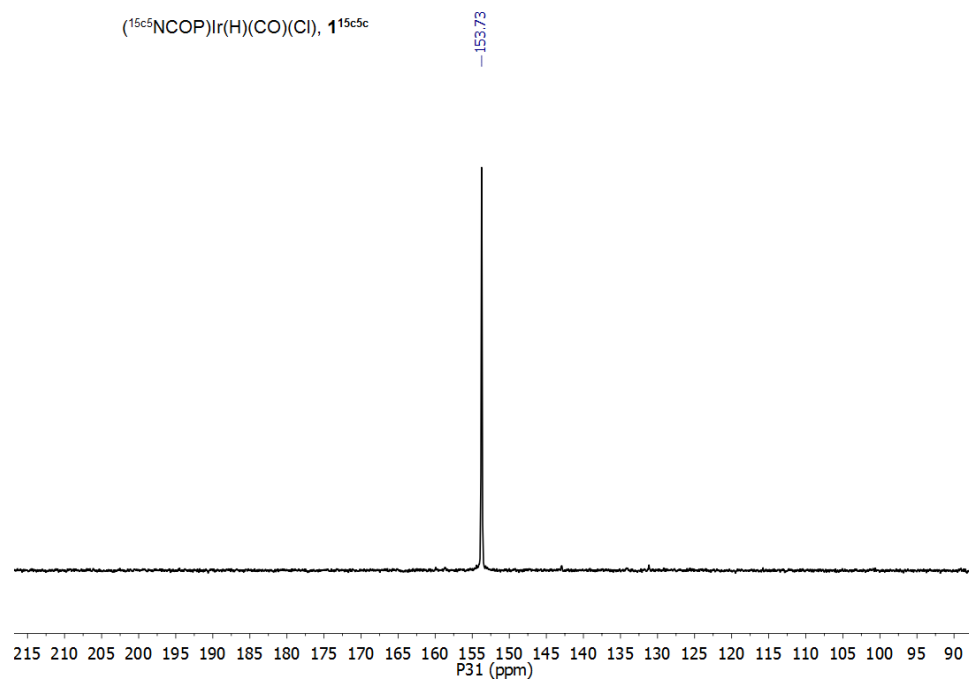
Figure 2.17 $^{31}P\{^1H\}$ NMR spectrum of $(^{15c5}NCOP^{iPr})Ir(H)(CO)(Cl)$ ($\mathbf{1^{15c5}}$) in C_6D_6.

Synthesis of (^{Et}NCOP^{iPr})Ir(H)(CO)(Cl) (1^{Et}). A procedure directly analogous to that of

1^{15c5} was used, affording **1**^{Et} as a brown-yellow oil in 90% yield. ^{1}H NMR (600 MHz, C$_6$D$_6$):

δ 6.98 (t, J = 7.7 Hz, 1H, ArH), 6.93 (d, J = 8.0 Hz, 1H, ArH), 6.75 (d, J = 7.3 Hz, 1H, ArH),

4.80 (d, J = 13.4 Hz, 1H, ArCHHN), 4.15 (dd, J = 14.4, 7.2 Hz, 1H, NCH_2CH$_3$), 3.47 (dd, J

= 13.4, 3.7 Hz, 1H, ArCHHN), 3.41 (dq, J = 14.3, 7.3 Hz, 1H, NCH_2CH$_3$), 2.96 (tq, J = 14.5,

7.2 Hz, 1H, CH(CH$_3$)$_2$), 2.66 (dq, J = 14.3, 7.3 Hz, 1H, NCH_2CH$_3$), 2.41 – 2.32 (m, 1H,

NCH_2CH$_3$), 1.98 (dp, J = 12.5, 6.9 Hz, 1H, CH(CH$_3$)$_2$), 1.34 (dd, J = 18.5, 7.3 Hz, 3H,

CH(CH_3)$_2$), 1.13 (dd, J = 16.1, 7.0 Hz, 3H, CH(CH_3)$_2$), 0.85 (ddd, J = 26.0, 17.4, 7.0 Hz, 6H,

CH(CH_3)$_2$), 0.77 (t, J = 7.1 Hz, 3H, NCH$_2$CH_3), 0.53 (t, J = 7.3 Hz, 3H, NCH$_2$CH_3), −18.48

(d, J = 20.8 Hz, 1H, Ir–H). ^{13}C{^{1}H} NMR (151 MHz, C$_6$D$_6$): δ 181.94 (s, Ir–CO), 161.98 (d,

J = 2.8 Hz, C_{Ar}), 148.89 (d, J = 5.7 Hz, C_{Ar}), 148.51 (d, J = 2.4 Hz, C_{Ar}), 126.08 (s, C_{Ar}),

117.46 (s, C_{Ar}), 108.95 (d, J = 12.2 Hz, C_{Ar}), 69.79 (d, J = 2.3 Hz, ArCH$_2$N), 56.36 (s,

NCH$_2$CH$_3$), 52.09 (d, J = 2.5 Hz, NCH$_2$CH$_3$), 32.43 (d, J = 33.7 Hz, CH(CH$_3$)$_2$), 29.17 (d, J

= 41.8 Hz, CH(CH$_3$)$_2$), 18.43 (d, J = 5.3 Hz (s, CH(CH$_3$)$_2$), 18.07 (s, CH(CH$_3$)$_2$), 17.73 (d, J

= 2.8 Hz, CH(CH$_3$)$_2$), 15.94 (s, CH(CH$_3$)$_2$), 12.77 (s, NCH$_2$$CH_3$), 8.70 (s, NCH$_2$$CH_3$).

^{31}P{^{1}H} NMR (162 MHz, C$_6$D$_6$): δ 154.20. IR (solid, cm^{-1}): ν(CO) 2011 cm^{-1}, ν(Ir−H) 2198

cm^{-1}. Note: The oily nature of **1**^{Et} precluded purification by re-crystallization and led to

deviation from the expected elemental analysis values. HRMS (ESI$^+$) m/z [**1**^{Et}+K]$^+$ Calcd for

C$_{18}$H$_{30}$ClIrKNO$_2$P 590.0969; Found 590.0975.
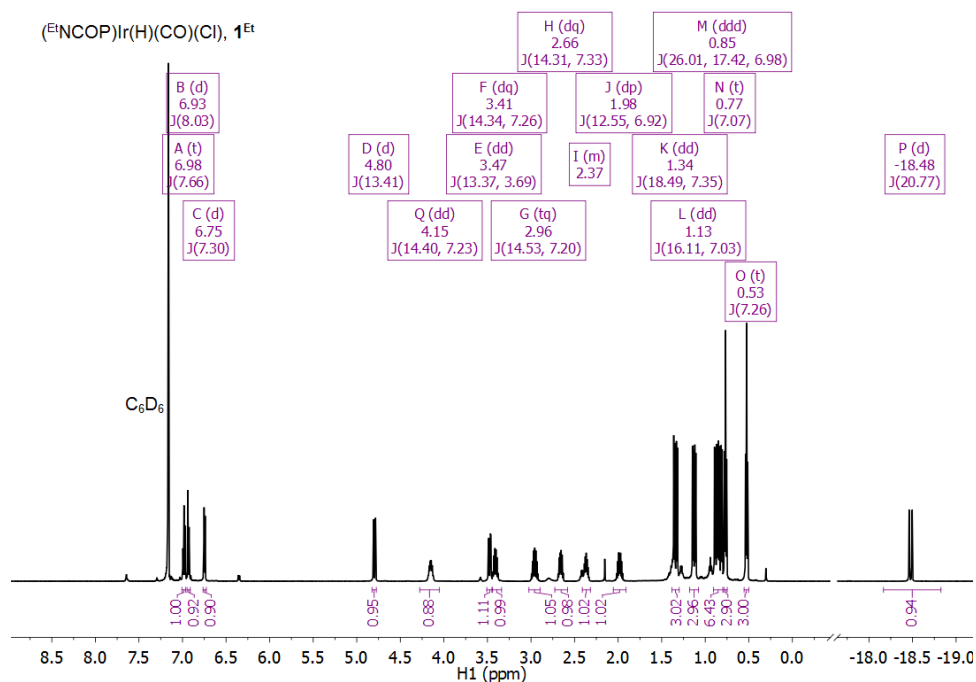
Figure 2.18 ^{1}H NMR spectrum of (^{Et}NCOP^{iPr})Ir(H)(CO)(Cl) (**1^{Et}**) in C_6D_6. Trace amounts of silicone grease (δ 0.29), toluene (δ 2.15, 7.03), and pentane (δ 0.94, 1.28).
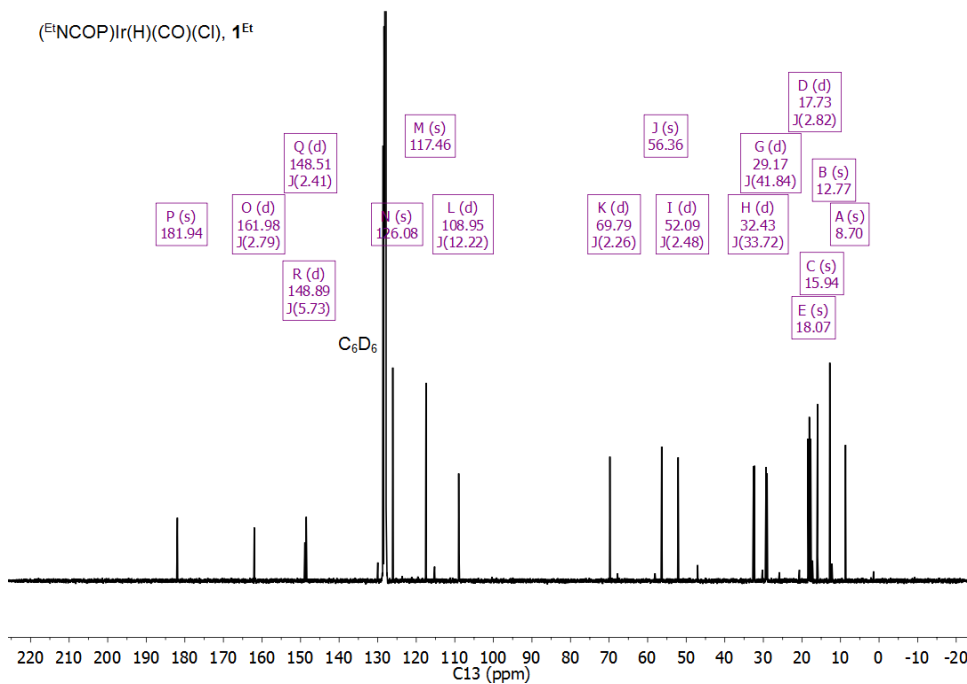
Figure 2.19 ^{13}C{^{1}H} NMR spectrum of (^{Et}NCOP^{iPr})Ir(H)(CO)(Cl) (**1^{Et}**) in C_6D_6. Trace amounts of silicone grease (δ 1.44), toluene (δ 20.65, 129.97), tetrahydrofuran (δ 25.82, 67.83), H grease (δ 30.25).

55

(^{Et}NCOP)Ir(H)(CO)(Cl), **1**^{Et}

−154.20

205 200 195 190 185 180 175 170 165 160 155 150 145 140 135 130 125 120 115 110 105 100
P31 (ppm)
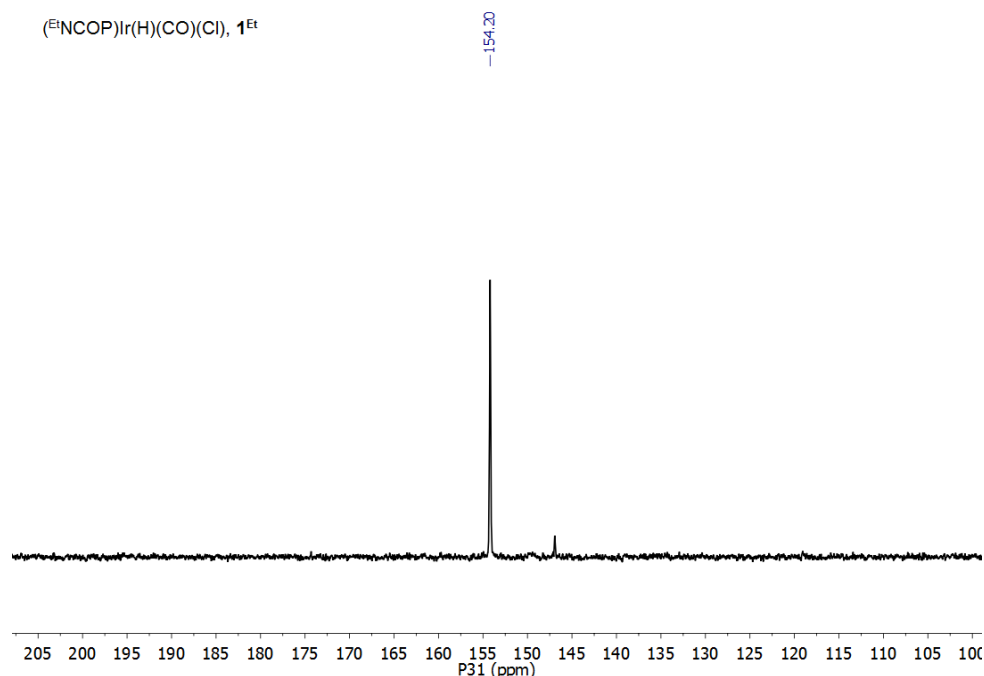
Figure 2.20 ^{31}P{^{1}H} NMR spectrum of (^{Et}NCOP^{iPr})Ir(H)(CO)(Cl) (**1**^{Et}) in C$_6$D$_6$.

Synthesis of (^{15c5}NCOP^{iPr})Ir(CO) (2^{15c5}). A 20-mL scintillation vial was charged with 0.100 g (0.143 mmol) **1**^{15c5} and 0.026 g (0.235 mmol) KO^{t}Bu. The solids were dissolved in 6 mL benzene and the resulting dark orange solution that was stirred for 3 h. Benzene was then removed under vacuum. The residue was stirred in 20 mL pentane for 48 h and filtered, yielding a bright yellow solution. Pentane was evaporated under vacuum, affording a bright yellow solid (0.074 g, 78% yield). ^{1}H NMR (600 MHz, C$_6$D$_6$): δ 7.02 (d, J = 7.8 Hz, 1H, ArH), 6.95 (t, J = 7.6 Hz, 1H, ArH), 6.73 (d, J = 7.3 Hz, 1H, ArH), 4.40 (dt, J = 11.6, 6.0 Hz, 2H, crown-CH_2), 4.10 (s, 2H, ArCH_2N), 3.87 (dt, J = 11.0, 5.5 Hz, 2H, crown-CH_2), 3.74 – 3.66 (m, 2H, crown-CH_2), 3.61 (dtd, J = 13.2, 5.6, 1.7 Hz, 2H, crown-CH_2), 3.49 – 3.24 (m, 12H, crown-CH_2), 2.10 (h, J = 7.0 Hz, 2H, CH(CH$_3$)$_2$), 1.19 (d, J = 7.1 Hz, 6H, CH(CH_3)$_2$), 1.17 (dd, J = 7.0, 3.8 Hz, 6H, CH(CH_3)$_2$). ^{13}C{^{1}H} NMR (151 MHz, C$_6$D$_6$): δ 198.81 (d, J = 2.5 Hz, Ir–CO), 167.27 (d, J = 8.2 Hz, C_{Ar}), 166.22 (d, J = 6.2 Hz, C_{Ar}), 153.93 (d, J = 3.3

56

Hz, C_{Ar}), 127.40 (s, C_{Ar}), 115.07 (s, C_{Ar}), 107.68 (d, $J = 12.5$ Hz, C_{Ar}), 73.07 (s, ArCH_2N),

71.06 – 70.84 (m, crown-CH_2), 70.68 (s, crown-CH_2), 63.45 (d, $J = 2.3$ Hz, crown-CH_2),

31.42 (d, $J = 37.9$ Hz, $CH(CH_3)_2$), 30.25 (s, $CH(CH_3)_2$), 18.45 (d, $J = 4.8$ Hz, CH(CH_3)$_2$),

17.72 (s, CH(CH_3)$_2$). ^{31}P{^{1}H} NMR (162 MHz, C_6D_6): δ 170.70. IR (solid, cm^{-1}): ν(CO)

1921 cm^{-1}. Anal. Calcd for $C_{24}H_{39}IrNO_6P$: C, 43.63; H, 5.95; N, 2.12. Found: C, 43.90; H,

5.98; N, 2.09.
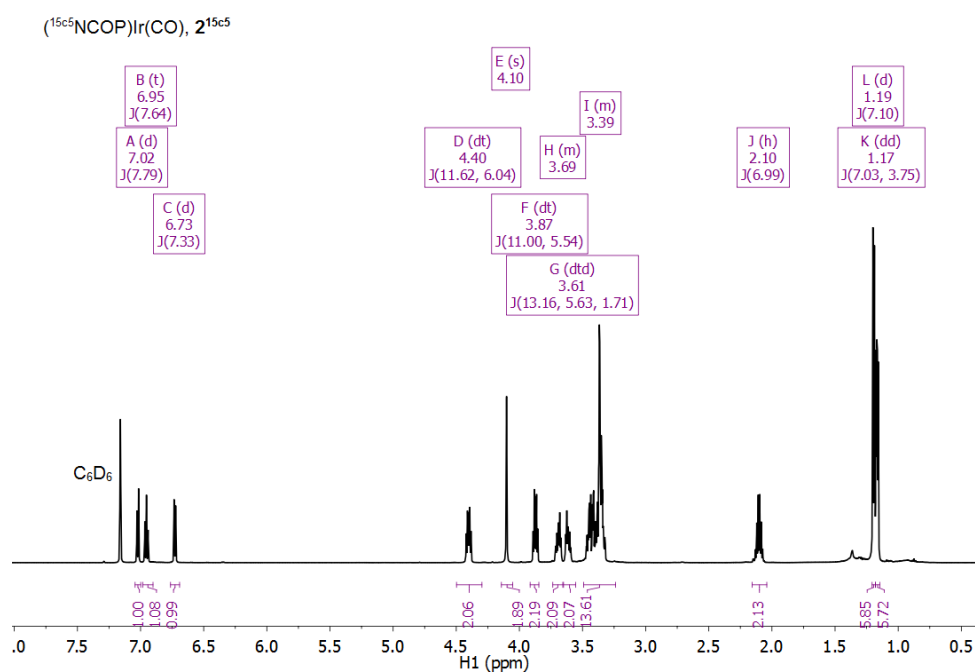
Figure 2.21 ^{1}H NMR spectrum of (^{15c5}NCOP^{iPr})Ir(CO) (2^{15c5}) in C_6D_6.

57
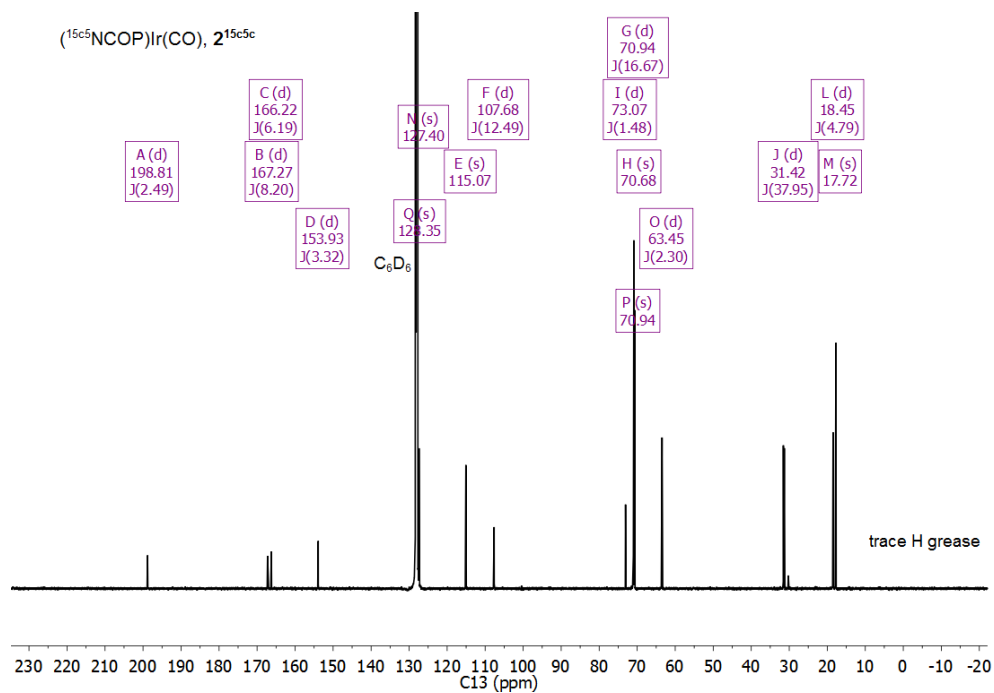
Figure 2.22 $^{13}C\{^1H\}$ NMR spectrum of ($^{15c5}NCOP^{iPr}$)Ir(CO) (2^{15c5}) in C_6D_6.
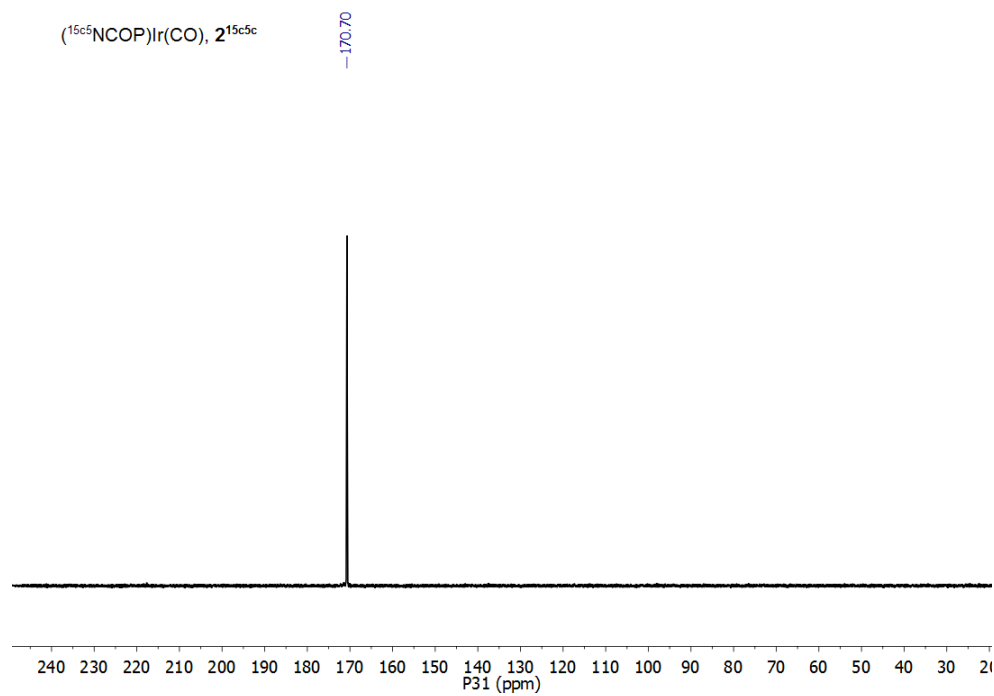
Figure 2.23 $^{31}P\{^1H\}$ NMR spectrum of ($^{15c5}NCOP^{iPr}$)Ir(CO) (2^{15c5}) in C_6D_6.

Synthesis of (^{Et}NCOP^{iPr})Ir(CO) (2^{Et}). A procedure directly analogous to that of 2^{15c5} was

used, affording 2^{Et} as a bright orange-yellow solid (0.051 g, 47 % yield). ^{1}H NMR (500

MHz, C$_6$D$_6$): δ 7.02 (d, J = 7.9 Hz, 1H, ArH), 6.96 (t, J = 7.6 Hz, 1H, ArH), 6.72 (d, J = 7.4

Hz, 1H, ArH), 3.77 (s, 2H, ArCH_2N), 2.93 (dqd, J = 12.3, 7.2, 1.7 Hz, 2H, NCH_2CH$_3$), 2.84

(dqd, J = 14.2, 7.1, 2.6 Hz, 2H, NCH_2CH$_3$), 2.11 (h, J = 7.0 Hz, 2H, CH(CH$_3$)$_2$), 1.28 (t, J =

7.1 Hz, 6H, NCH$_2$CH_3), 1.20 (dd, J = 7.0, 2.7 Hz, 6H, CH(CH_3)$_2$), 1.17 (dd, J = 7.0, 5.6 Hz,

6H, CH(CH_3)$_2$). ^{13}C{^{1}H} NMR (151 MHz, C$_6$D$_6$): δ 198.72 (d, J = 2.7 Hz, Ir–CO), 167.10 (d,

J = 8.3 Hz, C_{Ar}), 166.13 (d, J = 6.3 Hz, C_{Ar}), 155.19 (d, J = 2.8 Hz, C_{Ar}), 127.22 (s, C_{Ar}),

114.36 (s, C_{Ar}), 107.57 (d, J = 12.3 Hz, C_{Ar}), 70.54 (s, ArCH$_2$N), 58.89 (d, J = 2.3 Hz,

NCH$_2$CH$_3$), 31.44 (d, J = 37.6 Hz, CH(CH$_3$)$_2$), 18.43 (d, J = 5.1 Hz, CH(CH$_3$)$_2$), 17.69 (s,

CH(CH$_3$)$_2$), 13.69 (s, NCH$_2$$CH_3$). ^{31}P{^{1}H} NMR (162 MHz, C$_6$D$_6$): δ 171.58. IR (solid, cm^{-}

^{1}): ν(CO) 1922 cm^{-1}. Anal. Calcd for C$_{18}$H$_{29}$IrNO$_2$P: C, 42.01; H, 5.68; N, 2.72. Found: C,

42.82; H, 5.82; N, 2.62.
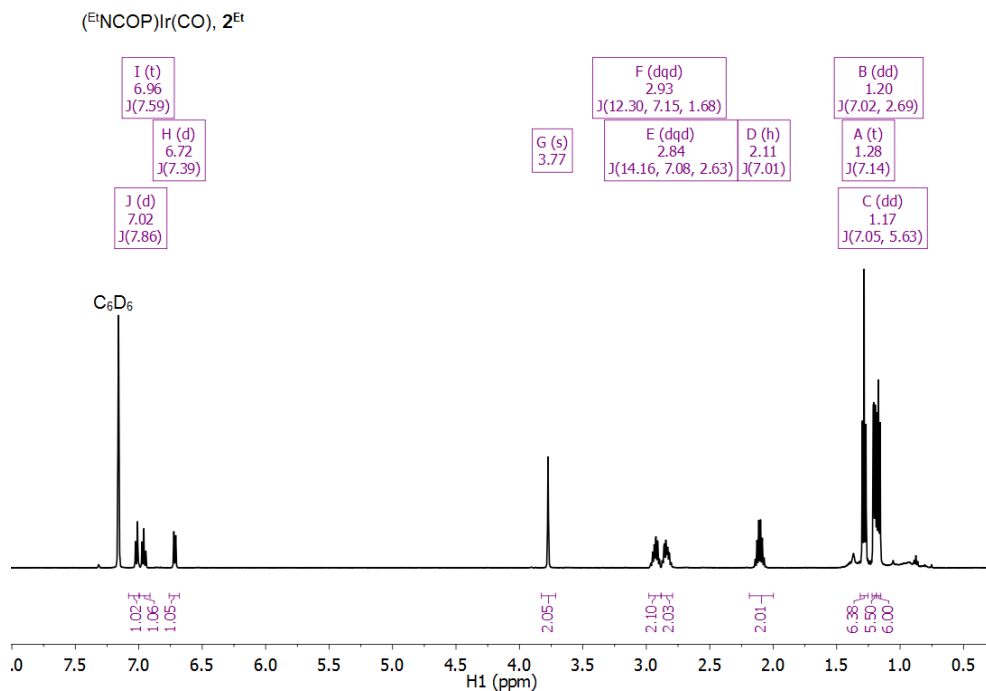
Figure 2.24 ^{1}H NMR spectrum of ([Et]NCOP[iPr])Ir(CO) (**2[Et]**) in C_6D_6. Trace amounts of pentane (δ 0.88) and H grease (δ 1.37).
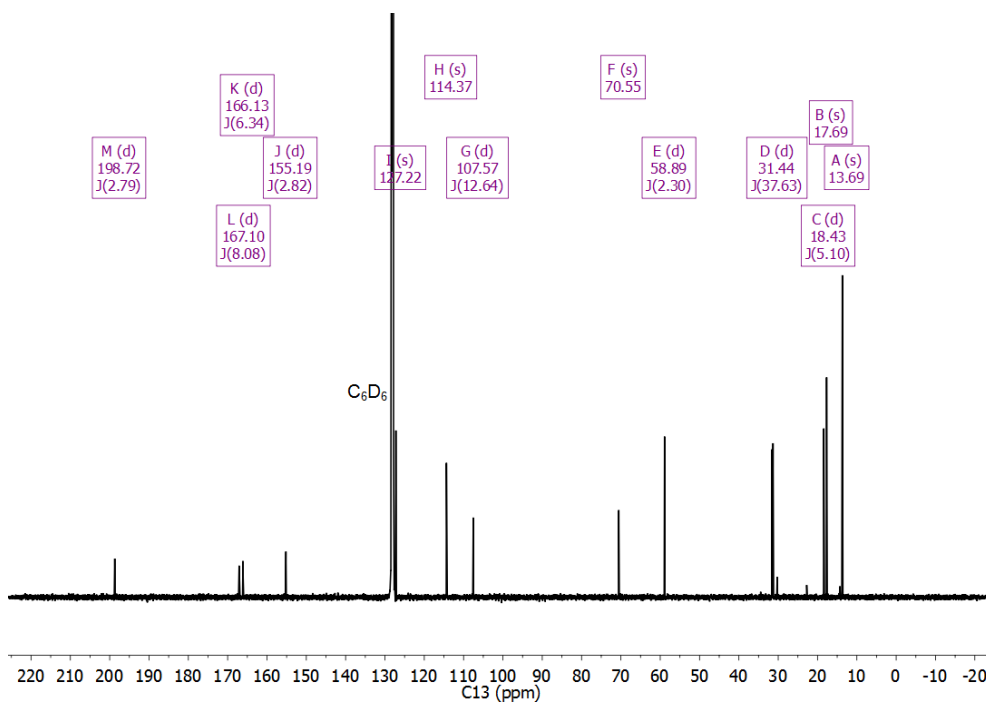
Figure 2.25 ^{13}C{^{1}H} NMR spectrum of ([Et]NCOP[iPr])Ir(CO) (**2[Et]**) in C_6D_6. Trace amounts of pentane (δ 14.31, 22.75, 34.45) and H grease (δ 30.25).

(^{Et}NCOP^{iPr})Ir(CO), **2^{Et}**

−171.58
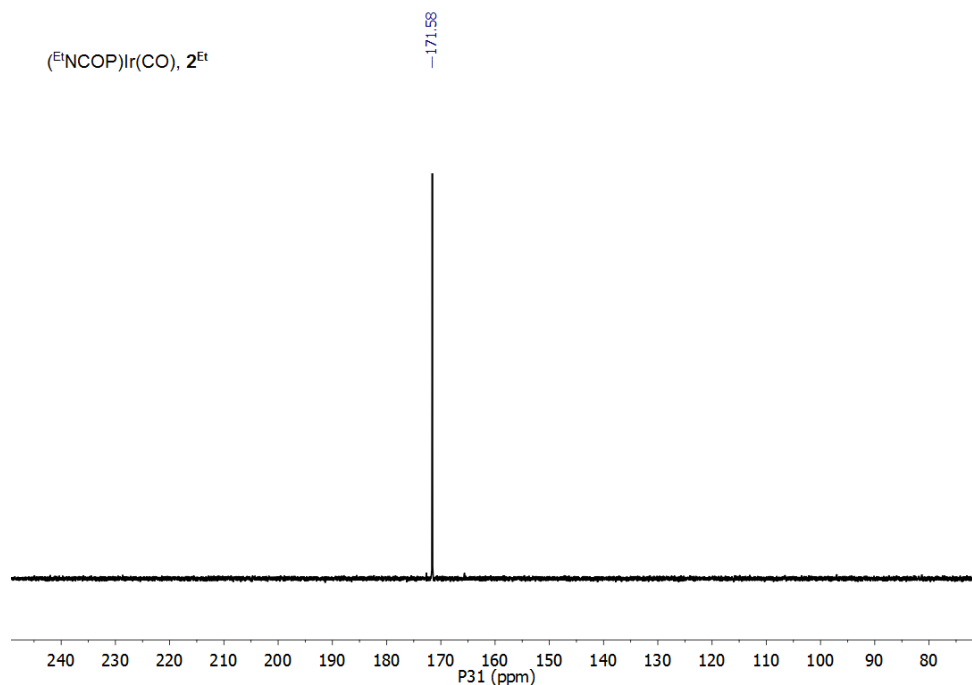
Figure 2.26 ^{31}P{^{1}H} NMR spectrum of (^{Et}NCOP^{iPr})Ir(CO) (**2^{Et}**) in C$_6$D$_6$.

Synthesis of (^{15c5}NCOP^{iPr})Ir(H)(CO)(I) (4^{15c5}). A 20-mL scintillation vial was charged with

21.3 mg (30.5 μmol) **1^{15c5}** and dissolved in acetone (0.5 mL). A solution of 14.2 mg (94.7

μmol) NaI in acetone (0.5 mL) was added to the initial vial resulting in a pale yellow

solution. The reaction mixture was allowed to stir for 48 h, during which time NaCl

precipitated. The mixture was stripped of solvent under vacuum, extracted with benzene (3

mL), and filtered. Benzene was removed from the filtrate under vacuum, affording an off-

white solid (22.2 mg, 92% yield). ^{1}H NMR (600 MHz, C$_6$D$_6$): δ 6.91 – 6.85 (m, 2H, Ar*H*),

6.78 – 6.74 (m, 1H, Ar*H*), 4.90 (d, *J* = 13.3 Hz, 1H, ArC*H*HN), 4.67 (dt, *J* = 11.9, 5.1 Hz,

1H, crown-C*H*), 4.08 (dd, *J* = 10.3, 3.9 Hz, 1H, ArCH*H*N), 4.06 (s, 1H, crown-C*H*), 3.89

(ddd, *J* = 14.2, 7.0, 4.7 Hz, 1H, crown-C*H*), 3.79 (dt, *J* = 10.5, 5.4 Hz, 1H, crown-C*H*), 3.59

– 3.50 (m, 2H, crown-C*H*$_2$), 3.41 – 3.22 (m, 15H, crown-C*H*$_2$), 3.33 (1H, C*H*(CH$_3$)$_2$), 2.04

(ddd, *J* = 19.6, 13.4, 6.6 Hz, 1H, C*H*(CH$_3$)$_2$), 1.20 (dd, *J* = 19.8, 7.3 Hz, 3H, CH(C*H*$_3$)$_2$), 1.02

(dd, *J* = 14.4, 7.1 Hz, 3H, CH(C*H*$_3$)$_2$), 0.80 (dd, *J* = 15.9, 6.8 Hz, 3H, CH(C*H*$_3$)$_2$), 0.74 (dd, *J*

= 19.5, 6.9 Hz, 3H, CH(CH_3)$_2$), −16.05 (d, J = 19.1 Hz, 1H, Ir–H). Note: The resonance for the CH(CH$_3$)$_2$ proton at δ 3.33 overlaps with the multiplet of the crown-ether protons (δ 3.41-3.22). ^{13}C{^{1}H} NMR (151 MHz, C$_6$D$_6$): δ 180.38 (d, J = 3.8 Hz, Ir–CO), 162.05 (d, J = 2.9 Hz, C_{Ar}), 148.02 (d, J = 2.2 Hz, C_{Ar}), 145.98 (dd, J = 5.3, 3.2 Hz, C_{Ar}), 125.98 (s, C_{Ar}), 117.55 (s, C_{Ar}), 108.96 (d, J = 12.4 Hz, C_{Ar}), 72.96 (d, J = 1.9 Hz, ArCH$_2$N), 71.30 (s, crown-CH$_2$), 70.96 (d, J = 16.1 Hz, crown-CH$_2$), 70.70 (s, crown-CH$_2$), 70.46 (d, J = 10.5 Hz, crown-CH$_2$), 70.38 (s, crown-CH$_2$), 68.59 (s, crown-CH$_2$), 63.75 (s, crown-CH$_2$), 61.78 (s, crown-CH$_2$), 36.58 (d, J = 35.6 Hz, CH(CH$_3$)$_2$), 28.08 (dd, J = 41.2, 2.5 Hz, CH(CH$_3$)$_2$), 18.87 (d, J = 6.4 Hz, CH(CH$_3$)$_2$), 17.79 (d, J = 1.8 Hz, CH(CH$_3$)$_2$), 17.69 (d, J = 5.1 Hz, CH(CH$_3$)$_2$), 15.55 (d, J = 5.2 Hz, CH(CH$_3$)$_2$). ^{31}P{^{1}H} NMR (162 MHz, C$_6$D$_6$): δ 153.87. IR (solid, cm^{-1}): ν(CO) 2014 cm^{-1}, ν(Ir−H) 2182 cm^{-1}. Anal. Calcd for C$_{24}$H$_{40}$IIrNO$_6$P: C, 36.55; H, 5.11; N, 1.78. Found: C, 36.48; H, 4.91; N, 1.66. HRMS (ESI$^+$) *m/z* [**4^{15c5}**+Na]$^+$ Calcd for C$_{24}$H$_{40}$IIrNNaO$_6$P 812.1165; Found 812.1165.

$(^{15c5}NCOP^{iPr})Ir(H)(CO)(I)$, 4^{15c5}
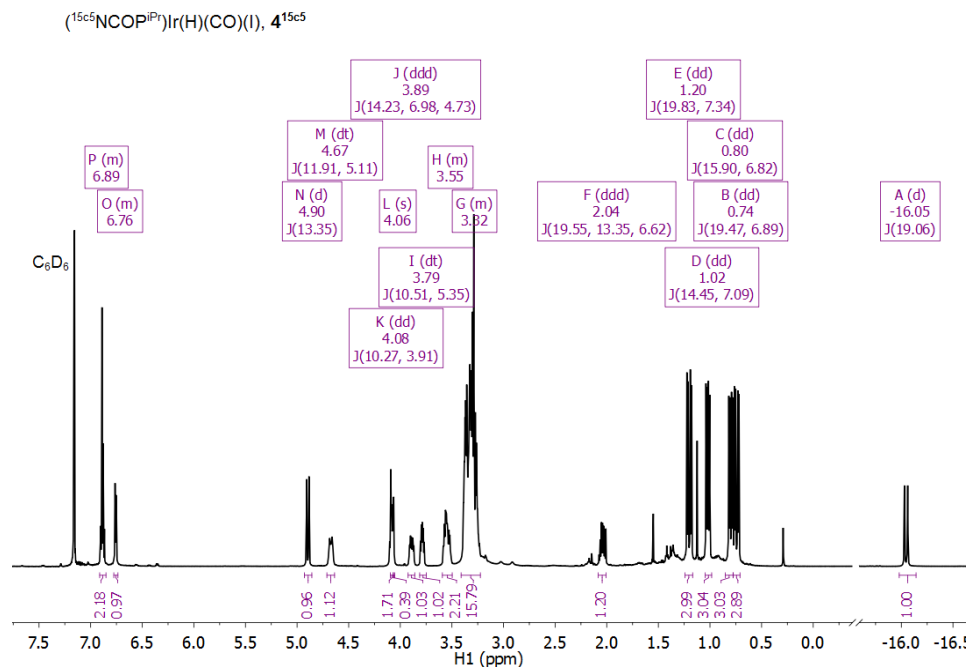
Figure 2.27 ^{1}H NMR spectrum of $(^{15c5}NCOP^{iPr})Ir(H)(CO)(I)$ (4^{15c5}) in C_6D_6. Trace amounts of silicone grease (δ 0.29), H grease (δ 1.36), THF (δ 1.42) and acetone (δ 1.55).
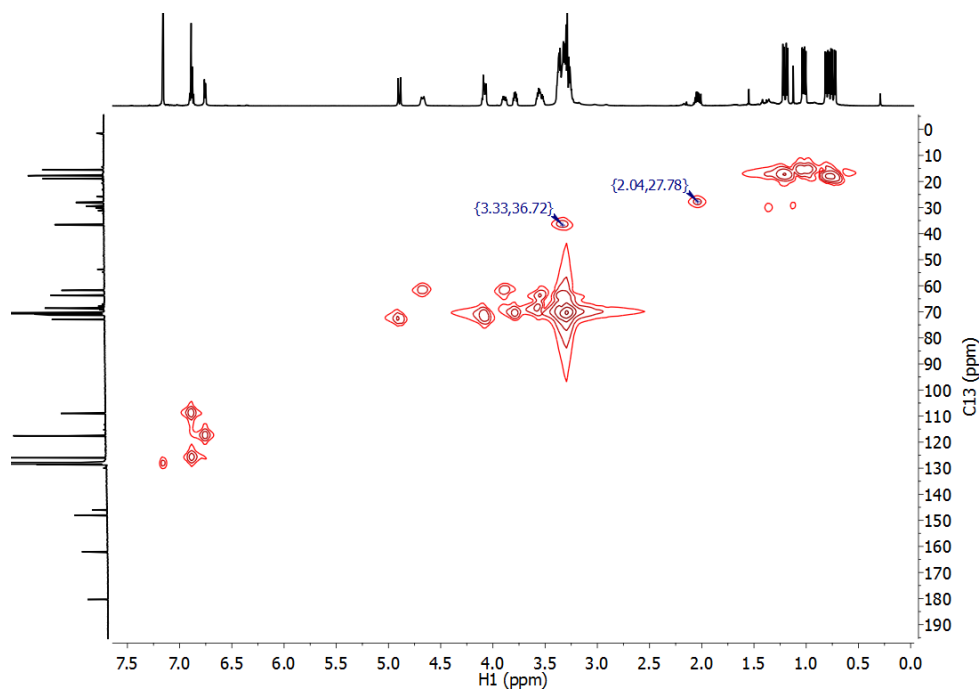
Figure 2.28 ^{1}H–^{13}C HMQC NMR spectrum of $(^{15c5}NCOP^{iPr})Ir(H)(CO)(I)$ (4^{15c5}) in C_6D_6, showing the correlation between a proton at δ 3.33 ($CH(CH_3)_2$) and a carbon resonance at δ 36.7 ($CH(CH_3)_2$).

63
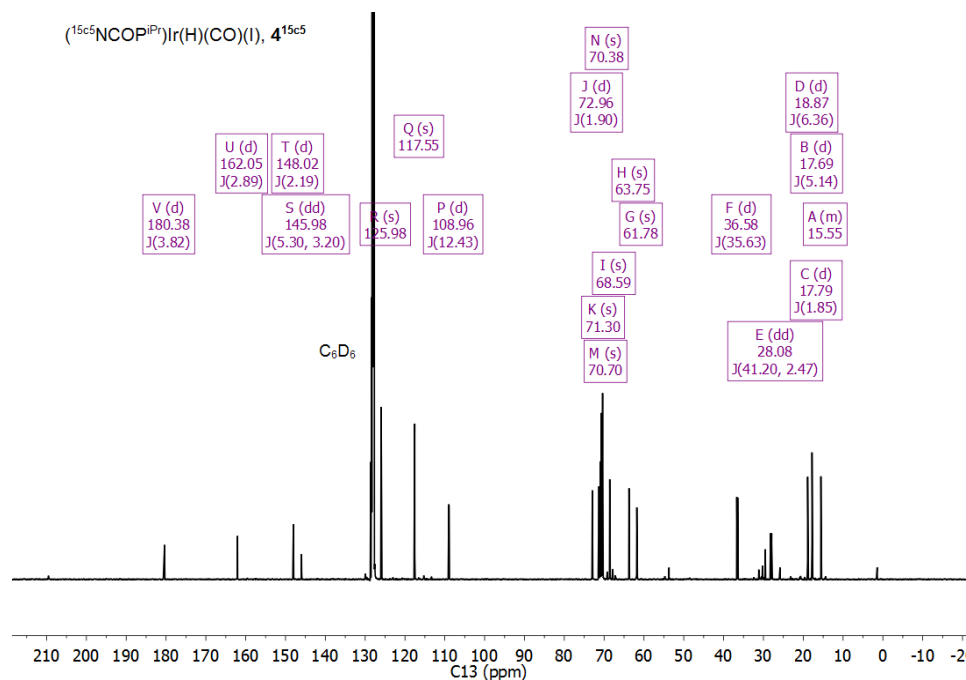
Figure 2.29 $^{13}C\{^1H\}$ NMR spectrum of ($^{15c5}NCOP^{iPr}$)Ir(H)(CO)(I) (4^{15c5}) in C_6D_6. Trace amounts of silicone grease (δ 1.43), H grease (δ 30.23), THF (δ 29.38, 67.83), and acetone (δ 29.54).
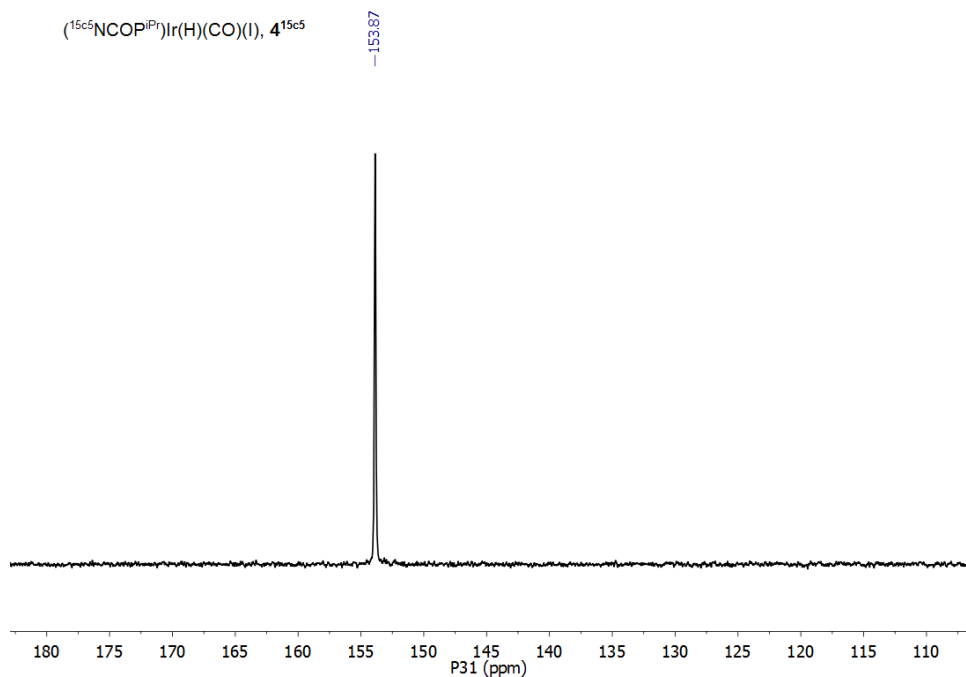
Figure 2.30 $^{31}P\{^1H\}$ NMR spectrum of ($^{15c5}NCOP^{iPr}$)Ir(H)(CO)(I) (4^{15c5}) in C_6D_6.

Synthesis of iminium complex [5^{15c5}]$^{2+}$. Complex **2^{15c5}** (3.7 mg, 5.6 μmol) was dissolved in CD$_3$CN (500 μL). To the resulting yellow solution was added a 2.5 μL aliquot of a 2.2 M solution of H$_2$O in CD$_3$CN (5.5 μmol). To this mixture was added Ca(OTf)$_2$ (3.3 mg, 9.8 μmol), resulting in discoloration of the solution to a pale yellow color. The reaction progress was monitored by ^{1}H and ^{31}P{^{1}H} NMR spectroscopy, yielding [5^{15c5}]$^{2+}$ in 70% yield (by ^{1}H NMR spectroscopy) as an orange solution. ^{1}H NMR (400 MHz, CD$_3$CN): δ 7.87 (dd, J = 10.9, 7.1 Hz, 1H, N=CH−CH$_2$), 7.05 − 7.00 (m, 2H, ArH), 6.97 (dd, J = 6.4, 2.9 Hz, 1H, ArH), 4.86 (d, J = 14.7 Hz, 1H, ArCHHN), 4.26 (d, J = 14.8 Hz, 1H, ArCHHN), 4.19 − 3.51 (m, 15H, crown-CH_2), 3.47 − 3.22 (m, 3H, crown-CH_2), 3.15 (dd, J = 14.6, 2.2 Hz, 1H, crown-CH_2), 2.83 − 2.68 (m, 1H, CH(CH$_3$)$_2$), 2.67 − 2.26 (m, 1H, CH(CH$_3$)$_2$), 1.37 (dd, J = 16.4, 7.0 Hz, 3H, CH(CH_3)$_2$), 1.29 (dd, J = 17.1, 7.3 Hz, 3H, CH(CH_3)$_2$), 1.10 (dd, J = 19.2, 7.0 Hz, 3H, CH(CH_3)$_2$), 0.93 (dd, J = 16.3, 6.9 Hz, 3H, CH(CH_3)$_2$), −19.36 (d, J = 16.6 Hz, 1H, Ir–H). ^{13}C NMR (151 MHz, CD$_3$CN): δ 189.78 (d, J = 6.2 Hz, Ir–CO), 172.70 (d, J = 3.5 Hz, C_{Ar}), 170.33 (m, N=CH−CH$_2$), 168.82 (s, C_{Ar}), 130.09 (s, C_{Ar}), 127.77 (s, C_{Ar}), 125.12 (s, C_{Ar}), 122.35 (s, *trans* Ir–NCCD$_3$), 120.23 (s, *cis* Ir–NCCD$_3$), 112.83 (d, J = 12.1 Hz, C_{Ar}), 71.16 (s, crown-CH$_2$), 70.94 − 70.19 (m, crown-CH$_2$), 69.90 (s, crown-CH$_2$), 61.49 (s, crown-CH$_2$), 55.05 (s, ArCH$_2$N), 54.76 (s, N=CH−CH$_2$), 32.69 (dd, J = 32.7, 4.1 Hz, CH(CH$_3$)$_2$), 31.01 (d, J = 35.7 Hz, CH(CH$_3$)$_2$), 18.08 (d, J = 5.0 Hz, CH(CH$_3$)$_2$), 17.84 (d, J = 1.2 Hz, CH(CH$_3$)$_2$), 17.53 (s, CH(CH$_3$)$_2$), 17.31, (s, CH(CH$_3$)$_2$). ^{31}P{^{1}H} NMR (162 MHz, CD$_3$CN): δ 159.08. IR (solid, cm^{-1}): ν_{CO} 2041 cm^{-1}, ν(N=CH−CH$_2$) 1617cm^{-1}.
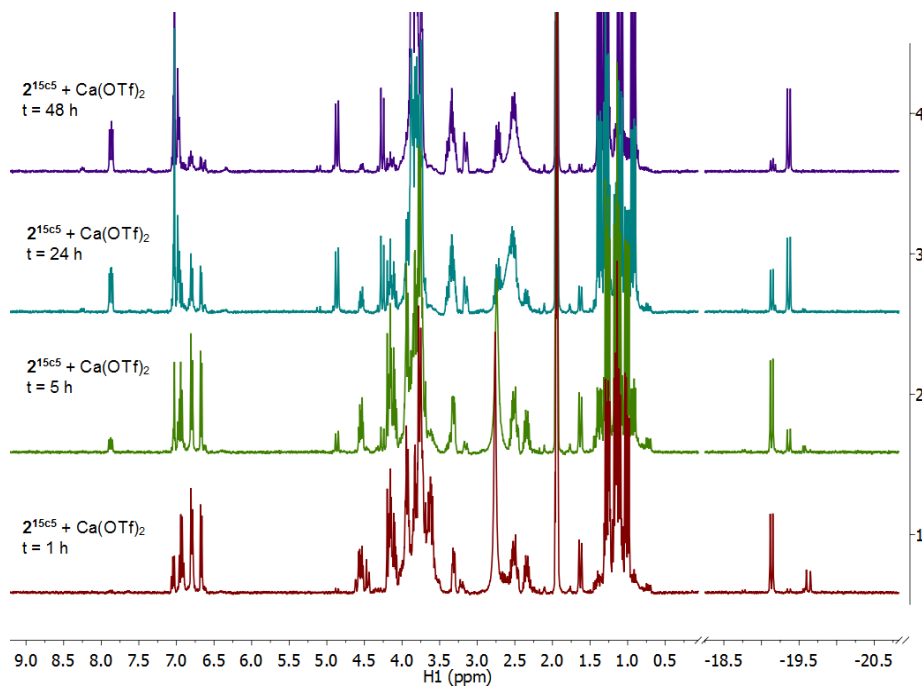
Figure 2.31 ^{1}H NMR spectra showing formation of $[\mathbf{5^{15c5}}]^{2+}$ by addition of Ca(OTf)$_2$ to $\mathbf{2^{15c5}}$ in CD$_3$CN in the presence of one equivalent of H$_2$O.
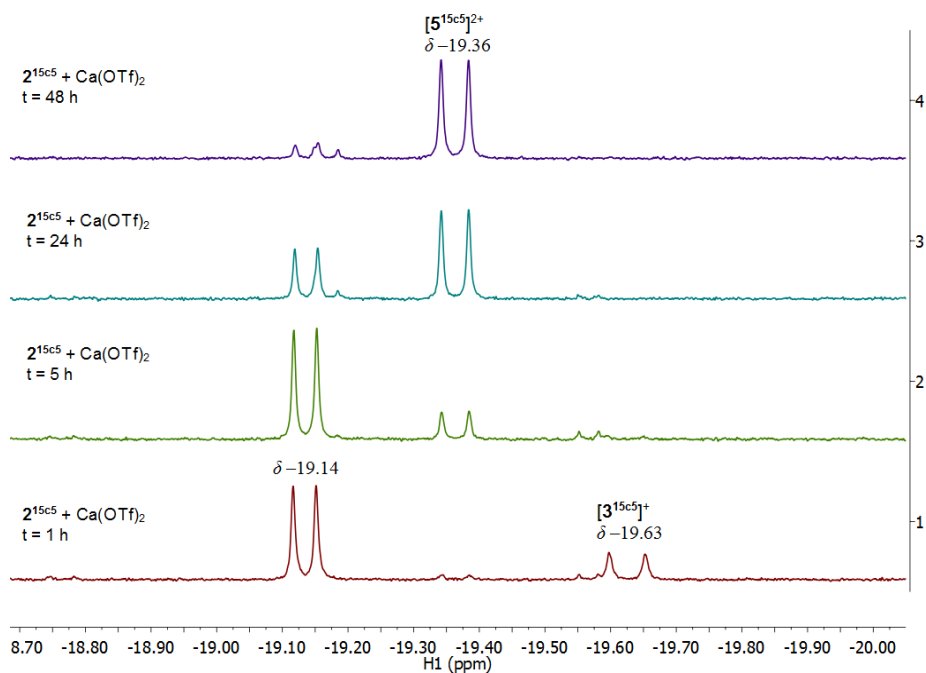
Figure 2.32 ^{1}H NMR spectra (hydride region) showing formation of $[\mathbf{5^{15c5}}]^{2+}$ by addition of Ca(OTf)$_2$ to $\mathbf{2^{15c5}}$ in CD$_3$CN in the presence of one equivalent of H$_2$O.
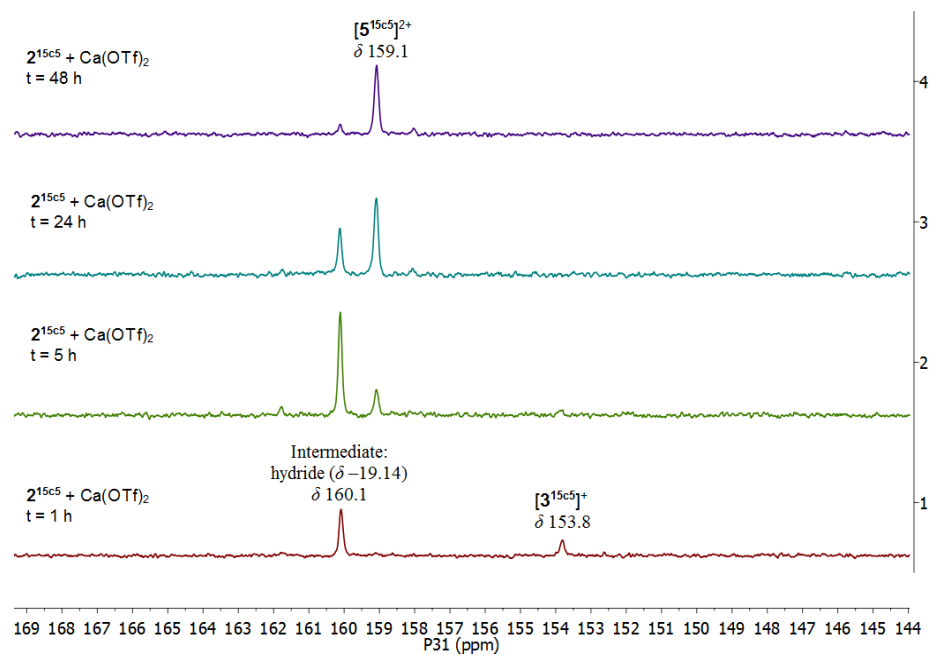
Figure 2.33 $^{31}P\{^1H\}$ NMR spectra showing formation of $[\mathbf{5^{15c5}}]^{2+}$ by addition of $Ca(OTf)_2$ to $\mathbf{2^{15c5}}$ in CD_3CN in the presence of one equivalent of H_2O.
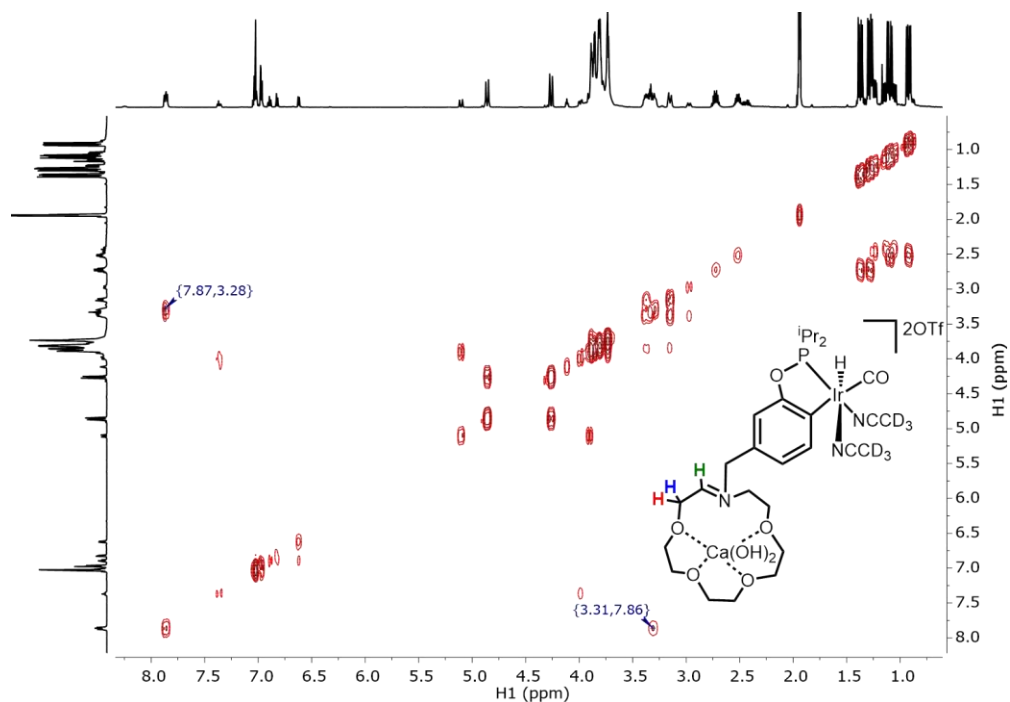
Figure 2.34 ^1H-^1H COSY NMR spectrum of $[\mathbf{5^{15c5}}]^{2+}$.
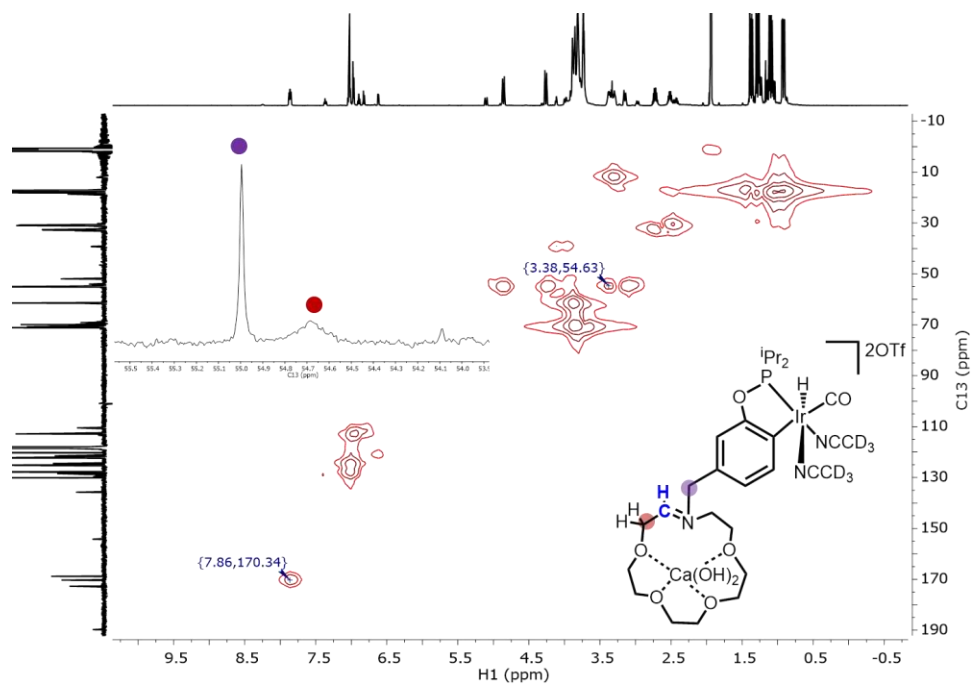
Figure 2.35 ^{1}H-^{13}C HMQC NMR spectrum of [**5^{15c5}**]$^{2+}$.
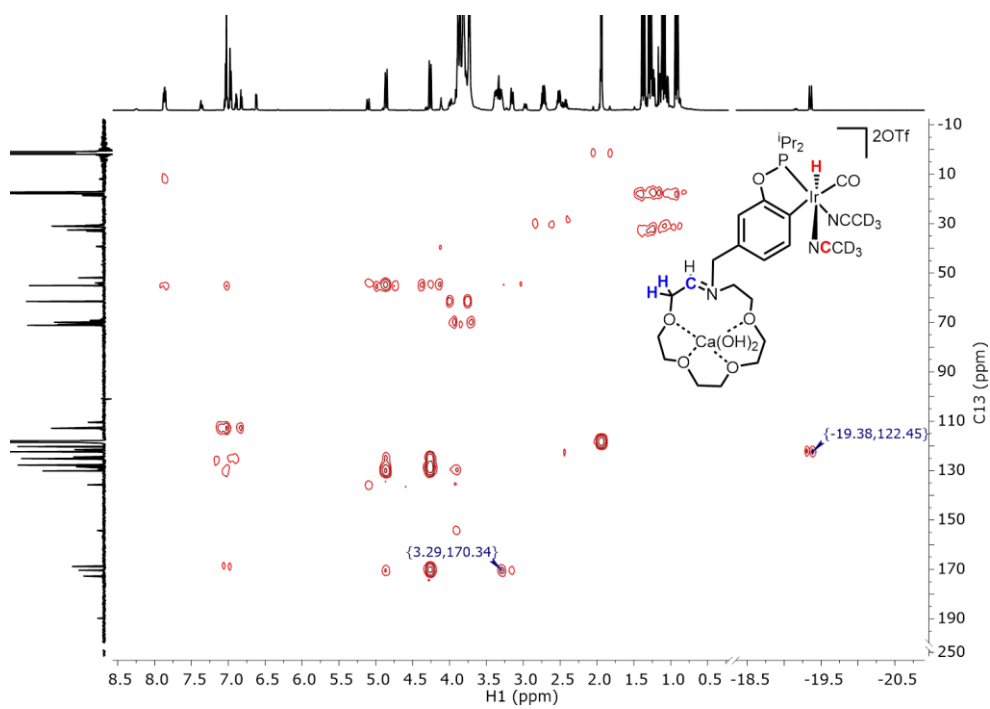
Figure 2.36 ^{1}H-^{13}C HMBC NMR spectrum of [**5^{15c5}**]$^{2+}$.

68
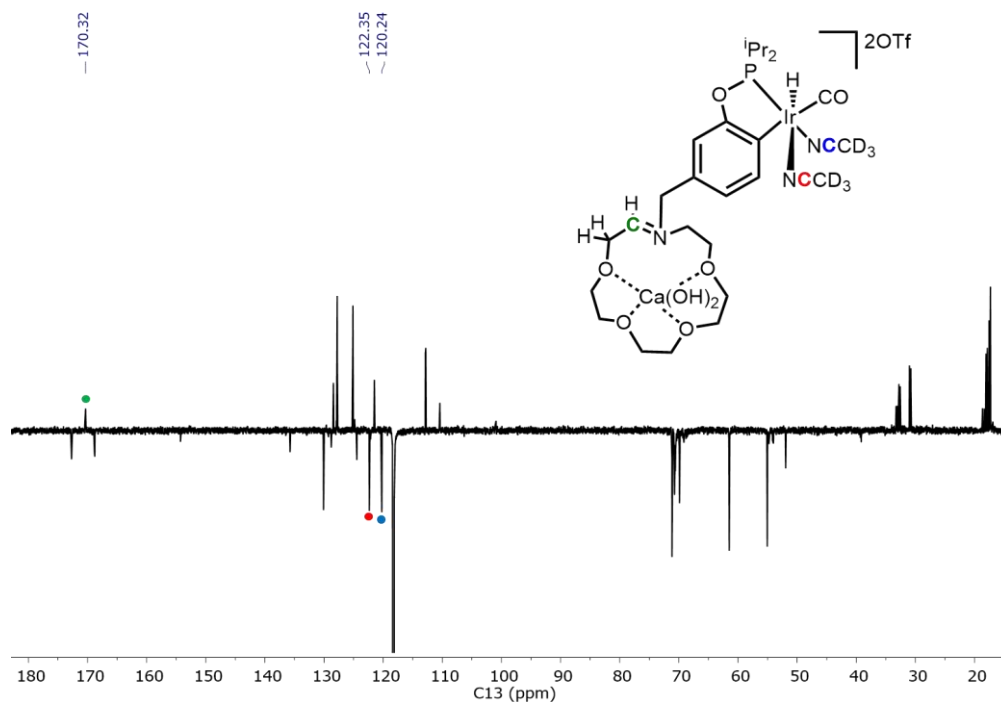
Figure 2.37 ^{13}C APT NMR spectrum of [5^{15c5}]$^{2+}$.
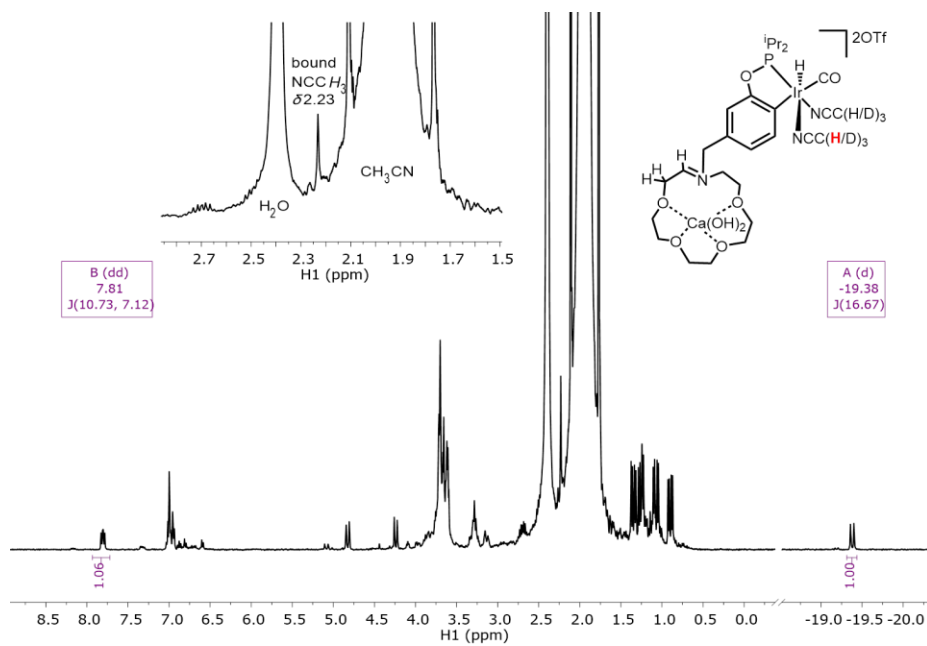
Figure 2.38 ^{1}H NMR spectrum of [5^{15c5}]$^{2+}$ formed upon addition of Ca(OTf)$_2$ to 2^{15c5} in a 1:1 mixture of CD$_3$CN and CH$_3$CN in the presence of H$_2$O.

Spectrophotometric titration of 1^{15c5} in CH₃CN. Complex 1^{15c5} (4.2 mg, 0.0060 mmol) was dissolved in 6.25 mL CH₃CN. A 2 mL aliquot of this solution was placed in a cuvette and an initial spectrum was obtained. Additional spectra were obtained after each addition of a 2 μL aliquot of a 0.25 M solution of DBU (conjugate acid pK_a = 24.34) in CH₃CN. An analogous experiment using up to 100 equiv NEt₃ as the base led to no observable spectral changes.

General procedure for reactivity of 1^{15c5} with metal cations. Complex 1^{15c5} (15.0 mg, 21.5 μmol) was dissolved in CD₃CN (1.5 mL). To the resulting golden yellow solution was added a 4 μL aliquot of a 5.6 M solution of H₂O (22.4 μmol) in CD₃CN. The mixture was equally split into three Teflon-capped NMR tubes. ¹H and ³¹P{¹H} NMR spectra were collected prior to salt addition. One equivalent of the corresponding salt (NaBAr$^F_4$, Ca(OTf)₂, or La(OTf)₃) was then added. Ca(OTf)₂ led to formation of [3^{15c5}][OTf] in 33% yield over the course of 24 h. La(OTf)₃ led to formation of [3^{15c5}][OTf] in 69% yield within 2.5 h. No further changes were observed after this time. NaBAr$^F_4$ led to 33% yield within 24 h. Subsequent additions of NaBAr$^F_4$ (up to three equivalents added) led to conversions of up to 76% yield of [3^{15c5}][OTf].

General procedure for reactivity of 1^{Et} with metal cations. Complex 1^{Et} (10.4 mg, 18.9 μmol) was dissolved in CD₃CN (1.2 mL). The resulting yellow solution was equally split into two Teflon-capped NMR tubes. One equivalent of the corresponding salt (LaI₃ or NaBAr$^F_4$) was then added. The reactions were monitored by ¹H and ³¹P{¹H} NMR spectroscopy. Within minutes of addition of LaI₃ complete conversion to 4^{Et} was observed. The reaction with NaBAr$^F_4$ led to a ~1:1 mixture of 1^{Et} and [3^{Et}][BAr$^F_4$] over the course of 24 h.

Titration of 4^{15c5} with LaI$_3$. In a N$_2$-filled glovebox a solution of 4^{15c5} (5.6 mg, 7.1 μmol) in acetone-d_6 was added to a Teflon-capped NMR tube. LaI$_3$ was added in increments of ~1 equivalent (~4.0 mg, 7.7 μmol) up to six equivalents. After each addition of LaI$_3$ ^{1}H NMR spectra were collected to monitor the shifts in the methylene linker protons and hydride resonances. After the initial shifts in the resonances immediately observed after each addition no further changes were observed even after stirring for extended periods of time.
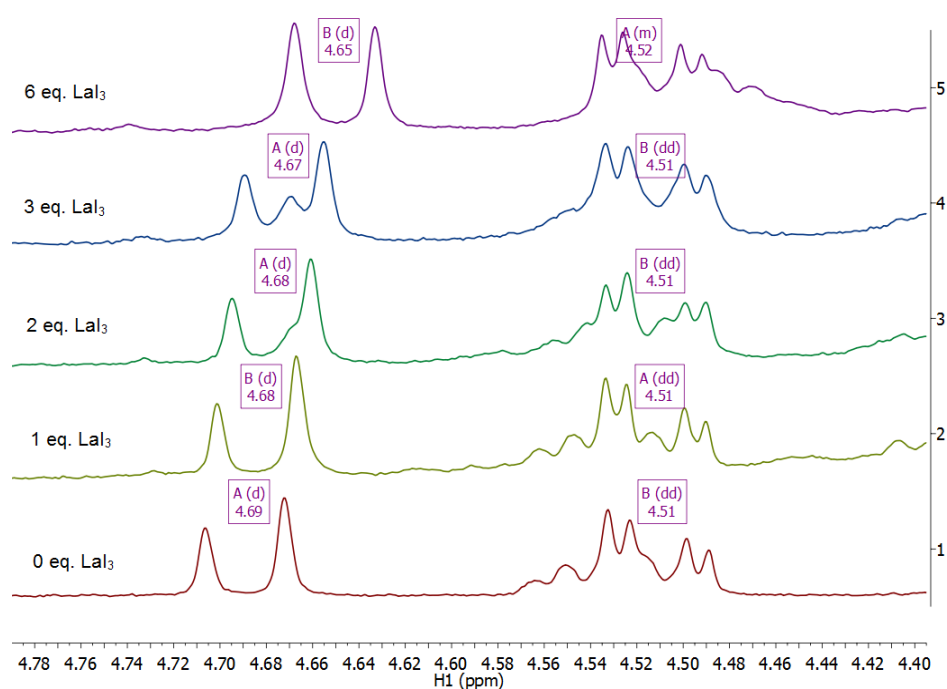
Figure 2.39 ^{1}H NMR spectra (diastereotopic benzylic linker protons) monitoring addition of LaI$_3$ to 4^{15c5} in acetone-d_6.

Monitoring protonation of 2^{15c5} by UV-vis. A cuvette equipped with a stir bar was charged with approximately 6.0 mg of LaI$_3$ (11.0 μmol). Separately prepared, a 2 μL aliquot of a 5.5 M solution of H$_2$O (11.0 μmol) in CH$_3$CN was added to 3 mL of a 0.139 mM solution of 2^{15c5} (0.417 μmol) in CH$_3$CN. The resulting mixture was added to the cuvette while stirring and UV-vis spectra were collected every 0.2 seconds.

General procedure for NMR scale addition of Lewis acids to 2^{15c5}. Complex **2^{15c5}** (5.0

mg, 7.6 μmol) was dissolved in CD$_3$CN. To the solution was added a 7 μL aliquot of a 1.1 M

solution of H$_2$O (7.6 μmol) in CD$_3$CN. The mixture was transferred to a Teflon-capped NMR

tube. ^{1}H and ^{31}P{^{1}H} NMR spectra were collected prior to salt addition. One equivalent of

the corresponding salt (LiI, CaI$_2$, LaI$_3$, LiOTf, Ca(OTf)$_2$, Zn(OTf)$_2$, La(OTf)$_3$, or Sc(OTf)$_3$)

was then added as a solid. With the exception of the Li$^+$ and Ca^{2+} salts, all solutions

immediately evolved from a bright yellow solution to colorless upon mixing, indicating

complete conversion to either **4^{15c5}** or [**3^{15c5}**][OTf]. ^{1}H and ^{31}P{^{1}H} NMR spectra were

collected after salt addition. In the cases of the Li$^+$ and Ca^{2+} salts, further spectra were

collected to monitor the cation-crown complexation or the slow protonation of the Ir(I)

complex **2^{15c5}** to a mixture of products. In forming [**5^{15c5}**]$^{2+}$ addition of more than 1 equiv of

Ca(OTf)$_2$ led to higher yields of product. Performing the reaction in the presence of 2 equiv

Ca(OTf)$_2$ pre-treated with D$_2$O (stirred in D$_2$O followed by drying under reduced pressure)

and 1 equiv D$_2$O led to deuterium incorporation to intermediate [**3^{15c5}**]$^+$ and eventual

formation of a final deuteride-containing [**5^{15c5}**]$^{2+}$ species.
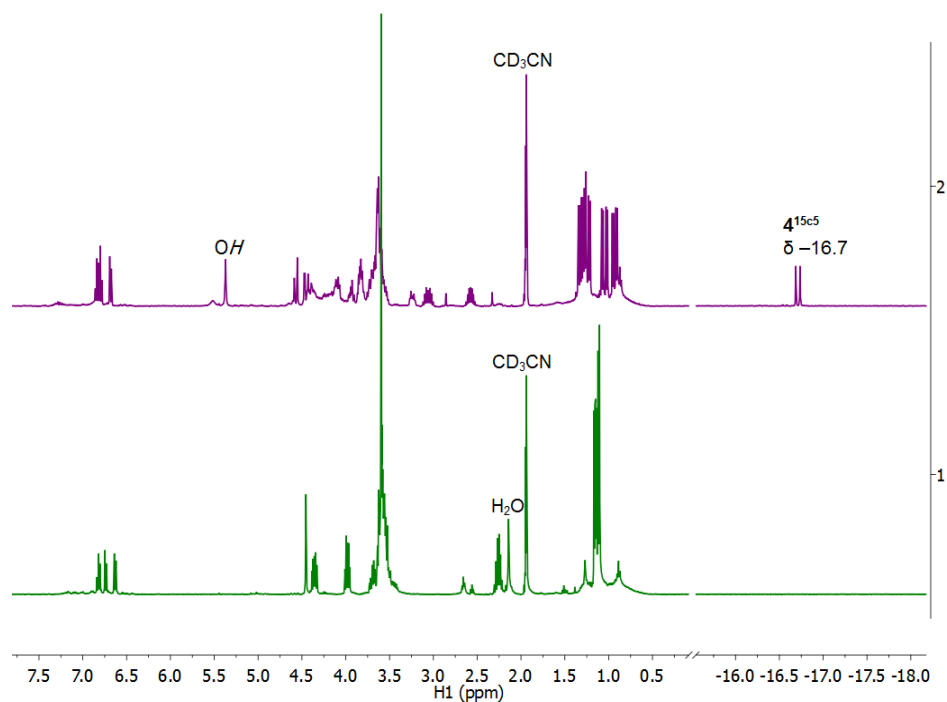
Figure 2.40 ^{1}H NMR spectra showing formation of **4^{15c5}** by addition of LaI$_3$ to **2^{15c5}** in CD$_3$CN in the presence of one equivalent of H$_2$O.
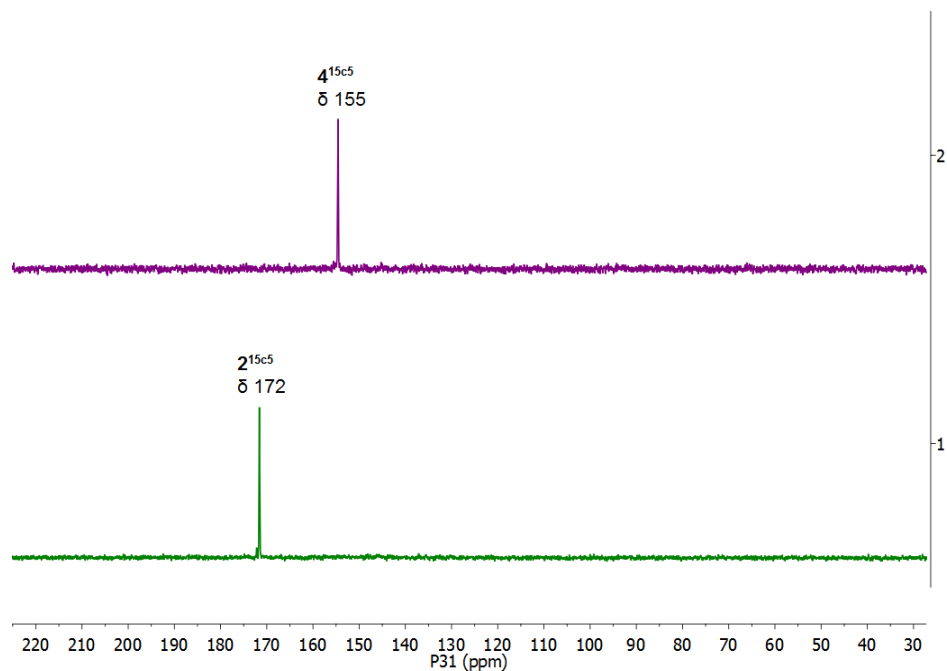
Figure 2.41 ^{31}P{^{1}H} NMR spectra showing formation of **4^{15c5}** by addition of LaI$_3$ to **2^{15c5}** in CD$_3$CN in the presence of one equivalent of H$_2$O.
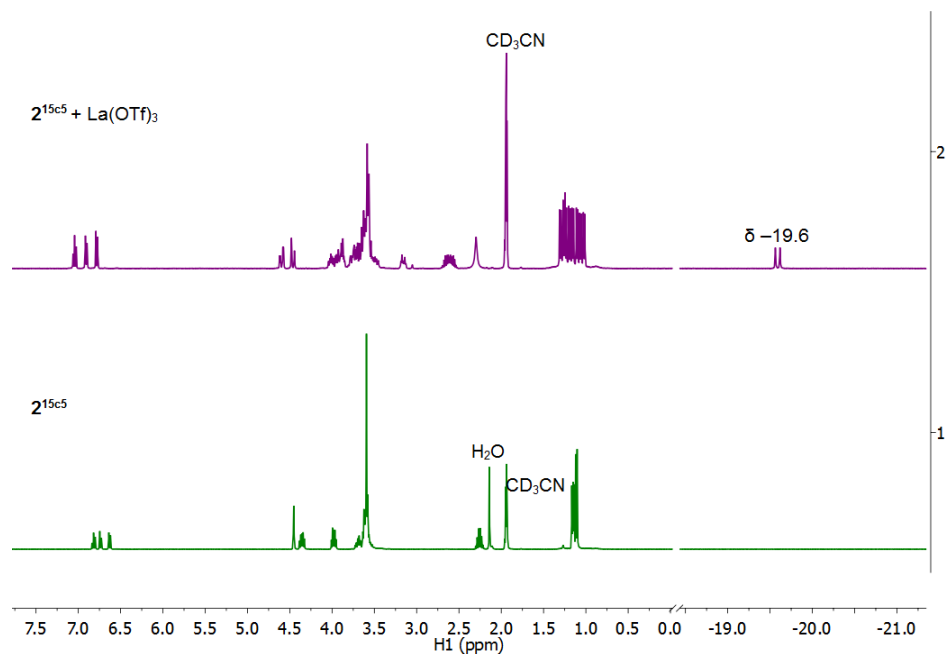
Figure 2.42 ^{1}H NMR spectra showing formation of [$\mathbf{3^{15c5}}$][OTf] by addition of La(OTf)$_3$ to $\mathbf{2^{15c5}}$ in CD$_3$CN in the presence of one equivalent of H$_2$O.
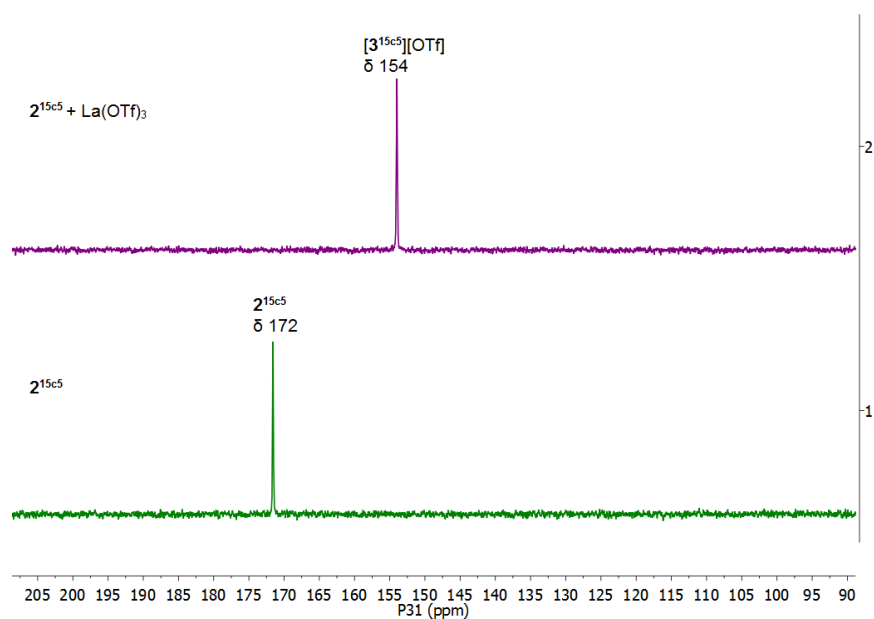
Figure 2.43 ^{31}P{^{1}H} NMR spectra showing formation of [$\mathbf{3^{15c5}}$][OTf] by addition of La(OTf)$_3$ to $\mathbf{2^{15c5}}$ in CD$_3$CN in the presence of one equivalent of H$_2$O.
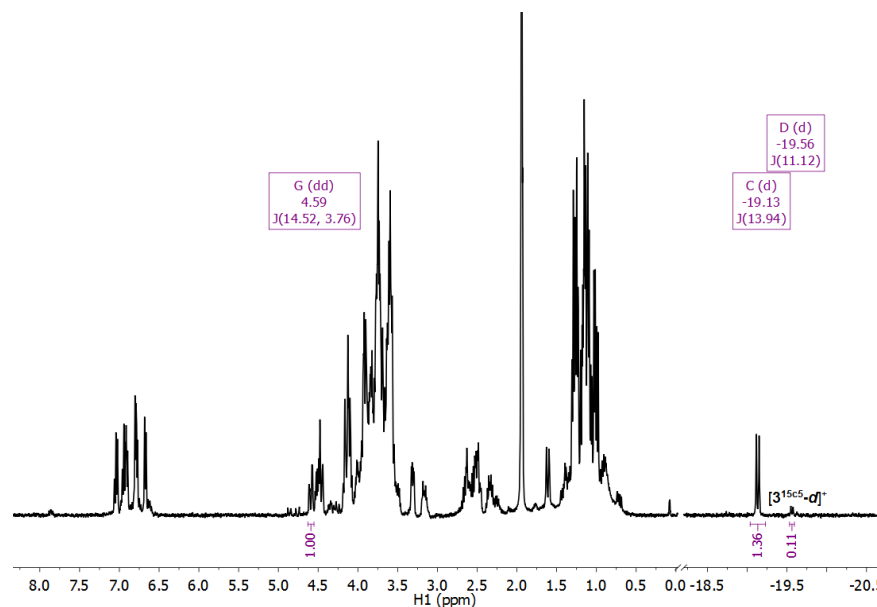
Figure 2.44 ^{1}H NMR spectrum obtained 30 minutes after mixing **2^{15c5}** with Ca(OTf)$_2$ (previously stirred in D$_2$O and pumped to dryness) in CD$_3$CN in the presence of 1 equiv D$_2$O. Deuterium incorporation into [**3^{15c5}**][OTf] was determined by the integration of the residual hydride (δ −19.56) relative to a diastereotopic benzylic proton (δ 4.59).

General procedure for NMR scale addition of Lewis acids to 2^{Et}. Complex **2^{Et}** (14.7 mg, 28.3 μmol) was dissolved in CD$_3$CN. To the bright yellow solution was added a 5 μL aliquot of a 5.5 M solution of H$_2$O (27.5 μmol) in CD$_3$CN. The mixture was equally split into three Teflon-capped NMR tubes. ^{1}H and ^{31}P\{^{1}H\} NMR spectra were collected prior to salt addition. One equivalent of the corresponding salt (LiOTf, Ca(OTf)$_2$, or La(OTf)$_3$) was then added. The solution to which La(OTf)$_3$ was added underwent decolorization within seconds. A slight decolorization was observed for the Ca(OTf)$_2$ reaction. The reactions of **2^{Et}** with Ca(OTf)$_2$ and La(OTf)$_3$ proceeded similarly in the presence of 12-crown-4. Addition of Ca(OTf)$_2$ as an aqueous solution (100 μL) to a solution of **2^{Et}** in CD$_3$CN precluded formation of [**3^{Et}**]$^+$. No changes were observed in the solution to which LiOTf was added. The presence of small amounts of strong acids (e.g. HI or HOTf) is sometimes responsible for Lewis acid-promoted reactivity, but an experiment containing excess NEt$_3$ still gave protonation at Ir.
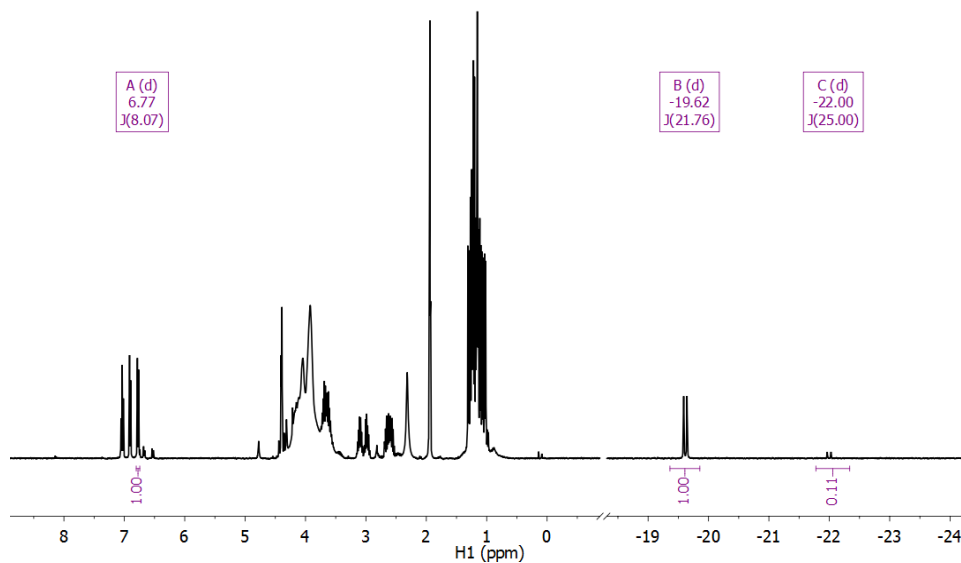
Figure 2.45 ^{1}H NMR spectrum showing La(OTf)$_3$-triggered protonation of **2^{Et}** to [**3^{Et}**][OTf] in CD$_3$CN in the presence of H$_2$O (δ 2.32) and 12-crown-4 (δ 3.92).
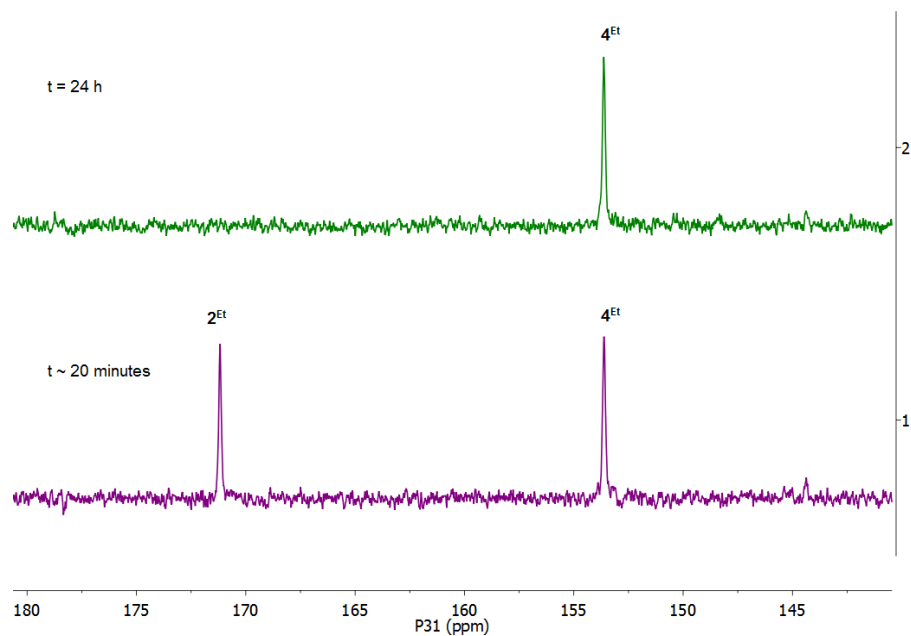
Figure 2.46 ^{31}P{^{1}H} NMR spectra showing LaI$_3$-triggered protonation of **2^{Et}** to **4^{Et}** in CD$_3$CN in the presence of NEt$_3$. Within minutes, a ~1:1 mixture of **2^{Et}** and **4^{Et}** was observed. Complete protonation of **2^{Et}** was achieved over the course of several hours.

76
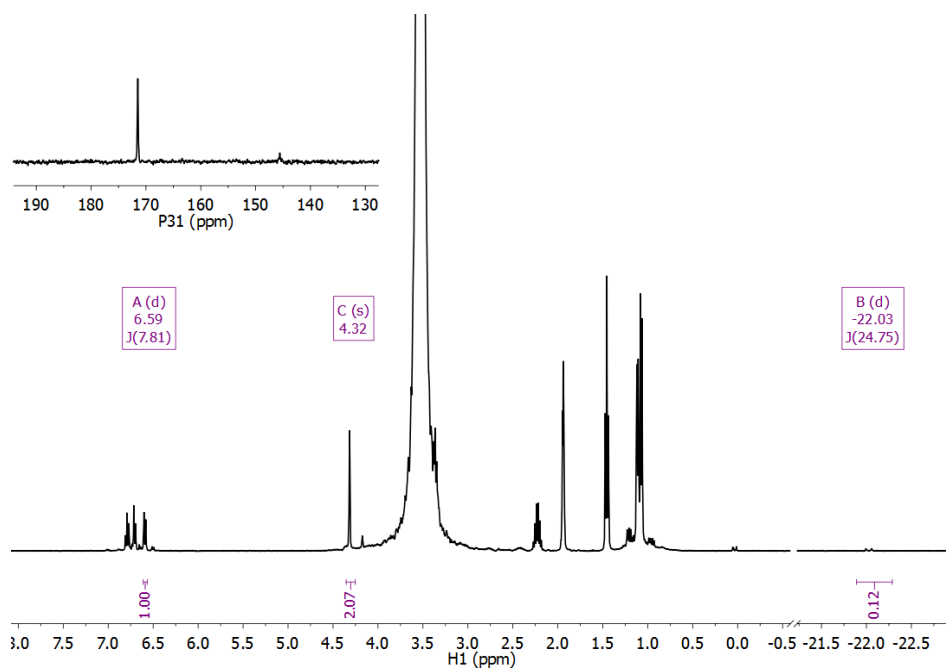
Figure 2.47 ^{1}H NMR spectrum showing the limited protonation of $\mathbf{1^{Et}}$ in CD$_3$CN by addition of Ca(OTf)$_2$ as an aqueous solution (500 μL). The inset shows the ^{31}P{^{1}H} NMR spectrum.

REFERENCES

(1)   Devillard, M.; Bouhadir, G.; Bourissou, D. Cooperation between Transition Metals and Lewis Acids: A Way To Activate H$_2$ and H-E Bonds. *Angew. Chem. Int. Ed.* **2015**, *54* (3), 730–732.

(2)   West, N. M.; Miller, A. J. M.; Labinger, J. A.; Bercaw, J. E. Homogeneous Syngas Conversion. *Coord. Chem. Rev.* **2011**, *255* (7–8), 881–898.

(3)   Shriver, D. F. Transition Metal Basicity. *Acc. Chem. Res.* **1970**, *3* (7), 231–238.

(4)   Muetterties, E. L.; Stein, J. Mechanistic Features of Catalytic Carbon Monoxide Hydrogenation Reactions. *Chem. Rev.* **1979**, *79* (6), 479–490.

(5)   Hazari, A.; Labinger, J. A.; Bercaw, J. E. A Versatile Ligand Platform That Supports Lewis Acid Promoted Migratory Insertion. *Angew. Chem. Int. Ed.* **2012**, *51* (33), 8268–8271.

(6)   Bielinski, E. A.; Lagaditis, P. O.; Zhang, Y.; Mercado, B. Q.; Würtele, C.; Bernskoetter, W. H.; Hazari, N.; Schneider, S. Lewis Acid-Assisted Formic Acid Dehydrogenation Using a Pincer-Supported Iron Catalyst. *J. Am. Chem. Soc.* **2014**, *136* (29), 10234–10237.

(7)   Roberts, C. C.; Matías, D. M.; Goldfogel, M. J.; Meek, S. J. Lewis Acid Activation of Carbodicarbene Catalysts for Rh-Catalyzed Hydroarylation of Dienes. *J. Am. Chem. Soc.* **2015**, *137* (20), 6488–6491.

(8)   Wade, C. R.; Gabbai, F. P. Cyanide Anion Binding by a Triarylborane at the Outer Rim of a Cyclometalated ruthenium(II) Cationic Complex. *Inorg. Chem.* **2010**, *49* (2), 714–720.

(9)   Wade, C. R.; Ke, I. S.; Gabbaï, F. P. Sensing of Aqueous Fluoride Anions by Cationic Stibine-Palladium Complexes. *Angew. Chem. Int. Ed.* **2012**, *51* (2), 478–481.

(10)   Fukuzumi, S.; Ohkubo, K. Metal Ion-Coupled and Decoupled Electron Transfer. *Coord. Chem. Rev.* **2010**, *254* (3–4), 372–385.

(11)   Fukuzumi, S.; Ohkubo, K.; Morimoto, Y. Mechanisms of Metal Ion-Coupled Electron Transfer. *Phys. Chem. Chem. Phys.* **2012**, *14* (24), 8472.

(12)   Tsui, E. Y.; Tran, R.; Yano, J.; Agapie, T. Redox-Inactive Metals Modulate the Reduction Potential in Heterometallic Manganese–oxido Clusters. *Nat. Chem.* **2013**, *5* (4), 293–299.

(13)   Tsui, E. Y.; Agapie, T. Reduction Potentials of Heterometallic Manganese-Oxido Cubane Complexes Modulated by Redox-Inactive Metals. *Proc. Natl. Acad. Sci.* **2013**, *110* (25), 10084–10088.

(14)   Park, Y. J.; Ziller, J. W.; Borovik, A. S. The Effects of Redox-Inactive Metal Ions on the Activation of Dioxygen: Isolation and Characterization of a Heterobimetallic Complex Containing a Mn^{III}–(μ-OH)–Ca^{II} Core. *J. Am. Chem. Soc.* **2011**, *133* (24),

9258–9261.

(15)   Park, Y. J.; Cook, S. A.; Sickerman, N. S.; Sano, Y.; Ziller, J. W.; Borovik, A. S. Heterobimetallic Complexes with M(III)-(μ-OH)-M(II) Cores (M(III) = Fe, Mn, Ga; M(II) = Ca, Sr, and Ba): Structural, Kinetic, and Redox Properties. *Chem. Sci.* **2013**, *4* (2), 717–726.

(16)   Amgoune, A.; Bourissou, D. σ-Acceptor, Z-Type Ligands for Transition Metals. *Chem. Commun.* **2011**, *47* (3), 859–871.

(17)   Chapman, A. M.; Haddow, M. F.; Wass, D. F. Frustrated Lewis Pairs beyond the Main Group: Synthesis, Reactivity, and Small Molecule Activation with Cationic Zirconocene--Phosphinoaryloxide Complexes. *J. Am. Chem. Soc.* **2011**, *133* (45), 18463–18478.

(18)   Barnett, B. R.; Moore, C. E.; Rheingold, A. L.; Figueroa, J. S. Cooperative Transition Metal/Lewis Acid Bond-Activation Reactions by a Bidentate (Boryl)iminomethane Complex: A Significant Metal–Borane Interaction Promoted by a Small Bite-Angle LZ Chelate. *J. Am. Chem. Soc.* **2014**, *136* (29), 10262–10265.

(19)   Kita, M. R.; Miller, A. J. M. Cation-Modulated Reactivity of Iridium Hydride Pincer-Crown Ether Complexes. *J. Am. Chem. Soc.* **2014**, *136* (41), 14519–14529.

(20)   Smith, J. B.; Miller, A. J. M. Connecting Neutral and Cationic Pathways in Nickel-Catalyzed Insertion of Benzaldehyde into a C–H Bond of Acetonitrile. *Organometallics* **2015**, *34* (19), 4669–4677.

(21)   Ozerov, O. V. Oxidative Addition of Water to Transition Metal Complexes. *Chem. Soc. Rev.* **2009**, *38* (1), 83–88.

(22)   Roberto, D.; Cariati, E.; Psaro, R.; Ugo, R. Formation of [Ir(CO)$_2$Cl]x (x = 2, n) Species by Mild Carbonylation of [Ir(cyclooctene)$_2$Cl]$_2$ Supported on Silica or in Solution: A New Convenient Material for the Synthesis of Iridium(I) Carbonyl Complexes. *Organometallics* **1994**, *13* (11), 4227–4231.

(23)   Goldberg, J. M.; Wong, G. W.; Brastow, K. E.; Kaminsky, W.; Goldberg, K. I.; Heinekey, D. M. The Importance of Steric Factors in Iridium Pincer Complexes. *Organometallics* **2015**, *34* (4), 753–762.

(24)   Adams, J. J.; Lau, A.; Arulsamy, N.; Roddick, D. M. Acceptor PCP Pincer Iridium Chemistry: (^{CF3}PCP)Ir^{III} Coordination Properties. *Organometallics* **2011**, *30* (4), 689–696.

(25)   Rybtchinski, B.; Ben-David, Y.; Milstein, D. Unexpected Isomerization of a Cis- into a Trans-Dihydride Complex . A Neutral Late Transition Metal Complex as a Hydride Donor. *Organometallics* **1997**, *16* (8), 3786–3793.

(26)   Kaljurand, I.; Kütt, A.; Soováli, L.; Rodima, T.; Mäemets, V.; Leito, I.; Koppel, I. a. Extension of the Self-Consistent Spectrophotometric Basicity Scale in Acetonitrile to a Full Span of 28 pK_a Units: Unification of Different Basicity Scales. *J. Org. Chem.* **2005**, *70* (3), 1019–1028.

(27)   Spasyuk, D. M.; Zargarian, D.; van der Est, A. New POCN-Type Pincer Complexes of Nickel(II) and Nickel(III). *Organometallics* **2009**, *28* (22), 6531–6540.

(28)   Adams, J. J.; Arulsamy, N.; Roddick, D. M. Acceptor PCP Pincer Iridium(I) Chemistry: Stabilization of Nonmeridional PCP Coordination Geometries. *Organometallics* **2011**, *30* (4), 697–711.

(29)   Lao, D. B.; Owens, A. C. E.; Heinekey, D. M.; Goldberg, K. I. Partial Deoxygenation of Glycerol Catalyzed by Iridium Pincer Complexes. *ACS Catal.* **2013**, *3* (10), 2391–2396.

(30)   Sola, E.; Navarro, J.; López, J. a.; Lahoz, F. J.; Oro, L. A.; Werner, H. Labile Hydrido Complexes of Iridium(III): Synthesis, Dynamic Behavior in Solution, and Reactivity toward Alkenes. *Organometallics* **1999**, *18* (17), 3534–3546.

(31)   Camp, A. M.; Kita, M. R.; Grajeda, J.; White, P. S.; Dickie, D. A.; Miller, A. J. M. Mapping the Binding Modes of Hemilabile Pincer–Crown Ether Ligands in Solution Using Diamagnetic Anisotropic Effects on NMR Chemical Shift. *Inorg. Chem.* **2017**, *56* (18), 11141–11150.

(32)   Tonks, I. A.; Bercaw, J. E. (dme)MCl$_3$(NNPh$_2$) (dme = dimethoxyethane; M = Nb, Ta): A Versatile Synthon for [Ta═NNPh$_2$] Hydrazido(2-) Complexes. *Inorg. Chem.* **2010**, *49* (10), 4648–4656.

(33)   Findlater, M.; Cartwright-Sykes, A.; White, P. S.; Schauer, C. K.; Brookhart, M. Role of Coordination Geometry in Dictating the Barrier to Hydride Migration in d^6 Square-Pyramidal Iridium and Rhodium Pincer Complexes. *J. Am. Chem. Soc.* **2011**, *133* (31), 12274–12284.

(34)   Pace, R. D.; Regmi, Y. The Finkelstein Reaction: Quantitative Reaction Kinetics of an S$_N$2 Reaction Using Nonaqueous Conductivity. *J. Chem. Educ.* **2006**, *83* (9), 1344–1348.

(35)   Rybtchinski, B.; Ben-David, Y.; Milstein, D. Unexpected Isomerization of a Cis - into a Trans - Dihydride Complex. A Neutral Late Transition Metal Complex as a Hydride Donor. *Organometallics* **1997**, *16* (17), 3786–3793.

(36)   Pearson, R. G. Hard and Soft Acids and Bases. *J. Am. Chem. Soc.* **1963**, *85* (3), 3533–3539.

(37)   Pearson, R. G. Hard and Soft Acids and Bases, HSAB, Part 1: Fundamental Principles. *J. Chem. Educ.* **1968**, *45* (9), 581.

(38)   Sheff, J. T.; Lucius, A. L.; Owens, S. B.; Gray, G. M. Generally Applicable NMR Titration Methods for the Determination of Equilibrium Constants for Coordination Complexes: Syntheses and Characterizations of Metallacrown Ethers with A,ω-Bis(phosphite)-Polyether Ligands and Determination of Equilibrium Binding. *Organometallics* **2011**, *30* (21), 5695–5709.

(39)   Di Bernardo, P.; Melchior, A.; Tolazzi, M.; Zanonato, P. L. Thermodynamics of lanthanide(III) Complexation in Non-Aqueous Solvents. *Coord. Chem. Rev.* **2012**, *256* (1–2), 328–351.

(40)   Kobayashi, S.; Manabe, K. Development of Novel Lewis Acid Catalysts for Selective Organic Reactions in Aqueous Media. *Acc. Chem. Res.* **2002**, *35* (4), 209–217.

(41)   Taylor, M. D.; Carter, C. P. Preparation of Anhydrous Lanthanide Halides, Especially Iodides. *J. Inorg. Nucl. Chem.* **1962**, *24* (4), 387–391.

(42)   Carter, F. L.; Murray, J. F. Preparation of the Anhydrous Rare Earth Trichlorides, Tribromides, and Triiodides. *Mater. Res. Bull.* **1972**, *7* (6), 519–523.

(43)   Perrin, D. D. Dissociation Contants of Inorganic Acids and Bases in Aqueous Solution. *Pure Appl. Chem.* **1969**, *20* (2), 133–236.

(44)   Beletskaya, I. P.; Voskoboynikov, A. Z.; Chuklanova, E. B.; Kirillova, N. I.; Shestakova, A. K.; Parshina, I. N.; Gusev, A. I.; Magomedov, G. K. I. Bimetallic Lanthanide Complexes with Lanthanide-Transition Metal Bonds. Molecular Structure of $(C_4H_8O)(C_5H_5)_2LuRu(CO)_2(C_5H_5)$. The Use of ^{139}La NMR Spectroscopy. *J. Am. Chem. Soc.* **1993**, *115* (6), 3156–3166.

(45)   Lance-Gómez, E. T.; Haschke, J. M. Preparation, Phase Equilibria, and Crystal Chemistry of La, Pr, and Nd Hydroxide Bromides and Hydroxide Iodides. *J. Solid State Chem.* **1978**, *23* (3–4), 275–279.

(46)   Fukuzumi, S.; Ohkubo, K. Quantitative Evaluation of Lewis Acidity of Metal Ions Derived from Theg Values of ESR Spectra of Superoxide: Metal Ion Complexes in Relation to the Promoting Effects in Electron Transfer Reactions. *Chem. Eur. J.* **2000**, *6* (24), 4532–4535.

(47)   Ozerov, O. V. Oxidative Addition of Water to Transition Metal Complexes. *Chem. Soc. Rev.* **2009**, *38* (1), 83–88.

(48)   Gillard, R. D.; Heaton, B. T.; Vaughan, D. H. Electrochemical Reduction of *trans*-[Rh(en)$_2$Cl$_2$]$^+$ and Subsequent Reactions with Oxygen. *J. Chem. Soc. A Inorganic, Phys. Theor.* **1970**, 3126.

(49)   Milstein, D.; Calabrese, J. C.; Williams, I. D. Formation, Structures, and Reactivity of Cis-Hydroxy-, Cis-Methoxy-, and Cis-Mercaptoiridium Hydrides. Oxidative Addition of Water to Ir(I). *J. Am. Chem. Soc.* **1986**, *108* (20), 6387–6389.

(50)   Morales-Morales, D.; Lee, D. W.; Wang, Z.; Jensen, C. M. Oxidative Addition of Water by an Iridium PCP Pincer Complex: Catalytic Dehydrogenation of Alkanes by IrH(OH){C$_6$H$_3$-2,6-(CH$_2$PBu$^t_2$)$_2$}. *Organometallics* **2001**, *20* (6), 1144–1147.

(51)   Millard, M. D.; Moore, C. E.; Rheingold, A. L.; Figueroa, J. S. Four-Coordinate Iridium(I) Monohydrides: Reversible Dinitrogen Binding, Bond Activations, and Deprotonations. *J. Am. Chem. Soc.* **2010**, *132* (26), 8921–8923.

(52)   Horváth, H.; Kathó, Á.; Udvardy, A.; Papp, G.; Szikszai, D.; Joó, F. New Water-Soluble Iridium(I)–N-Heterocyclic Carbene–Tertiary Phosphine Mixed-Ligand Complexes as Catalysts of Hydrogenation and Redox Isomerization. *Organometallics* **2014**, *33* (22), 6330–6340.

(53)   Grotjahn, D. B.; Gong, Y.; DiPasquale, A. G.; Zakharov, L. N.; Rheingold, A. L.

Bifunctional Imidazolylphosphine Ligands as Hydrogen Bond Donors Promote N−H and O−H Activation on Platinum. *Organometallics* **2006**, *25* (24), 5693–5695.

(54) Dolomanov, O. V.; Bourhis, L. J.; Gildea, R. J.; Howard, J. A. K.; Puschmann, H. OLEX2 : A Complete Structure Solution, Refinement and Analysis Program. *J. Appl. Cryst.* **2009**, *42* (2), 339–341.

(55) Bourhis, L. J.; Dolomanov, O. V.; Gildea, R. J.; Howard, J. a. K.; Puschmann, H. The Anatomy of a Comprehensive Constrained, Restrained Refinement Program for the Modern Computing Environment – Olex2 Dissected. *Acta Crystallogr. Sect. A Found. Adv.* **2015**, *71* (1), 59–75.

(56) Sheldrick, G. M. A Short History of SHELX. *Acta Cryst. Sect. A Found. Crystallogr.* **2008**, *64* (1), 112–122.

Chapter 3   HYDROFORMYLATION REACTION STUDIES WITH PINCER-CROWN ETHER COMPLEXES OF GROUP 9

Reproduced in part with permission from Camp, A. M.; Kita, M. R.; Grajeda, J.; White, P. S.; Dickie, D. A.; Miller, A. J. M. "Mapping the Binding Modes of Hemilabile Pincer-Crown Ether Ligands in Solution Using Diamagnetic Anisotropic Effects on NMR Chemical Shift." *Inorg. Chem.* **2017**, *56*, 11141-11150. Copyright American Chemical Society.

Section 3.1   Introduction

Hydroformylation, or the oxo process, refers to the catalytic addition of a formyl (CHO) group and a hydrogen atom to an alkene, yielding either linear (normal, *n*) or branched (*iso*) aldehydes (Scheme 3.1). This process represents one of the most successful examples of homogeneous catalysis applied on an industrial scale.[1] During 2008, almost 10.4 million metric tons of aldehydes were produced for further use in the synthesis of alcohols, esters, and amines. Aldehyde-derived products are used in the synthesis of specialty chemicals of importance to the fragrance, pharmaceutical, and agrochemical industries.[2]
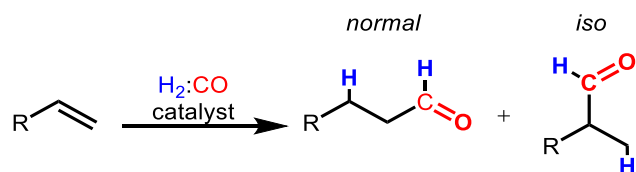
Scheme 3.1 Hydroformylation of alkenes.

Rhodium complexes are amongst the most widely used hydroformylation catalysts because they display high activity and chemoselectivity for aldehydes, with negligible

amounts of hydrogenation products (alkanes or alcohols) or alkene isomerization products (internal olefins).[3] A general scheme for rhodium-catalyzed hydroformylation of alkenes is depicted in Scheme 3.2.[4] Upon binding to the metal center, alkene insertion into a metal hydride bond generates a Rh-alkyl species. Migratory insertion followed by hydrogenolysis generates the aldehyde product. The scheme depicts formation of linear aldehydes. In the realm of aliphatic alkene hydroformylation the major challenge is the rational development of ligands that can impart control over the *n:iso* selectivity.[4,5] Both *n* and *iso* butyraldehydes resulting from the hydroformylation of propylene are funneled to a variety of chemicals, and the ratios required vary based on market needs.[6,7] The development of catalysts that can be fine-tuned to generate different ratios of aldehydes to satisfy shifts in demand would be highly beneficial.
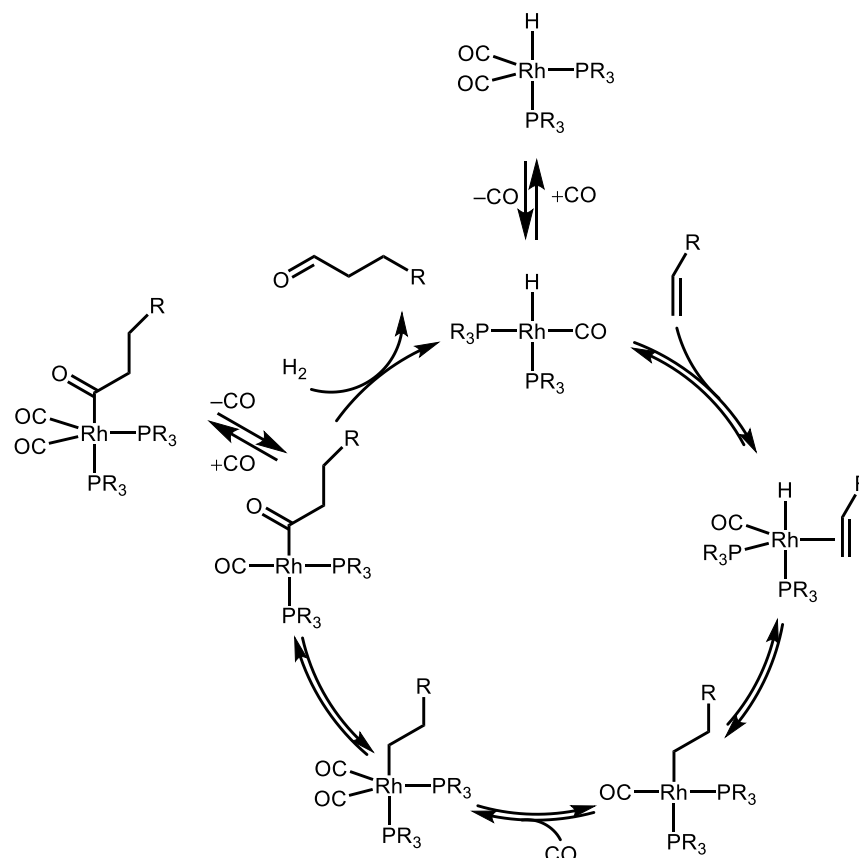
Scheme 3.2 Mechanism for rhodium-catalyzed hydroformylation of terminal alkenes. The cycle depicts formation of linear aldehydes exclusively, omitting the branched pathway to generate *iso* aldehydes.

Despite the fact that rhodium is scarce and expensive, other transition metals have received less attention due to the lower activity and chemoselectivity of complexes studied before.[1,8] The activity trend for unmodified metal carbonyl complexes is the following: Rh>>Co>Ir, Ru>Os>Pt>Pd>>Fe>Ni.[1] The main challenge in iridium-catalyzed hydroformylation lies in the fact that most complexes of this metal catalyze the hydrogenation of alkenes with great efficiency, yielding undesired alkyl products.[3] Due to its low chemoselectivity, iridium has therefore received little attention in the field.[9]

The use of cationic additives for distal regulation *via* host-guest interactions has been employed to control regio- and enantioselectivity in asymmetric hydroformylation.[10,11] We envisioned the use of catalytic systems featuring secondary binding pockets capable of supporting host-guest interactions in order to use additives to tune selectivity in hydroformylation catalysis (Figure 3.1).
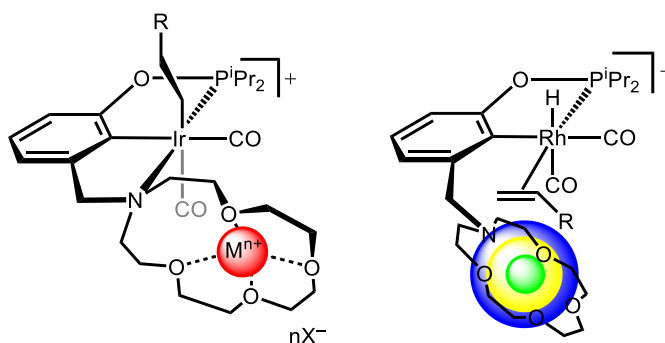
Figure 3.1 Host-guest interaction approaches for selectivity control in iridium- and rhodium-catalyzed hydroformylation. The green, yellow, and blue spheres represent varying steric profiles imparted by different additives in the crown.

It is well-established that Lewis acids in close proximity to the metal center can enhance the rates of CO migratory insertion into metal–carbon bonds.[12–16] For iridium-catalyzed hydroformylation, enhancements in rates of CO migratory insertion could impart aldehyde chemoselectivity by outcompeting undesired hydrogenation pathways. In the case of rhodium, additives of varying steric profiles in close proximity to the catalytically active site could impart control over regioselectivity. Pincer-crown ether ligands, featuring an aza-crown-ether macrocycle capable of binding cationic additives proved ideal candidates for these studies. Although rare, examples of hydroformylation with pincer complexes of rhodium, and even iridium, have been reported.[17–19]

Beller and co-workers recently showed that iridium complexes can produce aldehydes in greater than 80% yield, with only ~10% hydrogenation products.[20] Other groups have shown that competing hydrogenation can be suppressed with iridium catalysts by adding simple alkali metal additives.[21,22] Under certain conditions, selectivity for aldehydes could be increased to >90% in the presence of additives. The Behr group has also shown that iridium catalysts can be readily recovered and utilized in continuous feeds in a miniplant, with high activity and aldehyde chemoselectivity.[23,24]

The challenge of regioselectivity in rhodium-catalyzed hydroformylation of aliphatic alkenes remains an area of intense study.[4,5,7,25] Clarke and co-workers showed that the steric profiles of bidentate phosphoramidite-phosphine ligands can affect the binding mode and the geometries of the catalytically active species (Figure 3.2).[7] They found that these different coordination modes, on their own, did not strongly affect the selectivity for isobutyraldehyde formation. They concluded that further control over the coordination sphere was necessary in order to more controllably tune regioselectivity in hydroformylation. Supramolecular rhodium assemblies based on tris(meta-pyridyl)phosphine and zinc(II) porpholactone display the highest *iso* regioselectivity in propylene hydroformylation reported to date with ligand-supported systems (*n*:*iso* 0.84).[25]

bis-equatorial   axial-equatorial
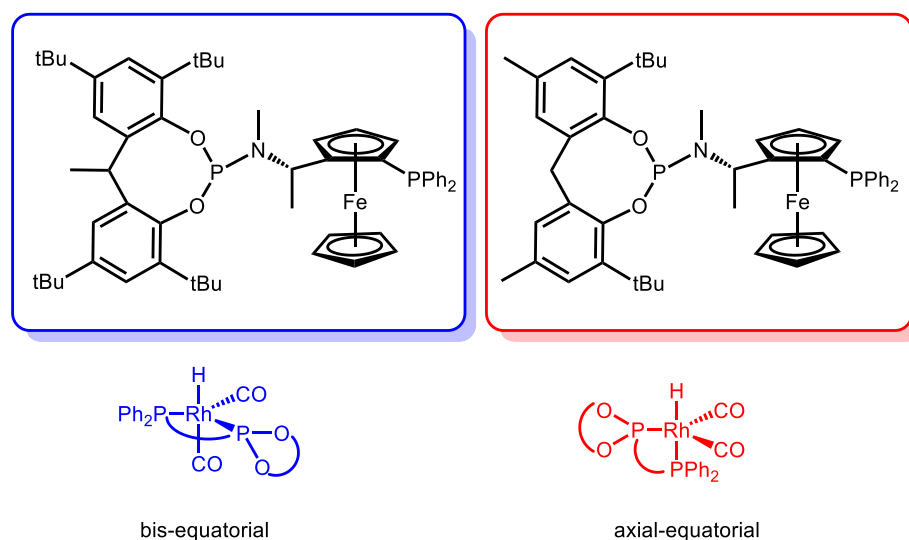
Figure 3.2 Bis-equatorial and axial-equatorial binding modes observed with phosphine-phosphoramidite ligands with varying steric profiles.

In this Chapter we describe the synthesis of pincer-crown ether complexes of iridium and rhodium, and their performance in alkene hydroformylation. Effects of alkali metal and ammonium additives through potential host-guest interactions, as well as the fate of the complexes after catalytic conditions, were also investigated.

Section 3.2   Synthesis of Iridium and Rhodium Pincer-Crown Ether Complexes

Given the typically detrimental role of halides in hydroformylation catalysis,[6] we targeted a halide-free hydridocarbonyl complex of iridium. Addition of $NaBAr^F_4$ (Ar^F is 3,5-bis(trifluoromethyl)phenyl) to κ^3-($^{15c5}NCOP^{iPr}$)Ir(H)(CO)(Cl) (**1**)[26] afforded the new cationic hydridocarbonyl complex [κ^4-($^{15c5}NCOP^{iPr}$)Ir(H)(CO)][BAr^F_4] (**2**) (Scheme 3.3).[27] Crystals of **2** suitable for an X-ray diffraction study were grown by slow evaporation of an Et_2O solution. Figure 3.3 shows that **2** adopts a tetradentate binding mode in the solid state, with a crown ether oxygen donor *trans* to the hydride. Multinuclear NMR spectroscopy studies reveal that this tetradentate binding mode is retained in solution in non-coordinating solvents such as methylene chloride.[27] Placing complex **2** under 1 atm of CO afforded the new

dicarbonyl complex $[\kappa^3\text{-}(^{15c5}NCOP^{iPr})Ir(H)(CO)_2][BAr^F_4]$ (**3**), on the basis of the downfield

hydride resonance at δ −9.43, which is indicative of a strong donor *trans* to the hydride.

Subjecting complex **3** to vacuum regenerated monocarbonyl **2**.
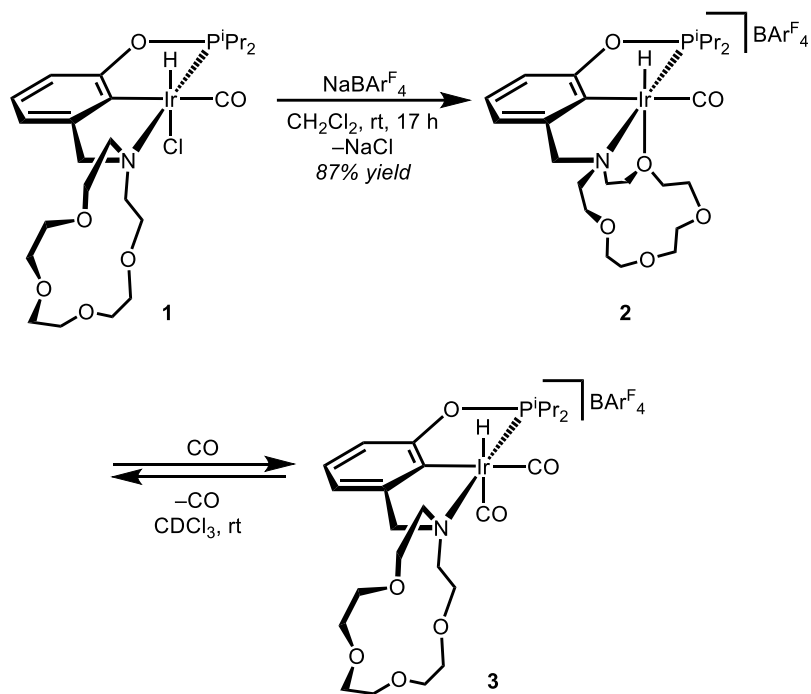
Scheme 3.3 Synthesis of complexes **2** and **3**.
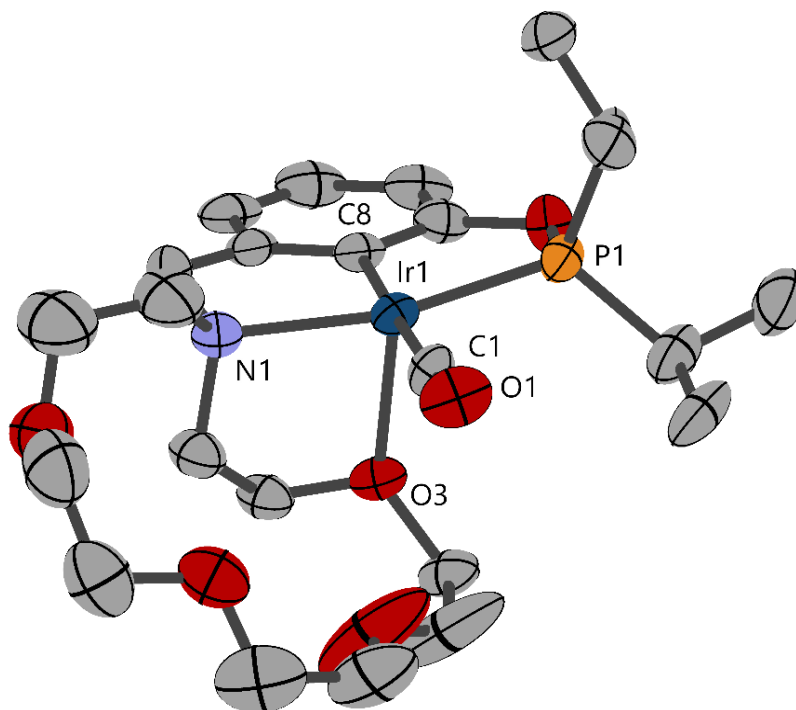
Figure 3.3 Structural representation of one of the two independent molecules of **2** in the asymmetric unit, with ellipsoids drawn at the 50% probability level. Hydrogen atoms and the $BArF_4$ counter ions are omitted for clarity. Selected distances (Å) and angles (°): Ir1–P1 2.252(3), Ir1–O3 2.282(7), Ir1–C8 2.025(8), Ir1–N1 2.185(8), Ir1–C1 1.940(9); P1–Ir1–O3 102.93(19), C1–Ir1–O3 96.1(3), C8–Ir1–O3 84.9(3), C1–Ir1–C8 178.5(4), N1–Ir1–O3 79.1(3).

Analogues supported by a methoxy-substituted pincer-crown ether ligand were also synthesized for this study. Incorporation of substituents on the ligand backbone allows for control over the primary coordination sphere at the metal center. The substitution pattern *ortho* to the phosphinite group was specifically chosen to prevent previously observed remetallation pathways.[26] Starting with complex κ^3-($^{MeO\text{-}15c5}NCOP^{iPr}$)Ir(H)(CO)(Cl) (**4**),[16] tetradentate complex [κ^4-($^{MeO\text{-}15c5}NCOP^{iPr}$)Ir(H)(CO)][$BArF_4$] (**5**) was synthesized in the same fashion as parent complex **2** (Scheme 3.4).
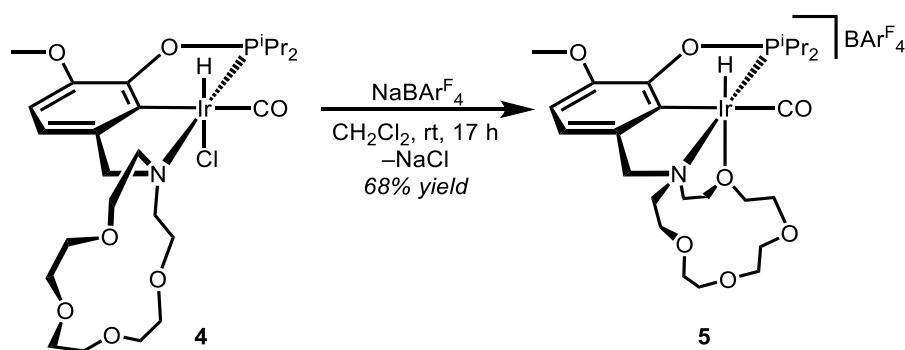
Scheme 3.4 Synthesis of complex **5**.

Rhodium complexes supported by a pincer-crown ether ligand framework were also targeted as hydroformylation catalysts. Metalation proceeded smoothly at room temperature by mixing 2 equiv of (^{15c5}NCOP^{iPr})H with [Rh(COE)$_2$Cl]$_2$ (COE = cyclooctene) in toluene, yielding tetradentate complex κ^4-(^{15c5}NCOP^{iPr})Rh(H)(Cl) (**6**) in 75% yield (Scheme 3.5). A doublet is observed by ^{31}P{^{1}H} NMR spectroscopy due to coupling to Rh (δ 198, J_{RhP} = 167.0 Hz). The hydride resonance in the ^{1}H NMR spectrum is a doublet of doublets (δ −22.9, J = 36.2, 27.0 Hz), due to coupling to both Rh and P. Single-crystal XRD data confirms the tetradentate binding mode in the solid state, with a *cis* configuration of the hydride and chloride ligands (Figure 3.4). The bond distances and angles are very similar to those for a previously reported iridium analogue.[28]
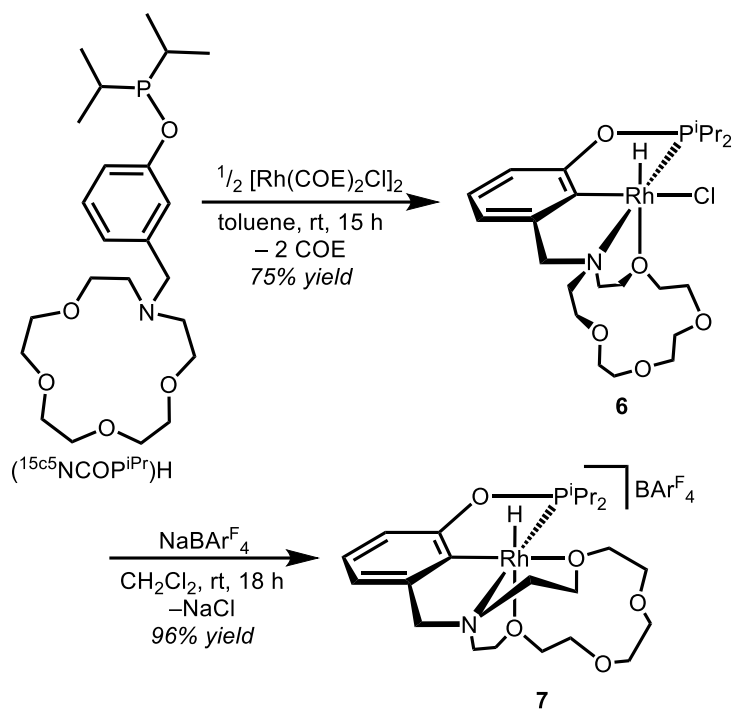
Scheme 3.5 Synthesis of complexes **6** and **7**.
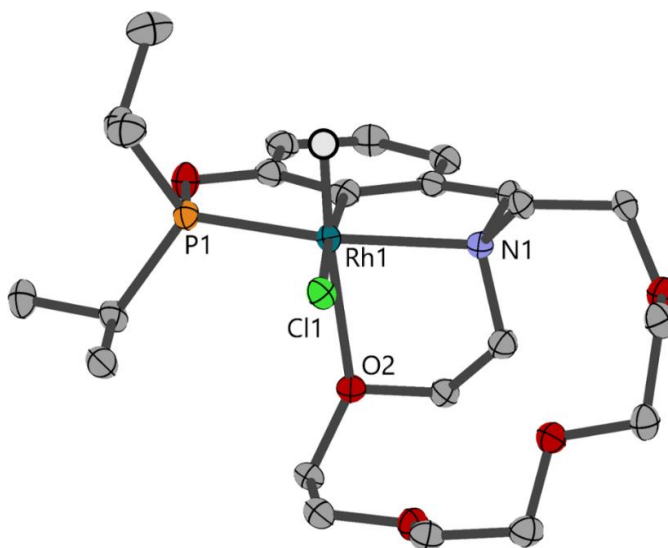
Figure 3.4 Structural representation of **6** with ellipsoids drawn at the 50% probability level. Hydrogen atoms of the ¹⁵ᶜ⁵NCOPⁱᴾʳ ligand are omitted for clarity. The hydride was found in the electron density difference map, and the Rh–H bond distance was restrained to 1.9 Å. Selected distances (Å) and angles (°): Rh1–P1 2.1878(9), Rh1–O2 2.368(3), Rh1–N1 2.231(3), Rh1–Cl1 2.4617(8); P1–Rh1–O2 101.22(7), P1–Rh1–Cl1 102.96(3), N1–Rh1–Cl1 94.68(8), N1–Rh1–O2 78.64(10), P1–Rh1–N1 162.34(8).

Abstraction of the chloride ligand from complex **6** with NaBAr$^F_4$ afforded

pentadentate species [κ^5-(^{15c5}NCOP^{iPr})Rh(H)][BAr$^F_4$] (**7**) in 96% yield. Pentadentate complex

7 features a hydride resonance slightly downfield to that of **6**, at δ −21.6. The ^{1}H NMR

spectrum confirms the presence of a BAr$^F_4$ counter ion, with the expected resonances in the

aromatic region integrating to 4H and 8H. The ^{31}P{^{1}H} NMR spectrum further confirms

conversion to a new species, with a new doublet at δ 193 (J_{RhP} = 163.8), 5 ppm upfield to that

of chloride complex **6**. Methoxy-substituted analogues κ^4-($^{MeO-15c5}$NCOP^{iPr})Rh(H)(Cl) (**8**)

and [κ^5-($^{MeO-15c5}$NCOP^{iPr})Rh(H)][BAr$^F_4$] (**9**) were accessed using the same synthetic

procedures as for the unblocked complexes (Scheme 3.6), and displayed similar

spectroscopic features.
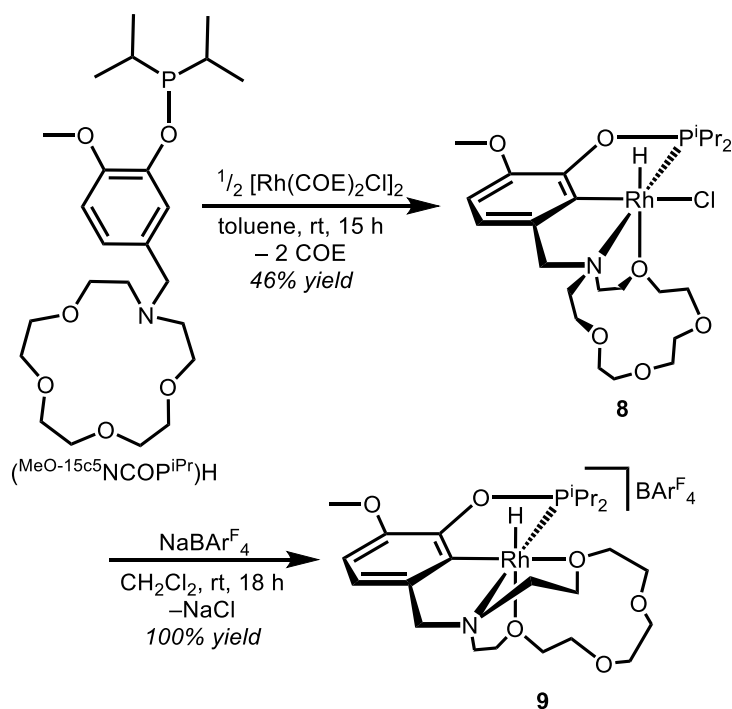
Scheme 3.6 Synthesis of complexes **8** and **9**.

Attempts at synthesizing rhodium carbonyl complexes proved unsuccessful. Placing

complexes **6** or **7** under 1 atm of CO in toluene-d_8 led to mixtures of products. Heating the

resulting mixtures to 90 °C did not simplify the product distribution. Over time, further decomposition was evident by NMR spectroscopy. We hypothesized that decomposition might result from acid generated through reductive elimination pathways triggered by carbonyl ligand binding. Addition of NEt_3 immediately after admission of CO to the mixture still did not generate clean conversion to a single carbonyl species. Methoxy-substituted pentadentate complex **9** similarly afforded mixtures of products when placed under 1 atm CO. Heating a solution of **9** in toluene-d_8 under 1 atm CO to 90 °C led to ligand decomposition. The presence of a singlet by $^{31}P\{^1H\}$ NMR spectroscopy (δ 68.5) indicates decomposition and dissociation from the rhodium metal center.

Section 3.3   Hydroformylation of Allylbenzene with Iridium Pincer-Crown Ether Complexes

Allylbenzene was chosen as a substrate for hydroformylation studies with iridium pincer-crown ether complexes. With this substrate, a number of possible products are expected under hydroformylation conditions (Scheme 3.7). The productive pathways involve formation of either *n* or *iso* aldehydes from terminal alkene functionalization. Some of the possible unproductive pathways are alkene hydrogenation to yield propylbenzene and alkene isomerization to yield β-methylstyrene.

Scheme 3.7 Products expected for allylbenzene substrate under hydroformylation conditions. Undesired products are denoted in red and desired products are denoted in green.

Tetradentate hydridocarbonyl complex [κ^4-(^{15c5}NCOP^{iPr})Ir(H)(CO)][BAr$^F_4$], **2**, was tested for allylbenzene hydroformylation under the conditions shown in Scheme 3.8, with 0.3 mol% loading of **2** relative to allylbenzene in 10 mL 1,2-dichloroethane solvent. We performed a time-dependence study to determine whether additives had any effects on the rate of hydrofunctionalization. Five reactors were loaded under standard catalytic conditions, pressurized with 20 bar of a 9:1 mixture of CO:H$_2$, and heated to 90 °C. The gas mixture, composed primarily of CO, was chosen in order to suppress undesired hydrogenation pathways.[19] Individual reactors were then cooled down after 0.5, 1, 1.5, 3, and 6 h (Figure 3.5). The reaction mixtures were then analyzed by ^{1}H NMR spectroscopy with hexamethyldisiloxane (HMDSO) as an internal standard.

Scheme 3.8 Hydroformylation of allylbenzene and derivatives with iridium pincer-crown ether complexes.
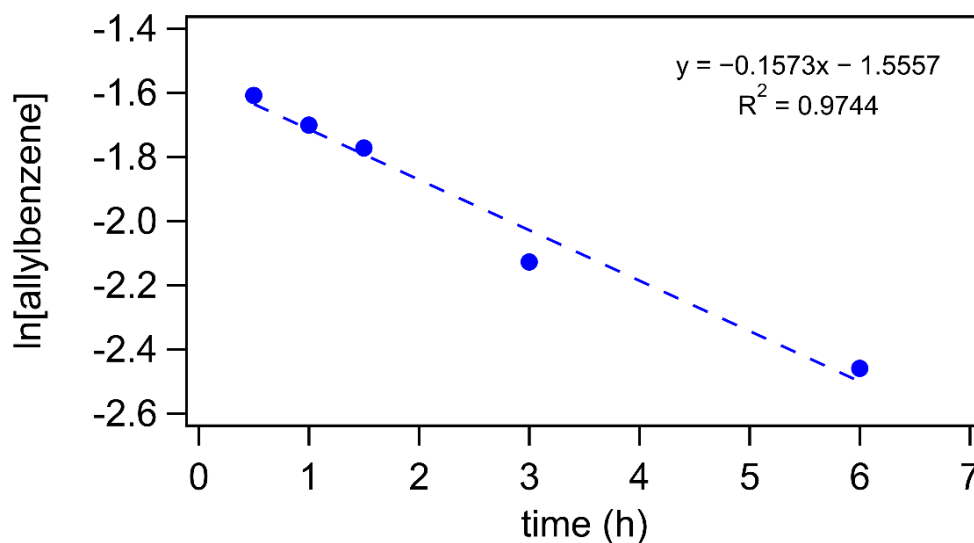
Figure 3.5 Consumption of allylbenzene over time with unblocked, tetradentate complex **2** as a catalyst, plotted as ln[allylbenzene] vs. time.

After 3 h, approximately half of the allylbenzene substrate had been consumed, with a 26% yield of aldehydes with a 2.3 *n:iso* ratio (Table 3.1, entry 1). Propylbenzene and β-methylstyrene were formed in 12% and 5% yields, respectively. Running the same reaction for 3 h in the presence of catalytic amounts (1.5 or 3 mol%) of LiOTf (OTf = trifluoromethanesulfonate) doubled the rates of product formation across the board after 3 h. Similar product distributions were maintained, even down to the *n:iso* ratio, but with over 80% conversion (Table 3.1, entries 2 and 3).

Table 3.1 Hydroformylation of allylbenzene in the presence of catalytic amounts of LiOTf. Yields determined by ^{1}H NMR spectroscopy after 3 h under standard catalytic conditions (2.2 mmol allylbenzene, 0.3 mol% **2**, 90 °C, 1,2-dichloroethane, 20 bar 9:1 CO:H$_2$).

Entry	LiOTf	conv.%	alkane%	isom.%	aldehydes%	n:iso
1	-	44	12	5	26	2.3
2	1.5 mol%	82	22	10	51	2.0
3	3 mol%	86	24	11	50	2.1

Running the reaction for 18 h resulted in complete consumption of allylbenzene substrate. A 61% combined yield of aldehydes (2.6 *n:iso* ratio) was obtained (Table 3.2, entry 1), along with propylbenzene (27% yield) and β-methylstyrene (12% yield). Carrying out the reaction in the presence of 3 mol% LiOTf did not affect chemoselectivity to any appreciable extent (Table 3.2, entry 2).

Table 3.2 Alkene hydroformylation with 0.3 mol % of **2** in the absence or presence of 3 mol% LiOTf. Yields determined by ^{1}H NMR spectroscopy after 18 h under standard catalytic conditions (2.2 mmol substrate, 0.3 mol% **2**, 90 °C, 1,2-dichloroethane, 20 bar 9:1 CO:H$_2$).

Entry	substrate	addit.	conv.%	alkane%	isom.%	ald.%	n:iso
1	allylbenzene	-	>99	27	12	61	2.6
2	allylbenzene	LiOTf	>99	26	11	62	2.1
3	2-allylanisole	-	>99	31	18	50	2.1
4	2-allylanisole	LiOTf	>99	29	10	61	2.1
5	allyl phenyl ether	-	>99	31	5	59	1.0
6	allyl phenyl ether	LiOTf	>99	35	7	57	1.0

We hypothesized that derivatives of allylbenzene with O-donors could enable chemoselectivity control by bridging the Li$^+$ cation in between the substrate and the macrocycle. Under standard hydroformylation catalytic conditions (Scheme 3.8), after 18 h, 2-allylanisole was found to undergo isomerization to a greater degree than allylbenzene, with an 18% yield of the isomerization product and aldehydes formed in 50% yield (Table 3.2,

entry 3). Allyl phenyl ether afforded 59% yield of aldehydes, with a 1.0 *n:iso* aldehyde ratio

(Table 3.1, entry 5). With 2-allylanisole, in the presence of catalytic amounts (3 mol%) of

LiOTf, the yield of aldehydes increased slightly to 61% (Table 3.1, entry 4), with the same

n:iso ratio of 2.1 and a decrease in isomerization to 10%. In the case of allyl phenyl ether,

product distribution remained essentially unchanged in the presence of LiOTf (Table 3.1,

entry 6).

Section 3.4   Identifying the Fate of the Iridium Pincer-Crown Ether Complex under Hydroformylation Reaction Conditions

In order to understand the origins of activity enhancement in the presence of LiOTf,

we embarked on mechanistic studies to try to determine the active species during catalysis.

Placing tetradentate complex **2** under 1 atm of CO in C_6D_5Cl led to initial formation of bis-

carbonyl species **3** (Ir–H δ −9.9) at room temperature. Heating this mixture to 90 °C to mimic

catalytic conditions, a new iridium species was generated (**10**), featuring a singlet at δ 175 by

$^{31}P\{^1H\}$ NMR spectroscopy (Scheme 3.9). This product is consistently formed upon heating

to 90 °C, including in the presence of 10% H_2 relative to CO. By ^1H NMR spectroscopy, it

became apparent that the new complex had undergone remetallation to a bidentate species,

with three new aromatic resonances at δ 6.4 (dd, J_{HH} = 7.6, 1.9), 6.8 (d, J_{HH} = 1.9 Hz), and

7.8 (d, J_{HH} = 7.5 Hz). The coupling between these protons was confirmed by a ^1H-^1H COSY

NMR spectrum.
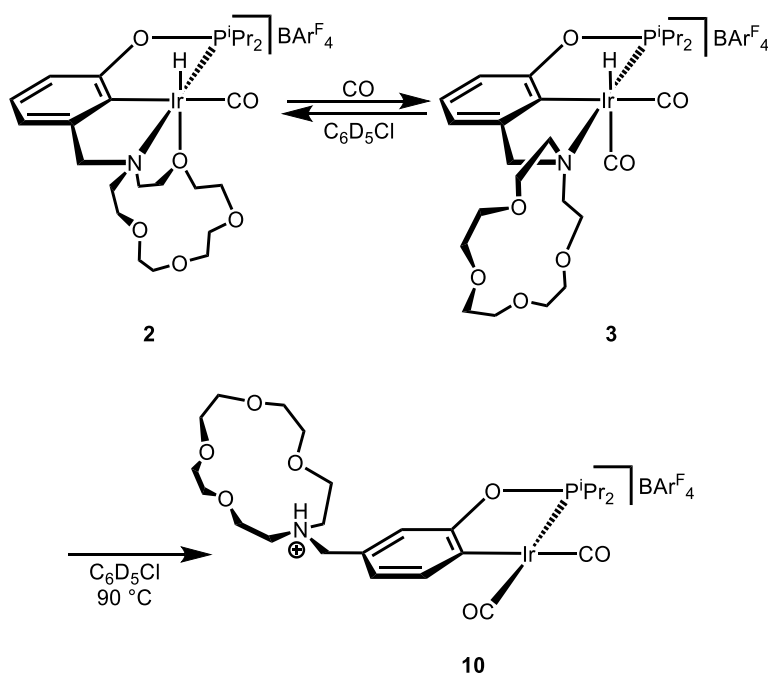
Scheme 3.9 Synthesis of iridium(I) bis-carbonyl species **10.**

Solid-state IR spectroscopy revealed the presence of two carbonyl ligands for

complex **10**, with CO stretching frequencies at 1989 and 2051 cm^{-1}. These values are

consistent with similar Ir(CO)$_2$Cl(PR$_3$) (R = Et, Cy, ^{t}Bu, ^{i}Pr) complexes.[29] This finding,

coupled with the ^{31}P{^{1}H} NMR resonance of δ 175, suggest that complex **10** is an Ir(I)

species.[26] Reductive elimination of the Ir–hydride onto the phenyl backbone of species **3**,

followed by C–H activation at the other position *ortho* to the phosphinite arm generates the

bidentate, remetallated species. A presumably intermolecular deprotonation from an unbound

aza-crown-ether group generates the observed Ir(I) species. That Ir(I) bis-carbonyl species **10**

exists in the protonated state is supported by the fact that addition of the base DBU (DBU =

1,8-diazabicyclo[5.4.0]undec-7-ene) yielded a closely related product, tentatively assigned as

neutral species κ^2-(^{15c5}NCOP^{iPr})Ir(CO)$_2$, with a peak at δ 171 by ^{31}P{^{1}H} NMR spectroscopy.

To determine whether species **10** could be present during catalysis, we characterized the iridium species at the end of a typical hydroformylation reaction. A reactor loaded with allylbenzene and 0.3 mol% of tetradentate complex **2** was pressurized and heated under standard conditions (20 bar 9:1 H_2:CO; 90 °C, 3 h). After venting, the solution was pumped to dryness under vacuum to afford a yellow oil. In C_6D_5Cl solution, ^1H NMR spectroscopy revealed similar resonances to those of an authentic sample of **10**. A closely-related singlet at δ 181 was observed by $^{31}P\{^1H\}$ NMR spectroscopy. Two CO stretches (ν_{CO} = 1985 and 2049 cm^{-1}) were observed by solid-state IR spectroscopy (Figure 3.6), closely matching those observed for authentic complex **10** (ν_{CO} = 1989 and 2051 cm^{-1}).
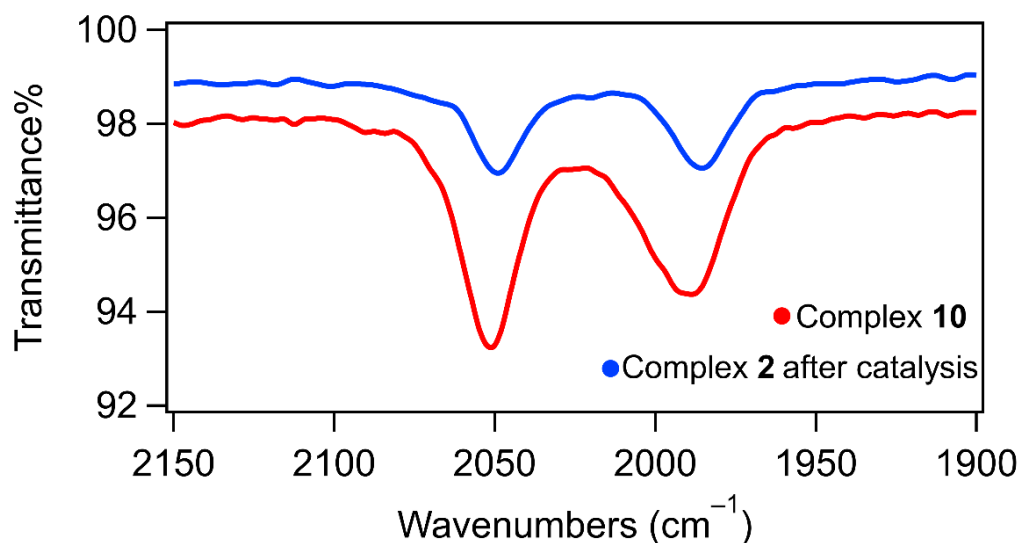
Figure 3.6 IR spectra of an authentic sample of **10** (red trace) and complex recovered after subjecting complex **2** to catalytic conditions (blue trace).

Section 3.5 Hydroformylation of Allylbenzene with a Methoxy-Blocked Iridium Pincer-Crown Ether Complex

In light of the observed remetallation reactivity with **2**, we turned our attention to the methoxy-blocked, tetradentate analogue, **5**. Inclusion of a methoxy substituent in the pincer

ligand backbone resulted in an almost three-fold rate enhancement, as measured by the consumption of allylbenzene over time (Figure 3.7). After 3 h, 54% of allylbenzene was consumed. Aldehydes were generated in 31% yield, with a 2.2 *n:iso* ratio (Table 3.3, entry 1). Propylbenzene and β-methylstyrene were formed in 15 and 8% yields, respectively.

The plot shows $y = -0.1573x - 1.5557$ $R^2 = 0.9744$ (blue) and $y = -0.4133x - 1.1018$ $R^2 = 0.9997$ (red), with axes ln[allylbenzene] vs. time (h).
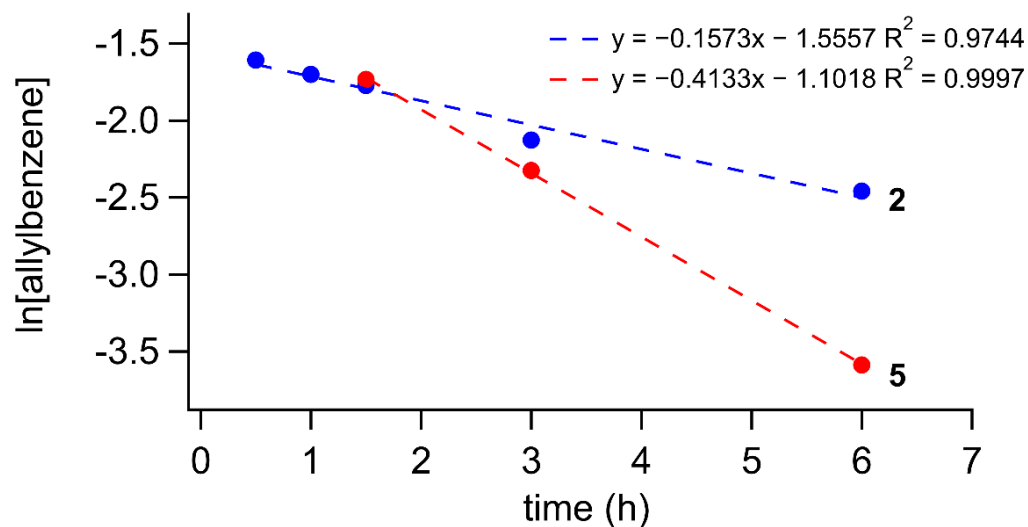
Figure 3.7 Consumption of allylbenzene over time with unblocked **2** (blue) and methoxy-blocked catalyst **5** (red), plotted as ln[allylbenzene] vs. time.

Table 3.3 Hydroformylation of allylbenzene with methoxy-blocked complex **5**. Yields determined by ^{1}H NMR spectroscopy after 3 h under standard catalytic conditions (2.2 mmol allylbenzene, 0.3 mol% **5**, 90 °C, 1,2-dichloroethane, 20 bar 9:1 $CO:H_2$). Unless otherwise noted, additives present in 2 mol%.

Entry	Addit.	conv.%	alkane%	isom.%	aldehydes%	*n:iso*
1	-	54	15	8	31	2.2
2	LiOTf	76	21	11	44	2.6
3	LiBArF4[a]	45	10	19	16	1.9
4	Li[Al(OC(CF3)3)4] [b]	45	10	20	16	2.0
5	MgOTf2	34	11	7	16	2.0
6	CeOTf4	57	9	43	5	0.6
7	[PPN][OTf]	62	16	10	36	2.2

[a] 0.4 mol%. [b] 0.7 mol%.

Catalytic amounts of LiOTf (2 mol%) enhanced the activity of methoxy-blocked complex **5**, albeit to a lesser degree than with unblocked **2**. The yield of aldehydes increased to 44%, with a similar *n:iso* ratio of 2.6 (Table 3.3, entry 2). The yields of propylbenzene and β-methylstyrene increased to 21 and 11%, respectively. LiOTf was the only additive found to effectively increase hydroformylation activity. In the presence of as low as 0.4 mol % LiBAr$^F_4$·2Et$_2$O, over 50% of the allylbenzene substrate remained unreacted after 3 h (Table 3.3, entry 3), with an enhancement in isomerization affording β-methylstyrene in 19% yield, at the expense of hydroformylation products (16% yield). Li[Al(OC(CF$_3$)$_3$)$_4$] in 0.7 mol% loading afforded very similar numbers as LiBAr$^F_4$·2Et$_2$O, similarly enhancing isomerization to the detriment of the yield of aldehydes.

MgOTf$_2$ (2 mol%) hindered activity (Table 3.3, entry 5), with 66% allylbenzene substrate remaining after 3 h, with only a 16% yield of aldehydes (vs. 31% in the absence of any additives). The *n:iso* ratio remain effectively unchanged at 2.0 relative to additive-free conditions (*n:iso*: 2.2). Ce(OTf)$_4$ was found to drastically suppress hydroformylation and promote isomerization, affording 43% yield of β-methylstyrene (Table 3.3, entry 6). Only 5% yield of aldehydes was obtained in a 0.6 *n:iso* ratio. Propylbenzene resulting from hydrogenation was detected in 9% yield, with 43% of allylbenzene substrate remaining at the end of the reaction. [PPN][OTf] (PPN = bis(triphenylphosphine)iminium) in 2 mol% loading did lead to a slight enhancement in activity, with 38% allylbenzene remaining after 3 h, without affecting product distribution, Table 3.3, entry 7).

The results summarized in Table 3.3 suggest that the combination of Li$^+$ and $^-$OTf increases the catalytic activity of complex **5** towards hydroformylation. Other Li$^+$ salts, such as LiBAr$^F_4$ and Li[Al(OC(CF$_3$)$_3$)$_4$], hinder hydroformylation in favor of isomerization.

Previous studies have shown that Li^+ greatly enhances the isomerization of allylbenzene to β-methylstyrene with iridium pincer-crown ether complexes.[30] It is possible that the enhanced solubility in 1,2-dichloroethane of $^-BAr^F_4$ and $^-[Al(OC(CF_3)_3)_4]$ salts relative to LiOTf is inducing rapid isomerization at room temperature before pressurization and heating. OTf salts of Mg^{2+} and Ce^{4+} also decrease aldehyde chemoselectivity. In the presence of $Ce(OTf)_4$, β-methylstyrene, resulting from isomerization, is the major product.

In an effort to rationalize the effects observed in the presence of additives, the fate of methoxy-blocked complex **5** was tested under catalytic conditions. A reactor loaded with allylbenzene and 0.3 mol% **5** in 10 mL 1,2-dichloroethane. It was pressurized with 20 bar of a 9:1 mixture of $CO:H_2$ and heated to 90 °C for 3 h. At this point it was cooled down and vented. The volatiles were removed under vacuum under gentle heating (60 °C). The residue was redissolved in CD_2Cl_2 and ^1H and $^{31}P\{^1H\}$ NMR spectra were acquired. Tetradentate complex **5** was present in the $^{31}P\{^1H\}$ NMR spectrum, but the main phosphine-containing product after the reaction was a new, as-of-yet unidentified, species at δ 143.

The hydride region in the ^1H NMR spectrum confirmed the presence of **5**, as well as additional minor hydride species further downfield (δ −9 to −13). A carbonyl stretch was detected by solid-state IR spectroscopy at 1954 cm^{-1} (Figure 3.8), suggesting that the major species during catalysis is a mono-carbonyl species. The cleaner reactivity displayed under catalytic conditions is a promising sign for the potential applicability of complex **5** in hydroformylation catalysis. Moving forward, it will be crucial to determine the fate of the more active, and seemingly more robust, complex **5**, which bears a methoxy protecting group.
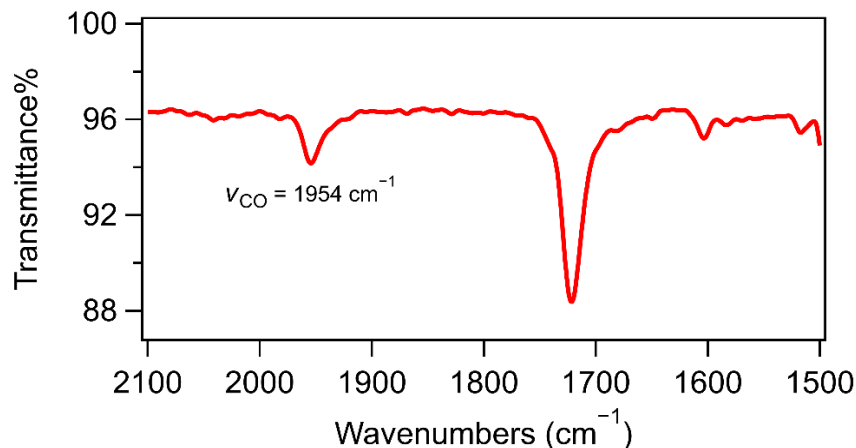
Figure 3.8 Solid-state IR spectrum obtained after subjecting methoxy-blocked complex **5** to catalytic conditions. The stretching frequency at 1720 cm^{-1} is attributed to residual aldehyde that was not removed under vacuum.

Section 3.6   Hydroformylation of 1-octene with Rhodium Pincer-Crown Ether Complexes

We next focused our attention on rhodium-catalyzed hydroformylation. In order to mimic industrially relevant conditions for propylene hydroformylation, 1-octene was chosen as a model substrate. Typical reaction conditions included pincer-crown ether complexes of rhodium in 0.4 mol% loading, 20 bar of 1:1 CO:H$_2$ in 0.75 mL toluene, ran at 95 °C for 1 h (Scheme 3.10). The compositions of the reaction mixtures were analyzed by gas chromatography (GC) with mesitylene as an internal standard. Under these conditions, hydroformylation to *n* or *iso* aldehydes was accessible, in addition to hydrogenation to octane, isomerization to internal alkenes, as well as hydroformylation of internal alkenes to generate other branched aldehydes.
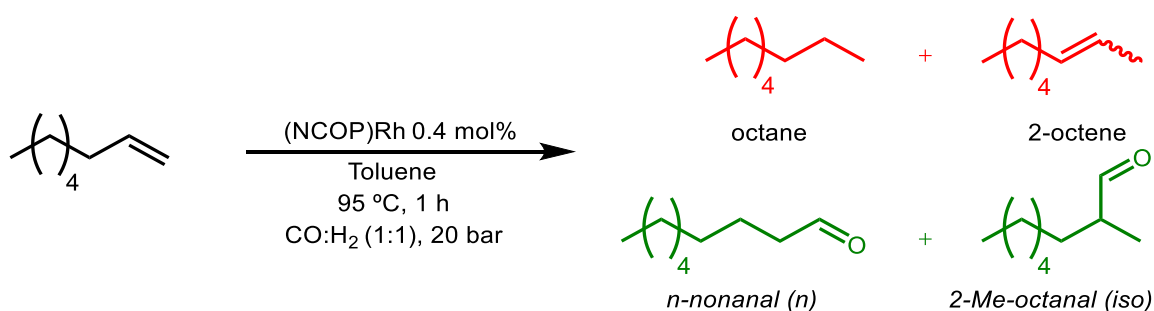
Scheme 3.10 Hydroformylation of 1-octene with rhodium pincer-crown ether complexes. Depicted in green are *n* and *iso* aldehyde products. Depicted in red are general structures for unproductive pathways of hydrogenation (octane) and isomerization (2-octene). Not depicted are other internal octene isomers or their corresponding hydroformylation products.

Both κ^4-(^{15c5}NCOP^{iPr})Rh(H)(Cl) (**6**) and [κ^5-(^{15c5}NCOP^{iPr})Rh(H)][BAr$^F_4$] (**7**) were

initially tested for 1-octene hydroformylation. Under typical catalytic conditions, both **6** and

7 displayed similar activity (Table 3.4), affording ~65% yield of aldehydes in a 1.4 *n:iso*

ratio, ~30% octane/octene isomers, and ~5% yield of other branched aldehydes. Under our

quantification conditions, it was not possible to separate and individually quantify different

octene isomers/octane or other branched aldehydes from one another.

Table 3.4 Hydroformylation of 1-octene with rhodium complexes **6** and **7**. Yields determined by GC after 1 h under standard catalytic conditions (0.6 mmol 1-octene, 0.4 mol% catalyst, 95 °C, 0.75 mL toluene, 20 bar 1:1 CO:H$_2$). Mesitylene added as an internal standard for quantification. *n+iso* reflects the yields of n-nonanal and 2-Me-octanal.

catalyst	*n+iso*%	*n:iso*	octane/octenes%	other aldehydes%
6	66	1.4	32	2
7	68	1.4	26	6

Isomerization to internal alkenes proved to be a challenging issue in the quantification

of the *n:iso* ratios. Hydroformylation of 2-octene could also afford 2-Me-octanal, affecting

the ratio *via* internal alkene hydroformylation, rather than by controlling 1-octene

functionalization through steric profile modifications. In order to elucidate the degree of

isomerization, a set of control experiments was designed under different gas compositions (Scheme 3.11).
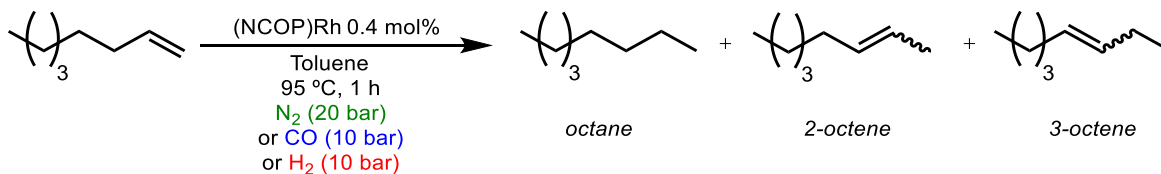
Scheme 3.11 Control experiments for hydrogenation/isomerization under different gas compositions (20 bar N_2, or 10 bar CO, or 10 bar H_2). 4-octene not depicted.

Under either N_2 or CO, hydridochloride complex **6** and pentadentate hydride complex **7** afforded similar product distributions (Table 3.5, entries 1-4). Between 80-90% of 1-octene substrate remained unreacted at the end of the reactions, along with 10-20% yield of isomerization/hydrogenation products. Pentadentate complex **5** displayed slightly higher activity under these conditions. In the presence of H_2, 1-octene was almost completely consumed with either **6** or **7** (Table 3.5, entries 5 and 6). At the end of the reaction, ~10% of 1-octene remained unreacted, with ~90% yield of isomerization and hydrogenation products. Under N_2 and CO, light yellow solutions were obtained after pressurization/heating. On the other hand, under H_2 alone, brown oils were observed in the reaction vials, a possible indicator of catalyst degradation to yield rhodium clusters. Rhodium carbonyl clusters, or even rhodium nanoparticles are known to be catalytically active for alkene hydrogenation and hydroformylation.[31–33]

Table 3.5 Quantification of isomerization/hydrogenation with complexes **6** and **7** under different gas compositions. Yields determined by GC after 1 h under standard catalytic conditions (0.6 mmol 1-octene, 0.4 mol% catalyst, 95 °C, 0.75 mL toluene). Mesitylene added as an internal standard for quantification.

Entry	gas	catalyst	1-octene%	octenes/octane%
1	N_2 (20 bar)	**6**	89	11
2	N_2 (20 bar)	**7**	78	22
3	CO (10 bar)	**6**	88	12
4	CO (10 bar)	**7**	78	22
5	H_2 (10 bar)	**6**	8	92
6	H_2 (10 bar)	**7**	13	87

Having established the extent of isomerization under different gas compositions, we sought to examine 2-Me-octanal production *via* 2-octene hydroformylation. Using either **6** or **7** as the catalyst, 2-octene was subjected to standard catalytic conditions for hydroformylation (Scheme 3.12). Both **6** and **7** resulted in partial isomerization of 2-octene to terminal 1-octene and its subsequent hydroformylation to afford n-nonanal in 14 and 8% yields, respectively. With hydridochloride complex **6**, 2-Me-octanal was produced in 28% yield and a 0.52 *n:iso* ratio (Table 3.6, entry 1). Other branched aldehydes were obtained in 16% yield. Octene isomers and octane were detected in 41% yield, including unreacted 2-octene that could not be independently quantified from the rest of the octene isomers. Complex **7** afforded a higher 42% yield of 2-Me-octanal (Table 3.6 entry 2), with an *n:iso* ratio of 0.20. Almost no octene isomers or octane were present after the reaction. This complex yielded higher numbers of other branched aldehydes, totaling 46%.
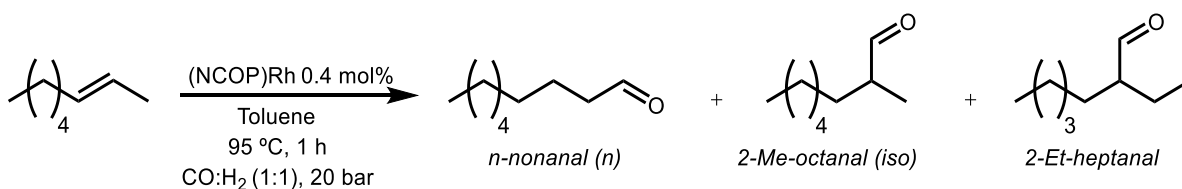
Scheme 3.12 Hydroformylation of 2-octene with rhodium pincer-crown ether complexes **6** or **7**. Only 2-Me-octanal and 2-Et-heptanal branched aldehydes depicted. n-nonanal depicted as a possible product *via* isomerization of 2-octene to 1-octene. Not depicted are other branched aldehydes.

Table 3.6 Hydroformylation of 2-octene with rhodium complexes **6** and **7**. Yields determined by GC after 1 h under standard catalytic conditions (0.6 mmol 1-octene, 0.4 mol% catalyst, 95 °C, 0.75 mL toluene, 20 bar 1:1 CO:H_2). Mesitylene added as an internal standard for quantification.

Entry	catalyst	octenes/octane %	n ald. %	iso ald.%	*n:iso*	other ald.%
1	**6**	41	14	28	0.52	16
2	**7**	4	8	42	0.20	46

In order to impart control over the regioselectivity for either linear or branched aldehydes, we envisioned expanding our portfolio of cationic additives beyond simple metal salts previously used with iridium. We expected ammonium additives with varying steric profiles to have greater effects on regioselectivity than simple metal cations upon binding to the crown. A family of butylammonium salts (Figure 3.9) was synthesized by protonating the corresponding amines with NH4PF6 in refluxing toluene.[34] Ammonium-crown complexation is based on hydrogen bonding interactions between the N–H groups and the O atoms in the macrocycle.[35] In order to maximize interactions between the additives and the crown, primary ammonium salts were targeted.

[^{n}BuNH$_3$][PF$_6$]   [^{s}BuNH$_3$][PF$_6$]   [^{t}BuNH$_3$][PF$_6$]
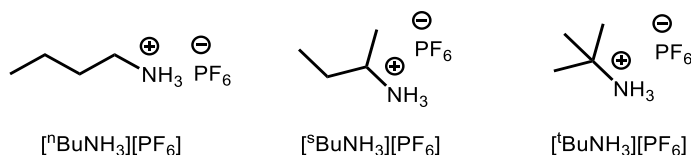
Figure 3.9 Butylammonium additives.

With these additives in hand, a study was undertaken to determine their effects on hydroformylation regioselectivity with pentadentate complex **7**. Addition of the ammonium salts (3-4 mol%), in combination with NaBAr$^F_4$ (2 mol%), led to a systematic decrease in the *n*:*iso* ratio with increasing steric bulk (Table 3.7, entries 2-4), all the way down to a ratio of 1.0. The yields of the desired *n* and *iso* aldehydes also decreased in the presence of the ammonium additives, affording higher yields of other branched aldehydes. This could be indicative of a role of the additives in accelerating isomerization to internal alkenes, which in turn undergo hydroformylation to different branched aldehydes. In order to assess the role of the Na$^+$ salt, [^{t}BuNH$_3$][PF$_6$] was mixed with NaBAr$^F_4$ in toluene-d_8. NMR spectroscopy suggests that anion-exchange takes place to yield toluene-soluble [^{t}BuNH$_3$][BAr$^F_4$]. ^{31}P{^{1}H} NMR spectroscopy ruled out the presence of any phosphorus-containing species.

Table 3.7 Hydroformylation of 1-octene with pentadentate **7** in the presence of [RNH$_3$][PF$_6$] and NaBAr$^F_4$. Ammonium PF$_6$ salts were added in 3-4 mol% loading. Yields determined by GC after 1 h under standard catalytic conditions (0.6 mmol 1-octene, 0.4 mol% **7**, 95 °C, 0.75 mL toluene, 20 bar 1:1 CO:H$_2$). Mesitylene added as an internal standard for quantification. *n*+*iso* reflects the yields of n-nonanal and 2-Me-octanal.

Entry	RNH$_3^+$ addit.	NaBAr$^F_4$	conv.%	octenes/ane %	n+iso %	n:iso	other ald.%
1	-	-	98	26	67	1.4	6
2	R = ^{n}Bu	2 mol%	96	30	55	1.2	11
3	R = ^{s}Bu	2 mol%	96	30	54	1.1	12
4	R = ^{t}Bu	2 mol%	96	24	52	1.0	20
5	-	2 mol%	96	46	32	1.2	19

The role of NaBAr$^F_4$ as an additive was also studied (Table 3.7, entry 5), resulting in a decrease in the *n:iso* ratio, as well as an increase in the yield of other branched aldehydes. The most pronounced effects imparted by NaBAr$^F_4$ were an increase in the degree of isomerization or hydrogenation from 26% to 46%, as well as a decrease in the total yield of the targeted n-nonanal and 2-Me-octanal products from 67% to 32% yield.

The catalytic activity of $[\kappa^5\text{-}(^{MeO\text{-}15c5}NCOP^{iPr})Rh(H)][BAr^F_4]$ (**9**) in hydroformylation was explored next. Complex **9** outperformed unblocked analogue **7**, with a chemoselectivity for *n* and *iso* aldehydes of 96% and a 1.3 *n:iso* ratio (Table 3.8, entry 1). Alkene isomers were only formed in 4% yield and other branched aldehydes were present in less than 1% yield. In the presence of ammonium additives and NaBAr$^F_4$, selectivity for *n* and *iso* aldehydes dropped considerably to ~50% in all cases (Table 3.8, entries 2-4), along with a drop in the *n:iso* ratio to ~1.1. Approximately 5% of 1-octene substrate remained in the presence of additives. Olefin isomerization or hydrogenation was greatly accelerated in the presence of these additives, with ~45% yields of internal alkenes across the board.

Table 3.8 Hydroformylation of 1-octene with methoxy-blocked pentadentate **9** in the presence of $[RNH_3][PF_6]$. Ammonium PF$_6$ salts added in 3-4 mol% loading. Yields determined by GC after 1 h under standard catalytic conditions (0.6 mmol 1-octene, 0.4 mol% **9**, 95 °C, 0.75 mL toluene, 20 bar 1:1 CO:H$_2$). Mesitylene added as an internal standard for quantification. *n+iso* reflects the yields of n-nonanal and 2-Me-octanal.

Entry	RNH$_3^+$ addit.	NaBAr$^F_4$	conv.%	octenes/ane %	*n+iso* %	*n:iso*	other ald.%
1	-	-	>99	4	96	1.3	<1%
2	R = ^{n}Bu	2 mol%	95	42	53	1.1	<1%
3	R = ^{s}Bu	2 mol%	95	44	51	1.1	<1%
4	R = ^{t}Bu	2 mol%	96	43	52	1.0	<1%

With both unblocked and methoxy-blocked pentadentate complexes **7** and **9**, *n:iso*

ratios dropped in the presence of ammonium salts. However, these additives seemed to

greatly enhance the rate of alkene isomerization. With unblocked **7**, the yields of other

branched aldehydes (products of internal alkene hydroformylation) increased to up to 20%

(from 6% in the absence of any additives). In the case of methoxy-blocked **9**, the yields of

internal alkenes increased from 4% to 42-44%, at the expense of production of n-nonanal and

2-Me-octanal. These studies suggest that the role of the additives in decreasing the *n:iso* ratio

could primarily be due to their enhancing the rate of olefin isomerization. Hydroformylation

of 2-octene also leads to formation of 2-Me-octanal, which could be decreasing the observed

n:iso ratios.

Section 3.7 Exploring the Fate of $[\kappa^5\text{-}(^{15c5}\text{NCOP}^{iPr})\text{Rh(H)}][\text{BAr}^F_4]$ under Hydroformylation Conditions

The fate of rhodium pincer-crown ether complexes in catalysis was studied next, in

order to help understand the mechanism by which they operate, as well as the role that

ammonium additives could be playing in affecting product selectivity. Aliquots (0.750 mL)

of a solution of pentadentate complex **7** in toluene-d_8 were placed in two Teflon-capped

NMR tubes. One tube was further loaded with 0.090 mL of 1-octene, to mimic typical

catalytic loadings (Scheme 3.14). ^{1}H and ^{31}P{^{1}H} NMR spectra were acquired, confirming

the presence of complex **7**. The solutions were transferred to GC vials and placed in the HEL

Cat18 reactor. They were then subjected to typical hydroformylation conditions, pressurized

to 20 bar 1:1 CO:H$_2$ and heated at 90 °C for 1 h. After cooling, the solutions were transferred

to Teflon-capped NMR tubes under an inert N$_2$ atmosphere. In both instances (with and

without 1-octene) no signals corresponding to the rhodium complex were detected by

^{31}P{^{1}H} or ^{1}H NMR spectroscopy (Figure 3.10). In the presence of 1-octene, both n-nonanal and 2-Me-octanal were present in the ^{1}H NMR spectrum, with a 1.6 *n:iso* ratio closely matching the values determined by GC.
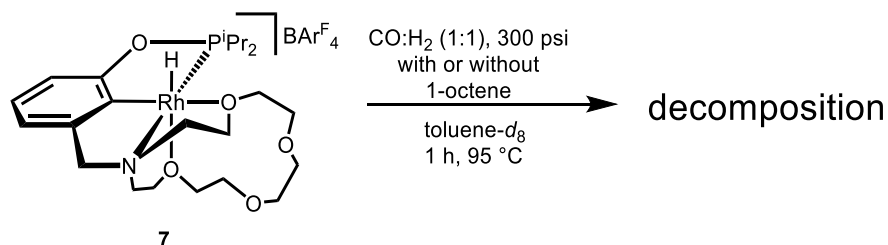
Scheme 3.13 Catalyst stability studies with pentadentate complex **7**. Samples were prepared under typical hydroformylation catalysis conditions, either with or without 1-octene.
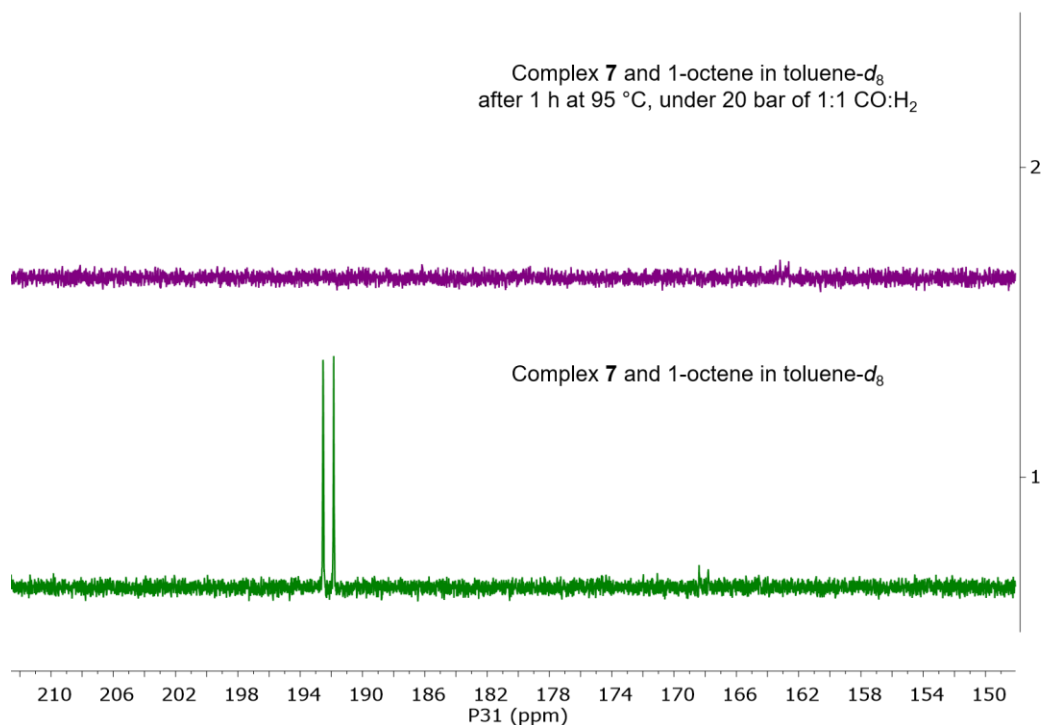
Figure 3.10 ^{31}P{^{1}H} NMR spectra obtained in toluene-d_8 before and after subjecting complex **7** to hydroformylation conditions. Similar effects were observed with and without 1-octene.

NMR spectroscopic experiments also revealed that 1-octene triggers slow complex decomposition. Addition of 1-octene to a solution of complex **7** in toluene-d_8 under typical concentrations of catalytic experiments resulted in slow loss of signal by ^{1}H NMR spectroscopy over the course of several days (Figure 3.11).
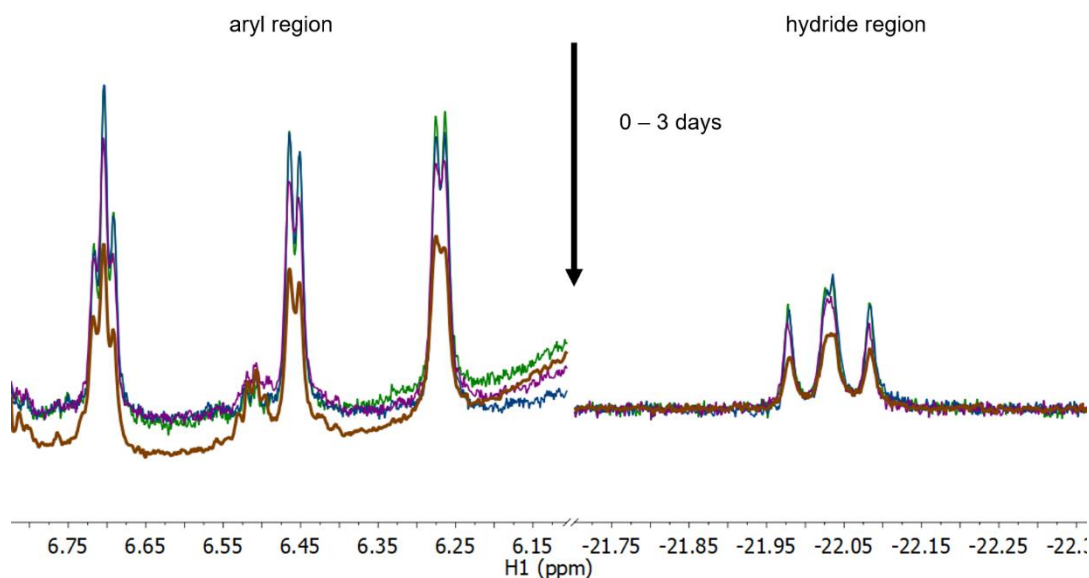
Figure 3.11 ^{1}H NMR spectra obtained over the course of several days after mixing 1-octene and complex **7** in toluene-d_8.

Although ammonium additives seem to affect control over regioselectivity in hydroformylation, at present it is not clear if this is due to steric control, or a simple rate enhancement of alkene isomerization. Given the propensity of rhodium pincer-crown ether complexes to undergo decomposition under catalytic conditions, even in the presence of substrate at room temperature, or under 1 atm of CO, it is clear that different avenues are to be pursued to access industrially-relevant catalysts. Phosphine ligands that form more robust molecular catalysts, with sites for additives to promote regioselectivity control, are currently being targeted.

Section 3.8 Experimental Details

General Considerations. Unless otherwise noted, all manipulations were carried out using standard Schlenk or glovebox techniques under a N_2 atmosphere. Under standard glovebox operating conditions, pentane, diethyl ether, benzene, toluene, and tetrahydrofuran were used without purging, such that traces of those solvents were present in the atmosphere and in the solvent bottles. ^1H, ^{31}P, ^{19}F, and ^{13}C spectra were recorded on 400, 500 or 600 MHz spectrometers at 298 K. NMR solvents were purchased from Cambridge Isotopes Laboratories, Inc. Dichloromethane-d_2 (CD_2Cl_2), C_6D_5Cl, and toluene-d_8 were freeze-pump-thaw degassed three times before drying by passage through a small column of activated alumina. ^1H and ^{13}C chemical shifts are reported in ppm relative to residual proteo solvent resonances. ^{31}P chemical shifts are reported relative to 85% H_3PO_4 external standard (δ 0). The compounds ($^{15c5}NCOP^{iPr}$)H,[28] ($^{MeO-15c5}NCOP^{iPr}$)H,[16] κ^3-($^{15c5}NCOP^{iPr}$)Ir(H)(CO)(Cl),[26] κ^3-($^{MeO-15c5}NCOP^{iPr}$)Ir(H)(CO)(Cl),[16] [Rh(COE)$_2$Cl]$_2$,[36] NaBAr$^F_4$,[37] LiBAr$^F_4$·3Et$_2$O,[28] Li[Al(OC(CF$_3$)$_3$)$_4$],[38] [^{n}BuNH$_3$][PF$_6$],[34] [^{s}BuNH$_3$][PF$_6$],[34] and [^{t}BuNH$_3$][PF$_6$][34] were synthesized as previously reported. All other reagents were commercially available and used without further purification. GC analysis was performed on a Agilent 6890 GC equipped with a HP-1 column (100 m × 0.25 mm I.D. × 0.50 μm film thickness), using GC ChemStation software. Elemental analyses were performed by Robertson Microlit Labs (Ledgewood, NJ). Infrared spectroscopy was carried out with a Thermo Scientific Nicolet iS5 FT-IR equipped with Quest Single Reflection ATR Accessory. High temperature and pressure catalysis was performed with a stainless steel HEL Cat18 parallel pressure autoclave or a Parr Series 5000 Multiple Reactor System operated by a Parr 4871 Process Controller equipped with six reactors with internal stirring. Each Parr reactor is individually pressure-

and temperature-controlled with maximum operating limits of 3000 psi (200 bar) and 300 °C. Each reactor is monitored by computer software SpecView 32. Single-crystal X-ray diffraction data were collected on a Bruker APEX-II CCD diffractometer at 100 K with Cu Kα radiation (λ = 1.54175 Å). Structures were solved using SHELXT and refined using SHELXL[39,40] software package within OLEX2.[41]

Synthesis of [κ⁴-(¹⁵ᶜ⁵NCOP^iPr)Ir(H)(CO)][BAr^F₄] (2). A 20-mL scintillation vial was charged with κ³-(¹⁵ᶜ⁵NCOP^iPr)Ir(H)(CO)(Cl) (0.0522 g, 0.0749 mmol), NaBAr^F₄ (0.0732 g, 0.0826 mmol), and CH_2Cl_2 (8 mL). The resulting yellow slurry was stirred for 17 h. The mixture was filtered, and the light-golden-yellow filtrate was concentrated to ~1 mL under vacuum. Pentane (5 mL) was added, and the solvent was removed under vacuum, affording **2** as an off-white solid (0.0997 g, 87% yield). Single crystals suitable for X-ray diffraction were grown by slow evaporation of an Et_2O solution of **2** into $(Me_3Si)_2O$. ¹H NMR (600 MHz, CD_2Cl_2): δ −25.67 (d, J = 21.4 Hz, 1H, Ir–*H*), 0.92 (dd, J = 16.8, 7.0 Hz, 3H, CH(C*H₃*)₂), 1.05 (dd, J = 20.9, 6.9 Hz, 3H, CH(C*H₃*)₂), 1.38 (dd, J = 18.9, 7.5 Hz, 3H, CH(C*H₃*)₂), 1.44 (dd, J = 14.8, 6.8 Hz, 3H, CH(C*H₃*)₂), 2.55 (overlapping m, 2H, C*H*(CH₃)₂), 3.06 (m, 1H, crown-C*H₂*), 3.58 (m, 9H, crown-C*H₂*), 3.78 (m, 4H, crown-C*H₂*), 3.93 (m, 1H, crown-C*H₂*), 4.01 (m, 2H, crown-C*H₂*), 4.18 (m, 1H, crown-C*H₂*), 4.28 (m, 2H, crown-C*H₂*), 4.58 (dd, J = 15.6, 2.9 Hz, 1H, ArC*H*HN), 4.63 (d, J = 15.7 Hz, 1H, ArCH*H*N), 6.80 (d, J = 7.7 Hz, 1H, Ar–*H*), 6.82 (d, J = 8.3 Hz, 1H, Ar–*H*), 7.07 (t, J = 7.8 Hz, 1H, Ar–*H*), 7.56 (s, 4H, *p*-B-Ar-*H*), 7.72 (s, 8H, *o*-B-Ar-*H*). ¹³C{¹H} NMR (151 MHz, CD_2Cl_2): δ 16.12 (d, J = 4.7 Hz, CH(*C*H₃)₂), 17.37 (d, J = 2.3 Hz, CH(*C*H₃)₂), 17.86 (d, J = 4.0 Hz, CH(*C*H₃)₂), 18.20 (d, J = 6.3 Hz, CH(*C*H₃)₂), 29.69 (d, J = 38.9 Hz, *C*H(CH₃)₂), 31.93 (d, J = 36.0 Hz, *C*H(CH₃)₂), 66.13 (d, J = 1.4 Hz, crown-*C*H₂), 67.50 (s, crown-*C*H₂), 69.08 (s, crown-*C*H₂),

69.42 (d, $J = 2.0$ Hz, crown-CH_2), 70.52 (d, $J = 2.4$ Hz, crown-CH_2), 70.66 (s, crown-CH_2),

70.83 (s, crown-CH_2), 71.75 (s, crown-CH_2), 73.12 (s, crown-CH_2), 75.69 (d, $J = 1.4$ Hz,

ArCH_2N), 78.56 (s, crown-CH_2), 110.16 (d, $J = 12.3$ Hz, C_{Ar}), 115.57 (s, C_{Ar}), 117.87 (p, $J =$

4.1 Hz, p-CH, BAr^F), 124.99 (q, $J = 272.4$ Hz, CF$_3$, BAr^F), 129.05 (s, C_{Ar}), 129.26 (qdd, $J =$

31.2, 5.8, 2.9 Hz, C–CF$_3$, BAr^F), 135.19 (s, o-CH, BAr^F), 145.87 (d, $J = 5.0$ Hz, C_{Ar}), 152.27

(d, $J = 3.3$ Hz, C_{Ar}), 162.14 (dd, $J = 99.7, 49.9$ Hz, B–C, BAr^F), 162.80 (d, $J = 1.4$ Hz, C_{Ar}),

183.35 (s, Ir–CO). ^{31}P{^{1}H} NMR (243 MHz, CD$_2$Cl$_2$): δ 152.77. IR (solid): $\nu_{CO} = 2041$ cm^{-1}.

Anal. Calcd for C$_{56}$H$_{52}$BF$_{24}$IrNO$_6$P: C, 44.11; H, 3.44; N, 0.92. Found: C, 44.38; H, 3.28; N,

0.95.
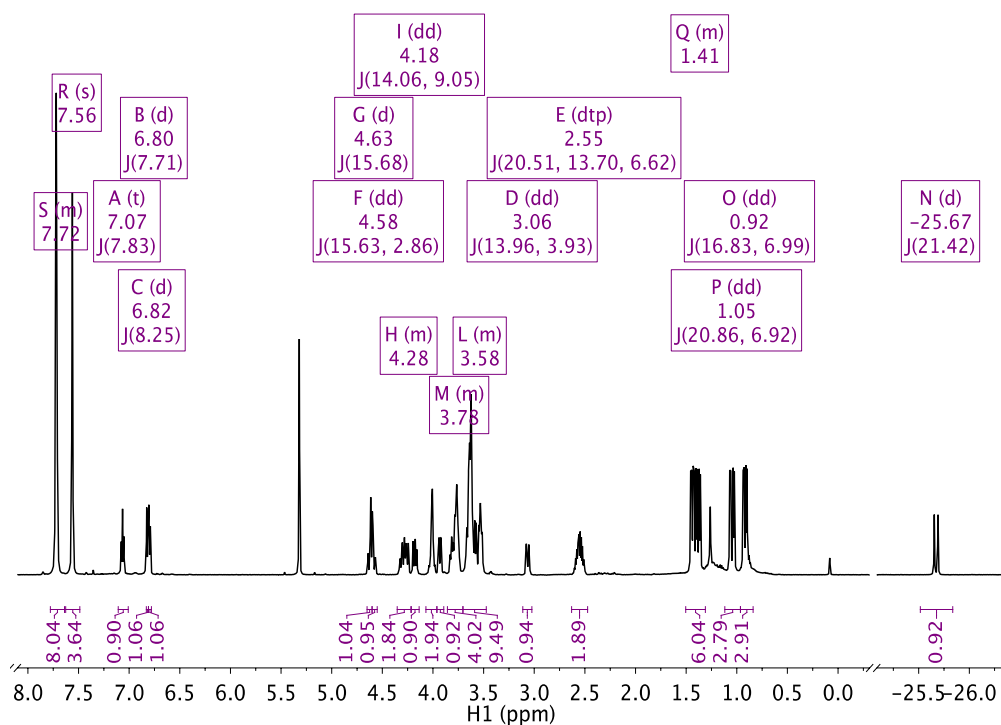
Figure 3.12 ^{1}H NMR spectrum of [κ^4-(^{15c5}NCOP^{iPr})Ir(H)(CO)][BAr$^F_4$] (**2**) in CD$_2$Cl$_2$.
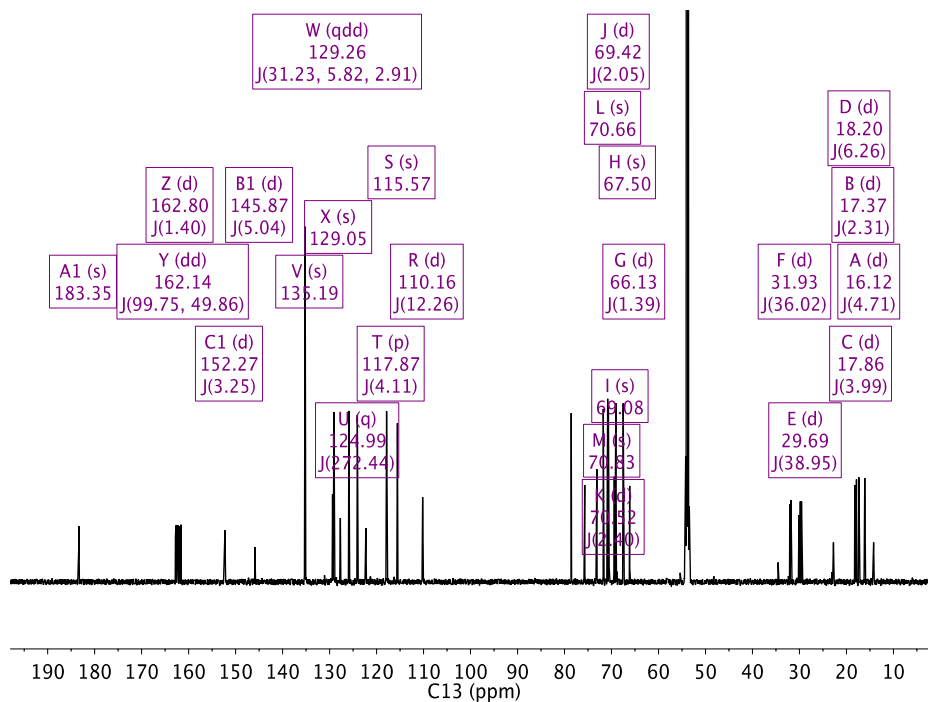
Figure 3.13 ^{13}C{^{1}H} NMR spectrum of [κ^4-(^{15c5}NCOP^{iPr})Ir(H)(CO)][BAr$^F_4$] (**2**) in CD$_2$Cl$_2$.
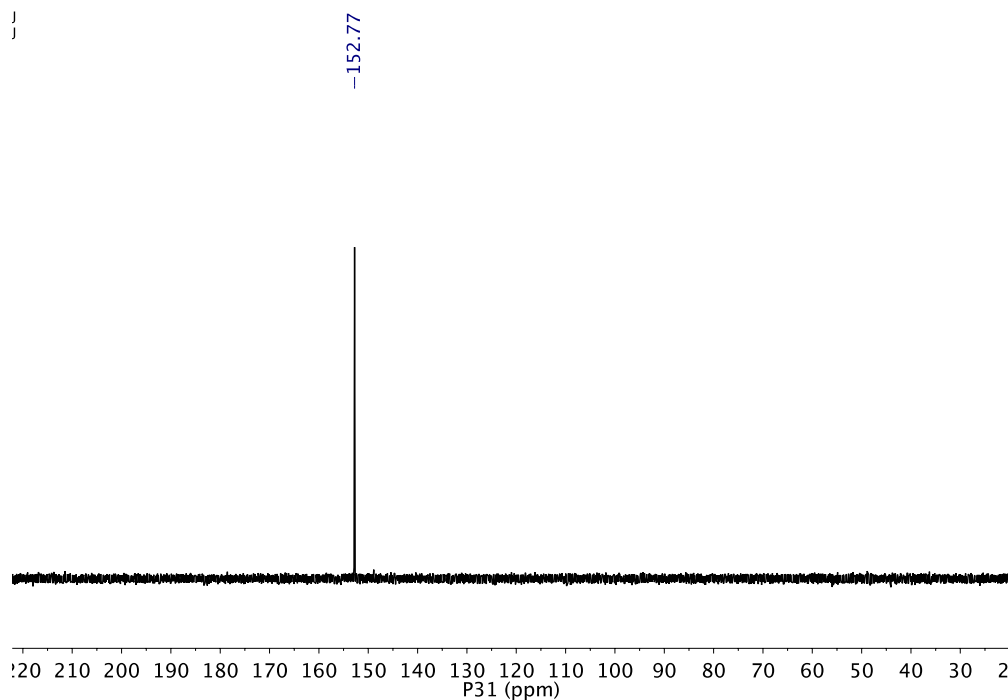
Figure 3.14 ^{31}P{^{1}H} NMR spectrum of [κ^4-(^{15c5}NCOP^{iPr})Ir(H)(CO)][BAr$^F_4$] (**2**) in CD$_2$Cl$_2$.

Synthesis of [κ³-(¹⁵c⁵NCOP^{iPr})Ir(H)(CO)₂][BAr^F₄] (3). A sample of **2** was dissolved in CDCl₃ and transferred to a Teflon-capped NMR tube. The tube was freeze-pump-thaw degassed three times, and 1 atm CO was added at room temperature. After 30 min, an equilibrium mixture of **2** and **3** was apparent by NMR spectroscopy. Backfilling again with CO saw further conversion to 87%. Complex **3** is stable only under a CO atmosphere, so this product was not isolated. ^{1}H NMR (600 MHz, CDCl₃): δ −9.42 (d, J = 20.8 Hz, 1H, Ir–H), 1.07−1.14 (m, 6H, CH(CH_3)₂), 1.15−1.26 (m, 6H, CH(CH_3)₂), 2.52 (m, 2H, CH(CH₃)₂, 3.56−3.82 (m, 14H, crown-CH_2), 3.83−3.92 (m, 2H, crown-CH_2), 4.03 (m, 1H, crown-CH_2), 4.21 (m, 1H, crown-CH_2), 4.46 (d, J = 14.7 Hz, 1H, ArCHHN), 4.59 (dd, J = 14.7, 3.43 Hz, 1H, ArCHHN), 6.85 (d, J = 8.2 Hz, 1H, Ar–H) 6.99 (d, J = 7.0 Hz, 1H, Ar–H), 7.08 (m, 1H, Ar–H). ^{13}C{^{1}H} NMR (151 MHz, CDCl₃): δ 16.45 (s, CH(CH₃)₂), 16.61 (s, CH(CH₃)₂), 17.29 (d, J = 2.6 Hz, CH(CH₃)₂), 17.43 (d, J = 3.4 Hz, CH(CH₃)₂), 30.64 (d, J = 42.1 Hz, CH(CH₃)₂), 33.88 (d, J = 34.8 Hz, CH(CH₃)₂), 67.14 (s, crown-CH₂), 67.55 (s, crown-CH₂), 67.71 (s, crown-CH₂), 69.76 (s, crown-CH₂), 69.89 (s, crown-CH₂), 70.07 (s, crown-CH₂), 70.27 (s, crown-CH₂), 70.48 (s, crown-CH₂), 70.48 (s, crown-CH₂), 70.55 (s, crown-CH₂), 70.95 (s, ArCH₂N), 111.02 (d, J = 12.3 Hz, C_{Ar}), 117.44 (p, J = 11.7 Hz, p-CH, BAr^F), 119.3 (s, C_{Ar}), 124.52 (q, J = 272.5 Hz, CF₃, BAr^F), 128.7 (s, C_{Ar}), 128.76 (qdd, J = 31.5, 5.9, 2.9 Hz, C–CF₃, BAr^F), 129.87 (d, J = 4.0 Hz, C_{Ar}), 134.76 (s, o-CH, BAr^F), 145.37 (d, J = 2.0 Hz, C_{Ar}), 161.13 (s, C_{Ar}), 161.54 (dd, J = 100.7, 48.67 Hz, B–C, BAr^F), 168.51 (d, J = 2.9 Hz, $trans$-CO), 169.81 (s, cis-CO). ^{31}P{^{1}H} NMR (243 MHz, C₆D₅Cl): δ 152.80. IR (CH₂Cl₂): ν_{CO} 2099, 2062 cm^{-1}.
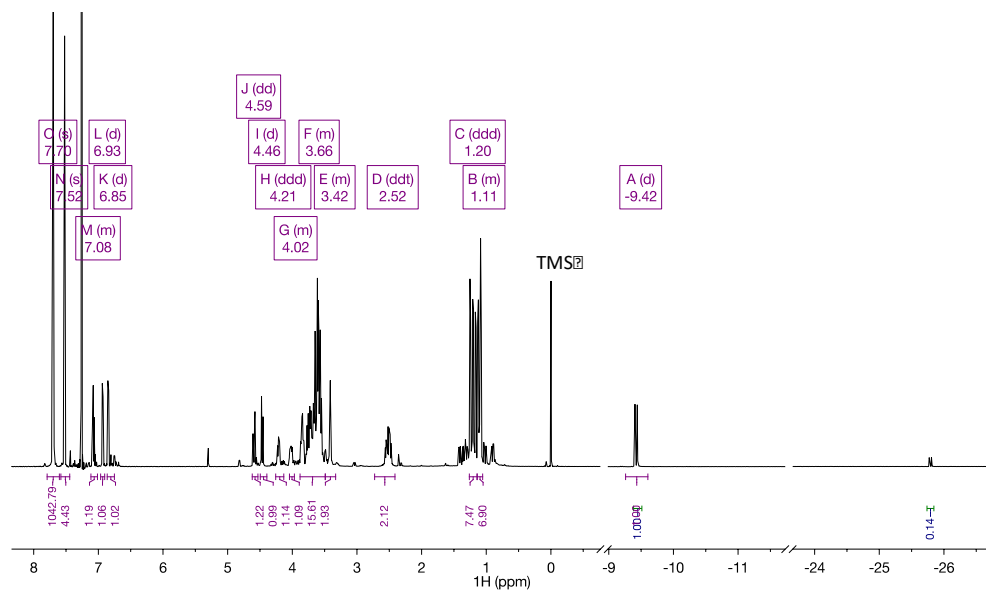
Figure 3.15 ^{1}H NMR spectrum of [κ^3-(^{15c5}NCOP^{iPr})Ir(H)(CO)$_2$][BAr$^F_4$] (**3**) in CDCl$_3$. Equilibrium formation of trace amounts of κ^4-[(^{15c5}NCOP^{iPr})Ir(H)(CO)][BAr$^F_4$] (**2**) is observed.
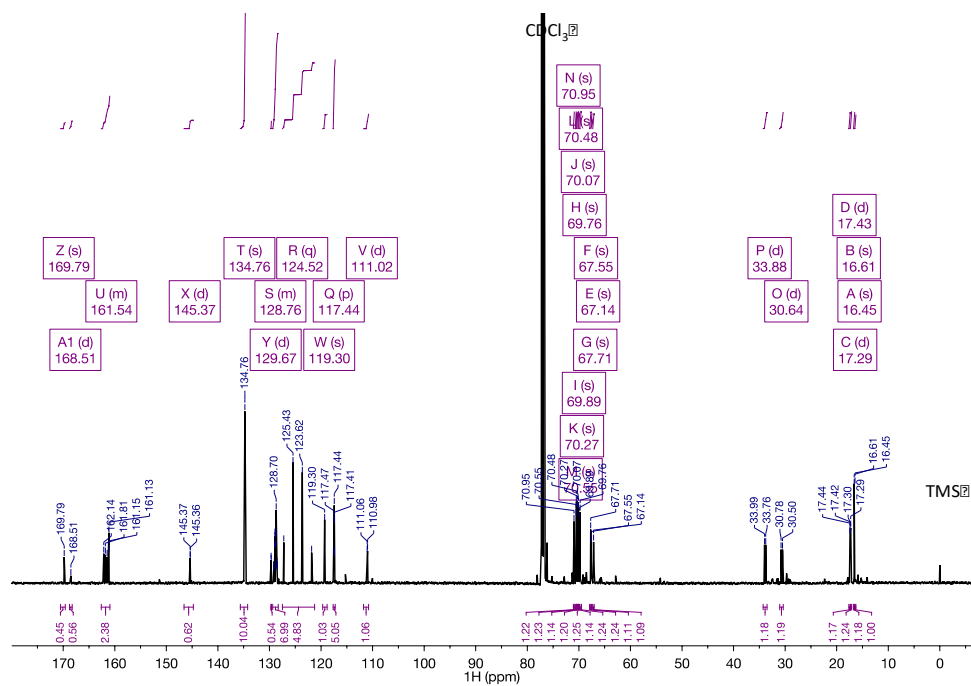
Figure 3.16 ^{13}C{H} NMR spectrum of [κ^3-(^{15c5}NCOP^{iPr})Ir(H)(CO)$_2$][BAr$^F_4$] (**3**) in CDCl$_3$. Equilibrium formation of trace amounts of κ^4-[(^{15c5}NCOP^{iPr})Ir(H)(CO)][BAr$^F_4$] (**2**) is observed.
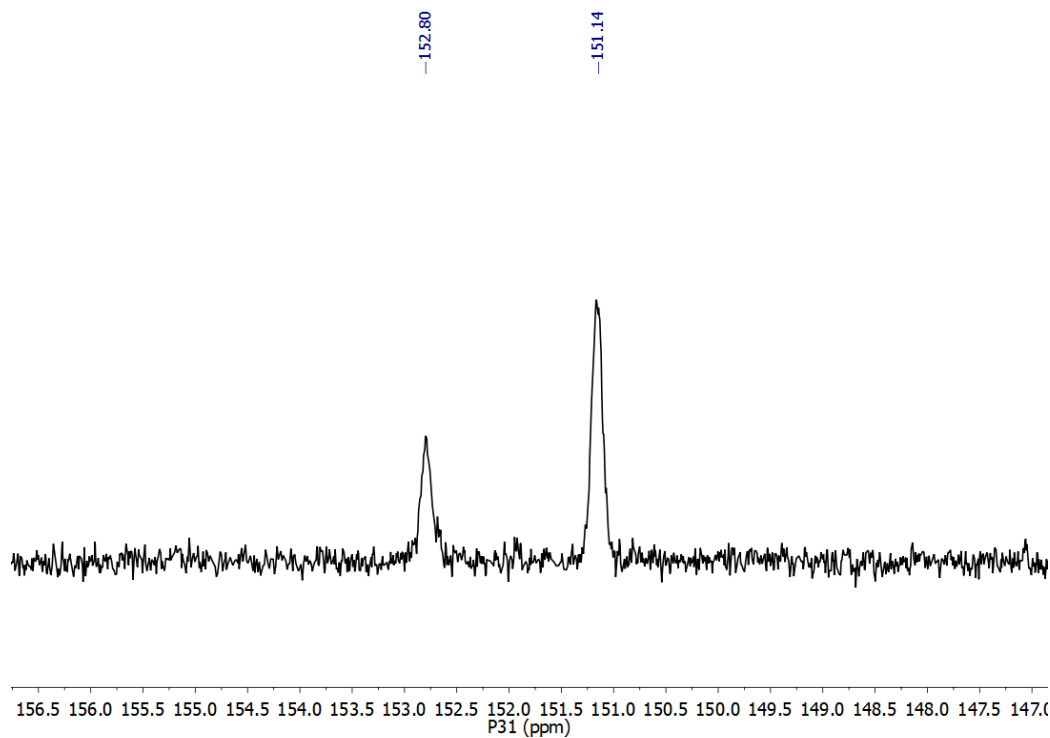
Figure 3.17 ^{31}P{^{1}H} NMR spectrum of [κ^3-(^{15c5}NCOP^{iPr})Ir(H)(CO)$_2$][BAr$^F_4$] (**3**) in C$_6$D$_5$Cl (δ 152.80). κ^4-[(^{15c5}NCOP^{iPr})Ir(H)(CO)][BAr$^F_4$] (**2**) also observed (δ 151.14).

Synthesis of [κ^4-($^{MeO-15c5}$NCOP^{iPr})Ir(H)(CO)][BAr$^F_4$] (5). A 20-mL scintillation vial was

charged with κ^3-($^{MeO-15c5}$NCOP^{iPr})Ir(H)(CO)(Cl) (0.3375 g, 0.4641 mmol), NaBAr$^F_4$ (0.4523

g, 0.5104 mmol), and CH$_2$Cl$_2$ (18 mL). The resulting yellow slurry was stirred for 17 h. The

mixture was filtered, and the amber-yellow filtrate was concentrated to ~1 mL under vacuum.

Pentane (10 mL) was added, and the solvent was removed under vacuum, affording **5** as a

yellow solid (0.4941 g, 68% yield). ^{1}H NMR (600 MHz, CD$_2$Cl$_2$): δ −25.65 (d, J = 21.4 Hz,

1H, Ir–*H*), 0.93 (dd, J = 16.7, 6.9 Hz, 3H, CH(C*H*$_3$)$_2$), 1.06 (dd, J = 20.8, 6.9 Hz, 3H,

CH(C*H*$_3$)$_2$), 1.44 (ddd, J = 26.4, 16.8, 7.2 Hz, 6H, CH(C*H*$_3$)$_2$), 2.48 – 2.67 (overlapping m,

2H, C*H*(CH$_3$)$_2$), 3.04 (dd, J = 14.0, 4.1 Hz, 1H, crown-C*H*$_2$), 3.46 – 4.34 (m, 22H,

overlapping crown-C*H*$_2$ and O–C*H*$_3$), 4.56 (overlapping m, 2H, ArC*H*$_2$N), 6.68 (d, J = 8.2

Hz, 1H, Ar–*H*), 6.79 (d, J = 8.2 Hz, 1H, Ar–*H*), 7.56 (s, 4H s, 4H, *p*-B-Ar-*H*), 7.72 (p, J =

2.2 Hz, 8H *o*-B-Ar-*H*). $^{31}P\{^1H\}$ NMR (162 MHz, CD$_2$Cl$_2$): δ 152.81. IR (solid): ν_{CO} = 2047

cm^{-1}.
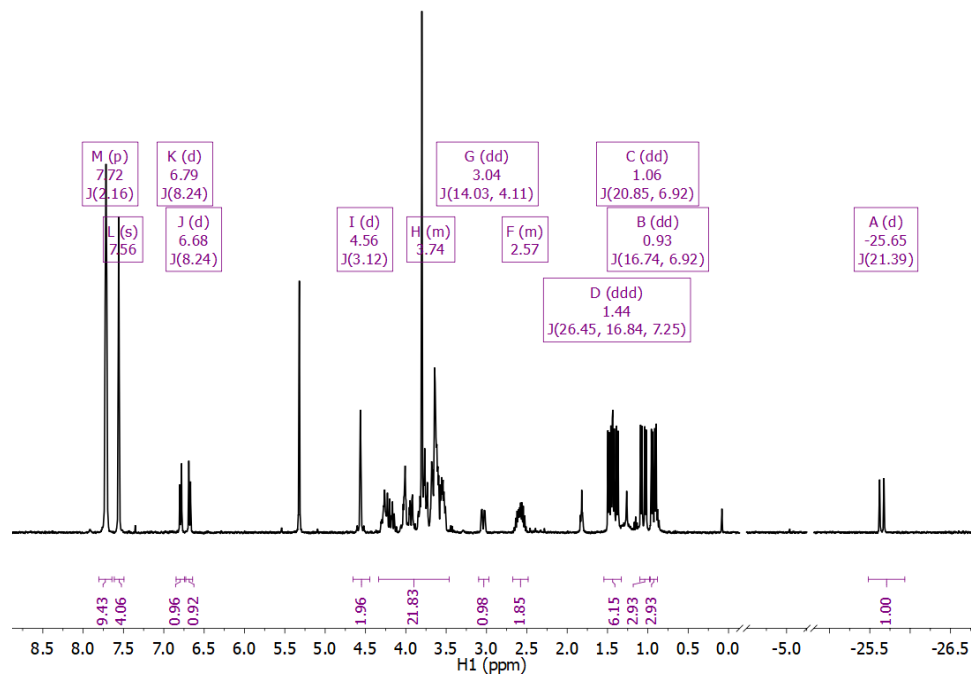
Figure 3.18 ^1H NMR spectrum of [κ^4-($^{MeO-15c5}$NCOP^{iPr})Ir(H)(CO)][BAr$^F_4$] (**5**) in CD$_2$Cl$_2$.

Figure 3.19 $^{31}P\{^1H\}$ NMR spectrum of $[\kappa^4\text{-}(^{MeO\text{-}15c5}NCOP^{iPr})Ir(H)(CO)][BAr^F_4]$ (**5**) in CD_2Cl_2.

Synthesis of $\kappa^4\text{-}(^{15c5}NCOP^{iPr})Rh(H)(Cl)$ (6). $[Rh(COE)_2Cl]_2$ (0.1151 g, 0.1604 mmol) was dissolved in 5 mL toluene. $(^{15c5}NCOP^{iPr})H$ (0.1434 g, 0.3248 mmol) was dissolved in 5 mL toluene in a separate vial. The $(^{15c5}NCOP^{iPr})H$ solution was added to the orange solution of rhodium dimer. The resulting solution turned light yellow over the course of several minutes. After stirring at room temperature for 15 h, the solvent was reduced to ~1 mL under vacuum. The product precipitated as an off-white solid upon addition of pentane (5 mL). The yellow supernatant was decanted and the off-white solid was further washed with 3 mL pentane and dried under vacuum (0.1393 g, 75% yield). ^1H NMR (600 MHz, CD_2Cl_2): δ −22.90 (dd, $J =$ 36.2, 27.0 Hz, 1H, Rh–*H*), 1.00 (dd, $J =$ 16.0, 6.9 Hz, 3H, CH(C*H$_3$*)$_2$), 1.23 (dd, $J =$ 19.0, 7.0 Hz, 3H, CH(C*H$_3$*)$_2$), 1.38 (dd, $J =$ 13.9, 7.0 Hz, 3H, CH(C*H$_3$*)$_2$), 1.45 (dd, $J =$ 16.4, 7.4 Hz, 3H, CH(C*H$_3$*)$_2$), 2.38 (dhd, $J =$ 13.8, 7.7, 6.9, 1.5 Hz, 1H, C*H*(CH$_3$)$_2$), 2.58 (dhept, $J =$ 9.4, 7.3 Hz, 1H, C*H*(CH$_3$)$_2$), 2.94–3.01 (m, 1H, crown-C*H$_2$*), 3.17 (dd, $J =$ 15.1, 3.6 Hz, 1H,

crown-C*H*$_2$), 3.35 (ddd, *J* = 11.1, 3.3, 1.3 Hz, 1H, crown-C*H*$_2$), 3.44 (ddd, *J* = 10.5, 7.0, 1.4

Hz, 1H, crown-C*H*$_2$), 3.50 (ddd, *J* = 12.0, 6.9, 1.3 Hz, 1H, crown-C*H*$_2$), 3.58–3.81 (m, 10H,

crown-C*H*$_2$), 3.98–4.06 (m, 2H, crown-C*H*$_2$), 4.15–4.21 (m, 2H, overlapping ArC*H*HN and

crown-C*H*$_2$), 4.42 (d, *J* = 15.7 Hz, 1H, ArCH*H*N), 4.66 (dd, *J* = 15.2, 10.8 Hz, 1H, crown-

C*H*$_2$), 4.84–4.94 (m, 1H, crown-C*H*$_2$), 6.51 (d, *J* = 7.8 Hz, 1H, Ar–*H*), 6.57 (d, *J* = 7.5 Hz,

1H, Ar–*H*), 6.77 (t, *J* = 7.7 Hz, 1H, Ar–*H*). ^{13}C{^{1}H} NMR (151 MHz, CD$_2$Cl$_2$): δ 16.62 (d, *J*

= 2.7 Hz, CH(*C*H$_3$)$_2$), 17.11 (d, *J* = 2.9 Hz, CH(*C*H$_3$)$_2$), 17.42 (d, *J* = 8.0 Hz, CH(*C*H$_3$)$_2$),

18.00 (s, CH(*C*H$_3$)$_2$, 28.81 (dd, *J* = 31.5, 3.7 Hz, *C*H(CH$_3$)$_2$), 31.30 (d, *J* = 23.6 Hz,

*C*H(CH$_3$)$_2$), 63.01 (d, *J* = 2.7 Hz, crown-*C*H$_2$), 63.63 (s, crown-*C*H$_2$), 67.35 (d, *J* = 2.3 Hz,

crown-*C*H$_2$), 69.51 (s, crown-*C*H$_2$), 69.86 (s, crown-*C*H$_2$), 70.68 (s, Ar*C*H$_2$N), 70.76 (s,

crown-*C*H$_2$), 70.96 (s, crown-*C*H$_2$), 72.22 (s, crown-*C*H$_2$), 72.89 (s, crown-*C*H$_2$), 75.26 (s,

crown-*C*H$_2$), 108.18 (d, *J* = 12.9 Hz, *C*$_{Ar}$), 114.48 (s, *C*$_{Ar}$), 124.00 (s, *C*$_{Ar}$), 148.44 (dd, *J* =

30.8, 7.0 Hz, *C*$_{Ar}$), 150.61 (s, *C*$_{Ar}$), 163.21 (dd, *J* = 5.3, 1.9 Hz, *C*$_{Ar}$). ^{31}P{^{1}H} NMR (243

MHz, CD$_2$Cl$_2$): δ 197.80 (d, *J* = 167.0 Hz).
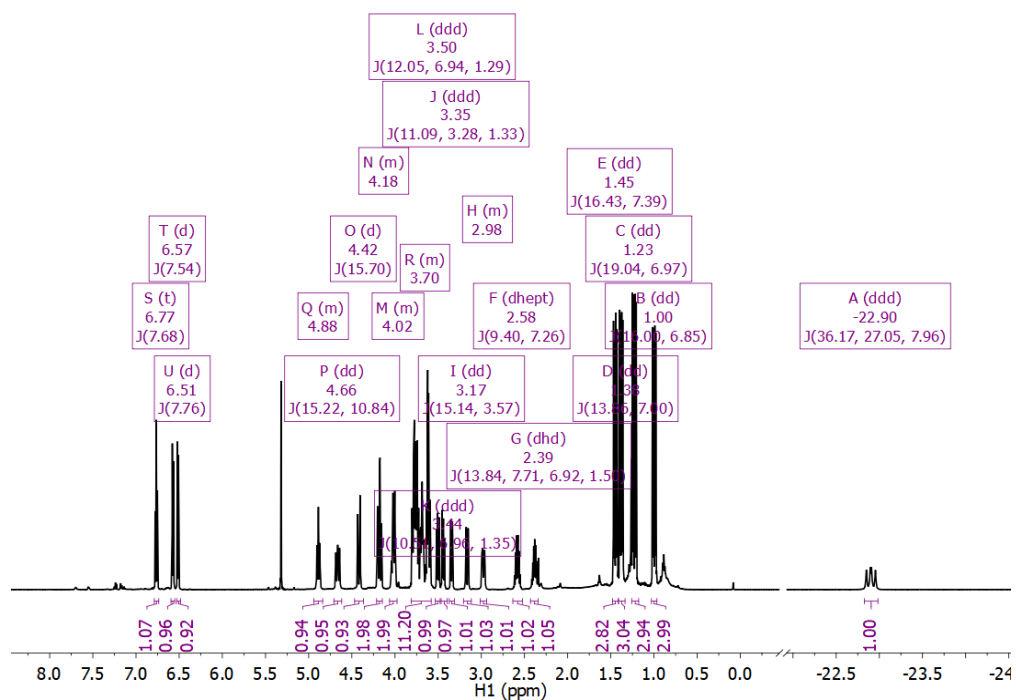
Figure 3.20 ^{1}H NMR spectrum of κ^4-(^{15c5}NCOP^{iPr})Rh(H)(Cl) (**6**) in CD$_2$Cl$_2$.
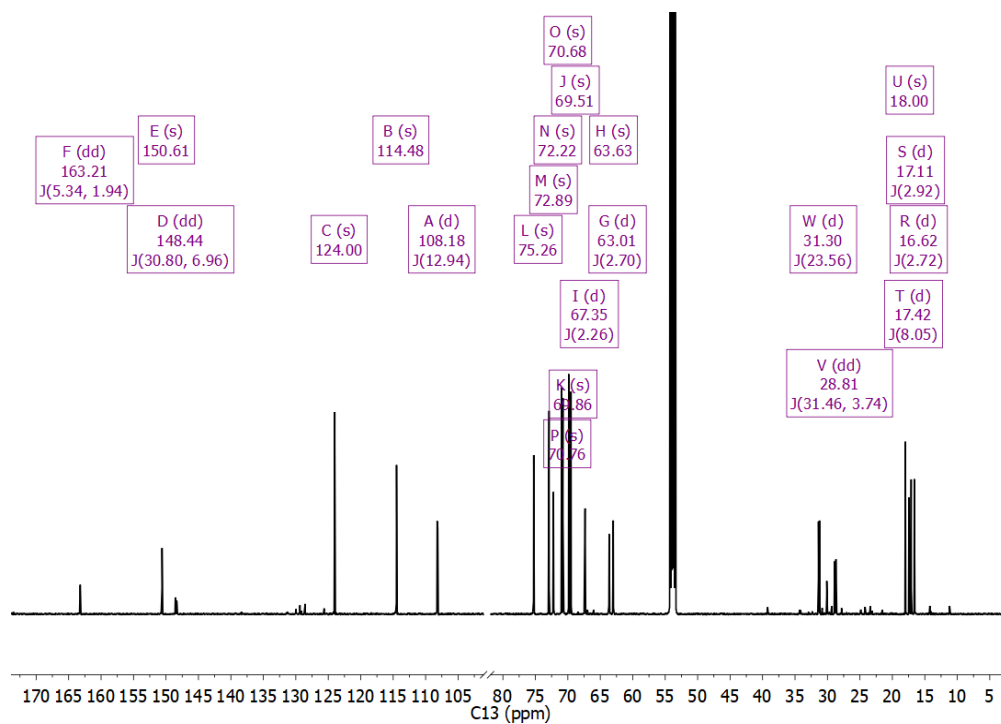
Figure 3.21 ^{13}C{^{1}H} NMR spectrum of κ^4-(^{15c5}NCOP^{iPr})Rh(H)(Cl) (**6**) in CD$_2$Cl$_2$.

124
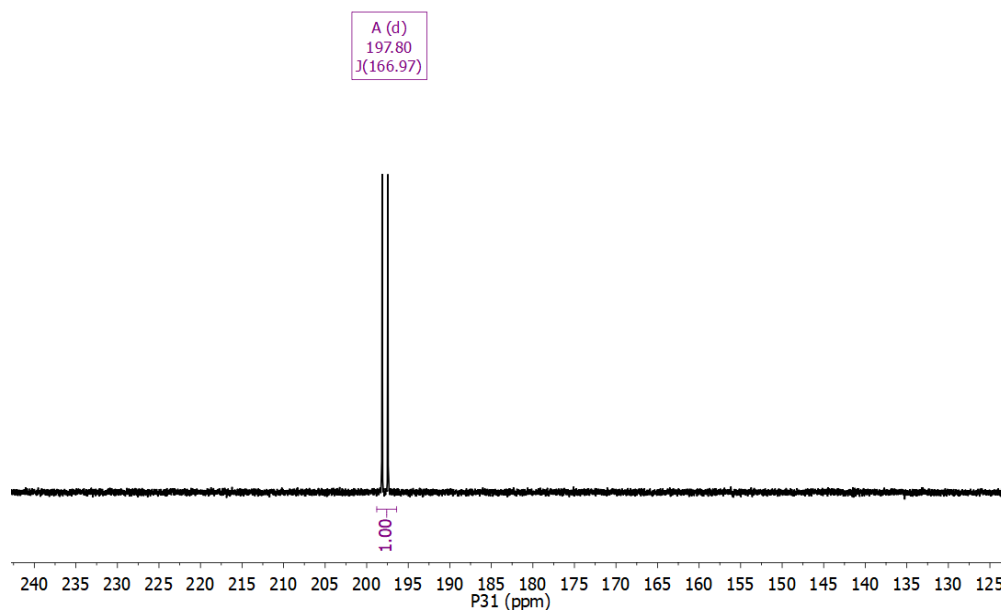
Figure 3.22 $^{31}P\{^{1}H\}$ NMR spectrum of κ^4-(^{15c5}NCOP^{iPr})Rh(H)(Cl) (**6**) in CD$_2$Cl$_2$.

Synthesis of [κ^5-(^{15c5}NCOP^{iPr})Rh(H)][BAr$^F_4$] (7). A scintillation vial was charged with

0.0200 g (0.0345 mmol) of **6** and 0.0309 g (0.0349 mmol) of NaBAr$^F_4$. CH$_2$Cl$_2$ (5 mL) was

added and the resulting slurry was allowed to stir for 18 h. The mixture was filtered and the

volume of the pale yellow filtrate was reduced to ~1 mL under vacuum. Pentane (5 mL) was

added and the solvent was pumped down under vacuum with vigorous stirring, yielding **7** as

a white solid (0.0465 g, 96% yield). ^{1}H NMR (600 MHz, CD$_2$Cl$_2$): δ −21.59 (dd, J = 34.7,

28.3 Hz, 1H, Rh–*H*), 1.10 – 1.19 (m, 6H, CH(C*H*$_3$)$_2$), 1.23 – 1.29 (m, 3H, CH(C*H*$_3$)$_2$), 1.35

(dd, J = 14.5, 7.1 Hz, 3H, CH(C*H*$_3$)$_2$), 2.41 (dh, J = 14.3, 7.0 Hz, 2H, C*H*(CH$_3$)$_2$), 3.05 (dq, J

= 14.2, 3.4 Hz, 1H, crown-C*H*$_2$), 3.30 (dt, J = 13.6, 4.1 Hz, 1H, crown-C*H*$_2$), 3.41 (ddd, J =

14.7, 11.0, 4.0 Hz, 1H, crown-C*H*$_2$), 3.49 (dt, J = 11.0, 3.8 Hz, 1H, crown-C*H*$_2$), 3.55 – 3.72

(m, 4H, crown-C*H*$_2$), 3.80 (dddd, J = 16.7, 13.8, 8.5, 2.8 Hz, 4H, crown-C*H*$_2$), 3.87 – 4.19

(m, 8H, overlapping ArC*H*HN and crown-C*H*$_2$), 4.24 (ddd, J = 12.5, 8.5, 4.0 Hz, 1H, crown-

CH$_2$), 4.31 (d, J = 16.0 Hz, 1H, ArCHHN), 6.60 (d, J = 7.9 Hz, 1H, Ar–H), 6.64 (d, J = 7.6 Hz, 1H, Ar–H), 6.90 (t, J = 7.8 Hz, 1H, Ar–H), 7.57 (s, 4H, p-B-Ar-H), 7.73 (dt, J = 4.7, 2.2 Hz, 8H, o-B-Ar-H). ^{13}C{^{1}H} NMR (151 MHz, CD$_2$Cl$_2$): δ 16.29 (s, CH(CH$_3$)$_2$), 16.34 (d, J = 2.0 Hz, CH(CH$_3$)$_2$), 16.82 (s, CH(CH$_3$)$_2$), 18.10 (s, CH(CH$_3$)$_2$), 28.28 (dd, J = 34.1, 2.9 Hz, CH(CH$_3$)$_2$)), 31.05 (d, J = 24.5 Hz, CH(CH$_3$)$_2$), 59.72 (s, crown-CH$_2$), 61.63 (d, J = 2.5 Hz, crown-CH$_2$), 65.80, 67.51 (s, crown-CH$_2$), 67.59 (s, crown-CH$_2$), 70.36 (s, crown-CH$_2$), 71.25 (s, crown-CH$_2$), 72.00 (s, crown-CH$_2$), 72.87 (s, crown-CH$_2$), 73.48 (s, crown-CH$_2$), 76.98 (s, crown-CH$_2$), 109.97 (d, J = 12.4 Hz, C$_{Ar}$), 117.14 (s, C$_{Ar}$), 117.89 (p, J = 4.1 Hz, p-CH, BAr^F), 125.02 (q, J = 272.4 Hz, CF$_3$, BAr^F), 125.88 (s, C$_{Ar}$), 129.28 (qdd, J = 31.6, 5.9, 2.8 Hz, C–CF$_3$, BAr^F), 135.22 (s, o-CH, BAr^F), 136.03 – 136.55 (m, C$_{Ar}$), 147.45 (s, C$_{Ar}$), 162.16 (dd, J = 99.8, 49.9 Hz, B–C, BAr^F), 163.28 (s, C$_{Ar}$). ^{31}P{^{1}H} NMR (243 MHz, CD$_2$Cl$_2$): δ 192.67 (d, J = 163.8 Hz).
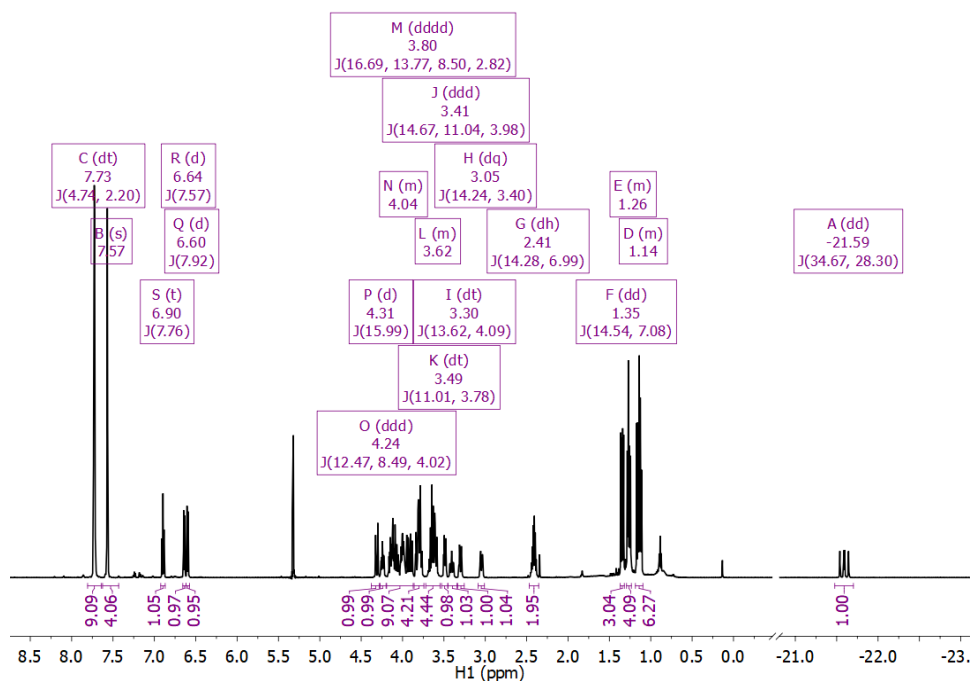
Figure 3.23 ^{1}H NMR spectrum of [κ^5-(^{15c5}NCOP^{iPr})Rh(H)][BAr$^F_4$] (**7**) in CD$_2$Cl$_2$.
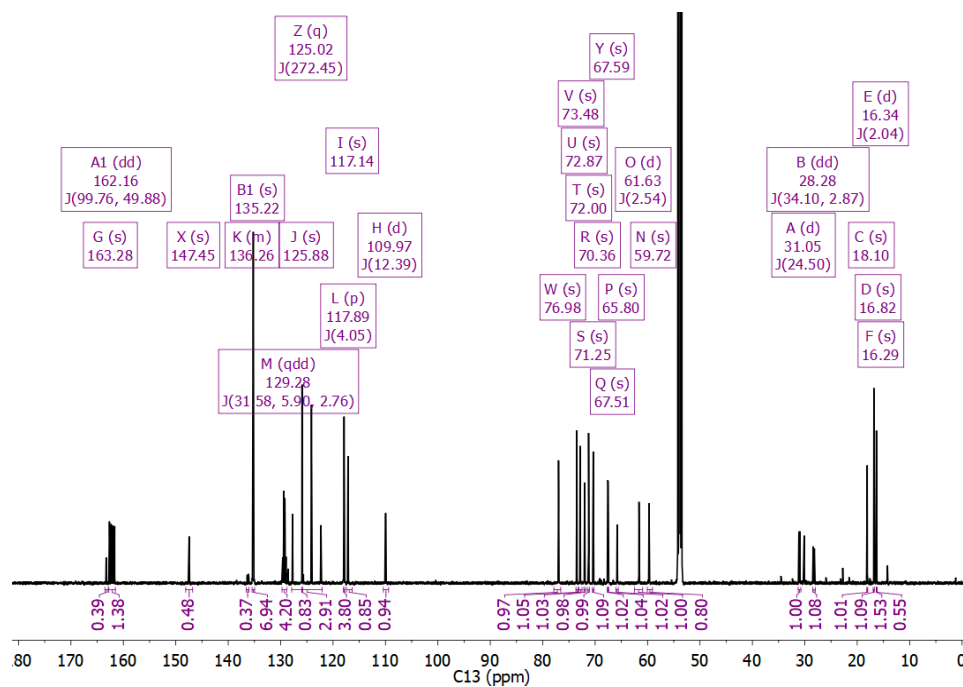
Figure 3.24 $^{13}C\{^1H\}$ NMR spectrum of $[\kappa^5\text{-}(^{15c5}NCOP^{iPr})Rh(H)][BAr^F_4]$ (**7**) in CD_2Cl_2.
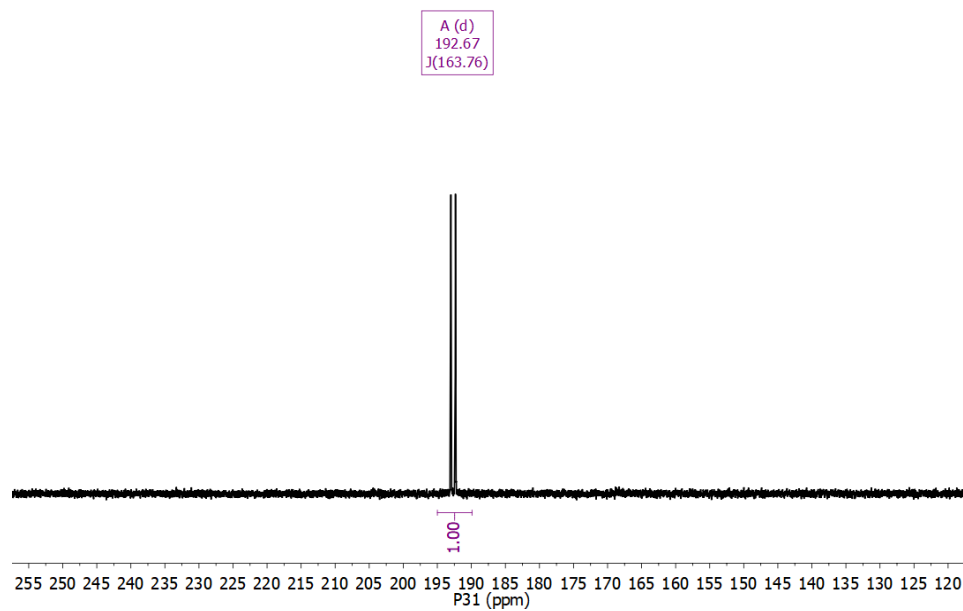
Figure 3.25 $^{31}P\{^1H\}$ NMR spectrum of $[\kappa^5\text{-}(^{15c5}NCOP^{iPr})Rh(H)][BAr^F_4]$ (**7**) in CD_2Cl_2.

Synthesis of κ⁴-(^(MeO-15c5)NCOP^(iPr))Rh(H)(Cl) (8). [Rh(COE)$_2$Cl]$_2$ (0.0711 g, 0.0991 mmol) was dissolved in 5 mL toluene. (^(MeO-15c5)NCOP^(iPr))H (0.0935 g, 0.198 mmol) was dissolved in 5 mL toluene in a separate vial. The (^(MeO-15c5)NCOP^(iPr))H solution was added to the orange solution of rhodium dimer. The solution turned light yellow over the course of several minutes. After stirring at room temperature for 15 h, the solvent was reduced to ~1 mL under vacuum. The product precipitated as a white solid upon addition of pentane (5 mL). The yellow supernatant was decanted. The white solid was further washed with 3 mL pentane and dried under vacuum (0.0558 g, 46% yield). ^{1}H NMR (500 MHz, toluene-d_8): δ −22.60 (m, 1H), 1.07 (dt, J = 16.1, 8.5 Hz, 3H), 1.19 − 1.37 (m, 6H), 1.42 (dd, J = 16.4, 7.4 Hz, 3H), 2.14 − 2.28 (m, 1H), 2.50 (m, 1H), 2.72 − 2.91 (m, 2H), 3.04 (dd, J = 22.0, 10.5 Hz, 2H), 3.12 − 4.09 (m, 18H), 4.77 (d, J = 13.7 Hz, 1H), 5.10 − 5.30 (m, 1H), 6.40 (m, 2H). ^{31}P{^{1}H} NMR (202 MHz, toluene-d_8) δ 198.27 (d, J = 167.9 Hz).
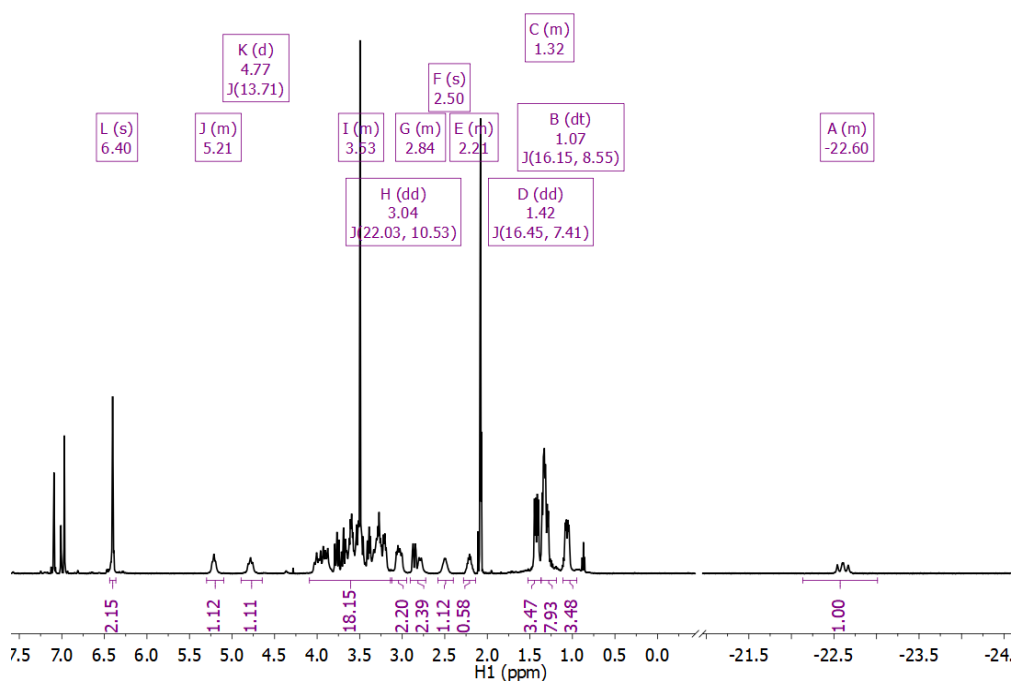
Figure 3.26 ^{1}H NMR spectrum of κ⁴-(^(MeO-15c5)NCOP^(iPr))Rh(H)(Cl) (**8**) in toluene-d_8.
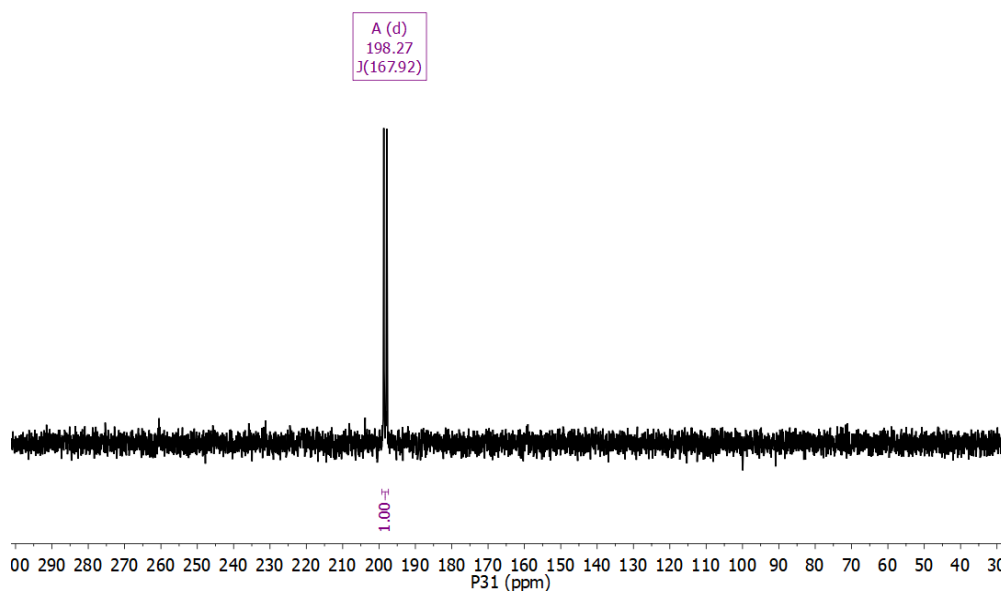
Figure 3.27 ^{31}P{^{1}H} NMR spectrum of κ^4-($^{\text{MeO-15c5}}$NCOP$^{\text{iPr}}$)Rh(H)(Cl) (**8**) in toluene-d_8.

Synthesis of [κ^5-($^{\text{MeO-15c5}}$NCOP$^{\text{iPr}}$)Rh(H)][BAr$^{\text{F}}_4$] (9). A scintillation vial was charged with

0.0208 g (0.0341 mmol) of **8** and 0.0320 g (0.0361 mmol) of NaBAr$^{\text{F}}_4$. CH$_2$Cl$_2$ (5 mL) was

added and the resulting slurry was allowed to stir for 18 h. The mixture was filtered and the

volume of the light pink filtrate was reduced to ~1 mL under vacuum. Pentane (5 mL) was

added and the solvent was pumped down under vacuum with vigorous stirring, yielding **9** as

a light pink solid in quantitative yield.^{1}H NMR (600 MHz, toluene-d_8) δ −22.03 (dd, $J =$

35.1, 28.3 Hz, 1H), 0.64 (dd, $J =$ 19.8, 7.1 Hz, 3H), 0.79 (dd, $J =$ 16.6, 6.8 Hz, 3H), 0.95

(ddd, $J =$ 22.7, 15.3, 7.1 Hz, 6H), 1.81 – 1.91 (m, 2H), 1.98 – 2.03 (m, 1H), 2.33 – 2.49 (m,

3H), 2.66 (ddt, $J =$ 29.9, 12.9, 3.6 Hz, 2H), 2.77 – 2.90 (m, 2H), 2.92 – 3.31 (m, 10H), 3.33 –

3.44 (m, 6H), 3.47 – 3.54 (m, 1H), 6.25 – 6.33 (m, 2H), 7.67 (s, 4H), 8.23 – 8.30 (m, 8H).

^{31}P{^{1}H} NMR (243 MHz, toluene-d_8) δ 193.02 (d, $J =$ 162.8 Hz).
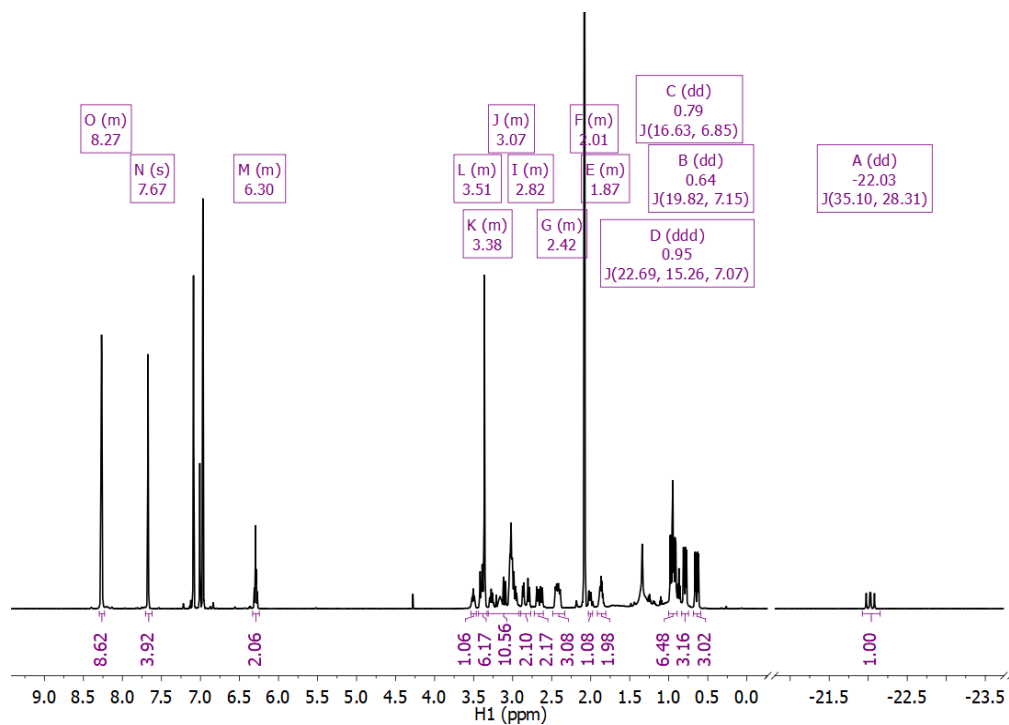
Figure 3.28 ^{1}H NMR spectrum of $[\kappa^5\text{-}(^{\text{MeO-15c5}}\text{NCOP}^{\text{iPr}})\text{Rh(H)}][\text{BAr}^F_4]$ (**9**) in toluene-d_8.
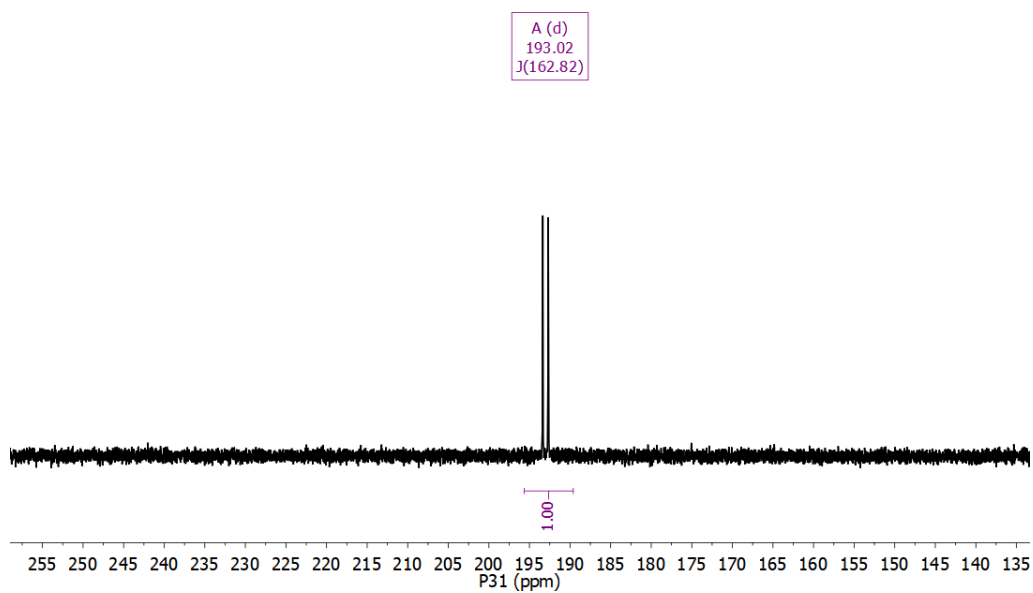
Figure 3.29 ^{31}P{^{1}H} NMR spectrum of $[\kappa^5\text{-}(^{\text{MeO-15c5}}\text{NCOP}^{\text{iPr}})\text{Rh(H)}][\text{BAr}^F_4]$ (**9**) in toluene-d_8.

Synthesis of [κ²-(¹⁵c⁵N(H)COPⁱPʳ)Ir(CO)₂][BArᶠ₄] (10). κ^4-

(¹⁵c⁵NCOPⁱPʳ)Ir(H)(CO)][BArᶠ₄] (**2**) (0.0503 g, 0.0330 mmol) was dissolved in 0.5 mL

C_6D_5Cl and placed in a Teflon-capped NMR tube. The solution was freeze-pump-thaw

degassed three times before being back-filled with CO and set to heat at 90 °C for 22 h.

$^{31}P\{^1H\}$ and ^1H NMR spectroscopy showed almost-complete (>95%) consumption of **2** to

afford **10** as the major species, with minor products observed in the $^{31}P\{^1H\}$ NMR spectrum.

Analytically pure complex was not isolated. Similar reactivity was observed in the presence

of 9:1 mixtures of CO:H₂. ^1H NMR (500 MHz, C_6D_5Cl): δ 0.86 (d, J = 7.1 Hz, 3H,

CH(CH_3)₂), 0.89 – 0.97 (m, 9H, CH(CH_3)₂), 1.95 (hept, J = 6.8 Hz, 2H, CH(CH₃)₂), 2.18 (dq,

J = 11.8, 3.7, 2.8 Hz, 2H, crown-CH_2), 2.67 (ddd, J = 12.3, 8.0, 3.7 Hz, 2H, crown-CH_2),

2.97 – 3.44 (m, 16H, crown-CH_2), 3.80 (s, 2H, ArCH_2N), 6.39 (dd, J = 7.6, 1.9 Hz, 1H, Ar–

H), 6.81 (d, J = 1.9 Hz, 1H, Ar–H), 7.60 (s, 4H, p-B-Ar-H), 7.79 (d, J = 7.5 Hz, 1H, Ar–H),

8.23 (dt, J = 4.9, 2.2 Hz, 8H, o-B-Ar-H). $^{31}P\{^1H\}$ NMR (202 MHz, C_6D_5Cl): δ 174.83. IR

(solid): v_{CO} = 1989 and 2051 cm⁻¹.
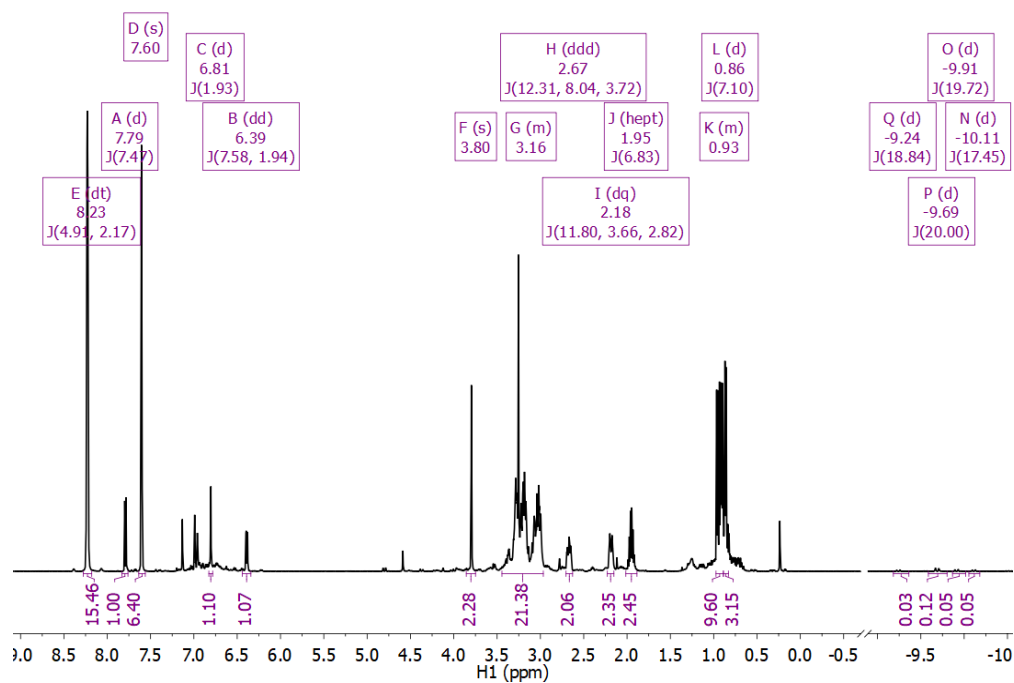
Figure 3.30 ^{1}H NMR spectrum of [κ^2-(^{15c5}N(H)COP^{iPr})Ir(CO)$_2$][BAr$^F_4$] (**10**) in C$_6$D$_5$Cl.
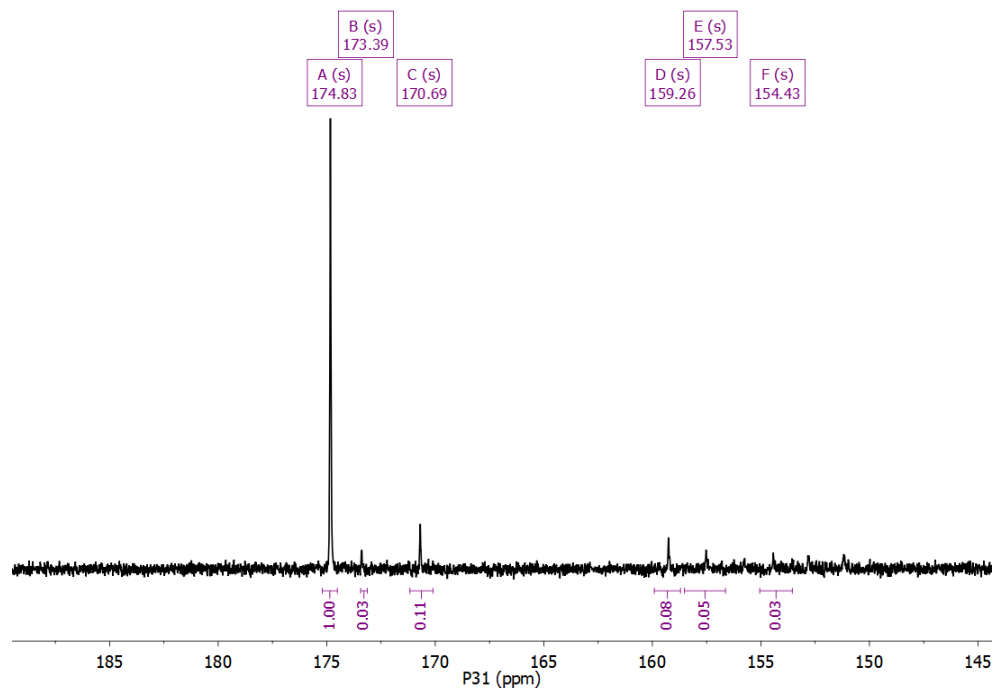
Figure 3.31 ^{31}P{^{1}H} NMR spectrum of [κ^2-(^{15c5}N(H)COP^{iPr})Ir(CO)$_2$][BAr$^F_4$] (**10**) in C$_6$D$_5$Cl.

Iridium Pincer-Crown Ether-Catalyzed Hydroformylation using the Series 5000 Parr Multireactor System. *CAUTION: When working with CO gas, especially under high pressures, the use of CO monitors is recommended.* These experiments were conducted with a personal monitor worn on the researcher's lab coat at all times and an additional monitor located near the syngas cylinder. All catalytic loadings were performed in a glovebox with degassed 1,2-dichloroethane. A stock solution of the desired iridium catalyst was prepared in 1,2-dichloroethane such that 1 mL was added to each reactor (0.0073 mmol/reactor). For example, 0.0797 g [κ^4-($^{MeO-15c5}$NCOP^{iPr})Ir(H)(CO)][BAr$^F_4$] (**5**) was dissolved in 7 mL of 1,2-dichloroethane and 1 mL aliquots of this stock solution were added to each of the six reactors. Next, 2.2 mmol of the corresponding substrate was added, along with the appropriate Lewis acid or ammonium salt. Additional 1,2-dichloroethane (9 mL) was added to each reactor. The reactor and vessel heads were secured in the box under N_2 atmosphere, and the sealed reactors were removed and connected to the multireactor system. The reactor manifold was purged with a 9:1 mixture of CO:H_2 and each vessel was subjected to three pressurization-venting cycles (5-10 bar) to ensure full replacement of the N_2 headspace with CO:H_2. The vessels were then pressurized to 20 bar with the 9:1 mixture of CO:H_2 and the temperature was set utilizing the SpecView 32 software. The $t = 0$ of the reaction was chosen as the time when the reactor vessels reached their set temperature. After the given reaction time, the vessels were cooled in an ice bath before venting the gas slowly. Once vented, 0.025 mL (0.12 mmol) hexamethyldisiloxane (HMDSO) was added directly as NMR standard *via* syringe. The reactor was shaken and a ~500 μL aliquot was removed and placed in an NMR tube fitted with a C_6D_6 capillary. ^{1}H NMR spectra were obtained utilizing a delay

time of 10 seconds per scan. Product yields were determined by integration relative to HMDSO.
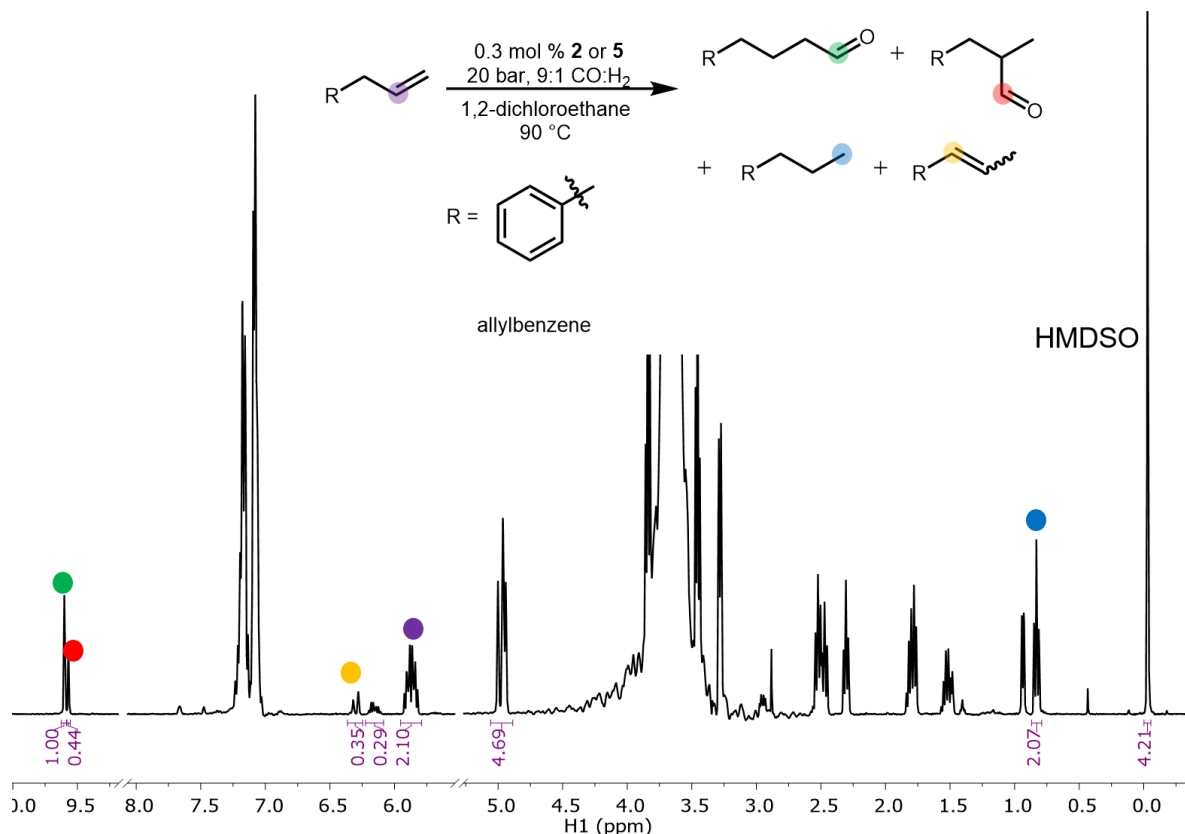
Figure 3.32 Typical ^{1}H NMR spectrum after multireactor catalysis. Conditions: 1,2-dichloroethane solution containing HMDSO internal standard and a C_6D_6 capillary. The product peaks are set to the representative number of protons (1H for each aldehyde product or alkene proton, or 3 H for propylbenzene) and relative integration against HMDSO internal standard is used to calculate the mmol of products:

$$mmol\ products = \frac{mmol\ std.}{\frac{std.integration}{\#\ protons\ std.}} = \frac{0.12}{\frac{4.21}{18}} = 0.51\ mmol\ linear\ aldehyde$$

Studies on the Fate of Iridium Catalysts. Reactors were loaded with allylbenzene (2.2 mmol) and 0.3 mol% of unblocked complex **2**. The reactor was pressurized and heated under standard conditions (20 bar 9:1 H_2:CO; 90 °C, 3 h). After venting, the solution was pumped to dryness under vacuum to afford a yellow oil. In C_6D_5Cl solution, ^{1}H NMR spectroscopy

revealed similar resonances to those of an authentic sample of **10**. A closely-related singlet at

δ 181 was observed $^{31}P\{^{1}H\}$ NMR spectroscopy. Two CO-stretching frequencies (ν_{CO} = 1985 and 2049 cm^{-1}) were observed by solid-state IR spectroscopy, closely matching those observed for authentic complex **10** (ν_{CO} = 1989 and 2051 cm^{-1}).
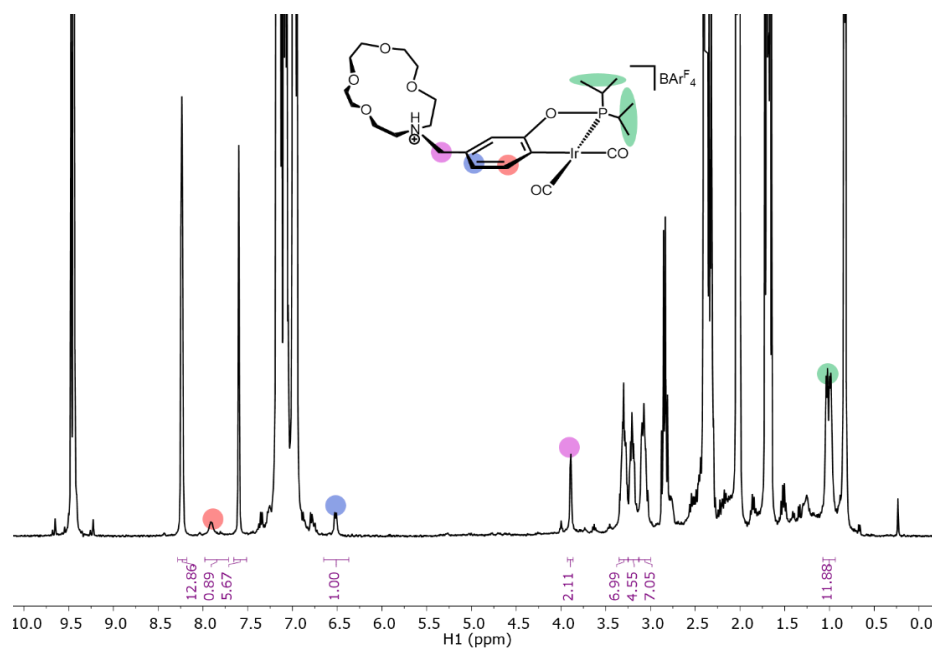
Figure 3.33 ^{1}H NMR spectrum in C$_6$D$_5$Cl acquired after a catalytic allylbenzene hydroformylation run with complex **2** as a catalyst.
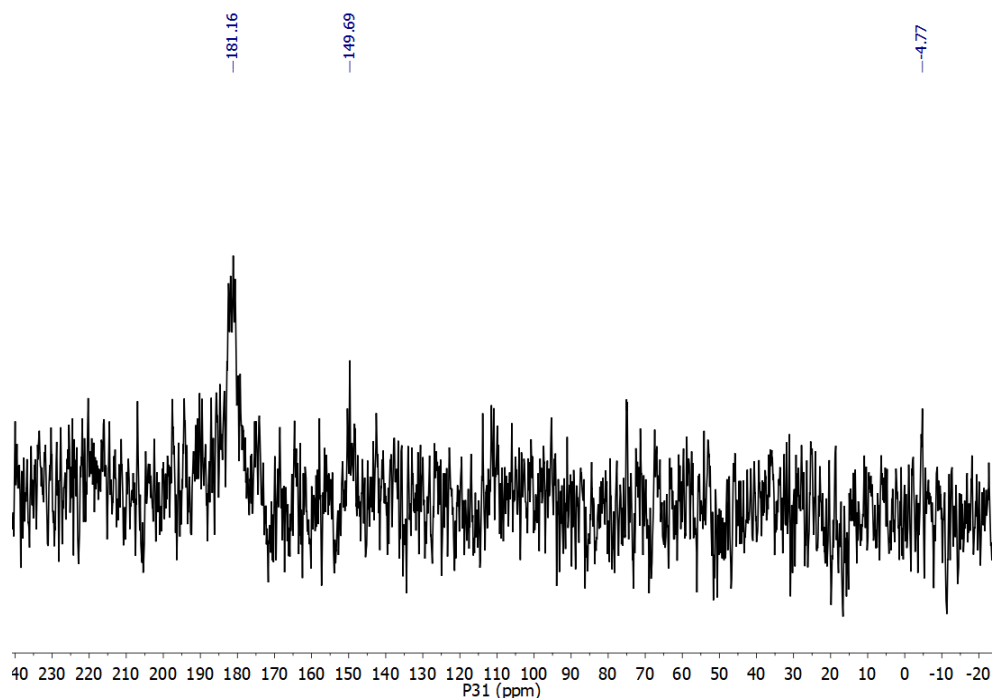
Figure 3.34 ^{31}P{^{1}H} NMR spectrum in C_6D_5Cl acquired after a catalytic allylbenzene hydroformylation run with complex **2** as a catalyst.

A similar experiment was conducted with methoxy-blocked complex **5**. Trace amounts of hydrides were present in the ^{1}H NMR spectrum. One major species was observed in the ^{31}P{^{1}H} NMR spectrum at δ 143. A carbonyl stretching frequency was present in the solid-state IR spectrum at 1954 cm^{-1} (Figure 3.7).
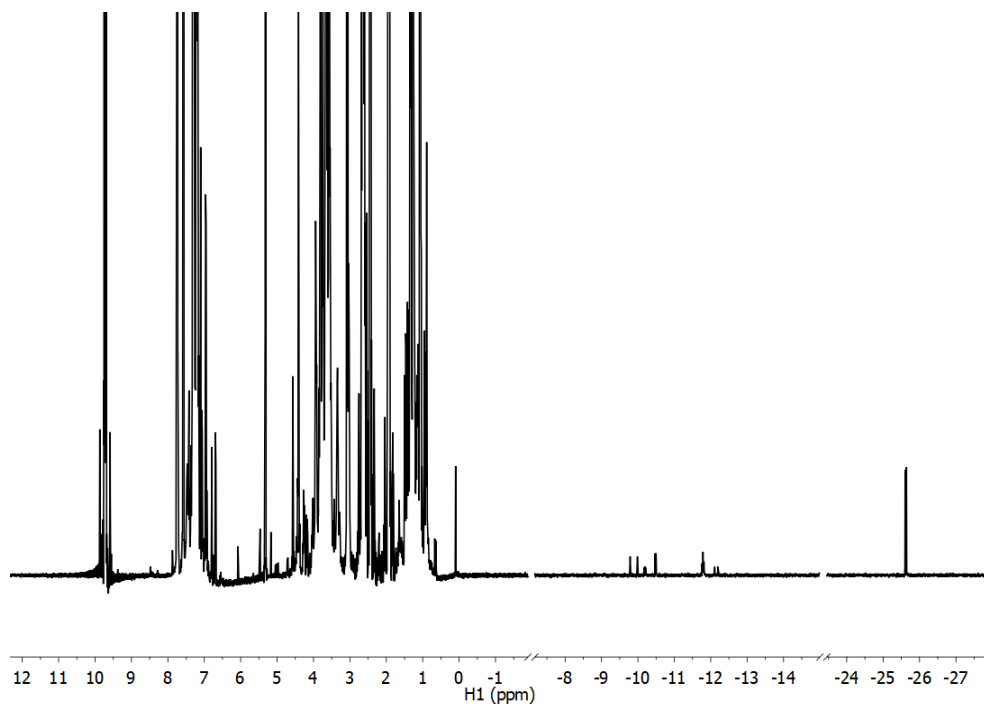
Figure 3.35 ^{1}H NMR spectrum in CD$_2$Cl$_2$ acquired after a catalytic allylbenzene hydroformylation run with complex **5** as a catalyst.
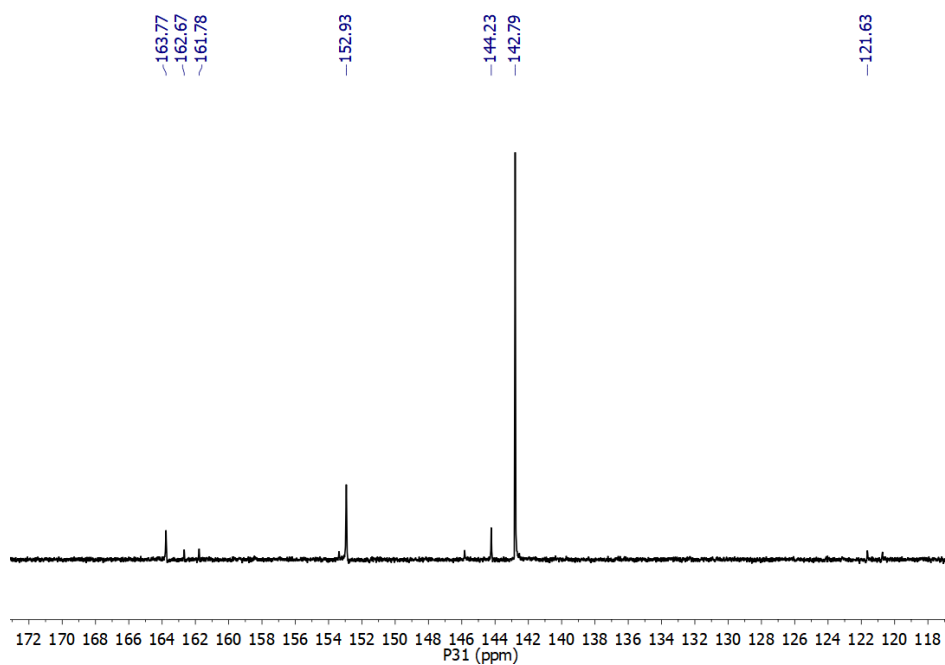
Figure 3.36 ^{31}P{^{1}H} NMR spectrum in CD$_2$Cl$_2$ acquired after a catalytic allylbenzene hydroformylation run with complex **5** as a catalyst.

Rhodium Pincer-Crown Ether-Catalyzed Hydroformylation using the HEL Cat18

Reactor. These experiments were conducted with a personal monitor worn on the researcher's lab coat at all times and a ToxgardII CO detector located near the syngas cylinder. All catalytic loadings were performed in a glovebox with degassed toluene. A stock solution of the desired rhodium catalyst was prepared in toluene such that 0.75 mL was added to a GC vial (0.0024 mmol/vial). For example, 0.0099 g [κ^5-(^{15c5}NCOP^{iPr})Rh(H)][BAr$^F_4$] (**7**) was dissolved in 2.2 mL of toluene and 0.75 mL aliquots of this stock solution were added to two GC vials. Next, 90 μL (0.57 mmol) 1-octene were added, along with the appropriate ammonium salt and NaBAr$^F_4$. The vials were capped with pre-cut septa caps in the box under N_2 atmosphere and placed in the HEL Cat18 reactor. The reactor was sealed and pressurized to 20 bar with a 1:1 mixture of CO:H_2 and the temperature was set to 95 °C using a IKA hot plate. The $t = 0$ of the reaction was chosen as the time when the reactor reached the set temperature. After 1h, the reactor was cooled in an ice bath before venting the gas slowly. Once vented, 0.10 mL aliquots of the resulting solutions were further diluted with 0.90 mL toluene in a new GC vial. A 5 μL aliquot (0.036 mmol) of methylstyrene was added to each dilution vial. The products were then analyzed by GC.
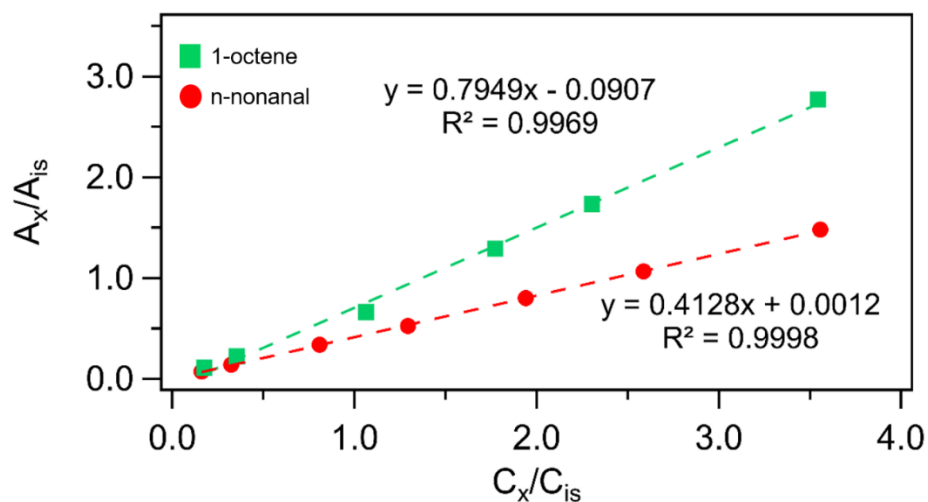
Figure 3.37 GC calibration curves for 1-octene and n-nonanal. A_x is area of analyte and A_{is} is area of mesitylene internal standard. C_x and C_{is} are concentrations of analyte and internal standard, respectively.

Table 3.9 Retention times for GC quantification in rhodium-catalyzed hydroformylation.

Analyte	Retention Time (min)
toluene	18.912
1-octene	21.821
trans-4-octene	22.381
trans-3-octene	22.613
cis-4-octene	22.681
cis-3-octene	22.742
n-octane	22.75
trans-2-octene	23.139
cis-2-octene	23.885
mesitylene	29.314
n-nonanal	31.301
2-Me-octanal	30.778
2-ethyl-heptanal	30.661
3-propyl-hexanal	30.531

Studies on the Fate of Rhodium Catalysts. A sample of 0.0099 g [κ^5-(^{15c5}NCOP^{iPr})Rh(H)][BAr$^F_4$] (**7**) was dissolved in 2.2 mL of toluene-d_8. A 0.75 mL aliquot of this solution was transferred to Teflon-capped NMR tube. To a second 0.75 mL aliquot of the

solution of **7** was added 1-octene (90 μL, 0.57 mmol) and the resulting solution was

transferred to a Teflon-capped NMR tube. ^{1}H and ^{31}P{^{1}H} NMR spectra were acquired

before and after catalytic conditions (20 bar 1:1 CO:H$_2$ and heated at 90 °C for 1 h). After 1

h, the HEL Cat18 reactor was transferred to a glovebox, and the resulting solutions were

transferred to Teflon-capped NMR tubes under N$_2$, followed by NMR spectra acquisition. No

resonances were observed by ^{31}P{^{1}H} NMR spectroscopy after the reactions (Figure 3.10).
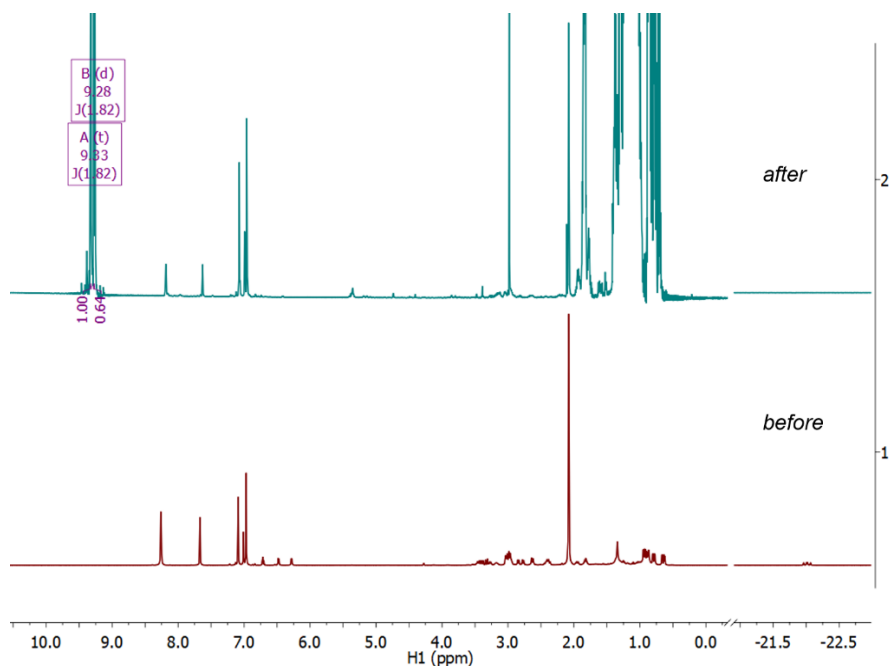
Figure 3.38 ^{1}H NMR spectra obtained of **7** and 1-octene in toluene-d_8 before and after pressurizing the mixture with 20 bar 1:1 CO:H$_2$ and heating to 95 °C.

Yet a third aliquot of the solution of **5** (0.375 mL) was mixed 1-octene (45 μL, 0.29

mmol) and placed in a Teflon-capped NMR tube. Over time, the signals of **5** began to

decrease in intensity by ^{1}H NMR spectroscopy (Figure 3.11).

Reactivity of [^{t}BuNH$_3$][PF$_6$] with NaBAr$^F_4$. [^{t}BuNH$_3$][PF$_6$] (0.0051 g, 0.023 mmol) and

NaBAr$^F_4$ (0.0210 g, 0.0237 mmol) were massed out in a vial. Toluene-d_8 (0.5 mL) was

added. The resulting solution was decanted from the white-solids left in the vial into a

Teflon-capped NMR tube. ^{1}H, ^{31}P{^{1}H}, and ^{19}F{^{1}H} NMR spectra were acquired. No resonances were observed by ^{31}P{^{1}H} NMR spectroscopy, indicating precipitation of NaPF$_6$.
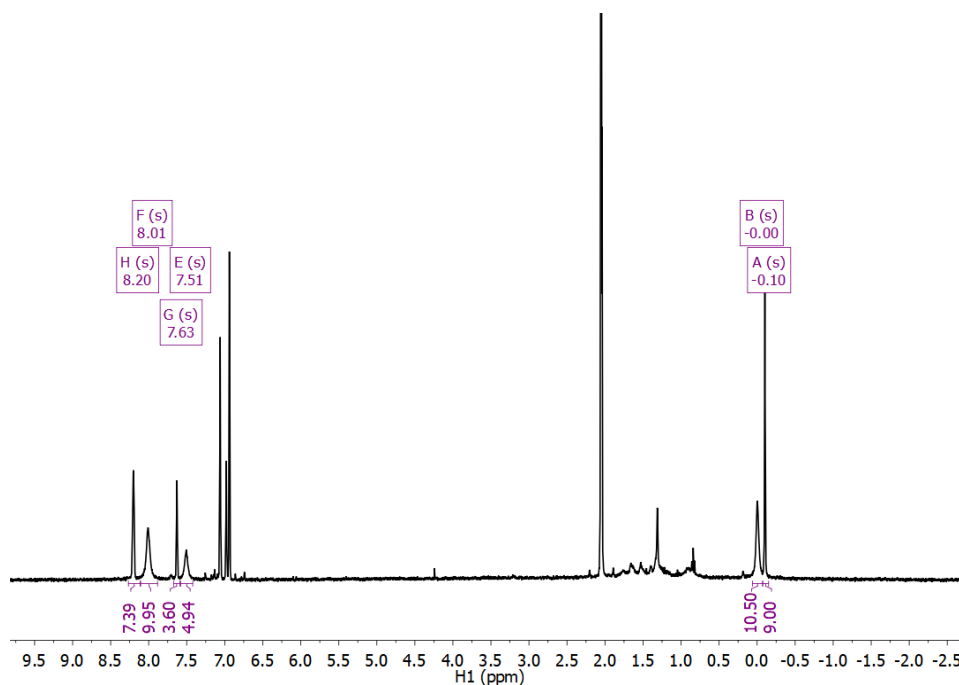
Figure 3.39 ^{1}H NMR spectrum acquired after mixing [^{t}BuNH$_3$][PF$_6$] and NaBAr$^F_4$ in toluene-d_8.
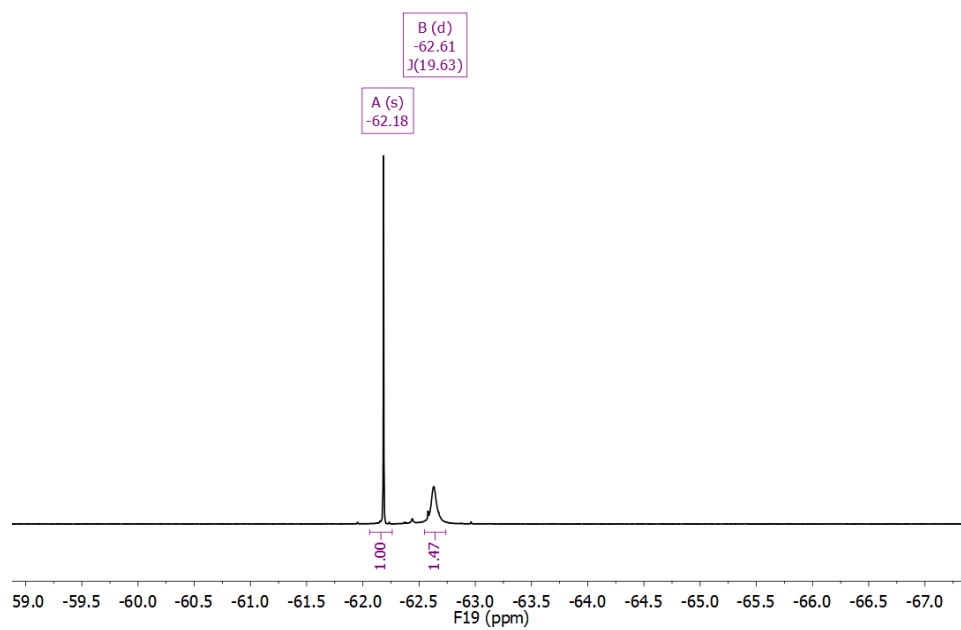
Figure 3.40 $^{19}F\{^1H\}$ NMR spectrum acquired after mixing [^{t}BuNH$_3$][PF$_6$] and NaBAr$^F_4$ in toluene-d_8.

REFERENCES

(1)   Franke, R.; Selent, D.; Börner, A. Applied Hydroformylation. *Chem. Rev.* **2012**, *112* (11), 5675–5732.

(2)   Whiteker, G. T.; Cobley, C. J. Applications of Rhodium-Catalyzed Hydroformylation in the Pharmaceutical, Agrochemical, and Fragrance Industries. In *Top Organomet Chem*; 2012; Vol. 42, pp 35–46.

(3)   Ternel, J.; Couturier, J.-L.; Dubois, J.-L.; Carpentier, J.-F. Rhodium versus Iridium Catalysts in the Controlled Tandem Hydroformylation-Isomerization of Functionalized Unsaturated Fatty Substrates. *ChemCatChem* **2015**, *7* (3), 513–520.

(4)   Nurttila, S. S.; Linnebank, P. R.; Krachko, T.; Reek, J. N. H. Supramolecular Approaches To Control Activity and Selectivity in Hydroformylation Catalysis. *ACS Catal.* **2018**, *8* (4), 3469–3488.

(5)   Clarke, M. Branched Selective Hydroformylation: A Useful Tool for Organic Synthesis. *Curr. Org. Chem.* **2005**, *9* (7), 701–718.

(6)   Puckette, T. A. Hydroformylation Catalysis at Eastman Chemical: Generations of Catalysts. *Top. Catal.* **2012**, *55* (7–10), 421–425.

(7)   How, R. C.; Hembre, R.; Ponasik, J. a.; Tolleson, G. S.; Clarke, M. L. A Modular Family of Phosphine-Phosphoramidite Ligands and Their Hydroformylation Catalysts: Steric Tuning Impacts upon the Coordination Geometry of Trigonal Bipyramidal Complexes of Type [Rh(H)(CO)$_2$(P^P*)]. *Catal. Sci. Technol.* **2016**, *6* (1), 118–124.

(8)   Pospech, J.; Fleischer, I.; Franke, R.; Buchholz, S.; Beller, M. Alternative Metals for Homogeneous Catalyzed Hydroformylation Reactions. *Angew. Chem. Int. Ed.* **2013**, *52* (10), 2852–2872.

(9)   Gonsalvi, L.; Guerriero, A.; Monflier, E.; Hapiot, F.; Peruzzini, M. The Role of Metals and Ligands in Organic Hydroformylation. In *Topics in Current Chemistry*; 2013; Vol. 342, pp 1–48.

(10)   Mon, I.; Jose, D. A.; Vidal-Ferran, A. Bis(phosphite) Ligands with Distal Regulation: Application in Rhodium-Mediated Asymmetric Hydroformylations. *Chem. Eur. J.* **2013**, *19* (8), 2720–2725.

(11)   Rovira, L.; Vaquero, M.; Vidal-Ferran, A. Asymmetric Hydroformylation of Heterocyclic Olefins Mediated by Supramolecularly Regulated Rhodium-Bisphosphite Complexes. *J. Org. Chem.* **2015**, *80* (20), 10397–10403.

(12)   LaCroce, S. J.; Cutler, A. R. Bimetallic Acyl Complexes. Use of Transition Organometallic Lewis Acids in Promoting Migratory Carbonyl Insertion. *J. Am. Chem. Soc.* **1982**, *104* (8), 2312–2314.

(13)   Butts, S. B.; Strauss, S. H.; Holt, E. M.; Stimson, R. E.; Alcock, N. W.; Shriver, D. F. Activation of Coordinated Carbon Monoxide toward Alkyl and Aryl Migration (Carbon Monoxide Insertion) by Molecular Lewis Acids and X-Ray Structure of the

Reactive Intermediate. *J. Am. Chem. Soc.* **1980**, *102* (15), 5093–5100.

(14)   Nolan, S. P.; Lopez de la Vega, R.; Hoff, C. D. Thermochemical Study of the Lewis Acid Promoted Carbonyl Insertion Reaction. *J. Am. Chem. Soc.* **1986**, *108* (24), 7852–7853.

(15)   Kwak, J. H.; Dagle, R.; Tustin, G. C.; Zoeller, J. R.; Allard, L. F.; Wang, Y. Molecular Active Sites in Heterogeneous Ir–La/C-Catalyzed Carbonylation of Methanol to Acetates. *J. Phys. Chem. Lett.* **2014**, *5* (3), 566–572.

(16)   Gregor, L. C.; Grajeda, J.; Kita, M. R.; White, P. S.; Vetter, A. J.; Miller, A. J. M. Modulating the Elementary Steps of Methanol Carbonylation by Bridging the Primary and Secondary Coordination Spheres. *Organometallics* **2016**, *35* (17), 3074–3086.

(17)   Tian, R.; Ng, Y.; Ganguly, R.; Mathey, F. A New Type of Phosphaferrocene–Pyrrole–Phosphaferrocene P-N-P Pincer Ligand. *Organometallics* **2012**, *31* (6), 2486–2488.

(18)   Wu, Q.; Zhou, F.; Shu, X.; Jian, L.; Xu, B.; Zheng, X.; Yuan, M.; Fu, H.; Li, R.; Chen, H. Synthesis and Application of PNP Pincer Ligands in Rhodium-Catalyzed Hydroformylation of Cycloolefins. *RSC Adv.* **2016**, *6* (109), 107305–107309.

(19)   Musa, S.; Filippov, O. a.; Belkova, N. V.; Shubina, E. S.; Silantyev, G. a.; Ackermann, L.; Gelman, D. Ligand-Metal Cooperating PC(sp^3)P Pincer Complexes as Catalysts in Olefin Hydroformylation. *Chem. Eur. J.* **2013**, *19* (50), 16906–16909.

(20)   Piras, I.; Jennerjahn, R.; Jackstell, R.; Spannenberg, A.; Franke, R.; Beller, M. A General and Efficient Iridium-Catalyzed Hydroformylation of Olefins. *Angew. Chem. Int. Ed.* **2011**, *50* (1), 280–284.

(21)   Andreina Moreno, M.; Haukka, M.; Pakkanen, T. A. Promoted Iridium Complexes as Catalysts in Hydroformylation of 1-Hexene. *J. Catal.* **2003**, *215* (2), 326–331.

(22)   Behr, A.; Kämper, A.; Nickel, M.; Franke, R. Crucial Role of Additives in Iridium-Catalyzed Hydroformylation. *Appl. Catal. A Gen.* **2015**, *505*, 243–248.

(23)   Behr, A.; Kämper, A.; Kuhlmann, R.; Vorholt, A. J.; Franke, R. First Efficient Catalyst Recycling for the Iridium-Catalysed Hydroformylation of 1-Octene. *Catal. Sci. Technol.* **2015**, *6*, 208–214.

(24)   Kämper, A.; Warrelmann, S. J.; Reiswich, K.; Kuhlmann, R.; Franke, R.; Behr, A. First Iridium-Catalyzed Hydroformylation in a Continuously Operated Miniplant. *Chem. Eng. Sci.* **2016**, *144*, 364–371.

(25)   Wang, X.; Nurttila, S. S.; Dzik, W. I.; Becker, R.; Rodgers, J.; Reek, J. N. H. Tuning the Porphyrin Building Block in Self-Assembled Cages for Branched-Selective Hydroformylation of Propene. *Chem. Eur. J.* **2017**, *23* (59), 14769–14777.

(26)   Grajeda, J.; Kita, M. R.; Gregor, L. C.; White, P. S.; Miller, A. J. M. Diverse Cation-Promoted Reactivity of Iridium Carbonyl Pincer-Crown Ether Complexes. *Organometallics* **2016**, *35* (3), 306–316.

(27)   Camp, A. M.; Kita, M. R.; Grajeda, J.; White, P. S.; Dickie, D. A.; Miller, A. J. M.

Mapping the Binding Modes of Hemilabile Pincer–Crown Ether Ligands in Solution Using Diamagnetic Anisotropic Effects on NMR Chemical Shift. *Inorg. Chem.* **2017**, *56* (18), 11141–11150.

(28) Kita, M. R.; Miller, A. J. M. Cation-Modulated Reactivity of Iridium Hydride Pincer-Crown Ether Complexes. *J. Am. Chem. Soc.* **2014**, *136* (41), 14519–14529.

(29) Gusev, D. G. Donor Properties of a Series of Two-Electron Ligands. *Organometallics* **2009**, *28* (3), 763–770.

(30) Kita, M. R.; Miller, A. J. M. An Ion-Responsive Pincer-Crown Ether Catalyst System for Rapid and Switchable Olefin Isomerization. *Angew. Chem. Int. Ed.* **2017**, *56* (20), 5498–5502.

(31) How, R. C.; Dingwall, P.; Hembre, R. T.; Ponasik, J. A.; Tolleson, G. S.; Clarke, M. L. Composition of Catalyst Resting States of Hydroformylation Catalysts Derived from Bulky Mono-Phosphorus Ligands, Rhodium Dicarbonyl Acetylacetonate and Syngas. *Mol. Catal.* **2017**, *434*, 116–122.

(32) Guerrero, M.; T. Than Chau, N.; Noel, S.; Denicourt-Nowicki, A.; Hapiot, F.; Roucoux, A.; Monflier, E.; Philippot, K. About the Use of Rhodium Nanoparticles in Hydrogenation and Hydroformylation Reactions. *Curr. Org. Chem.* **2013**, *17* (4), 364–399.

(33) Alsalahi, W.; Tylus, W.; Trzeciak, A. M. Green Synthesis of Rhodium Nanoparticles That Are Catalytically Active in Benzene Hydrogenation and 1-Hexene Hydroformylation. *ChemCatChem* **2018**, *10* (9), 2051–2058.

(34) Saba, S.; Hernandez, R.; Choy, C. C.; Carta, K.; Bennett, Y.; Bondi, S.; Kolaj, S.; Bennett, C. A Simple and Efficient One-Step Protocol for the Preparation of Alkyl-Substituted Ammonium Tetrafluoroborate and Hexafluorophosphate Salts. *J. Fluor. Chem.* **2013**, *153*, 168–171.

(35) Späth, A.; König, B. Molecular Recognition of Organic Ammonium-Ions in Solution Using Synthetic Receptors. *Beilstein J. Org. Chem.* **2010**, *6* (32), doi:10.3762/bjoc.6.32.

(36) Giordano, G.; Crabtree, R. H.; Heintz, R. M.; Forster, D.; Morris, D. E. Di-μ-Chloro-Bis(η^4-1,5-Cyclooctadiene)-Dirhodium(I). In *Inorganic Syntheses*; 2007; pp 88–90.

(37) Yakelis, N. A.; Bergman, R. G. Safe Preparation and Purification of Sodium Tetrakis[(3,5-Trifluoromethyl)phenyl]borate (NaBAr$^F_{24}$): Reliable and Sensitive Analysis of Water in Solutions of Fluorinated Tetraarylborates. *Organometallics* **2005**, *24* (14), 3579–3581.

(38) Raabe, I.; Reisinger, A.; Krossing, I. *Experiments In Green And Sustainable Chemistry*; Roesky, H. W., Kennepohl, D. K., Eds.; 2009.

(39) Sheldrick, G. M. Crystal Structure Refinement with SHELXL. *Acta Crystallogr. Sect. C Struct. Chem.* **2015**, *71* (1), 3–8.

(40) Sheldrick, G. M. A Short History of SHELX. *Acta Cryst. Sect. A Found. Crystallogr.*

2008, *64* (1), 112–122.

(41)   Dolomanov, O. V.; Bourhis, L. J.; Gildea, R. J.; Howard, J. A. K.; Puschmann, H. OLEX2 : A Complete Structure Solution, Refinement and Analysis Program. *J. Appl. Cryst.* **2009**, *42* (2), 339–341.

Chapter 4　SYNTHESIS AND CHARACTERIZATION OF STABLE GOLD(III) PNP PINCER COMPLEXES

Section 4.1　Introduction

Because of their air and moisture tolerance, gold complexes can enable catalytic transformations under ambient conditions that are otherwise inaccessible to more reactive precious metal catalysts.[1–3] In light of this, the field of Au organometallic chemistry has grown rapidly over the last decade.[4–6] Within the field, Au(III) complexes remain underexplored compared to Au(I) complexes, as the former are readily reduced or undergo protodemetalation.[7,8] However, in recent years, increased efforts have been directed at accessing new Au(III) complexes and exploring their reactivity.[6,9–20]

Direct catalytic functionalization of an alkene with a carboxylic acid has long been recognized as an important area of research, as it directly yields esters, avoiding the step of olefin hydration to an alcohol and the complications of water removal to drive the esterification.[21,22] Towards this goal, in 2012, the Tilset group reported the efficient microwave synthesis of a cyclometalated Au(III) complex with 2-(p-tolyl)pyridine (tpy) and two trifluoroacetate (OAc^F) ligands.[11] Facile ethylene (C_2H_4) insertion into the Au–O bond of

the OAc^F ligand has been accomplished in trifluoroacetic acid (HOAc^F).[23] The product of ethylene insertion at the site trans to the pyridine donor was found to be thermodynamically favored. Attempts at protonating the resulting acetoxyalkyl ligand with trifluoroacetic acid to complete a catalytic cycle proved unsuccessful. Addition of stronger Brønsted acids led to protonation of the sp^2 carbon of the chelating tpy ligand rather than the sp^3 carbon atoms of the acetoxyalkyl ligand at the Au(III) center, consistent with previous findings.[12] More recently, this system was employed for the catalytic functionalization of acetylene with HOAc^F *via* a double insertion pathway.[24]

We envisioned using a LXL-type pincer ligand framework to position a strong σ-donor *trans* to the active site, which could facilitate protonolysis of an acetoxyalkyl ligand. Pincer ligands have long been recognized as convenient platforms for the formation of thermally stable complexes, many of which serve as robust catalysts for a variety of chemical transformations.[25,26] In the realm of Au(III) chemistry, the use of pincer ligands remains underexplored.[8,27–32] Bochmann *et al.* recently reported a Au(III) trifluoroacetate complex supported by a CNC pincer ligand of the XLX-type (CNC = 2,6-bis(4-^{t}BuC$_6$H$_3$)$_2$pyridine dianion).[7,33] Notably, this complex also inserts ethylene into the Au–O bond, albeit more slowly than the complex reported by our group.[13]

The PNP ligand (PNP = bis(2-diisopropylphosphinophenyl)amide) reported by Liang and co-workers was identified as an interesting target for Au(III) chemistry.[34] This ligand and its close relatives support a tremendous wealth of coordination chemistry, with tridentate pincer binding modes observed across the periodic table.[35–42] For coinage metals, however, PNP ligands often favor dinuclear coordination modes with bridging amides, such that each metal is only bound in a bidentate fashion.[43] The first PNP gold complexes, recently reported

by van der Vlugt and coworkers, are structurally and electronically intriguing dinuclear gold systems that do not adopt pincer binding modes.[44,45]

In this Chapter, we describe the synthesis and characterization of the first PNP Au(III) mononuclear pincer complexes, along with initial efforts at generating acetoxyalkyl species by reaction with C_2H_4. Density Functional Theory (DFT) studies reveal the thermodynamically challenging nature of C_2H_4 functionalization with these complexes, and provide insight into their electronic structure.

Section 4.2   Synthesis of Gold(III) PNP Pincer Complexes

Pincer complexes were initially targeted by salt metathesis with the [Li][PNP] and Au(III) chloride precursors, but the conditions applied did not afford any observable reaction. Microwave synthesis, thoroughly explored in our lab for metallation with gold,[11] was attempted next. Microwave reactions of H[PNP], $NaAuCl_4 \cdot 2H_2O$, and 1 equiv of $HOAc^F$ in 1:1 mixtures of $H_2O:CH_3CN$ afforded royal blue [(PNP)Au(Cl)][OAc^F] (**1**) in ~10% yield. The reaction yields were improved to 19% by switching to neat $HOAc^F$ as solvent (Scheme 4.1). The obtained material was spectroscopically pure, but analytical purity was elusive even after extensive efforts at purification. Au nanoparticles were considered as a possible NMR-silent impurity, but transmission electron microscopy (TEM) studies did not detect any nanoparticles.
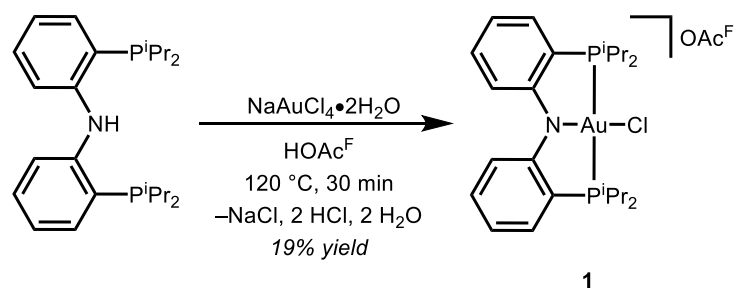
Scheme 4.1 Synthesis of **1**.

Complex **1** features a singlet (δ 84) in the ^{31}P{^{1}H} NMR spectrum and a singlet (δ −77) in the ^{19}F{^{1}H} NMR spectrum. The ^{1}H NMR spectrum reveals C$_{2v}$ symmetry of the complex in solution, with single resonances for the protons on both sets of aryl groups on the molecule. Two resonances arise from the inequivalent *iso*-propyl methyl groups. These resonances exhibit virtual coupling ascribed to the two magnetically nonequivalent ^{31}P nuclei. The symmetry displayed in solution is consistent with isoelectronic Pd complexes, supported by similar backbone-substituted PNP ligands, reported by the Ozerov group.[35,36] Crystals suitable for X-ray diffraction were grown by layering a concentrated solution of **1** in CH$_2$Cl$_2$ with Et$_2$O. The solid-state structure confirms the C$_{2v}$ symmetry, with the C$_2$ axis coinciding with the N–Au–Cl bonds (Figure 4.1).[46] The crystal structure features a co-crystallized HOAc^F molecule that forms a hydrogen bonding interaction with the outer-sphere OAc^F counterion.
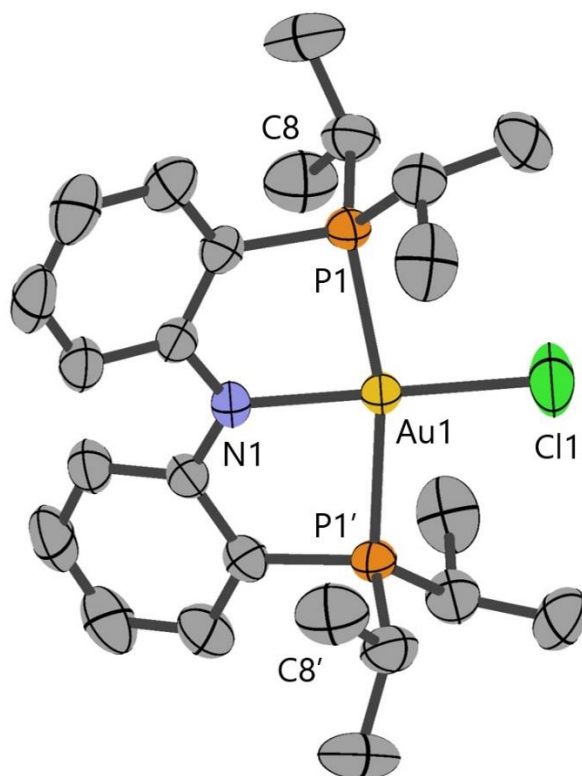
Figure 4.1 Structural representation of cation of **1** with ellipsoids drawn at the 50% probability level. Hydrogen atoms, OAc^F counter-anion, and HOAc^F omitted for clarity. Selected bond lengths (Å) and angles (°): Au1–N1: 2.004(3), Au1–Cl1: 2.2753(14), Au1–P1: 2.3381(8); P1−Au1−P1': 166.77(4), N1−Au1−P1: 83.38(2), Cl1−Au1−P1: 96.62(2).

The deep royal blue color of chloro complex **1** was investigated by UV-vis

spectroscopy and Time-Dependent Density Functional Theory (TD-DFT) calculations. In

CH$_2$Cl$_2$, an absorbance maximum in the visible range was detected at 587 nm (Figure 4.2).

On the basis of TD-DFT calculations including CH$_2$Cl$_2$ solvation with the continuum SMD

model, this absorption band is assigned to the HOMO → LUMO electronic excitation

($\lambda_{max,calc}$ = 535 nm). The natural transition orbitals (NTOs) associated with this transition

(Figure 4.3) are ligand-to-metal charge transfer (LMCT) in nature. The donor orbital features

lone pair character located on the amido site of the pincer ligand, whereas the acceptor orbital

has σ^* character centered upon the metal center. The orthogonal σ/π symmetry of these two

orbitals is consistent with the small oscillator strength of the transition (f = 0.0055).
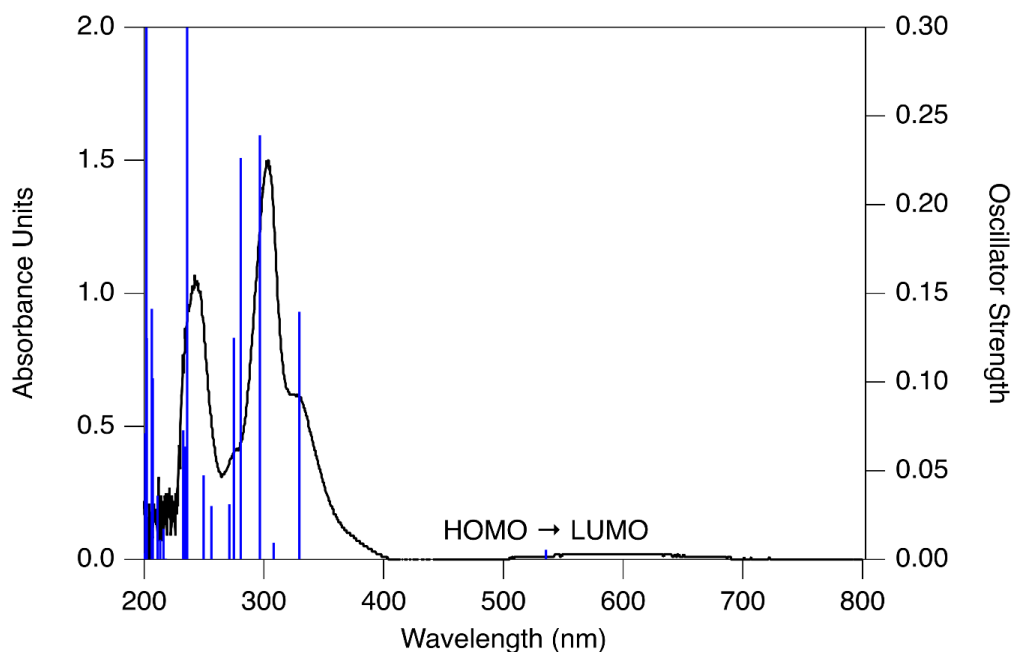
Figure 4.2 Experimental (black line) and calculated (vertical blue lines) UV-Vis spectrum of **1** in CH₂Cl₂ at the TD-DFT(ωB97XD) level.
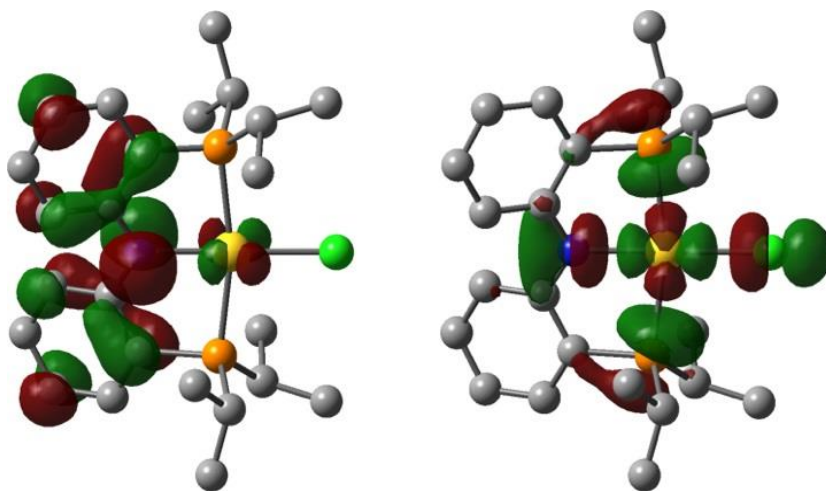
Figure 4.3 Donor amido lone pair (left) and acceptor σ* (right) NTOs for the HOMO → LUMO transition in the UV-Vis spectrum of **1** (isovalue = 0.04).

Dehalogenation of chloro complex **1** was carried out by addition of 1 equiv AgOAc^F, resulting in the precipitation of AgCl and formation of the trifluoroacetate-bound complex [(PNP)Au(OAc^F)][OAc^F] (**2**) as the sole (PNP)Au complex seen by NMR spectroscopy (Scheme 4.2). This new complex displays ^{1}H NMR signals that are very similar to those of chloro complex **1**, indicating C$_{2v}$ symmetry in solution. Complex **2** features a single resonance by ^{31}P{^{1}H} NMR in CD$_2$Cl$_2$ solvent at δ 92. The ^{19}F{^{1}H} NMR spectrum in CD$_2$Cl$_2$ features a sharp new singlet (δ −73) attributed to the bound OAc^F ligand and a broad singlet (δ −77) assigned to an outer-sphere OAc^F unit in rapid exchange with residual AgOAc^F in solution. In DOAc^F solution, only one resonance (δ −78) is observed in the ^{19}F{^{1}H} NMR spectrum, indicating rapid exchange between bound and free OAc^F. Despite extensive efforts to completely remove Ag$^+$ from the obtained product, ICP-MS indicated ~25% Ag in the mixture.
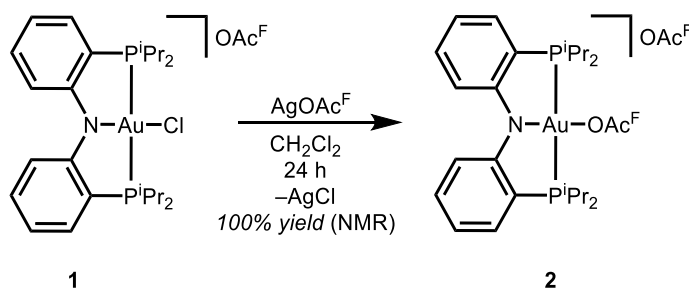
Scheme 4.2 Synthesis of trifluoroacetate-bound complex, **2**.

The product resulting from a reaction of **1** with excess AgOAc^F grew as single crystals from a CH$_2$Cl$_2$ solution undergoing slow diffusion with pentane (Figure 4.4). The crystallographic data (**2'**) revealed the expected [(PNP)Au(OAc^F)]$^+$ cation. The asymmetric unit of **2'** features an [Ag$_4$(OAc^F)$_6$]$^{2-}$ dianion as a tetrasilver paddlewheel structure that is generated by an inversion center (Figure 4.5). This kind of tetrameric structure has been

observed with Ag complexes, but is not common.[47] Unlike in solution, the C_2 axis of symmetry in the Au cation of **2'** is not retained in the solid state. Comparing structural features of **2'** to other Au(III) OAc^F complexes provides insight into the *trans* influence of the PNP amido nitrogen. The cation of **2'** features an Au–OAc^F distance (Au1–O1: 2.039(3) Å) that is intermediate between the Au–O distances *trans* to C (2.111(5) Å) and *trans* to N (1.993(5) Å) in the (tpy)Au($OAc^F)_2$ complex.[11] The Au–OAc^F distance is slightly longer than those of the (CNC)Au trifluoroacetate complex reported by Bochmann and co-workers, with a pyridine bound *trans* to the OAc^F ligand (2.0078(16) and 2.0156(17) Å).[7]
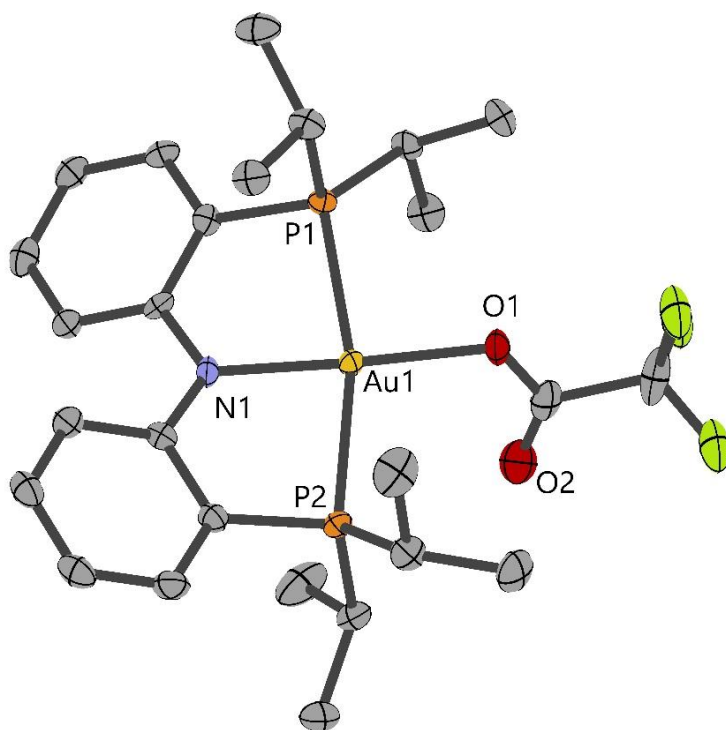
Figure 4.4 Structural representation of cation of **2'** with ellipsoids drawn at the 50% probability level. Hydrogen atoms and counter-anion omitted for clarity. The CF_3 group was disordered over two sites. Selected bond lengths (Å) and angles (°): Au1–N1: 1.992(3), Au1–O1: 2.039(3), Au1–P1: 2.3402(10), Au1–P2: 2.3545(10); P1−Au1−P2: 165.38(4), N1−Au1−O1: 177.58(13), N1−Au1−P1: 82.82(10), N1−Au1−P2: 83.07(10), O1−Au1−P1: 94.80(9), O1−Au1−P2: 99.28(9).
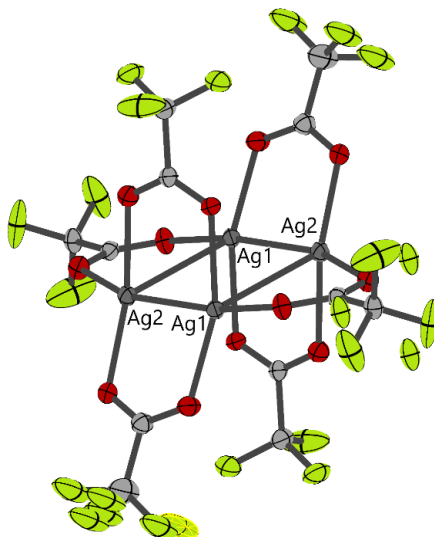
Figure 4.5 Structural representation of the counter-anion in complex **2'**, with ellipsoids drawn at the 50% probability level. CF$_3$ groups were disordered over two sites. The [Ag$_4$(OAc^F)$_6$]$^{2-}$ counter-anion appears as a tetrameric paddlewheel structure that is generated by an inversion center. Selected bond lengths (Å): Ag1–Ag2: 2.9283(4), Ag1–Ag2: 2.8903(4).

Trifluoroacetate-bound complex **2** is also deep blue in color. UV-vis spectroscopy reveals an absorbance maximum of 614 nm, red-shifted relative to **1** (Figure 4.6). TD-DFT calculations on **2** are consistent with an electronic transition in the visible region that is of a HOMO → LUMO nature with low intensity ($\lambda_{max,calc}$ = 541 nm, f = 0.0047; Figure 4.7) and red-shifted with respect to the calculated transition for **1** ($\lambda_{max,calc}$ = 535 nm).
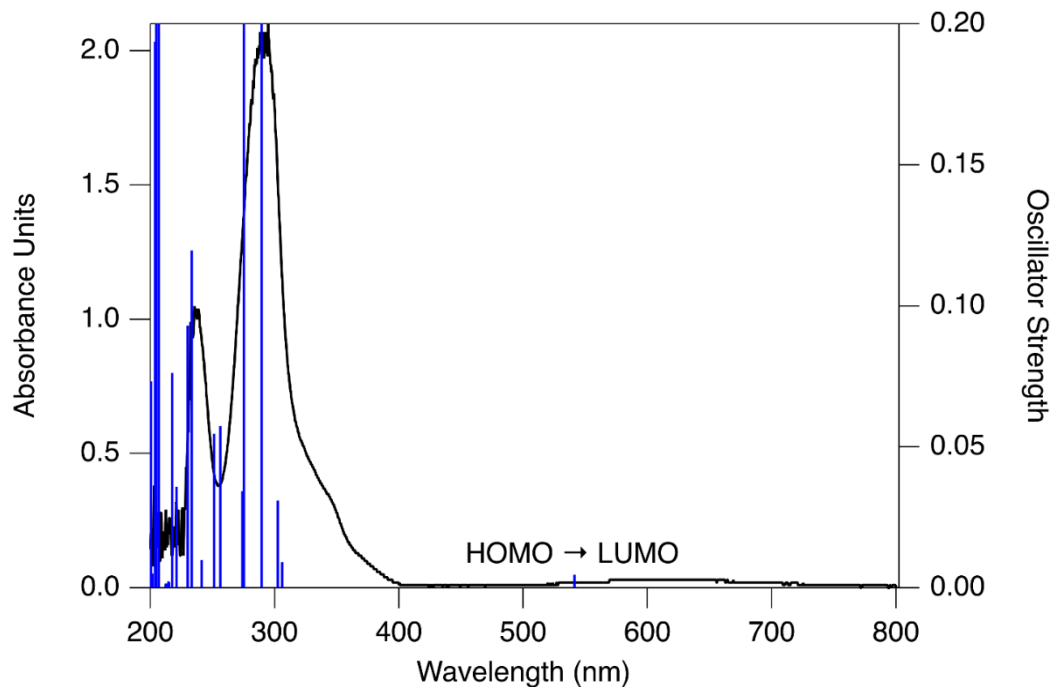
Figure 4.6 Experimental (black line) and calculated (vertical blue lines) UV-Vis spectrum of **2** in CH$_2$Cl$_2$ at the TD-DFT(ωB97XD) level.
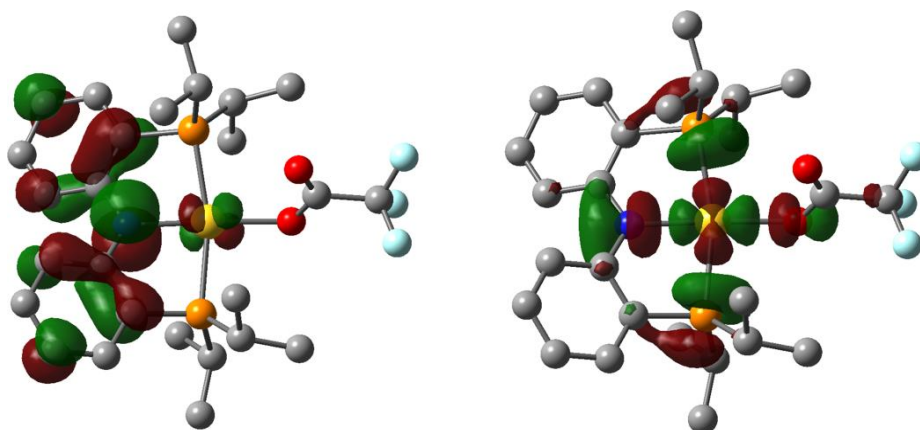
Figure 4.7 Donor amido lone pair (left) and acceptor σ* (right) NTOs for the HOMO $\rightarrow$ LUMO transition in the UV-Vis spectrum of **2** (isovalue = 0.04).

Section 4.3   Reactivity of Trifluoroacetate-Bound Complex 2 Towards Ethylene

Complex **2** proved to be stable towards C$_2$H$_4$ insertion into the Au–OAc^F bond. Reactions in CH$_2$Cl$_2$ or HOAc^F, even at 50-60 °C under 20 bar of C$_2$H$_4$, yielded primarily

starting material **2**, with trace amounts of other species observed by ^{19}F{^{1}H} and ^{31}P{^{1}H} NMR spectroscopy. Reactions at 60 °C in DOAc^F, under 1 atm of C$_2$H$_4$, resulted in deuterium incorporation into the aryl backbone of the ligand, primarily in the position *para* to the amido nitrogen (Scheme 4.3). This could be the result of Lewis acid-catalyzed C$_{aryl}$−H bond activation, possibly due to residual Ag$^+$.[48] Reactions at higher temperatures (100 °C) in C$_6$D$_5$Cl, resulted in decolorization and decomposition to intractable mixtures.
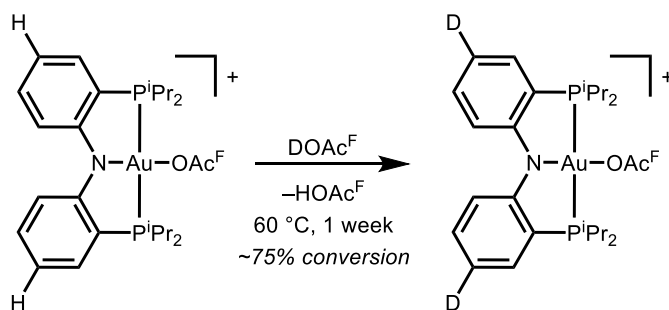
Scheme 4.3 Deuteration of complex **2** in DOAc^F.

DFT studies of the attempted insertion reaction reveal that formation of the gold alkyl product is slightly exergonic ($\Delta G° = -3.4$ kcal/mol) in HOAc^F (Scheme 4.4). The formal insertion process could proceed via trifluoroacetate dissociation and ligand nucleophilic attack, or by ethylene association and insertion. Formation of the monocationic, five-coordinate species is calculated to be 23 kcal/mol uphill. This intermediate could lead to an intramolecular ethylene insertion; however, other Au(III) systems feature high energy insertion barriers, which could prevent C$_2$H$_4$ insertion.[23] Formation of the putative dicationic C$_2$H$_4$-bound intermediate required for the intermolecular addition of an OAc^F anion is uphill by over 30 kcal/mol. It is worth noting that isoelectronic, dicationic Pd(II) and Pt(II) complexes [(PN$_{py}$P)M(C$_2$H$_4$)]$^{2+}$ (M = Pd or Pt; PN$_{py}$P = 2,6-

bis(diphenylphosphinomethyl)pyridine) are synthetically accessible and readily react with weakly basic nucleophiles, like MeOH and H_2O, to generate insertion products.[49–51]
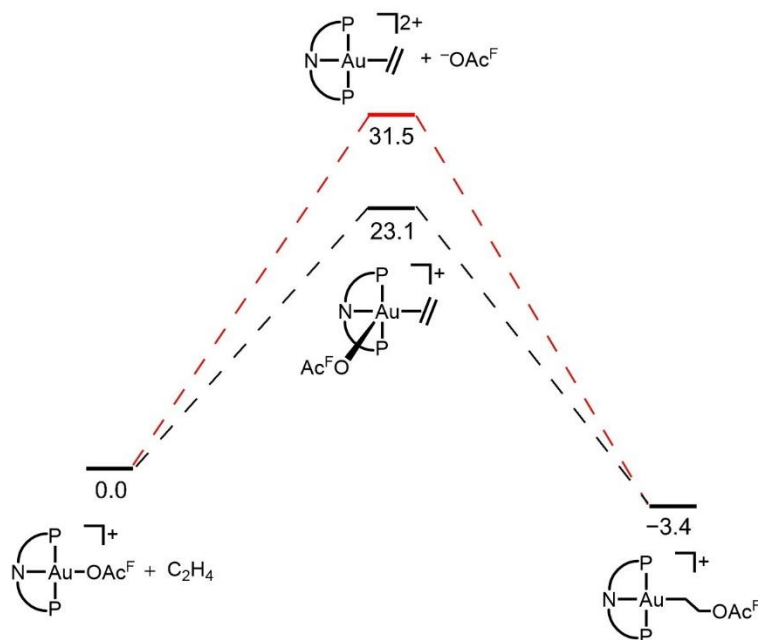
Scheme 4.4 Free energy profile (in kcal/mol) for the insertion of C_2H_4 into complex **2**, computed in HOAc^F solution, including reactant, intermediate and product. Both substitution (red line) and addition (black line) pathways were considered.

The incorporation of a dianionic pincer ligand of the LXX form could enable alkene insertion reactivity by avoiding the highly-charged reaction intermediates invoked with the complexes described in this Chapter. Indeed, DFT reveals that ligand substitution of OAc^F by ethylene with a Au complex supported by a dianionic PNC [(PNC = (2-diisopropylphosphinophenyl)(2'-diisopropylmethylphenyl)amide) an analogue of PNP with a carbon anion in place of a P atom] pincer ligand is uphill by 21.3 kcal/mol (Scheme 4.5).

$\Delta G_{rxn} = 21.3$ kcal/mol
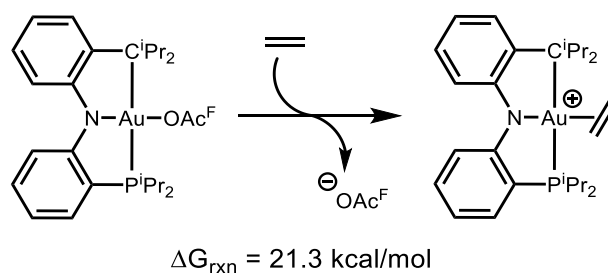
Scheme 4.5 ΔG_{rxn} (kcal/mol) for ligand substitution by C_2H_4 at a Au(III) center supported by a dianionic PNC pincer system computed in HOAc^F solution.

Section 4.4   Conclusions

The synthesis and characterization of the first PNP Au(III) pincer complexes has been described. Microwave synthesis generates Au–Cl complex **1**. Subsequent dehalogenation generates trifluoroacetate-bound complex **2**, with a OAc^F ligand bound *trans* to the amido group in the PNP ligand backbone. No reactivity with C_2H_4 was observed under the attempted reaction conditions. This reluctance to react is ascribed to the high energy of the putative intermediates in the formal insertion reaction.

Section 4.5   Experimental Details

General Considerations. All manipulations were carried out using standard Schlenk or glovebox techniques under a N_2 or Argon atmosphere, unless otherwise stated. The microwave oven used was of the type Milestone MicroSYNTH with a rotor of the type SK-10. Under standard glovebox operating conditions, pentane, diethyl ether, benzene, toluene, and tetrahydrofuran were used without purging, such that traces of those solvents were present in the atmosphere and in the solvent bottles. ^{1}H, ^{31}P{^{1}H}, ^{13}C{^{1}H}, ^{19}F{^{1}H}, ^{1}H-^{1}H COSY, and ^{1}H-^{1}H-NOESY NMR spectra were recorded on 400, 500, or 600 MHz spectrometers at 298 K. NMR solvents were purchased from Cambridge Isotopes Laboratories, Inc. ^{1}H and ^{13}C chemical shifts are reported in ppm relative to residual proteo

solvent resonances. ^{31}P chemical shifts are reported relative to 85% H_3PO_4 external standard

(δ 0). ^{19}F chemical shifts are reported relative to $CFCl_3$ external standard (δ 0). H[PNP] was

synthesized as previously reported.[34] All other reagents were commercially available and

used without further purification. Elemental analyses were performed by Robertson Microlit

Labs (Ledgewood, NJ). UV/vis spectra were collected with an Ocean Optics USB2000+

spectrometer with a DT-MINI-2GS deuterium/tungsten halogen light source. High

temperature and pressure reactions were performed with a Parr Series 5000 Multiple Reactor

System operated by a Parr 4871 Process Controller equipped with six reactors with internal

stirring. Each reactor is individually pressure- and temperature-controlled with maximum

operating limits of 3000 psi (200 bar) and 300 °C. Each reactor is monitored by computer

software SpecView 32. High-resolution mass spectrometry (HRMS) was carried out with a

LTQ FT (ICR 7T) (ThermoFisher, Bremen, Germany) mass spectrometer. Measurements

were made on complexes dissolved in acetonitrile. Samples were introduced via a micro-

electrospray source at a flow rate of 3 µL/min. Xcalibur (ThermoFisher, Breman, Germany)

was used to analyze the data. Molecular formula assignments were determined with

Molecular Formula Calculator (v 1.2.3). Low-resolution mass spectrometry (linear ion trap)

provided independent verification of molecular weight distributions. All observed species

were singly charged, as verified by unit *m/z* separation between mass spectral peaks

corresponding to the ^{12}C and $^{13}C^{12}C_{c-1}$ isotope for each elemental composition. Samples were

analyzed with an Element XR inductively coupled plasma (ThermoFisher, Bremen,

Germany) mass spectrometer (ICP-MS). Samples were introduced via a peristaltic pump

connected to an Elemental Scientific SC autosampler (Omaha, Nebraska). Transmission

electron microscopy images were obtained using a JEOL 2010F-FasTEM with an

acceleration voltage of 200 kV. Samples were prepared by drop casting on the lacey carbon film on a 400 mesh copper grid. EDS analysis was performed on Oxford Instruments, INCA Energy TEM 250 attached to the scope. Single crystal X-ray diffraction data was collected on a Bruker D8 Venture equipped with a Photon 100 detector at 298 K and using Mo Kα radiation ($\lambda = 0.71073$ Å) or a Bruker APEX-II CCD diffractometer at 100 K with Cu Kα radiation ($\lambda = 1.54175$ Å). Using Olex2[52] and WinGX,[53] the structure of **1** was solved with the ShelXT[54] structure solution program in the Bruker Apex 3 suite[55] and refined with the ShelXL[56] refinement package. Using Olex2,[52] the structure of **2'** was solved with the ShelXT[54] intrinsic phasing program and refined with the ShelXL[56] refinement package using Least Squares minimization. Multiple CF_3 groups were disordered in the structure of **2'** and were modeled using DFIX, DANG, and EADP to restrain and constrain the disordered fluorine atom sites.

Synthesis of [(PNP)Au(Cl)][OAc^F] (1). Under air, H[PNP] (0.143 g, 0.356 mmol) and NaAuCl4·2H2O (0.142 g, 0.358 mmol) were placed in a microwave vessel equipped with a stir bar. To this mixture was added HOAc^F (30 mL). The resulting orange-brown slurry was heated in the microwave oven at 120 °C for 30 minutes. The mixture was allowed to cool down, and the resulting blue slurry was passed through a frit padded with Celite. The filtrate was pumped down under vacuum to a blue oily solid. In an N2-filled glovebox, the residue was extracted with CH2Cl2 (15 mL) and filtered through Celite into three different vials. The blue solution in each vial was concentrated to ~1 mL, layered with Et2O (18 mL), and placed at −30 °C. The resulting blue crystals were combined into a single vial, redissolved in CH2Cl2, filtered through Celite, and the filtrate was once again set to recrystallize by layering with Et2O (18 mL), affording **1** (0.0503 g, 0.0674 mmol) as a blue crystalline solid (19%

yield). ^{1}H NMR 600 MHz, CD$_2$Cl$_2$): δ 1.34 – 1.43 (m, 12 H, CH(CH_3)$_2$), 1.43 – 1.51 (m, 12 H, CH(CH_3)$_2$), 3.20 (heptd, J = 7.2, 2.8 Hz, 4 H, CH(CH$_3$)$_2$), 6.99 (t, J = 7.5 Hz, 2 H, Ar-H), 7.36 – 7.44 (overlapping m, 4 H, Ar-H), 7.63 (dt, J = 8.7, 2.3 Hz, 2 H, Ar-H). ^{13}C{^{1}H} NMR (151 MHz, CD$_2$Cl$_2$): δ 17.75 (s, CH(CH_3)$_2$), 17.91 (s, CH(CH_3)$_2$), 27.22 (t, J = 14.1 Hz, CH(CH$_3$)$_2$), 112.24 (t, J = 26.0, 24.8 Hz, C$_{Ar}$), 117.85 (t, J = 5.4 Hz, C$_{Ar}$), 123.81 (t, J = 4.6 Hz, C$_{Ar}$), 133.95 (t, J = 2.1, 1.3 Hz, C$_{Ar}$), 134.98 (C$_{Ar}$), 160.51 (t, J = 6.9 Hz, C$_{Ar}$). $^-$OCOCF$_3$ was not observed by ^{13}C NMR. ^{31}P{^{1}H} NMR (162 MHz, CD$_2$Cl$_2$): δ 84.49. ^{19}F{^{1}H} NMR (376 MHz, CD$_2$Cl$_2$): δ −76.65. UV/Vis [CH$_2$Cl$_2$] λ_{max} (log ε) = 587 (2.53) nm. HRMS (ESI+) m/z: [**1** – O$_2$C$_2$F$_3$]$^+$ 632.16798 (calcd. 632.167136). C$_{26}$H$_{36}$AuClF$_3$NO$_2$P$_2$ (745.94) calcd. C 41.86, H 4.86, N 1.88; found C 40.45, H 4.62, N 1.61.

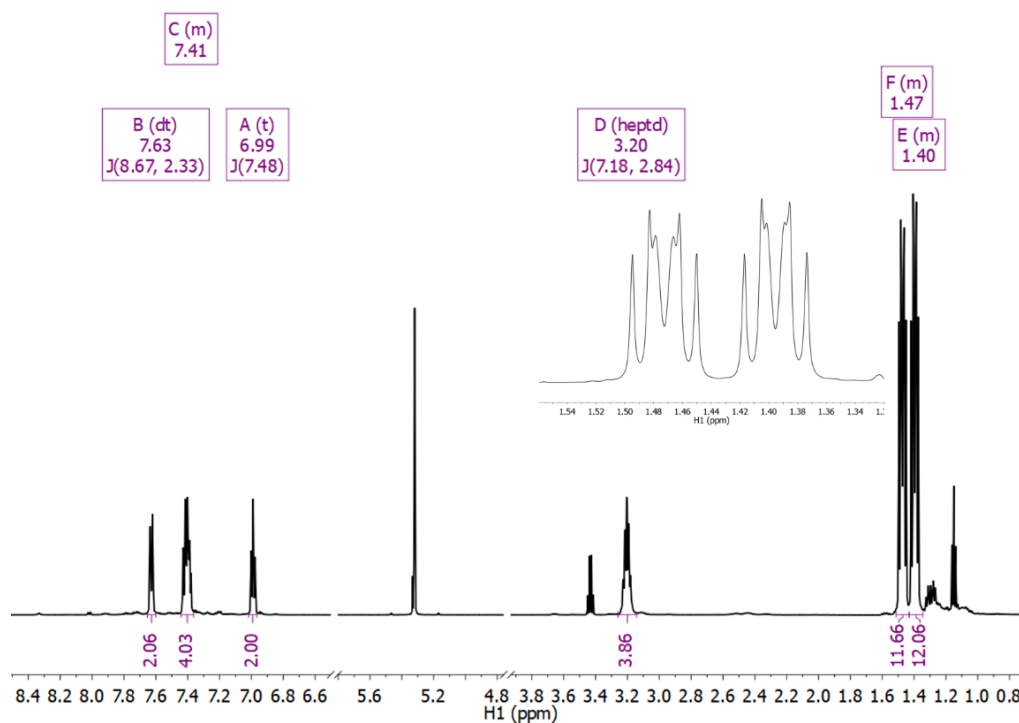**Figure 4.8** ^{1}H NMR spectrum of **1** in CD$_2$Cl$_2$ (600 MHz). Inset shows splitting pattern for *iso*-propyl methyl groups. Et$_2$O present in the sample (δ 1.15 and 3.43).
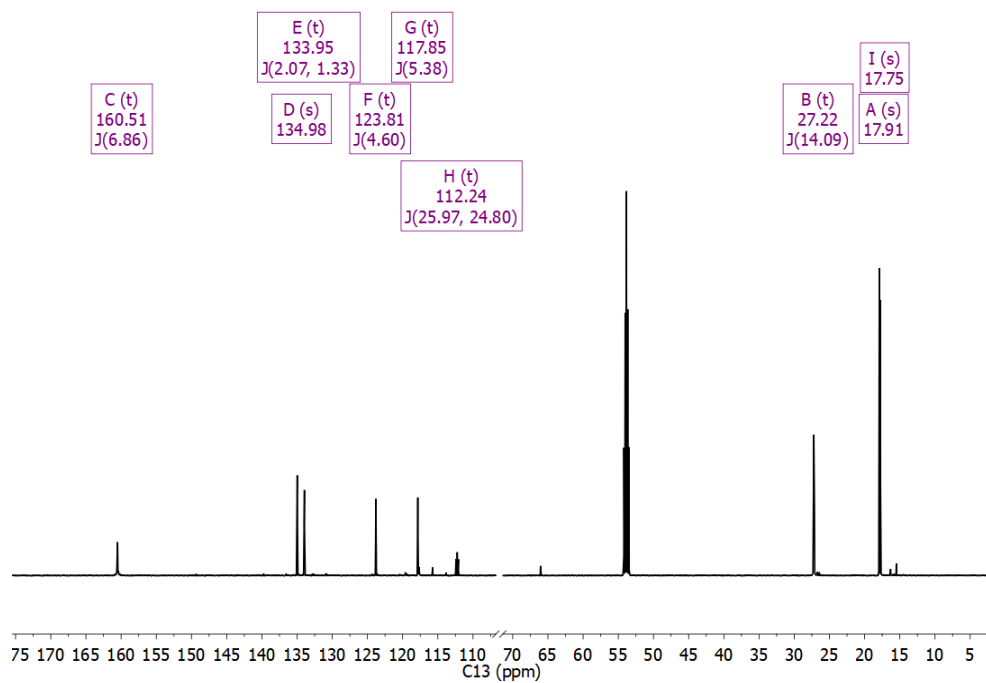
Figure 4.9 ^{13}C{^{1}H} NMR spectrum of **1** in CD$_2$Cl$_2$ (151 MHz). Et$_2$O present in the sample (δ 15.49 and 66.04).
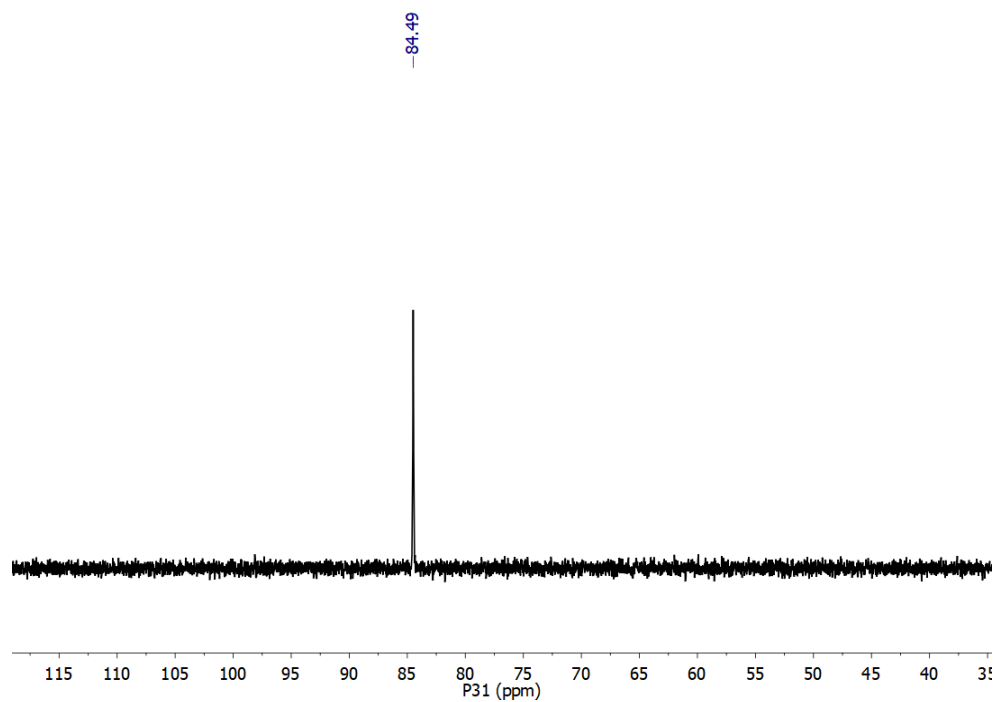

Figure 4.10 ^{31}P{^{1}H} NMR spectrum of **1** in CD$_2$Cl$_2$ (162 MHz).
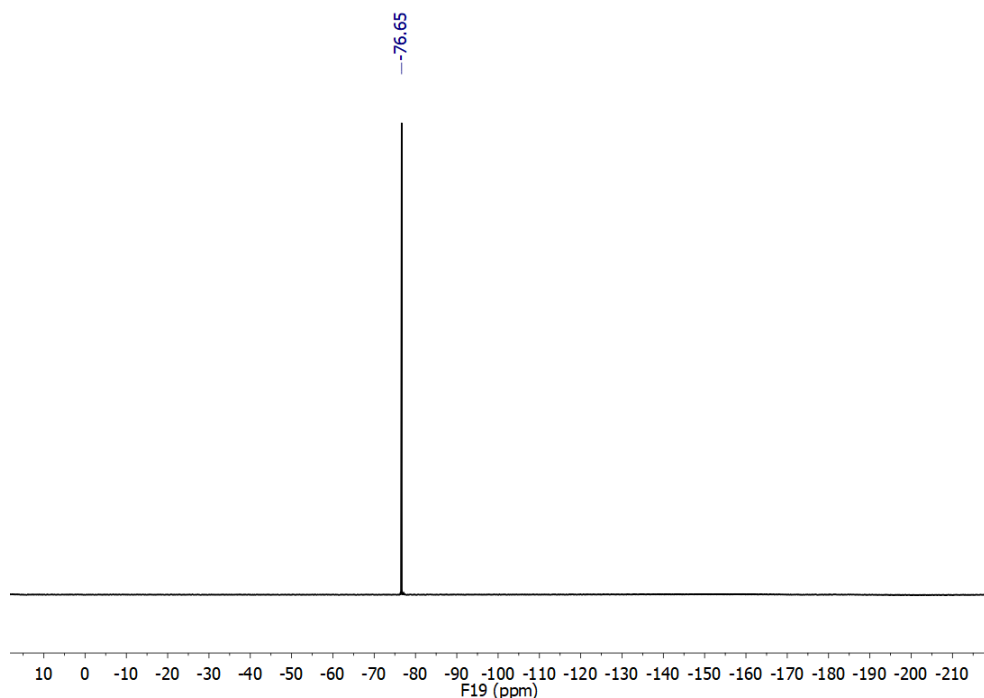
−76.65

Figure 4.11 $^{19}F\{^1H\}$ NMR spectrum of **1** in CD_2Cl_2 (376 MHz).

Synthesis of [(PNP)Au(OAc^F)][OAc^F] (2). A sample of chloride complex **1** (0.0176 g,

0.0236 mmol) was massed out in a scintillation vial. AgOAc^F (0.0053 g, 0.024 mmol) was

added to the vial. CH_2Cl_2 (5 mL) was added, and the resulting blue solution was left stirring

in the dark for 24 h. At this point, the resulting blue/white slurry was filtered, and the blue

filtrate was stripped of solvent under vacuum, affording compound **2** as a blue solid. The

blue residue was recrystallized by slow diffusion of pentane (8 mL) into a concentrated

solution of **2** in CH_2Cl_2 (2 mL). NMR spectroscopy revealed full conversion to

trifluoroacetate-bound species **2**. Attempts at purifying the complex beyond ~75% by

removing excess Ag$^+$ proved unsuccessful, as evidenced by $^{19}F\{^1H\}$ NMR and ICP-MS.

Single crystals suitable for XRD analysis were obtained from a different reaction carried out

with excess AgOAc^F, by slow diffusion of pentane into a CH_2Cl_2 solution of the complex.

The asymmetric unit of **2'** features an $[Ag_4(OAc^F)_6]^{2-}$ counter-anion as a Ag-tetrameric

paddlewheel structure that is generated by an inversion center. The NMR spectra obtained for these crystals match those reported below from preparative-scale reactions. ^{1}H NMR (600 MHz, CD$_2$Cl$_2$): δ 1.31 – 1.39 (m, 12H, CH(CH_3)$_2$), 1.39 – 1.47 (m, 12H, CH(CH_3)$_2$), 3.12 (hd, J = 7.1, 2.6 Hz, 4H, CH(CH$_3$)$_2$), 6.98 – 7.04 (m, 2H, Ar-H), 7.36 – 7.39 (m, 2H, Ar-H), 7.41 (ddq, J = 8.5, 7.2, 1.3 Hz, 2H, Ar-H), 7.60 (dt, J = 8.6, 2.3 Hz, 2H, Ar-H). ^{13}C{^{1}H} NMR (151 MHz, CD$_2$Cl$_2$): δ 17.47 (s, CH(CH$_3$)$_2$), 17.77 (s, CH(CH$_3$)$_2$), 27.52 (t, J = 13.6 Hz, CH(CH$_3$)$_2$), 111.24 (t, J = 26.8 Hz, C$_{Ar}$), 118.41 (t, J = 5.2 Hz, C$_{Ar}$), 124.54 (t, J = 4.5 Hz, C$_{Ar}$), 133.77 (t, J = 3.0 Hz, C$_{Ar}$), 135.30 (s, C$_{Ar}$), 160.06 (t, J = 6.8 Hz, C$_{Ar}$). $^-$OCOCF$_3$ was not observed by ^{13}C NMR. ^{31}P{^{1}H} NMR (243 MHz, CD$_2$Cl$_2$): δ 92.20. ^{19}F{^{1}H} NMR (376 MHz, CD$_2$Cl$_2$): δ −76.53, −73.24. ^{1}H NMR (600 MHz, DOAc^F) δ 1.24 – 1.33 (m, 12H, CH(CH_3)$_2$), 1.33 – 1.41 (m, 12H, CH(CH_3)$_2$), 3.04 (hd, J = 7.2, 2.6 Hz, 4H, CH(CH$_3$)$_2$), 6.84 – 6.96 (m, 2H, Ar-H), 7.16 – 7.34 (overlapping m, 4H, Ar-H), 7.51 (dt, J = 8.6, 2.5, 1.5 Hz, 2H, Ar-H). ^{31}P{^{1}H} NMR (243 MHz, CD$_2$Cl$_2$): δ 93.51. ^{19}F{^{1}H} NMR (376 MHz, CD$_2$Cl$_2$): δ −78.31. UV/Vis [CH$_2$Cl$_2$] λ_{max} (log ε) = 614 (2.63) nm. HRMS (ESI+) m/z: [$\mathbf{2}$ – O$_2$C$_2$F$_3$]$^+$ 710.18039 (calcd. 710.183316).
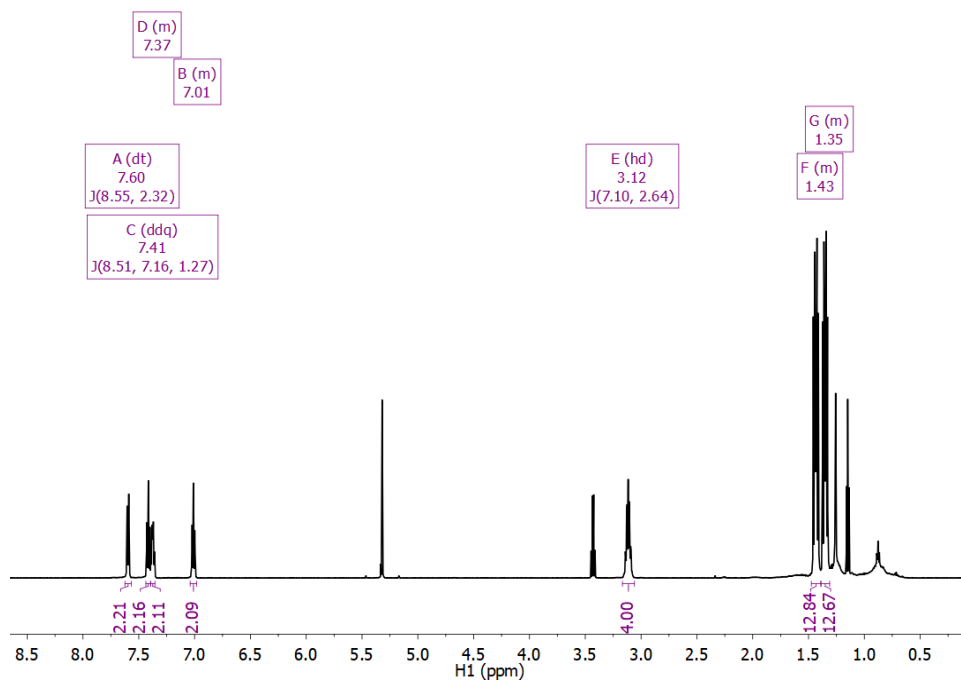
Figure 4.12 ^{1}H NMR spectrum of **2** in CD$_2$Cl$_2$ (600 MHz). Et$_2$O (δ 1.15 and 3.43) and H-grease (δ 0.88 and 1.26) present in the sample.
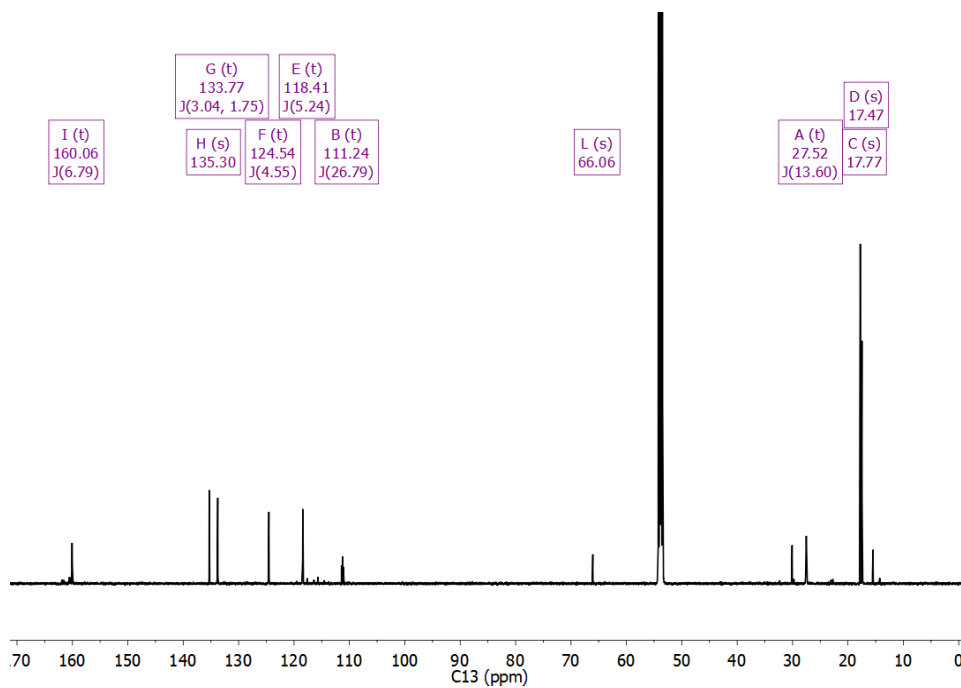
Figure 4.13 ^{13}C{^{1}H} NMR spectrum of **2** in CD$_2$Cl$_2$ (151 MHz). Et$_2$O (δ 15.49 and 66.06) and H grease (δ 30.08) present in the sample.

166
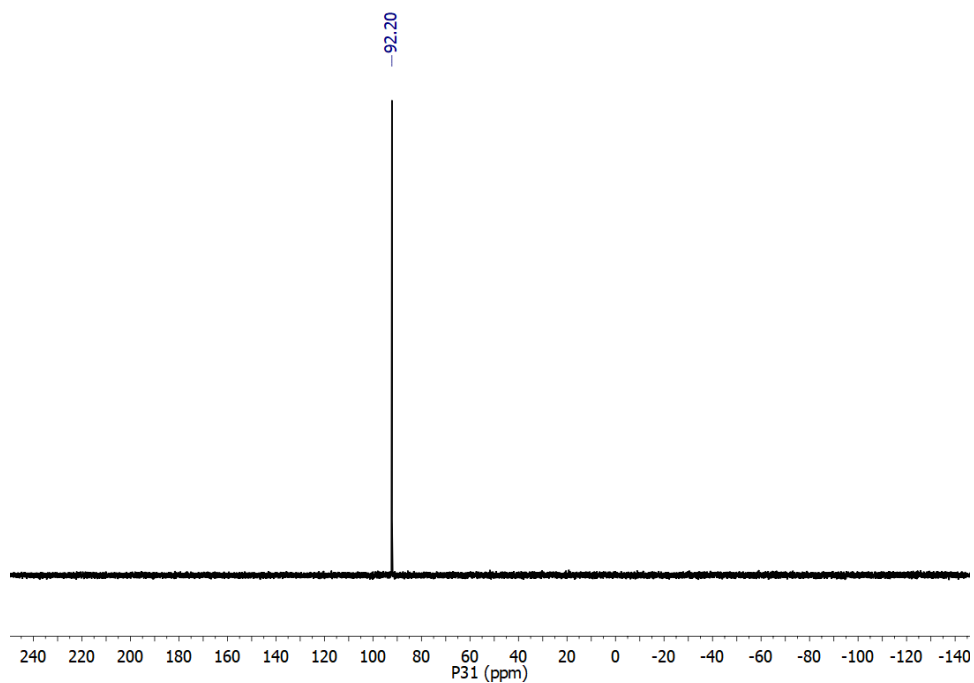
Figure 4.14 $^{31}P\{^1H\}$ NMR spectrum of **2** in CD_2Cl_2 (243 MHz).
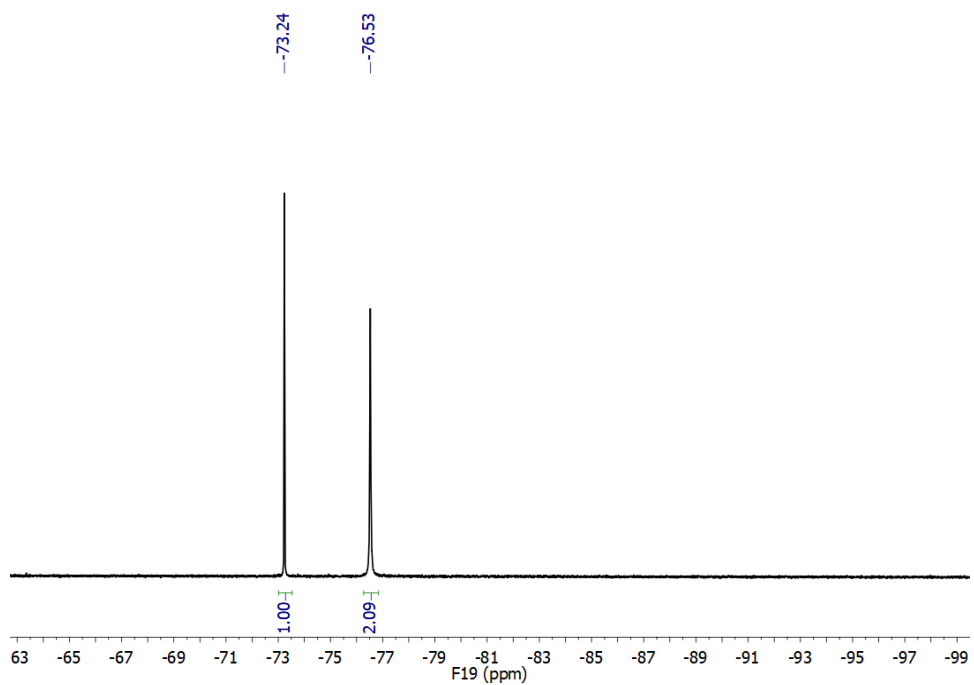
Figure 4.15 $^{19}F\{^1H\}$ NMR spectrum of **2** in CD_2Cl_2 (376 MHz).

Figure 4.16 ^{1}H-^{1}H NOESY NMR spectrum of **2** in CD$_2$Cl$_2$ (500 MHz).

Figure 4.17 ^{1}H-^{1}H COSY NMR spectrum of **2** in CD$_2$Cl$_2$ (500 MHz). The inset shows the aromatic region.
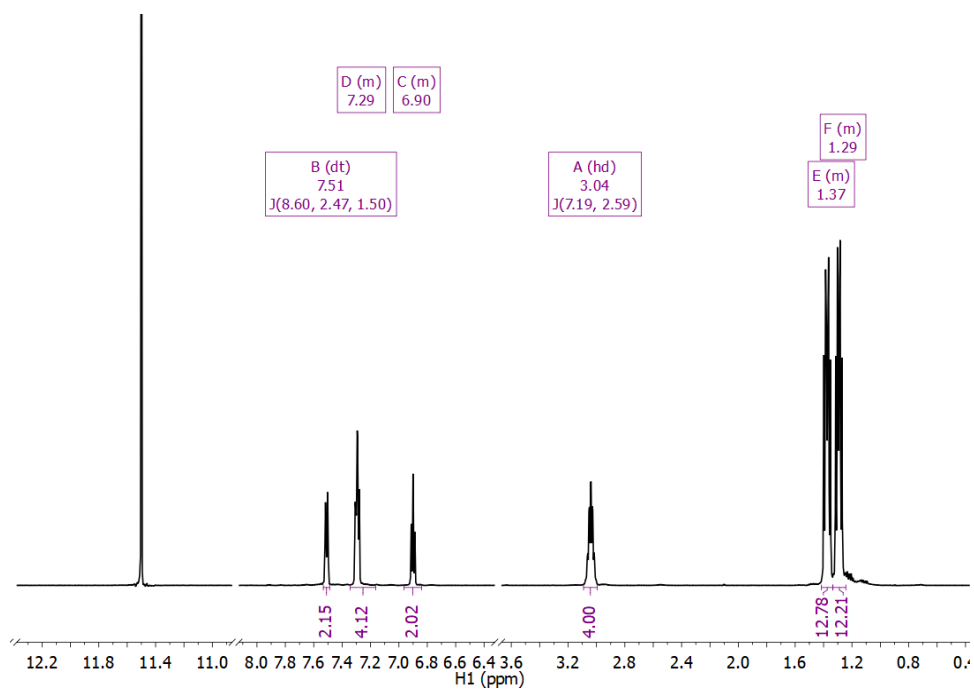
Figure 4.18 ^{1}H NMR spectrum of **2** in DOAc^F (600 MHz).
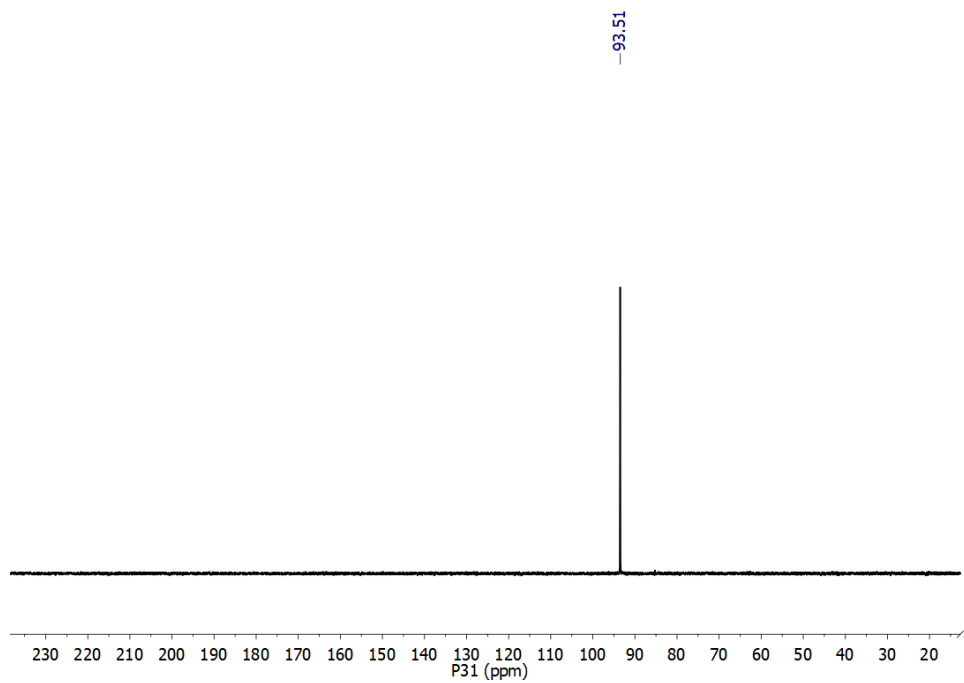
Figure 4.19 ^{31}P{^{1}H} NMR spectrum of **2** in DOAc^F (243 MHz).
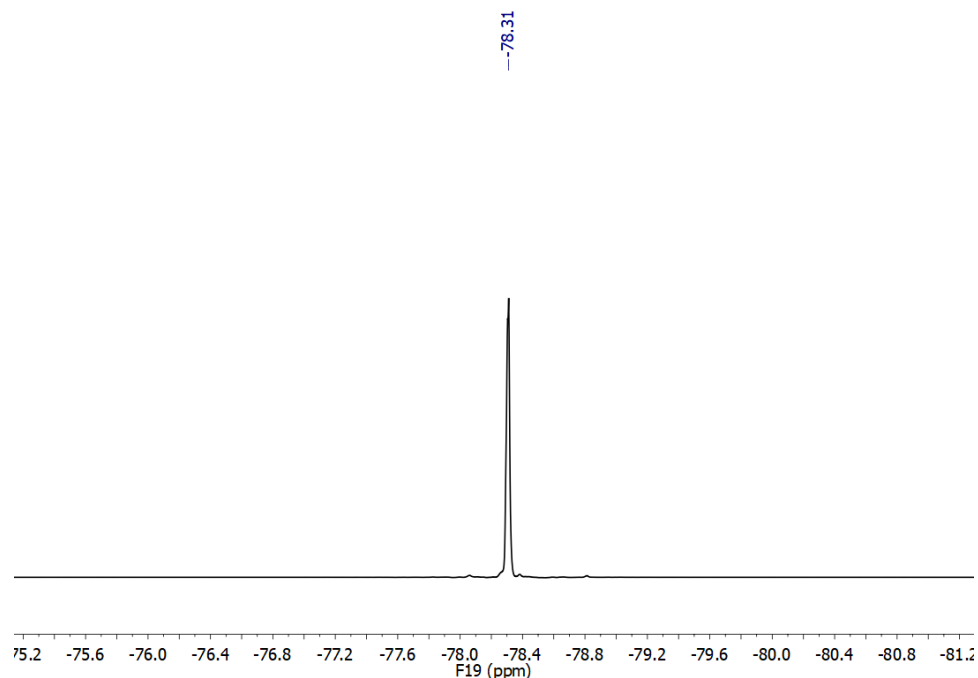
Figure 4.20 $^{19}F\{^{1}H\}$ NMR spectrum of **2** in DOAc^{F} (376 MHz).

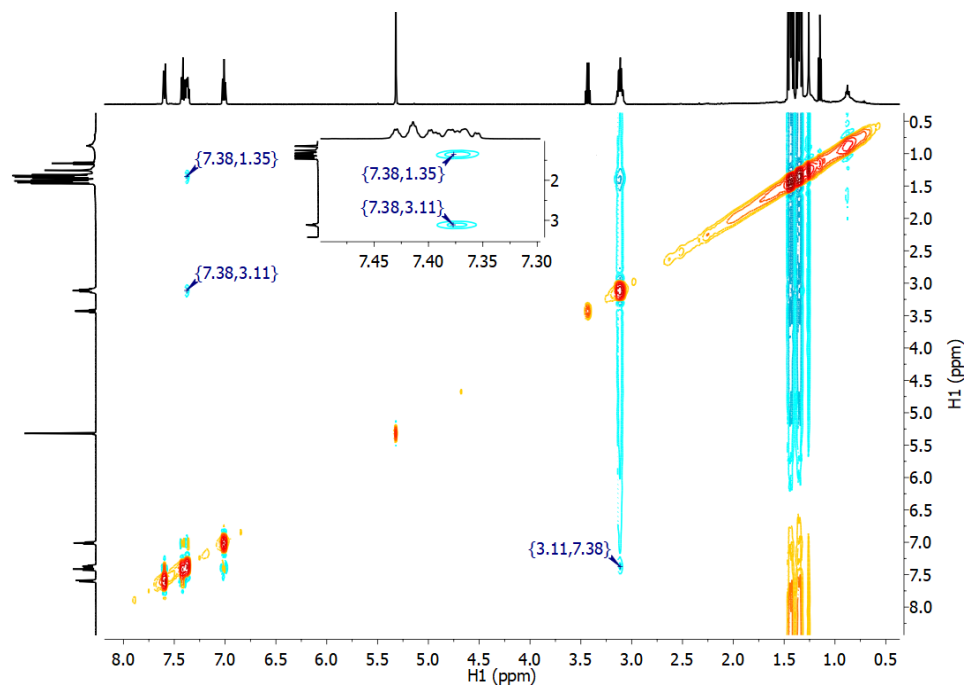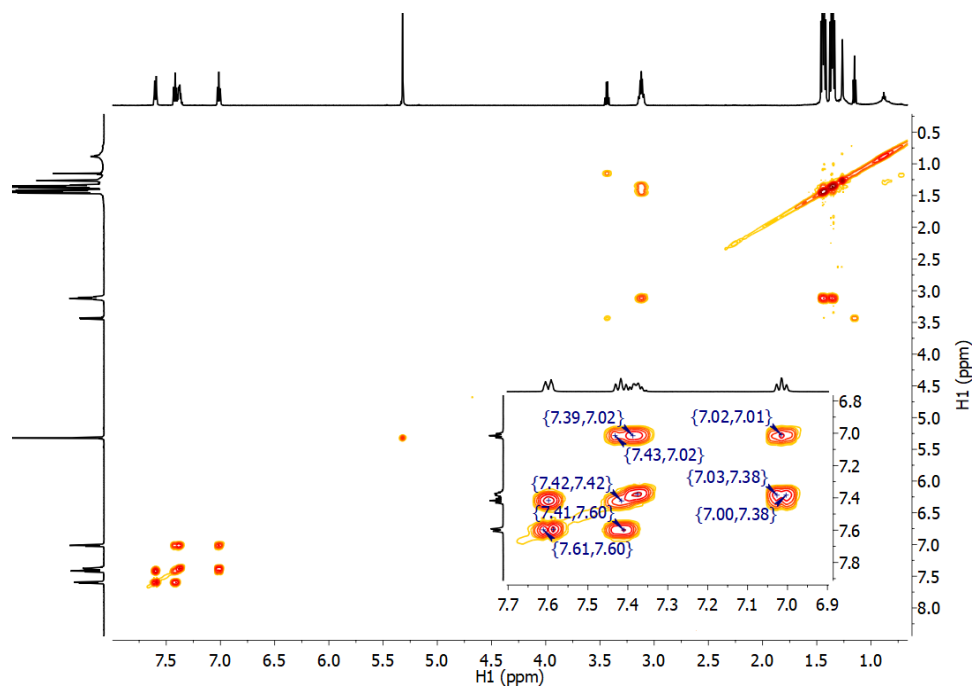**Complex 2 under high pressure of C₂H₄.** In a typical experiment, trifluoroacetate-bound complex **2** (5-10 mg) was dissolved in CH_2Cl_2 or HOAc^{F} (10 mL) in a Teflon liner. The liner was placed in a Parr reactor and sealed. The sealed reactors were connected to the multireactor system. The reactor manifold was purged with C_2H_4 and each vessel was subjected to three pressurization-venting cycles (approximately 5 bar) to ensure full replacement of the headspace with C_2H_4. The vessels were then pressurized to 20 bar of C_2H_4 and the temperature was set to 50-60 °C utilizing the SpecView 32 software. After approximately 15 h, the vessels were allowed to cool to room temperature. The reactor contents were pumped to dryness under vacuum and the resulting blue solids analyzed by NMR in CD_2Cl_2, revealing primarily starting material, as well as some minor unidentified products.
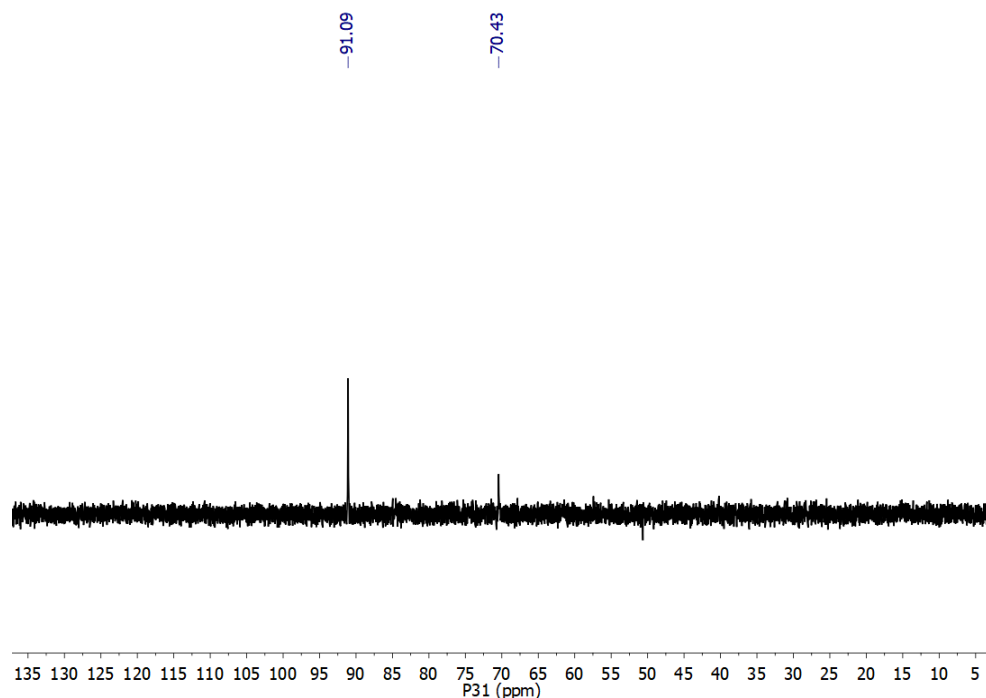
Figure 4.21 $^{31}P\{^1H\}$ NMR spectrum in CD_2Cl_2 obtained after heating **2** in HOAc^F at 60 °C under 20 bar of C_2H_4 for 15 h (202 MHz).

Reactivity of complex 2 in DOAc^F. A sample of trifluoroacetate-bound complex **2** (0.0125 g, 0.0152 mmol) was dissolved in DOAc^F and placed in a Teflon-capped NMR tube. The blue solution was freeze-pump-thawed three times and back-filled with 1 atm of C_2H_4. No reaction was observed, even after heating at 60 °C for 6 h. After heating at 60 °C for one week, incorporation of deuterium primarily into the position *para* to the amido group (δ 6.90) was observed. No significant changes were observed by $^{31}P\{^1H\}$ and $^{19}F\{^1H\}$ NMR spectroscopy.
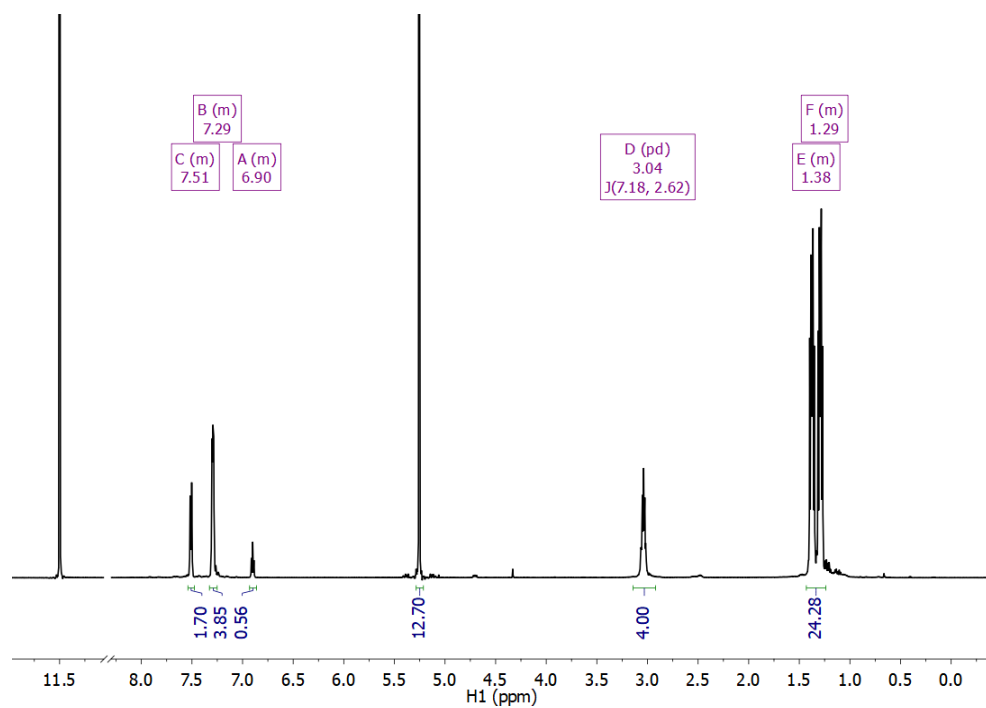
Figure 4.22 ^{1}H NMR spectrum of **2** after heating at 60 °C for one week in DOAc^F under 1 atm C$_2$H$_4$ (δ 5.26) (600 MHz).
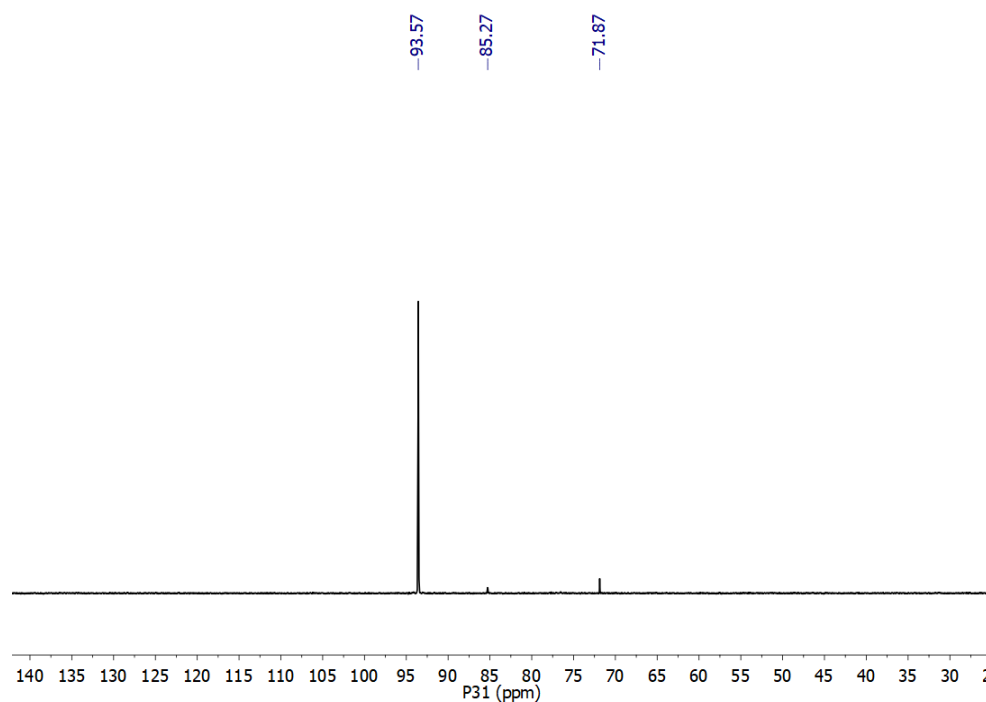
Figure 4.23 ^{31}P{^{1}H} NMR spectrum of **2** after heating at 60 °C for one week in DOAc^F under 1 atm C$_2$H$_4$ (243 MHz).

172

TEM images of 1 and 2.
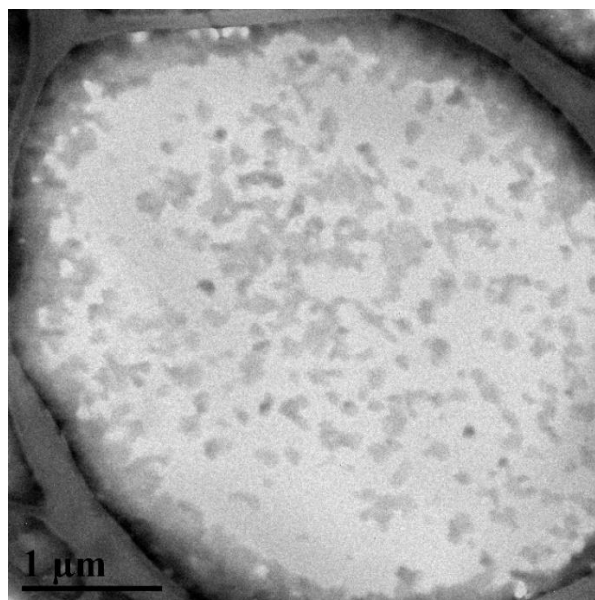
Figure 4.24 Bright field TEM image of a sample of complex **1** showing no presence of any metal nanoparticles.
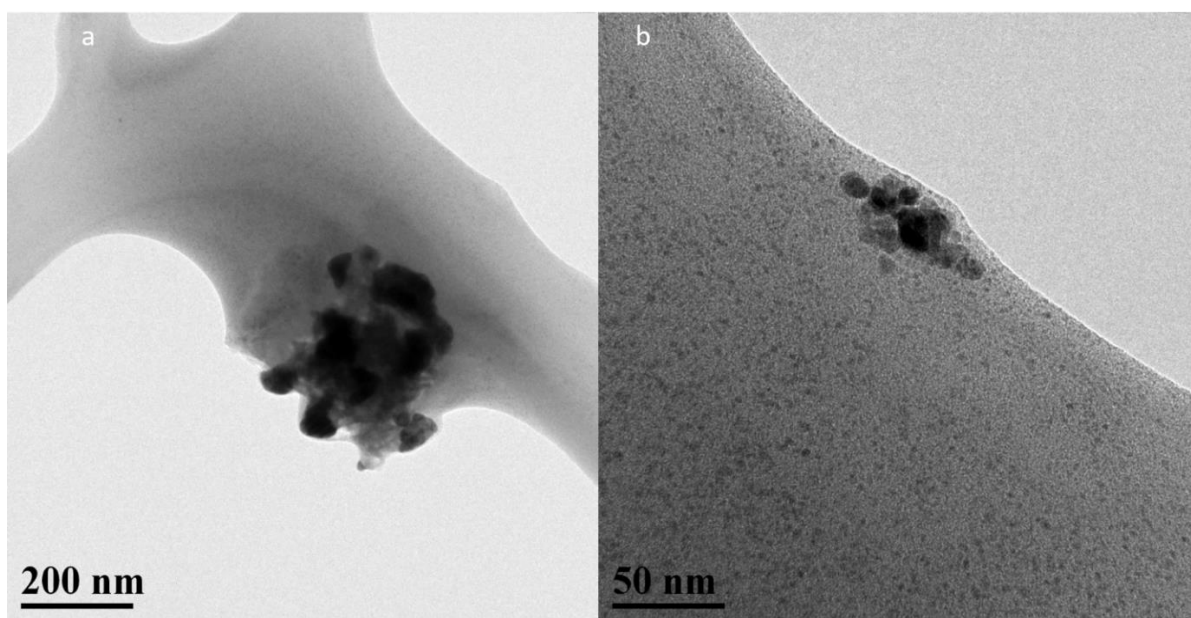
Figure 4.25 Bright field TEM images of a sample of complex **2**. Both (a) and (b) show different-sized clusters of Ag species present in the sample as detected by EDS analysis.
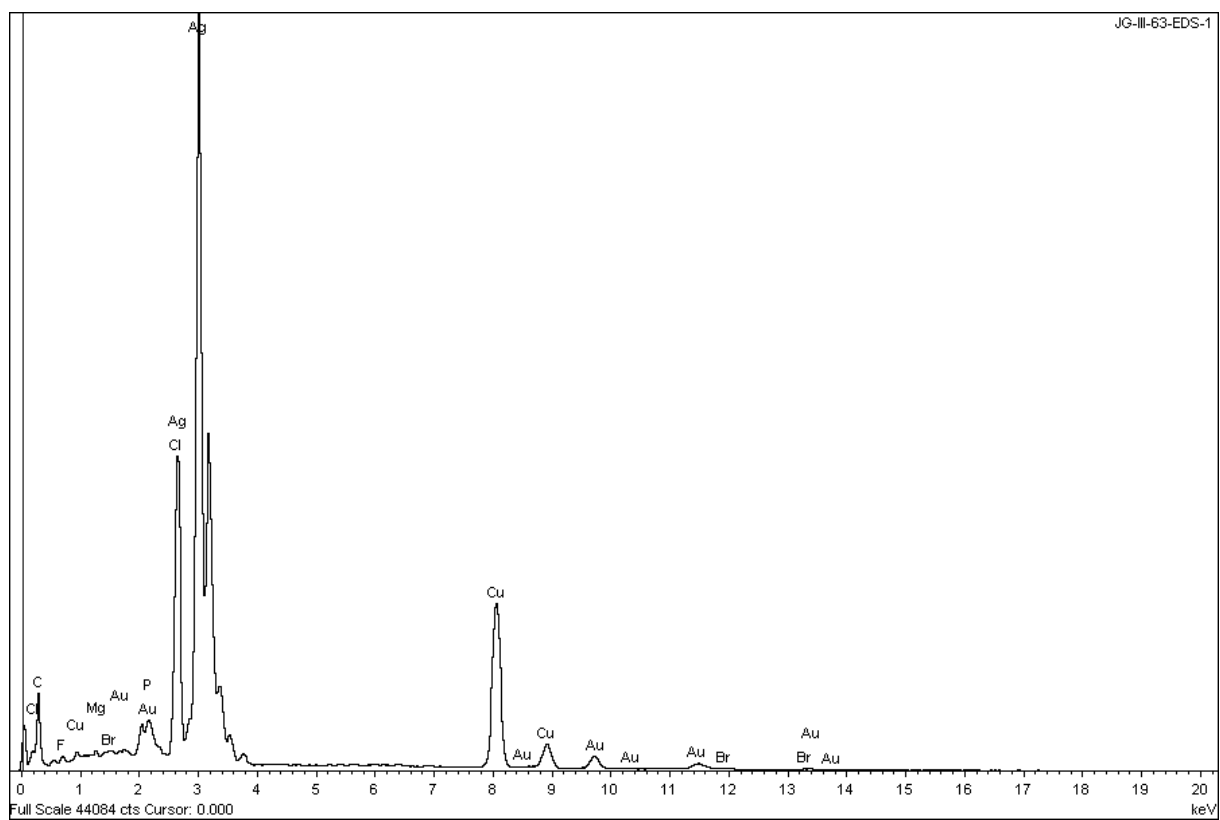
Figure 4.26 Representative EDS spectrum obtained for a sample of **2**.

REFERENCES

(1)   Li, Z.; Brouwer, C.; He, C. Gold-Catalyzed Organic Transformations. *Chem. Rev.* **2008**, *108* (8), 3239–3265.

(2)   Arcadi, A. Alternative Synthetic Methods through New Developments in Catalysis by Gold. *Chem. Rev.* **2008**, *108* (8), 3266–3325.

(3)   Hashmi, A. S. K. Gold-Catalyzed Organic Reactions. *Chem. Rev.* **2007**, *107* (7), 3180–3211.

(4)   Venugopal, A.; Shaw, A. P.; Törnroos, K. W.; Heyn, R. H.; Tilset, M. Synthesis of a Coordinatively Labile Gold(III) Methyl Complex. *Organometallics* **2011**, *30* (12), 3250–3253.

(5)   Joost, M.; Amgoune, A.; Bourissou, D. Reactivity of Gold Complexes towards Elementary Organometallic Reactions. *Angew. Chem. Int. Ed.* **2015**, *54* (50), 15022–15045.

(6)   Kumar, R.; Nevado, C. Cyclometalated Gold(III) Complexes: Synthesis, Reactivity, and Physicochemical Properties. *Angew. Chem. Int. Ed.* **2017**, *56* (8), 1994–2015.

(7)   Smith, D. A.; Roşca, D.-A.; Bochmann, M. Selective Au–C Cleavage in (C ∧ N ∧ C)Au(III) Aryl and Alkyl Pincer Complexes. *Organometallics* **2012**, *31* (17), 5998–6000.

(8)   Johnson, M. W.; DiPasquale, A. G.; Bergman, R. G.; Toste, F. D. Synthesis of Stable Gold(III) Pincer Complexes with Anionic Heteroatom Donors. *Organometallics* **2014**, *33* (16), 4169–4172.

(9)   Schmidbaur, H.; Schier, A. Gold(III) Compounds for Homogeneous Catalysis: Preparation, Reaction Conditions, and Scope of Application. *Arab. J. Sci. Eng.* **2012**, *37* (5), 1187–1225.

(10)   Akhmadullina, N. S.; Borissova, A. O.; Garbuzova, I. A.; Retivov, V. M.; Sandu, R. A.; Kargin, Y. F.; Shishilov, O. N. Gold(III) Carboxylate Complexes with N, N-Chelating Ligands: Synthesis, Structure, and Features of IR Spectra. *Z. Anorg. Allg. Chem.* **2013**, *639* (2), 392–397.

(11)   Langseth, E.; Görbitz, C. H.; Heyn, R. H.; Tilset, M. Versatile Methods for Preparation of New Cyclometalated Gold(III) Complexes. *Organometallics* **2012**, *31* (18), 6567–6571.

(12)   Langseth, E.; Scheuermann, M. L.; Balcells, D.; Kaminsky, W.; Goldberg, K. I.; Eisenstein, O.; Heyn, R. H.; Tilset, M. Generation and Structural Characterization of a gold(III) Alkene Complex. *Angew. Chem. Int. Ed.* **2013**, *52* (6), 1660–1663.

(13)   Savjani, N.; Roşca, D.-A.; Schormann, M.; Bochmann, M. Gold(III) Olefin Complexes. *Angew. Chem. Int. Ed.* **2013**, *52* (3), 874–877.

(14)   Rekhroukh, F.; Brousses, R.; Amgoune, A.; Bourissou, D. Cationic Gold(III) Alkyl

Complexes: Generation, Trapping, and Insertion of Norbornene. *Angew. Chem. Int. Ed.* **2015**, *54* (4), 1266–1269.

(15)   Ball, L. T.; Lloyd-Jones, G. C.; Russell, C. A. Gold-Catalyzed Oxidative Coupling of Arylsilanes and Arenes: Origin of Selectivity and Improved Precatalyst. *J. Am. Chem. Soc.* **2014**, *136* (1), 254–264.

(16)   Roşca, D.-A.; Wright, J. A.; Bochmann, M. An Element through the Looking Glass: Exploring the Au–C, Au–H and Au–O Energy Landscape. *Dalton Trans.* **2015**, *44* (48), 20785–20807.

(17)   Wu, C.-Y.; Horibe, T.; Jacobsen, C. B.; Toste, F. D. Stable gold(III) Catalysts by Oxidative Addition of a Carbon–Carbon Bond. *Nature* **2015**, *517*, 449–454.

(18)   Pintus, A.; Rocchigiani, L.; Fernandez-Cestau, J.; Budzelaar, P. H. M.; Bochmann, M. Stereo- and Regioselective Alkyne Hydrometallation with Gold(III) Hydrides. *Angew. Chem. Int. Ed.* **2016**, *55* (40), 12321–12324.

(19)   Miró, J.; del Pozo, C. Fluorine and Gold: A Fruitful Partnership. *Chem. Rev.* **2016**, *116* (19), 11924–11966.

(20)   Levin, M. D.; Chen, T. Q.; Neubig, M. E.; Hong, C. M.; Theulier, C. A.; Kobylianskii, I. J.; Janabi, M.; O'Neil, J. P.; Toste, F. D. A Catalytic Fluoride-Rebound Mechanism for C(sp^3)-CF$_3$ Bond Formation. *Science* **2017**, *356*, 1272–1276.

(21)   Gu, Y.; Shi, F.; Deng, Y. Esterification of Aliphatic Acids with Olefin Promoted by Brønsted Acidic Ionic Liquids. *J. Mol. Catal. A Chem.* **2004**, *212* (1–2), 71–75.

(22)   Morin, R. D.; Bearse, A. E. Catalytic Esterification of Olefins with Organic Acids. *Ind. Eng. Chem.* **1951**, *43* (7), 1596–1600.

(23)   Langseth, E.; Nova, A.; Tråseth, E. A.; Rise, F.; Øien, S.; Heyn, R. H.; Tilset, M. A Gold Exchange: A Mechanistic Study of a Reversible, Formal Ethylene Insertion into a Gold(III)–Oxygen Bond. *J. Am. Chem. Soc.* **2014**, *136* (28), 10104–10115.

(24)   Holmsen, M. S. M.; Nova, A.; Balcells, D.; Langseth, E.; Øien-Ødegaard, S.; Heyn, R. H.; Tilset, M.; Laurenczy, G. Trans -Mutation at Gold(III): A Mechanistic Study of a Catalytic Acetylene Functionalization via a Double Insertion Pathway. *ACS Catal.* **2017**, *7* (8), 5023–5034.

(25)   van Koten, G. The Monoanionic ECE-Pincer Ligand: A Versatile Privileged Ligand Platform—General Considerations. *Top. Organomet. Chem.* **2013**, *40*, 1–20.

(26)   Morales-Morales, D. Pincer Complexes. Applications in Catalysis. *Rev. Soc. Quím. Méx.* **2004**, *48*, 338–346.

(27)   Fernandez-Cestau, J.; Bertrand, B.; Pintus, A.; Bochmann, M. Synthesis, Structures, and Properties of Luminescent (C∧N∧C)gold(III) Alkyl Complexes: Correlation between Photoemission Energies and C–H Acidity. *Organometallics* **2017**, *36* (17), 3304–3312.

(28)   Rocchigiani, L.; Fernandez-Cestau, J.; Agonigi, G.; Chambrier, I.; Budzelaar, P. H.

M.; Bochmann, M. Gold(III) Alkyne Complexes: Bonding and Reaction Pathways. *Angew. Chem. Int. Ed.* **2017**, *56* (44), 13861–13865.

(29) Roşca, D.-A.; Fernandez-Cestau, J.; Morris, J.; Wright, J. A.; Bochmann, M. Gold(III)-CO and gold(III)-CO$_2$ Complexes and Their Role in the Water-Gas Shift Reaction. *Sci. Adv.* **2015**, *1* (9), e1500761.

(30) Kumar, R.; Krieger, J.-P.; Gómez-Bengoa, E.; Fox, T.; Linden, A.; Nevado, C. The First Gold(III) Formate: Evidence for β-Hydride Elimination. *Angew. Chem. Int. Ed.* **2017**, *56* (42), 12862–12865.

(31) Kumar, R.; Linden, A.; Nevado, C. Luminescent (N^C^C) Gold(III) Complexes: Stabilized Gold(III) Fluorides. *Angew. Chem. Int. Ed.* **2015**, *54* (48), 14287–14290.

(32) Kleinhans, G.; Hansmann, M. M.; Guisado-Barrios, G.; Liles, D. C.; Bertrand, G.; Bezuidenhout, D. I. Nucleophilic T-Shaped (LXL)Au(I)-Pincer Complexes: Protonation and Alkylation. *J. Am. Chem. Soc.* **2016**, *138* (49), 15873–15876.

(33) Roşca, D.-A.; Smith, D. A.; Bochmann, M. Cyclometallated Gold(III) Hydroxides as Versatile Synthons for Au–N, Au–C Complexes and Luminescent Compounds. *Chem. Commun.* **2012**, *48* (58), 7247–7249.

(34) Liang, L.-C.; Chien, P.-S.; Lin, J.-M.; Huang, M.-H.; Huang, Y.-L.; Liao, J.-H. Amido Pincer Complexes of Nickel(II): Synthesis, Structure, and Reactivity. *Organometallics* **2006**, *25* (6), 1399–1411.

(35) Fan, L.; Yang, L.; Guo, C.; Foxman, B. M.; Ozerov, O. V. N−C Cleavage in Pincer PNP Complexes of Palladium. *Organometallics* **2004**, *23* (20), 4778–4787.

(36) Fan, L.; Foxman, B. M.; Ozerov, O. V. N−H Cleavage as a Route to Palladium Complexes of a New PNP Pincer Ligand - SI. *Organometallics* **2004**, *23* (3), 326–328.

(37) Kosanovich, A. J.; Shih, W.-C.; Ramírez-Contreras, R.; Ozerov, O. V. N–H Cleavage as a Route to New Pincer Complexes of High-Valent Rhenium. *Dalton Trans.* **2016**, *45* (46), 18532–18540.

(38) Whited, M. T.; Grubbs, R. H. Synthesis and Reactivity of Iridium(III) Dihydrido Aminocarbenes. *Organometallics* **2008**, *27* (22), 5737–5740.

(39) Adhikari, D.; Pink, M.; Mindiola, D. J. Mild Protocol for the Synthesis of Stable Nickel Complexes Having Primary and Secondary Silyl Ligands. *Organometallics* **2009**, *28* (7), 2072–2077.

(40) Kurogi, T.; Carroll, P. J.; Mindiola, D. J. A Terminally Bound Niobium Methylidyne. *J. Am. Chem. Soc.* **2016**, *138* (13), 4306–4309.

(41) Kamitani, M.; Pinter, B.; Searles, K.; Crestani, M. G.; Hickey, A.; Manor, B. C.; Carroll, P. J.; Mindiola, D. J. Phosphinoalkylidene and -Alkylidyne Complexes of Titanium: Intermolecular C–H Bond Activation and Dehydrogenation Reactions. *J. Am. Chem. Soc.* **2015**, *137* (37), 11872–11875.

(42) Kurogi, T.; Kamitani, M.; Manor, B. C.; Carroll, P. J.; Mindiola, D. J. Reactivity

Studies of a Zirconium Methylidene Complex: Group Transfer and Methylenation Reactions. *Organometallics* **2017**, *36* (1), 74–79.

(43) Harkins, S. B.; Peters, J. C. A Highly Emissive Cu_2N_2 Diamond Core Complex Supported by a [PNP] - Ligand. *J. Am. Chem. Soc.* **2005**, *127* (7), 2030–2031.

(44) Vreeken, V.; Broere, D. L. J.; Jans, A. C. H.; Lankelma, M.; Reek, J. N. H.; Siegler, M. A.; van der Vlugt, J. I. Well-Defined Dinuclear Gold Complexes for Preorganization-Induced Selective Dual Gold Catalysis. *Angew. Chem. Int. Ed.* **2016**, *55* (34), 10042–10046.

(45) Vreeken, V.; Siegler, M. A.; van der Vlugt, J. I. Controlled Interconversion of a Dinuclear Au Species Supported by a Redox-Active Bridging PNP Ligand Facilitates Ligand-to-Gold Electron Transfer. *Chem. Eur. J.* **2017**, *23* (23), 5585–5594.

(46) CCDC 1812837 (for **1**), and 1812838 (for **2′**) contain the supplementary crystallographic data for this Chapter. These data can be obtained free of charge from The Cambridge Crystallographic Data Centre.

(47) Ni, J.; Wei, K.-J.; Liu, Y.; Huang, X.-C.; Li, D. Silver Coordination Polymers Based on Neutral Trinitrile Ligand: Topology and the Role of Anion. *Cryst. Growth Des.* **2010**, *10* (9), 3964–3976.

(48) Lotz, M. D.; Camasso, N. M.; Canty, A. J.; Sanford, M. S. Role of Silver Salts in Palladium-Catalyzed Arene and Heteroarene C–H Functionalization Reactions. *Organometallics* **2017**, *36* (1), 165–171.

(49) Hahn, C.; Morvillo, P.; Vitagliano, A. Olefins Coordinated at a Highly Electrophilic Site − Dicationic Palladium(II) Complexes and Their Equilibrium Reactions with Nucleophiles. *Eur. J. Inorg. Chem.* **2001**, *2001* (2), 419–429.

(50) Hahn, C.; Morvillo, P.; Herdtweck, E.; Vitagliano, A. Coordination of Alkenes at a Highly Electrophilic Site. New Dicationic Platinum(II) Complexes: Synthesis, Structure, and Reactions with Nucleophiles §. *Organometallics* **2002**, *21* (9), 1807–1818.

(51) Hahn, C. Enhancing Electrophilic Alkene Activation by Increasing the Positive Net Charge in Transition-Metal Complexes and Application in Homogeneous Catalysis. *Chem. Eur. J.* **2004**, *10* (23), 5888–5899.

(52) Dolomanov, O. V.; Bourhis, L. J.; Gildea, R. J.; Howard, J. A. K.; Puschmann, H. OLEX2 : A Complete Structure Solution, Refinement and Analysis Program. *J. Appl. Cryst.* **2009**, *42* (2), 339–341.

(53) Farrugia, L. J. WinGX and ORTEP for Windows : An Update. *J. Appl. Cryst.* **2012**, *45* (4), 849–854.

(54) Sheldrick, G. M. SHELXT – Integrated Space-Group and Crystal-Structure Determination. *Acta Crystallogr. Sect. A Found. Adv.* **2015**, *71* (1), 3–8.

(55) Bruker. APEX3 Bruker AXS Inc., Madison, Wisconsin, U. APEX3. Madison, Wisconsin, USA. 2016.

(56)   Sheldrick, G. M. Crystal Structure Refinement with SHELXL. *Acta Crystallogr. Sect. C Struct. Chem.* **2015**, *71* (1), 3–8.